MICROSCOPIC NMR IMAGING

A thesis presented in partial fulfilment of
the requirements for the degree of
Doctor of Philosophy
in Physics at
Massey University

by

Craig David Eccles

1987

ABSTRACT

A commercial 60MHz nuclear magnetic resonance spectrometer has been modified to perform non-invasive, high resolution, two dimensional proton density imaging on samples smaller than 10mm.

Orthogonal magnetic field gradients are applied during the experiment to impart a spatial tag to the nuclear spins. The resultant nuclear signal detected by the spectrometer corresponds to a sampling of Fourier space. The exact trajectory in this space depends on the magnitude and timing of the applied gradients. The technique used in this work samples k space in a radial fashion and is termed filtered back projection. Image reconstruction is implemented on a 16 bit personal computer using a two dimensional fast Fourier transform algorithm.

Due to the small volume elements employed the available signal to noise ratio limits the resolution attainable. It is therefore important that the S/N be maximized within the system. To this end careful attention has been paid to the transfer of the nuclear signal from sample to spectrometer. Signal averaging is also used to improve the S/N although this does result in long imaging times (typically 30 to 60 minutes). At present a resolution of about 30µm is achievable for a slice thickness of 1.5mm and a S/N of 40. At the time of initial publication in June 1986, this corresponded to a voxel resolution an order of magnitude better than that obtained by other workers in this field.

The orthogonal field gradients used are capable of generating gradients of up to $2Tm^{-1}$. This provides the possibility of measuring self diffusion coefficients in an intact sample, using the pulsed field gradient spin echo technique - something which would be difficult to achieve with a large scale imaging system. This thesis reports the first measurements of localised self-diffusion coefficients using a combination of the PFGSE technique and NMR imaging.

ACKNOWLEDGEMENTS

I would like to thank the following people for their involvment in this work.

My supervisor Professor Paul Callaghan for providing continuing encouragement, technical and theoretical support when it was needed. For his boundless enthusiasm which has been a great source of inspiration, and for showing a great deal of patience while this manuscript has been written.

Dr Robert O'Driscoll and the team in the electronics workshop for providing technical assistance on a number of occasions.

The mechanical workshop staff for manufacturing various parts of the imaging probe.

Dr Al Roland and Maureen Whineray of Massey's Botany department for providing the plant stem micrographs.

Dr Ian Brooking of the Plant Physiology Division of the DSIR for supplying the wheat samples used in this work.

Dr Colin Jenner of the Waite Research Institute, Adelaide for supplying his expertise in the area of wheat grain physiology.

Fellow post graduate students; James Conway, Peter Daivis, Mark Huirua and Yang Xia for their friendship and support.

Massey University for providing financial support in the form of a Graduate Assistantship and for providing the opportunity to carry out this research.

TABLE OF CONTENTS

LIST OF FIGURES

LIST OF TABLES

SYMBOL TABLE

$P_{\pm}$	Probability that the nuclear spin will be aligned (-) with or opposed (+) to B_0.	38
p	Wire circumference.	42
p_2	$= T_2\Delta f$.	54
Q	Quality factor of rf coil.	41
Re[ ]	Real part of complex term in brackets.	25
R	Rf coil radius	38
$\mathbf{r}$	Image space position vector.	16
r_c	Rf coil resistance.	41
r	Rf coil wire radius.	38
$\mathbf{S}$(FBP)	Smoothing function used in FBP.	71
$\mathbf{S}$(FZ)	Smoothing function used in FZ.	52
S_k	Spatial frequency domain data.	45
S_r	Image domain data.	45
T	Total sampling time.	45
T_1	Spin-lattice relaxation time.	10
T_2	Spin-spin relaxation time.	10
T_2^*	Transverse relaxation time.	12
T_c	Coil temperature in Kelvin.	41
T_r	Experiment repetition time.	76
T_s	Sample temperature in Kelvin.	38
V_c	Volume of coil.	42
V_s	Volume of sample.	38
V_c	Carrier level.	99
V_m	Modulation level.	99

γ	Gyromagnetic ratio.	3
Δf	Frequency domain bandwidth of spectrometer.	41
Δy	Slice thickness.	46
Δz	Spatial resolution in the final image.	38
$\Delta\omega$	Offset from resonance.	146
δ	Skin depth.	42
θ	Tip angle.	9
$\boldsymbol{\mu}$	Magnetic moment vector.	3
μ_0	Permeability of free space.	40
μ_r	Relative permeability.	42
ξ	Induced EMF amplitude.	10
ρ	Proton density function.	16
ρ	Coil wire resistivity.	42

σ	Coil proximity factor.	42
$\boldsymbol{\tau}$	Torque.	3
τ	Short time interval.	12
τ_c	Molecular correlation time.	10
φ	Projection angle.	35
Ψ	Filtered profile.	36
ω_0	Larmor precession frequency due to B_0.	5
ω_1	Larmor precession frequency due to B_1.	8

1.1 Introduction

In 1973 Lauterbur[1] and Mansfield and Grannell[2] proposed a technique which would enable information concerning the position of hydrogen nuclei, within a biological sample, to be determined using nuclear magnetic resonance.

In normal NMR spectroscopy, the resonant frequency depends on the strength of an applied external magnetic field and is modified by the local electronic and nuclear environment. Complex molecules may therefore contain nuclei which are otherwise identical, but which have different resonant frequencies. It is this variation in resonant frequency which is of interest to the NMR spectroscopist.

In NMR imaging, the applied magnetic field is deliberately varied in such a way as to produce a field strength which is effectively different for each point within the sample. By resonantly stimulating the nuclear system and observing the transient response, it is possible, using standard Fourier transform techniques, to reconstruct an image of nuclear density as a function of position.

NMR imaging is one of the few techniques currently available which allows investigation of the structure of an object in a totally non-invasive fashion. Much research effort in this field has therefore been directed toward the development of large scale imaging systems for medical use. However, due to the inherent insensitivity of NMR these machines have limited spatial resolution - typically of order 1mm.

Much useful work could be done if imaging were carried out at the microscopic level, a regime which reveals details unresolved by the human eye at the near point. For the normal eye this corresponds to spatial resolutions of less than 100μm. In chapter 5 we shall discover that high spatial resolution is only possible when the size of the imaging system is small. The standard NMR spectrometer is therefore ideally suited to investigations of this nature.

Some early imaging experiments carried out on spectrometers produced transverse resolutions of between 0.2 and 0.3mm[3,4]. More recently Hall et al. [5] obtained images showing chemical shift information with 0.1mm spatial resolution on long samples with no slice selection. This thesis describes an imaging system, based on a modified 60MHz ^{1}H spectrometer, which has enabled resolutions of ~30μm to be obtained for 1.5mm selectively excited slices.

1.2 Organisation of thesis

This thesis is divided into 11 chapters. Chapter 2 provides a brief semiclassical introduction to NMR while chapter 3 introduces the methods of spatial differentiation and selective excitation which are central to the imaging technique. Chapter 4 extends these techniques to two dimensions by discussing the most commonly used image reconstruction algorithms; filtered back projection (FBP) and Fourier zeugmatography (FZ).

In chapter 5, the all important subject of the signal to noise ratio in imaging is considered while chapter 6 uses the results from this chapter to calculate the signal to noise ratio and spatial resolution which can be expected when an image is reconstructed using FBP or FZ. A comparison of the two techniques is presented at the end of this chapter, along with a discussion on ways in which the spatial resolution might be improved.

Chapters 7 and 8 consider the hardware aspects of the project, chapter 7 providing a brief description of the major elements of the FX-60 spectrometer and chapter 8 a detailed discussion of those modifications and additions to the spectrometer which have made microscopic imaging possible.

The experimental results presented in chapter 9 follow the improvements in image quality and resolution which have occured during the development of the instrument. Results from more complex experiments, such as diffusion contrast imaging are also presented in this chapter.

Chapter 10 presents the relevant theory for a series of experiments which we hope to implement on the imaging system in the near future while concluding remarks are given in chapter 11.

2 NMR theory

2.1 Introduction

Many nuclei possess an inherent magnetic moment and angular momentum. Using a semiclassical approach these two quantites can be represented by the vectors $\boldsymbol{\mu}$ and $\mathbf{I}$ which are related by the expression

$$\boldsymbol{\mu} = \gamma \mathbf{I} \tag{2.1}$$

with the proportionality constant, γ, being termed the gyromagnetic ratio.

The angular momentum has a magnitude which is proportional to $\hbar = h/2\pi$, where h is Planck's constant

$$|\mathbf{I}| = \sqrt{[I(I+1)]}\,\hbar \tag{2.2}$$

and I is some integer or half integer value, termed the spin quantum number.

Of all nuclei, the hydrogen nucleus, which has spin I=1/2, is the most important in NMR imaging, because of its abundance in biological tissue and high gyromagnetic ratio.

The first step in observing the resonance phenomenon is to place the nuclei of interest in a large uniform magnetic field $\mathbf{B_0}$ which we shall direct along the z axis. In such a field the z component of the angular momentum for a spin half particle in an energy eigenstate will be

$$I_z = \pm 1/2\hbar \tag{2.3}$$

(see figure 2.1).

2.2 The precession equations

Because of its magnetic moment and angular momentum the nucleus will experience a torque $\boldsymbol{\tau} = \boldsymbol{\mu} \times \mathbf{B_0}$ which causes it to precess about $\mathbf{B_0}$. The magnitude of the precession frequency can be determined by solving the equation of motion for such a system.

Since torque is just the time rate of change of angular momentum we see that

$$d\mathbf{I}/dt = \boldsymbol{\mu} \times \mathbf{B_0}. \tag{2.4}$$

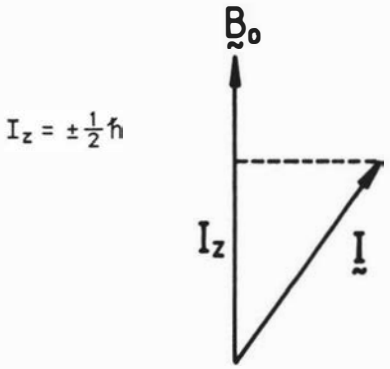

Figure 2.1 Components of the angular momentum vector **I** for a spin $\frac{1}{2}$ particle in a magnetic field $\mathbf{B}_0$.

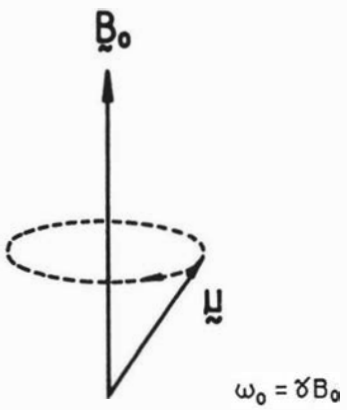

Figure 2.2 Precession of the nuclear moments about the z axis due to the applied field $\mathbf{B}_0$.

Using the result from equation 2.1 we therefore obtain

$$d\boldsymbol{\mu}/dt = \gamma \boldsymbol{\mu} \times \mathbf{B_0} \tag{2.5}$$

In component form this expression expands to give, for a general field **B**

$$\begin{aligned} d\mu_x/dt &= \gamma(\mu_y B_z - \mu_z B_y) \\ d\mu_y/dt &= \gamma(\mu_z B_x - \mu_x B_z) \\ d\mu_z/dt &= \gamma(\mu_x B_y - \mu_y B_x). \end{aligned} \tag{2.6}$$

Our initial interest is for the case where $B_x = B_y = 0$ and $B_z = B_0$. We then have

$$\begin{aligned} d\mu_x/dt &= \gamma \mu_y B_0 \\ d\mu_y/dt &= -\gamma \mu_x B_0 \\ d\mu_z/dt &= 0. \end{aligned} \tag{2.7}$$

Solutions to these are

$$\begin{aligned} \mu_x &= \mu_0 \sin \gamma B_0 t \\ \mu_y &= \mu_0 \cos \gamma B_0 t \\ \mu_z &= \pm 0.5 \gamma \hbar \end{aligned} \tag{2.8}$$

where $\mu_0 = \gamma \hbar \sqrt{[0.5(1+0.5)]}$.

These semiclassical solutions imply a precession of the magnetic moment about the z axis at an angular frequency $\omega_0 = \gamma B_0$ - see figure 2.2.

Thus far we have only considered the motion of a single spin for which, strictly speaking, a formal quantum mechanical description is required. However, since we are always interacting with a macroscopic sample we must consider the combined effect of a large number of spins. For spins experiencing magnetic interactions, the quantum mechanics may be incorporated as follows.

We know that a spin 1/2 particle can occupy two states, characterized by the quantum number m which can be either ±1/2 (spin up or spin down).

At room temperature approximately half the spins in our sample will be in the spin up state and half in the spin down state. Since the magnetic moment is a vector quantity it is reasonable to define a net magnetization $\mathbf{M}$ which is equal to the vector sum of the precessing nuclear moments, that is

$$\mathbf{M} = \sum_{i=0}^{N_h} \boldsymbol{\mu}_i \tag{2.9}$$

where N_h is the number of nuclei per unit volume.

Since the azimuthal phase angle of the precessing nuclei is random and evenly distributed over the range $0 \rightarrow 2\pi$ we can safely assume that the net equilibrium magnetization (due to the slight population difference between the two states) will lie along the main field axis (see figure 2.3).

Because the energy levels of the two states are different we should be able to induce a transition between them by introducing a time dependent perturbation of the appropriate frequency. Since the potential energy difference between the two levels is

$$\begin{aligned} \Delta E &= (-\boldsymbol{\mu}.\mathbf{B})_{\text{spin down}} - (-\boldsymbol{\mu}.\mathbf{B})_{\text{spin up}} \\ &= \gamma \hbar B_0 \end{aligned} \tag{2.10}$$

we have that

$$\omega_0 = \Delta E/\hbar = \gamma B_0 \tag{2.11}$$

which is just the precession frequency observed earlier. Resonant frequencies in NMR tend to lie in the radio frequency (rf) range; the system used in this work operates at 60MHz.

We are now in a position to determine the behaviour of the net magnetization during the application of a transverse magnetic field oscillating at radio frequencies.

For the purposes of this analysis it is convenient to represent the oscillating magnetic component of the rf field, B_1, as two counter-rotating fields lying in the x-y plane (any component along the z axis will have little effect as $B_0 \gg B_1$).

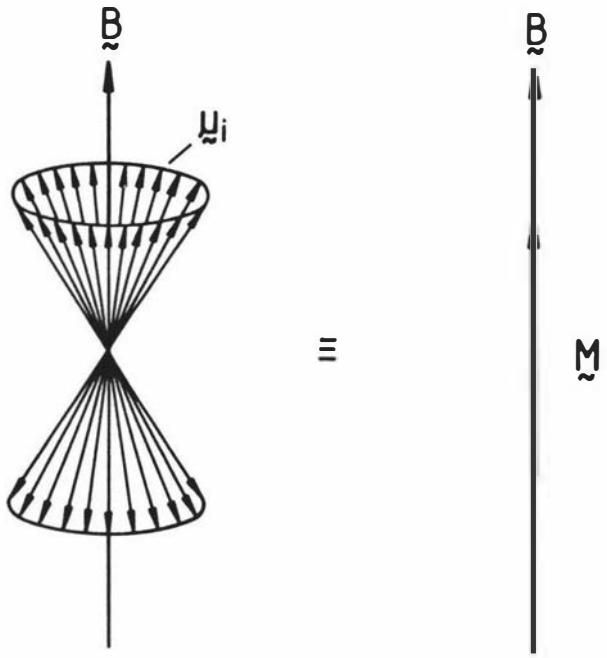

Figure 2.3 Macroscopic magnetization due to randomly distributed magnetic moments and a population difference between the $m=\pm\frac{1}{2}$ state.

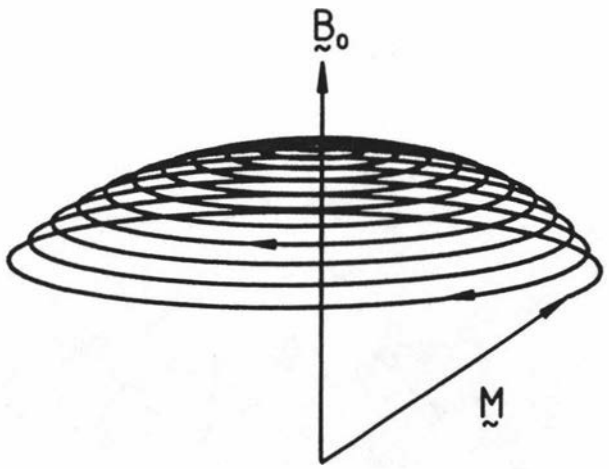

Figure 2.4 Motion of the magnetization vector **M** in the lab frame during the application of an rf field of frequency $\omega_0 = \gamma B_0$.

$$\mathbf{i}2B_1 = [\mathbf{i}\, B_1 \cos(\omega_0 t) - \mathbf{j}\, B_1 \sin(\omega_0 t)] + [\mathbf{i}\, B_1 \cos(\omega_0 t) + \mathbf{j}\, B_1 \sin(\omega_0 t)]. \quad (2.12)$$

Let us consider the two counter-rotating fields in turn. The first rotates in a clockwise fashion about the z axis at angular frequency ω_0. In that frame of reference the individual magnetic moments appear stationary and so B_z must be zero (since $\omega = \gamma B$). This component of the rf field is therefore capable of interacting strongly with the magnetic moments despite its small size when compared with B_0. The second term corresponds to a field rotating counter-clockwise to the precessing moments at $2\omega_0$. In this frame $B_z = 2B_0$. Since $2B_0 >> B_1$ (typically thousands of times larger) this component will have negligible effect on **M**. This is the well known rotating frame approximation (ref. 6 page 21).

Using only the first term we therefore obtain

$$\begin{aligned} dM_x/dt &= \gamma[M_y B_0 + M_z B_1 \sin(\omega_0 t)] \\ dM_y/dt &= \gamma[M_z B_1 \cos(\omega_0 t) - M_x B_0] \\ dM_z/dt &= -\gamma[M_x B_1 \sin(\omega_0 t) + M_y B_1 \cos(\omega_0 t)] \end{aligned} \quad (2.13)$$

where we have used equation 2.9 to re-express the precession equations in terms of **M** rather than **μ**.

Solving these equations we find

$$\begin{aligned} M_x &= M_0 \sin \omega_1 t \sin \omega_0 t \\ M_y &= M_0 \sin \omega_1 t \cos \omega_0 t \\ M_z &= M_0 \cos \omega_1 t. \end{aligned} \quad (2.14)$$

Equation 2.14 implies that on the application of a rotating magnetic field, of the appropriate frequency, the net magnetization performs two motions - a precession about B_0 at ω_0 and a precession about B_1 at $\omega_1 = \gamma B_1$ (see figure 2.4). From the frame of reference in which $B_z = 0$ this motion becomes a simple precession about B_1 with angular frequency ω_1 (see figure 2.5).

At frequencies away from ω_0 the B_z field will no longer be zero in the rotating frame and so the magnetization will precess about an effective field $\mathbf{B}_{eff}$ (fig. 2.6). It is clear from this diagram

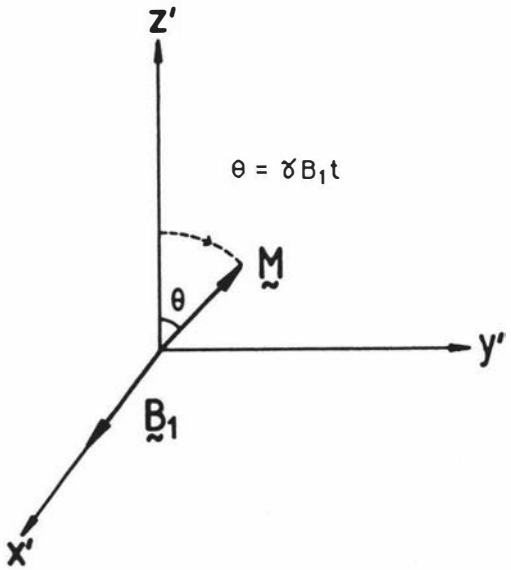

Figure 2.5 Precession of the magnetization vector **M** about the rf field in the frame of reference rotating clockwise about $\mathbf{B_0}$ at $\omega_0 = \gamma B_0$.

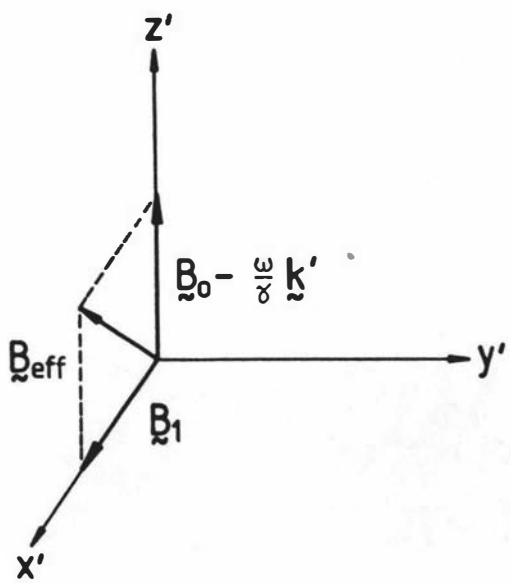

Figure 2.6 Magnetic fields in the frame of reference rotating clockwise about $\mathbf{B_0}$ at some angular frequency ω

that the interaction between $\mathbf{B_1}$ and $\mathbf{M}$ is strongest when $\omega = \omega_0$; hence the resonance term in NMR.

The simplest, and most important, NMR experiment consists of a short rf pulse which is of sufficient duration to tip the magnetization vector through 90° and leave it precessing in the x-y plane. This precessing magnetization induces an oscillating EMF in the solenoidal coil used to supply the pulse (see figure 2.7). The EMF is then amplified and detected by the spectrometer.

2.3 Relaxation processes

The induced EMF, $\xi(t)$, won't last forever as dipolar interactions between adjacent nuclei produce a range of resonant frequencies which cause a dephasing of the nuclear magnetic moments. This results in a reduction of the transverse magnetization. The dephasing effect is referred to as spin-spin relaxation and it may be shown to produce an exponential decay of the induced EMF (the free induction decay) with a characteristic decay time T_2, that is

$$\xi(t) \propto M_{xy}(t) = M_0 \exp(j\omega t) \exp(-t/T_2). \qquad (2.15)$$

where complex notation has been used to represent the magnetization component in the x-y plane.

In addition to a dephasing in the transverse plane, which simply results in a redistribution of the nuclear energy, dephasing of the longitudinal magnetization also occurs due to transverse components of the external field oscillating at the Larmor frequency. This process results in a reduction of the net spin energy by energy exchange with the surrounding medium, or lattice. This return to thermal equilibrium, referred to variously as longitudinal or spin-lattice relaxation is characterised by the equation

$$M_z = M_0\{1-\exp(-t/T_1)\} \qquad (2.16)$$

where T_1 is termed the spin-lattice relaxation time. (Note that this expression describes the return to equilibrium following a 90° pulse). When equations 2.6 are modified to include the effects of relaxation they are referred to as the Bloch equations - see equation A.1.

We shall be concerned with proton nuclear magnetic resonance in dielectric materials. Here the relaxation mechanism occurs via fluctuating dipolar interactions as the molecules containing the protons undergo thermal motion. T_1 processes arise from the spectral components of this motion at ω_0 and $2\omega_0$[7] while T_2 processes include an additional contribution at zero frequency. For the short correlation times ($\tau_c^{-1} >> \omega_0$) applicable for the tumbling motion of small molecules in a liquid, extreme narrowing conditions exist, the spectral density function being "thinly spread". This results in long values for T_1 and T_2, typically of order seconds.

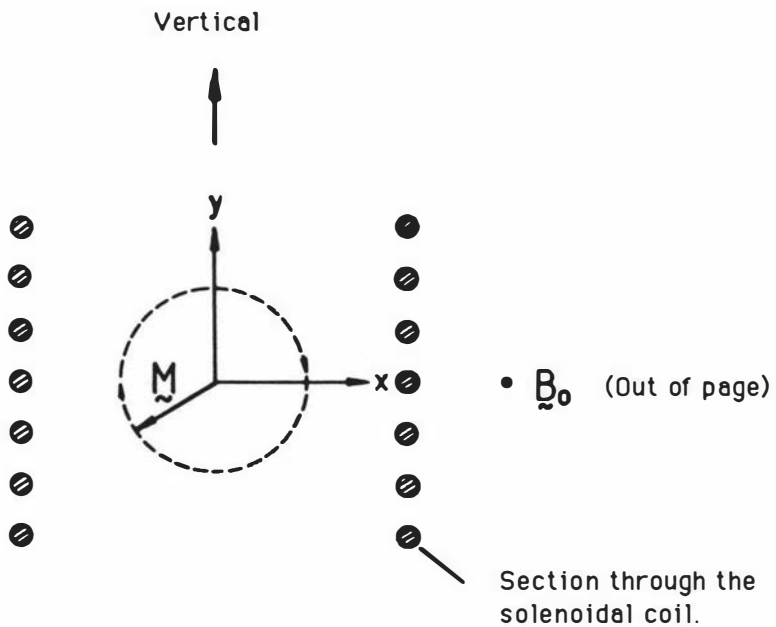

Figure 2.7 Orientation of the solenoidal coil used to supply the rf pulse and detect the nuclear precession.

In the solid regime, the spectral density is concentrated in the vicinity of zero frequency so that T_2 is short (~μs) and T_1 is long (~seconds). For proton NMR in biological tissue an intermediate situation often exists. Protons may be attached to biological macromolecules undergoing slow local motion. For these, T_2 may range from 100μs to 1ms. We shall be concerned in this study with protons associated with water molecules. These protons may be in rapid exchange with solid or semisolid macromolecular sites and their transverse relaxation is in consequence considerably more rapid than in pure water.

T_1 always exceeds T_2 and defines a minimum repetition time between experiments. Each experiment lasts ~T_2 seconds since this is as long as the free induction decay lasts and so if $T_1 >> T_2$, as is the case in many of the experiments in this work, a lot of time will be wasted waiting for the nuclear system to re-equilibrate. This results in an effective sensitivity reduction which exacerbates the insensitivity problem inherent in imaging in the microscopic regime.

2.4 Spin echoes

The transverse relaxation process leads to a spectral broadening termed "homogeneous" since it is common to each nucleus in the ensemble. By contrast, inhomogeneous broadening refers to variations in ω_0 between nuclei in the ensemble. One example is the contribution due to inhomogeneities in the main field. Each nucleus experiences a slightly different B_0 and therefore precesses faster or slower than the mean. Within a period characterised by the time constant T_2^* the system will have completely dephased.

In contrast to homogeneous T_2 processes it is possible to reverse this inhomogeneous dephasing process and produce what is known as a spin echo. If at a time τ after the application of the 90° pulse we apply a 180° pulse the direction of dephasing will be reversed resulting in an echo at time 2τ (see figure 2.8). The sign of the spin echo depends on the relative phase of the applied pulses. If the original rf pulse is considered to be applied along the x' axis the 180° pulse may be applied along either the y' or x' axis resulting in a positive or negative echo respectively (figure 2.9 and 2.10). Any reduction in the echo amplitude will be due to T_2, or diffusion processes.

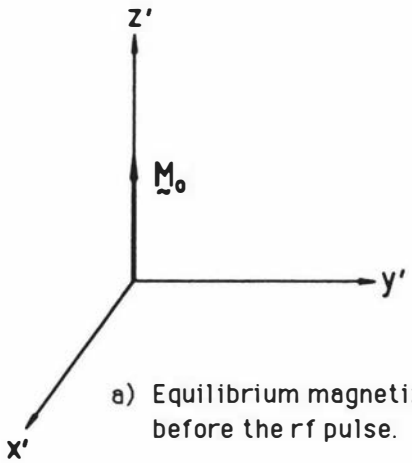

a) Equilibrium magnetization before the rf pulse.

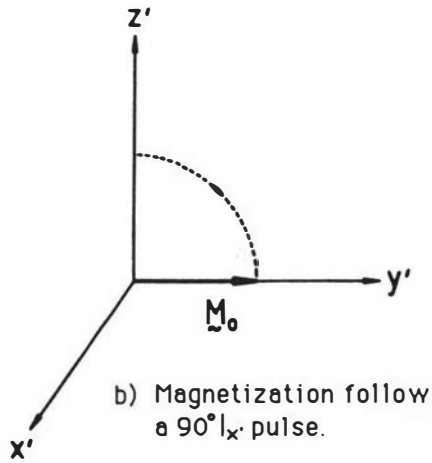

b) Magnetization following a $90°|_{x'}$ pulse.

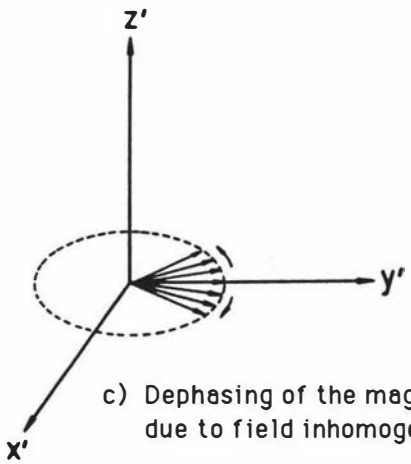

c) Dephasing of the magnetization due to field inhomogeneities.

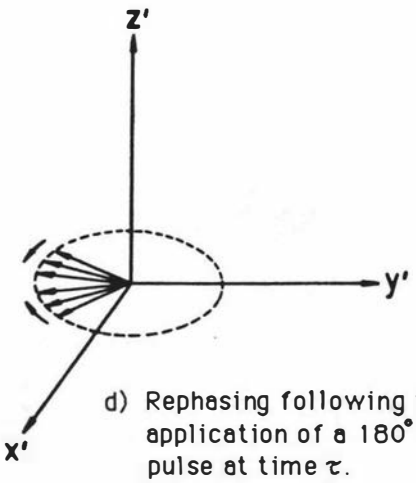

d) Rephasing following the application of a $180°|_{x'}$ pulse at time τ.

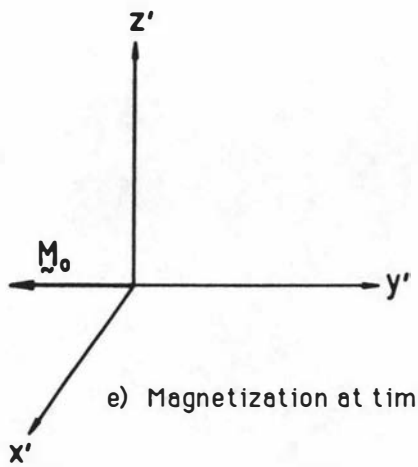

e) Magnetization at time 2τ.

Figure 2.8 Response of the magnetization vector to a $[90°|_{x'} - \tau - 180°|_{x'}]$ pulse sequence.

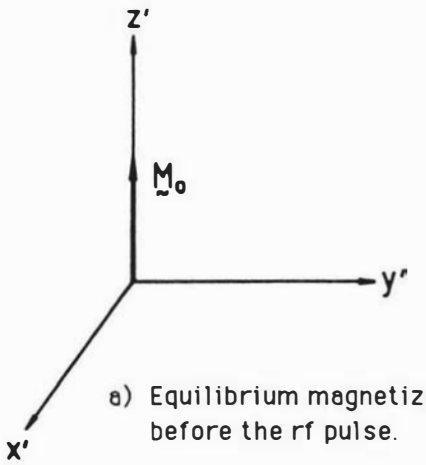

a) Equilibrium magnetization before the rf pulse.

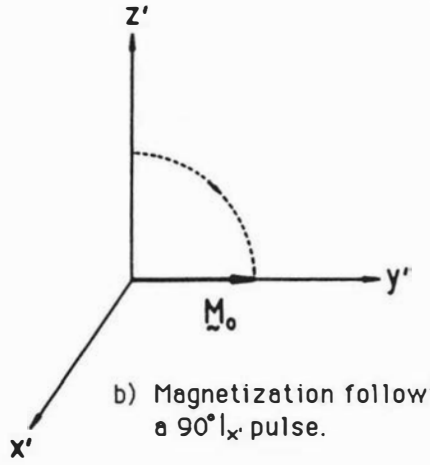

b) Magnetization following a $90°|_{x'}$ pulse.

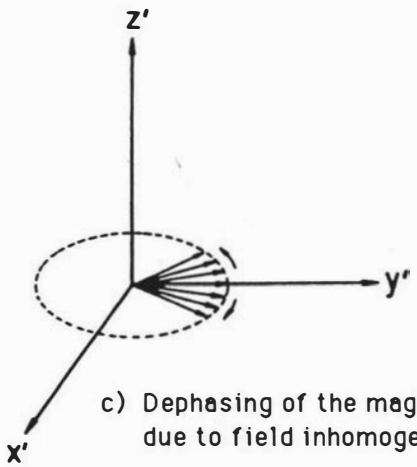

c) Dephasing of the magnetization due to field inhomogeneities.

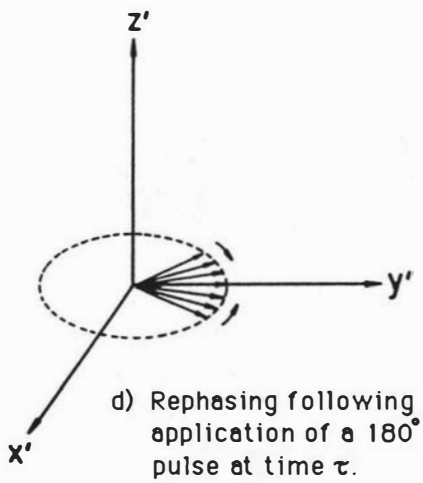

d) Rephasing following the application of a $180°|_{y'}$ pulse at time τ.

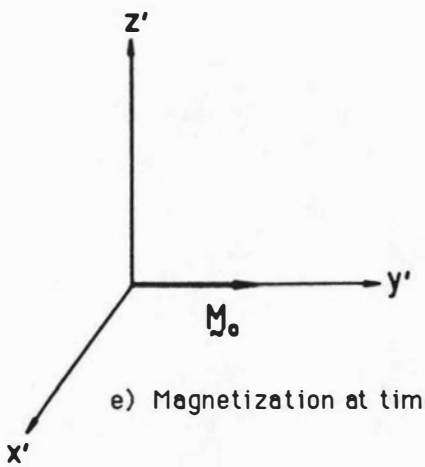

e) Magnetization at time 2τ.

Figure 2.9 Response of the magnetization vector to a $[90°|_{x'} - \tau - 180°|_{y'}]$ pulse sequence.

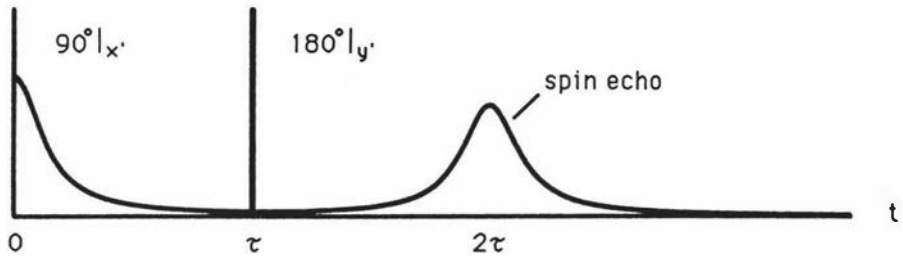

a) Nuclear signal for a [90°|x' – τ – 180°|y'] pulse sequence.

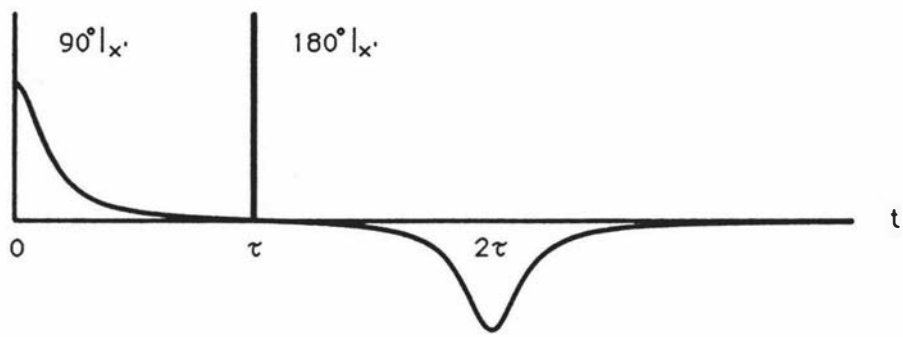

b) Nuclear signal for a [90°|x' – τ – 180°|x'] pulse sequence.

Figure 2.10 Spin echo formation.

3 Imaging theory

3.1 Introduction

In conventional high resolution spectroscopic NMR experiments it is normal to have the sample immersed in a highly homogeneous magnetic field, so that each chemically identical nucleus resonates at the same frequency. This results in narrow spectral lines the width of which should ideally be given by $1/\pi T_2$ (see figure 3.1), where T_2 is the spin-spin relaxation time determined by local variations in the field due to the influence of neighbouring nuclei.

However as we have seen most systems will produce a line-width given by $(\pi T_2^*)^{-1}$ where T_2^* is the effective free induction decay time and combines the broadening due to spin-spin interactions with that due to field inhomogeneity across the sample.

Consider a system in which the field has been purposefully adjusted so as to vary linearly across the sample. From equation 2.11 we know that the resonant frequency will also vary linearly across the sample (fig. 3.2). And so, for an applied field gradient **G**, given by ∇B_z, the resonant frequency will be

$$\omega = \gamma(B_0 + \mathbf{G}.\mathbf{r}). \tag{3.1}$$

For a finite sample the narrow Lorenztian lineshape will therefore be broadened to give a spectral profile characterized by the shape of the sample and the orientation of the gradient.

If the sample is stimulated by a 90° pulse and then subject to a linear gradient the observed nuclear signal from a volume element dV will be

$$d\xi(\mathbf{G},t) \propto \rho(\mathbf{r}) \exp[j(\omega_0 + \gamma\mathbf{G}.\mathbf{r})t]\, dV \tag{3.2}$$

where $\rho(\mathbf{r})$ is the spin density function, with units of nuclei m^{-3} and the proportionality constant depends on the coil parameters used (see section 5.1). T_2 broadening has not been included in the above equation as we assume its effect to be negligible when compared to that produced by the applied gradient. Suppose we consider the signal which is produced in the heterodyne detection frame and neglect the oscillation at ω_0. Furthermore we shall define an area density function $\rho(z,x)$ applicable to the imaging of spin slices in the z,x plane. Initially we shall consider the influence of a gradient applied in the z direction. The signal from area element dzdx is then

$$d\xi(k_z) \propto \rho(z,x) \exp(j2\pi k_z z)\, dz\, dx \tag{3.3}$$

Note that for the purposes of this analysis we have expressed ξ in terms of the variable $k_z = (2\pi)^{-1}\gamma G_z t$ which has units of reciprocal space.

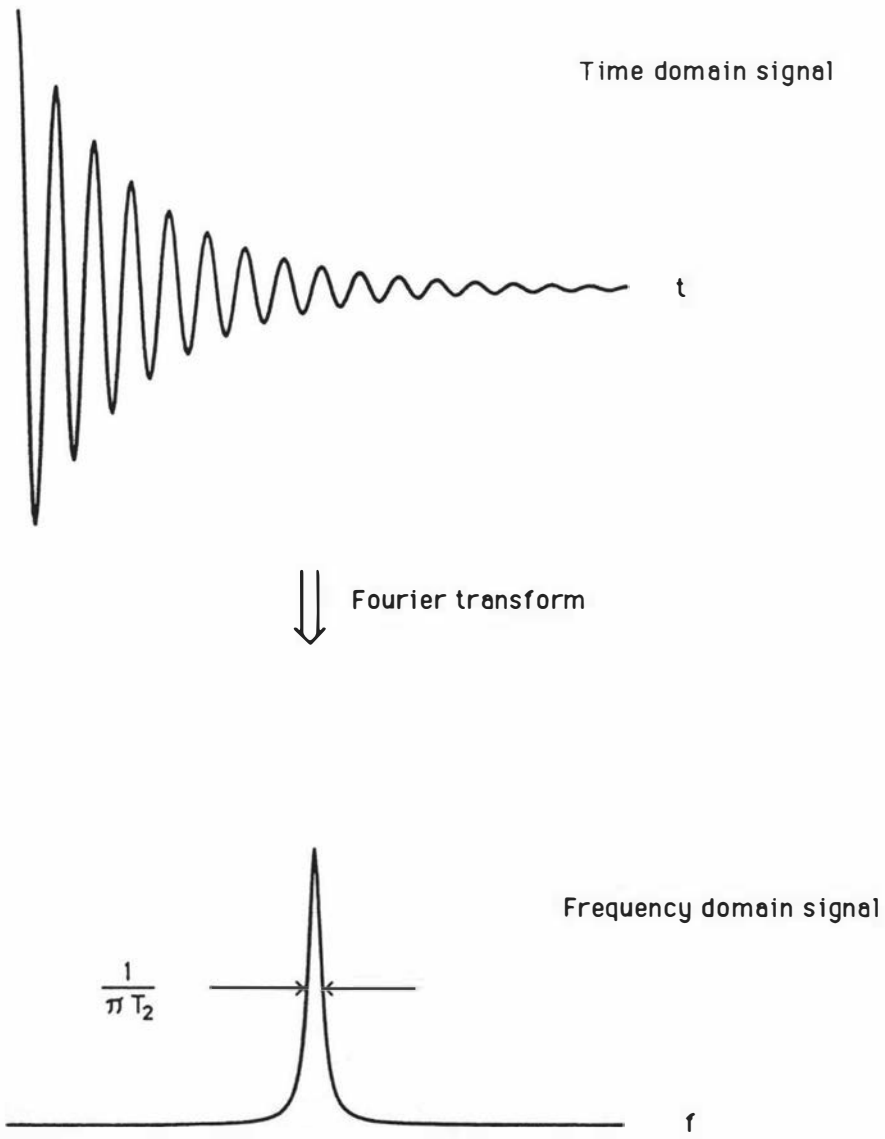

Figure 3.1 Time and frequency domain signals in NMR.

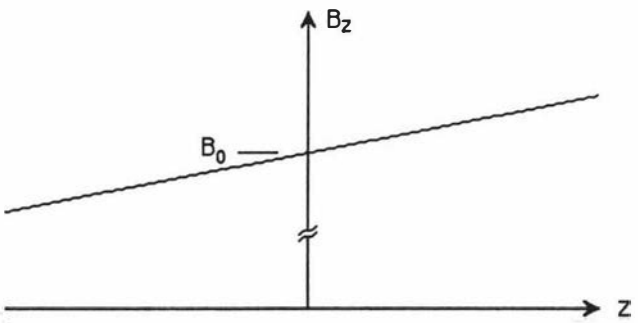

Figure 3.2 Effect of adding a gradient to the main magnetic field.

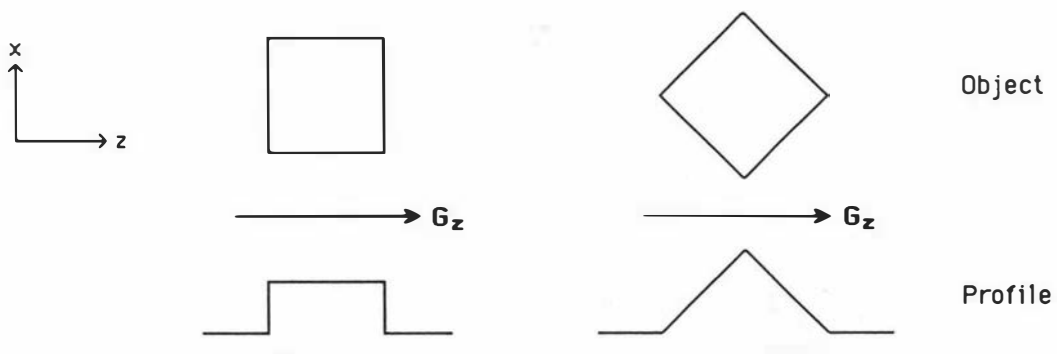

Figure 3.3 Spin density profile as a function of object orientation.

Integrating along the z and x axes gives the total signal

$$\xi(k_z) \propto \int_{-\infty}^{\infty}\int \rho(z,x)\, \exp(j2\pi k_z z)dzdx \tag{3.4}$$

where we have assumed that the detection phase has been set to zero (most spectrometers allow the phase to be adjusted manually).

The frequency domain signal may be found by Fourier transforming $\xi(k_z)$. This analysis is simplified since the inner integral is clearly the inverse transform of $\rho(z,x)$ taken along the z axis (the conjugate variables being z and k_z). Therefore

$$\xi(k_z) \propto \int_{-\infty}^{\infty} F^{-1}\{\rho(z,x)\}\, dx \tag{3.5}$$

and so the frequency domain signal will be

$$F(\xi(k_z)) \propto F\left[\int_{-\infty}^{\infty} F^{-1}\{\rho(z,x)\}\, dx\right] = \int_{-\infty}^{\infty} F[\{F^{-1}\{\rho(z,x)\}]\, dx$$

$$\propto \int_{-\infty}^{\infty} \{\rho(z,x)\}dx. \tag{3.6}$$

The spectral data may therefore be identified as a projection of the spin density in the sample onto the z axis - see figure 3.3 for an example. For this reason it is referred to as a **projection profile.**

This procedure, often referred to as one dimensional imaging, enables us to obtain information about the distribution of nuclear spins along the z axis. Unfortunately we have no information regarding the distribution of spins along the x axis. One way to obtain this information would be to selectively excite a strip of spins in the z direction. If this strip could be moved stepwise in the x direction a series of projection profiles could be obtained which correspond to the functions

$$F\{\xi(k_z)\} \propto \int_{x-a}^{x+a} \{\rho(z,x)\}\, dx \qquad (3.7)$$

where 2a is the strip width (see fig. 3.4). For sufficiently small values of 2a the resultant projections would, when displayed appropriately, give a reasonable representation of the two dimensional spin distribution. In fact it turns out that this technique is rather insensitive (ref. 8 page 169) and so more sophisticated methods are used in most modern imaging systems - see chapter 4.

3.2 Selective excitation

The ability to be able to selectively excite a narrow slice of spins in an efficient manner is of prime importance in imaging whether it be used to differentiate spins in the x direction as in the above discussion or to select out a slice along the y axis. (The longitudinal axis of the sample is constrained by the nature of the electromagnet geometry to lie along the y axis).

Recall that the procedure for obtaining a projection profile entails applying a 90° pulse in the absence of a field gradient. The reason for this is as follows. Most 90° rf pulses are 10-20μs long and so can stimulate spins with resonant frequencies over the range 25-50kHz. However because the degree of stimulation varies over this bandwidth (see figure 3.5) a smaller range of frequencies is uniformly excited. This isn't normally a problem in spectroscopic studies since the range of frequencies present in the signal is usually less than 1kHz. However when a gradient is applied the range of frequencies present in the nuclear signal may be much greater (up to 50kHz in our system). This means that those spins away from the origin will experience a much smaller rf pulse and will therefore be tipped through an angle of less than 90°.

If the rf pulse is made particularly broad, say 1ms, and applied simultaneously with a y gradient then only those spins with resonant frequencies in a 1kHz bandwidth around ω_0 will be stimulated in an appreciable manner. It is of course assumed that the pulse amplitude has been proportionately reduced so that $\gamma B_1 \tau$ remains equal to $\pi/2$. Spins with resonant frequencies outside this bandwidth will experience little or no rf field and so will remain unaffected. In this way a narrow slice of spins may be selectively excited. The rf spectral profile is of the sinc form, $\sin(\Delta\omega)/\Delta\omega$ and so does not produce a well defined slice. In a linear response model the nuclear turn angles would show a similar modulation along the y axis. This suggests that a rectangular slice might be stimulated by applying an rf pulse with sinc modulation in the time domain. In fact the response of the nuclear spin system is highly non-linear. The Bloch equations yield a simple analytical solution where the rf pulse amplitude is constant with time[9], but the

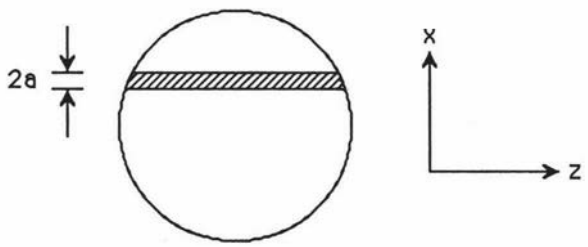

Figure 3.4 Selective excitation of a slice of spins.

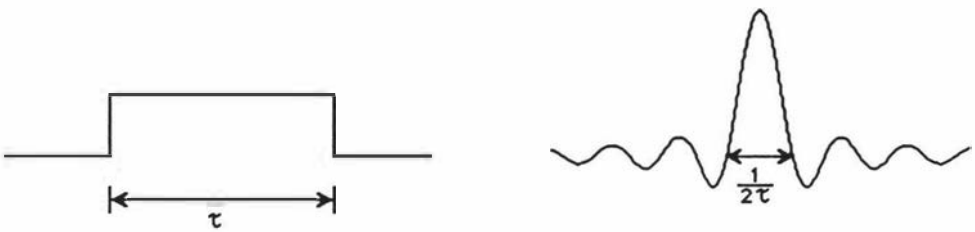

Figure 3.5 Rf pulse in the time and frequency domains.

suggested sinc modulated pulse response is more difficult to obtain. As a first approximation a linear description is employed. This is due to Bailes and Bryant[10].

In the rotating reference frame we will have the situation depicted in figure 3.6. Since $B_{z'}$ varies with position and $B_{x'}$ with time the situation is clearly complicated. In fact the Bloch equations describing the motion of the nuclear moments (in the absence of relaxation) give

$$\begin{aligned} dM_{x'}/dt &= \gamma M_{y'} G_y y \\ dM_{y'}/dt &= \gamma\{M_{z'} B_1(t) - M_{x'} G_y y\} \\ dM_{z'}/dt &= -\gamma M_{y'} B_1(t). \end{aligned} \tag{3.8}$$

Bailes and Bryant have simplified these equations by considering the situation from a frame of reference in which $B_y = G_y y = 0$ (fig. 3.7). This frame rotates clockwise about the z' axis at an angular frequency of $\gamma G_y y$. In this frame $\mathbf{B_1}$ will rotate counter-clockwise at the angular frequency $\gamma G_y y$. If we assume that the two reference frames coincide at the start of the rf pulse, when $t=-\tau$, the Bloch equations become

$$\begin{aligned} dM_{x''}/dt &= -\gamma M_{z''} B_{y''} = -\gamma M_{z''} B_1(t) \sin[\gamma G_y y(t+\tau)] \\ dM_{y''}/dt &= \gamma M_{z''} B_{x''} = \gamma M_{z''} B_1(t) \cos[\gamma G_y y(t+\tau)] \\ dM_{z''}/dt &= \gamma\{ M_{x''} B_{y''} - M_{y''} B_{x''} \} \\ &= \gamma\{M_{x''} B_1(t) \sin[\gamma G_y y(t+\tau)] - M_{y''} B_1(t) \cos[\gamma G_y y(t+\tau)]\} \end{aligned} \tag{3.9}$$

As a further simplification (the linear response assumption) Bailes and Bryant assume the tip angle to be small so that $M_{z''}$ is constant. In this case we have

$$\begin{aligned} dM_{x''}/dt &= -\gamma M_0 B_1(t) \sin[\gamma G_y y(t+\tau)] \\ dM_{y''}/dt &= \gamma M_0 B_1(t) \cos[\gamma G_y y(t+\tau)] \\ dM_{z''}/dt &= 0. \end{aligned} \tag{3.10}$$

If we treat $M_{x''}$ and $M_{y''}$ as components of a complex number the first two equations may be re-expressed as

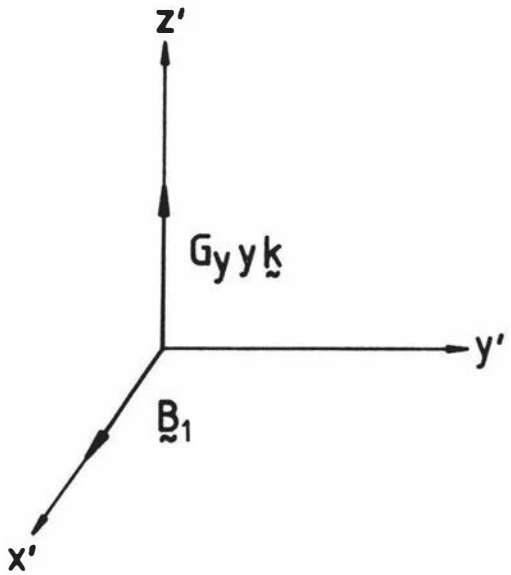

Figure 3.6 Magnetic fields applied during a selective pulse in a frame of reference rotating clockwise about B_0 at ω_0.

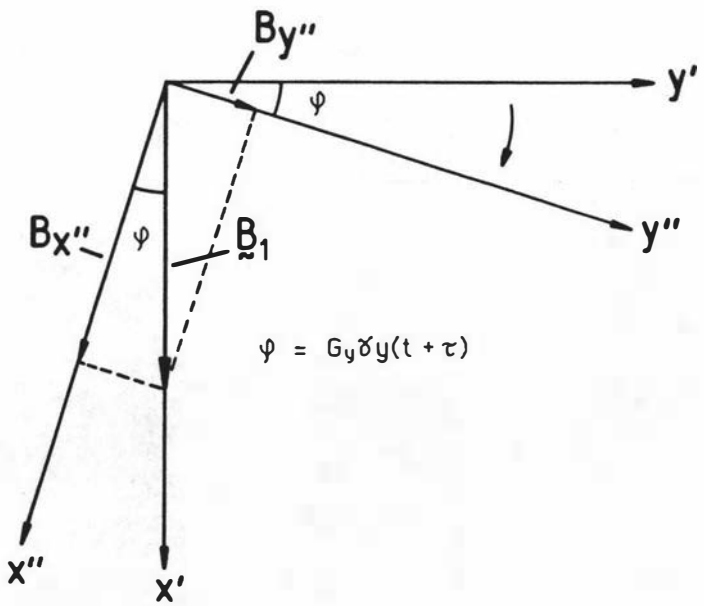

Figure 3.7 Situation in the frame of reference where $B_{z''} = 0$

$$d\mathbf{M}_{x''y''}/dt = \gamma M_0 B_1(t) \exp[-j\gamma G_y y(t+\tau)]. \tag{3.11}$$

Integrating with respect to t gives

$$\mathbf{M}_{x''y''} = \gamma M_0 \exp[-j\gamma G_y y\tau] \int_{-\tau}^{\tau} B_1(t) \exp[-j\gamma G_y y t]\, dt$$

$$= \gamma M_0 \exp[-j\gamma G_y y\tau]\, \mathbf{F}\{B_1(t)\}. \tag{3.12}$$

During the rf pulse the S'' frame has rotated through the angle $\gamma G_y y 2\tau$ with respect to the S' frame and so

$$\mathbf{M}_{x'y'} = \gamma M_0 \exp[j\gamma G_y y\tau]\, \mathbf{F}\{B_1(t)\}. \tag{3.13}$$

From this result we see that the $M_{y'}$ moment has not been left on the y' axis but at an angle $\gamma G_y y\tau$ to it. This dephasing may be removed by applying a y gradient of magnitude $-G_y y$ for a time τ to give

$$\mathbf{M}_{x'y'} = \gamma M_0 \mathbf{F}\{B_1(t)\}$$

$$\Rightarrow \quad M_{y'} = \gamma M_0\, \mathrm{Re}[\mathbf{F}\{B_1(t)\}]. \tag{3.14}$$

The y' magnetization at time τ is therefore proportional to the real part of the Fourier transform of the applied rf pulse. As we wish to excite a rectangular slice of spins it therefore follows that we should excite with a sinc modulated pulse rather than a rectangular one as originally proposed (see figure 3.8).

In situations where rapid gradient reversals are not possible (the case in our system) we can rephase the spins by the application of a short non-selective 180° pulse followed by a gradient pulse of length τ (see figure 3.9).

For large tip angles the $M_z = M_0$ simplification no longer holds. Hoult[11] has shown how the non-linear case can be treated using perturbation theory. In the present work, however, the Bloch equations are solved in their exact form using the Runge-Kutta method specified in appendix A. Figures 3.10 and 3.11 plot $M_{x'}$ and $M_{y'}$ as a function of postion for tip angles of 30°and 90°.

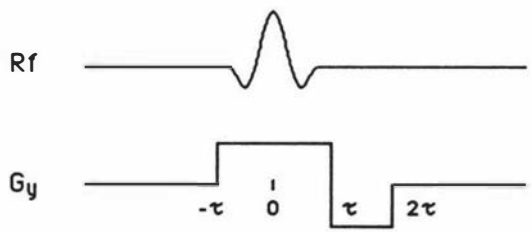

Figure 3.8 Pulse sequence used to selectively excite a slice of spins along the y axis.

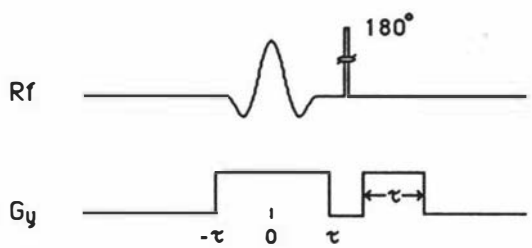

Figure 3.9 An alternative rephasing method used when G_y must remain positive.

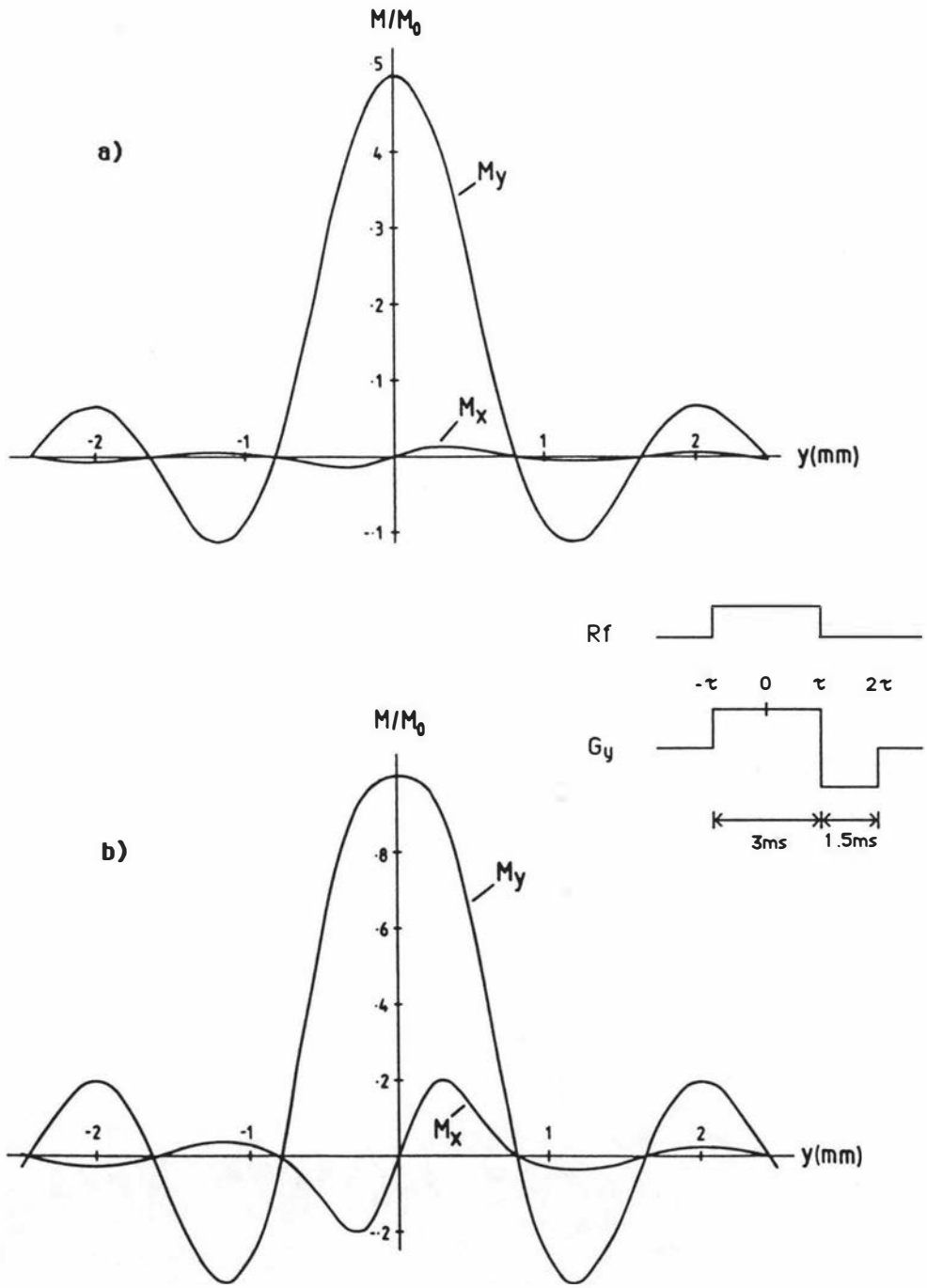

Figure 3.10 Transverse magnetization at time 2τ as a function of position due to selective excitation with a square rf pulse for a tip angle at y=0 of, a) 30° and b) 90°.

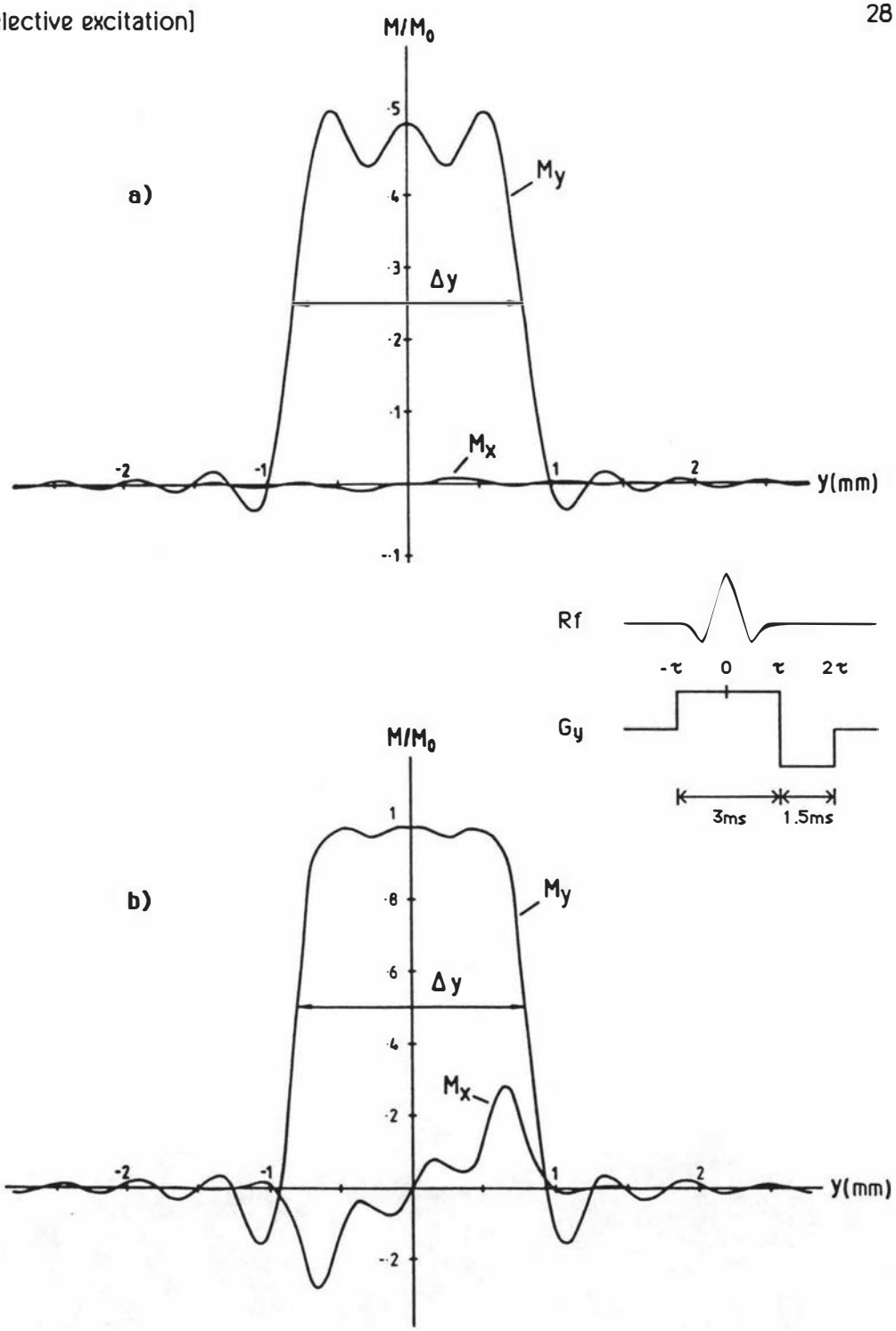

Figure 3.11 Transverse magnetization at time 2τ as a function of position due to selective excitation with a sinc modulated rf pulse for a tip angle at y=0 of, a) 30° and b) 90°.

The relative merit of the different rf pulse shapes may be determined by integrating the $M_y(y)$ curves with respect to position. For the conditions considered in figures 3.10 and 3.11 the sinc pulse produces the greater signal amplitude by a factor of ~2 for 30° pulses. These results have been verified experimentally (see figure 3.12).

It is noteworthy that the major effects of the non-linearity show up in the out of phase magnetization M_x. This implies that the main consequence of non-ideality is the imposition of small phase distortions. In fact the non-ideal responses for φ = 90° are not really a problem as optimum signal amplitudes are obtained for small tip angles and short repetition times (see section 6.9).

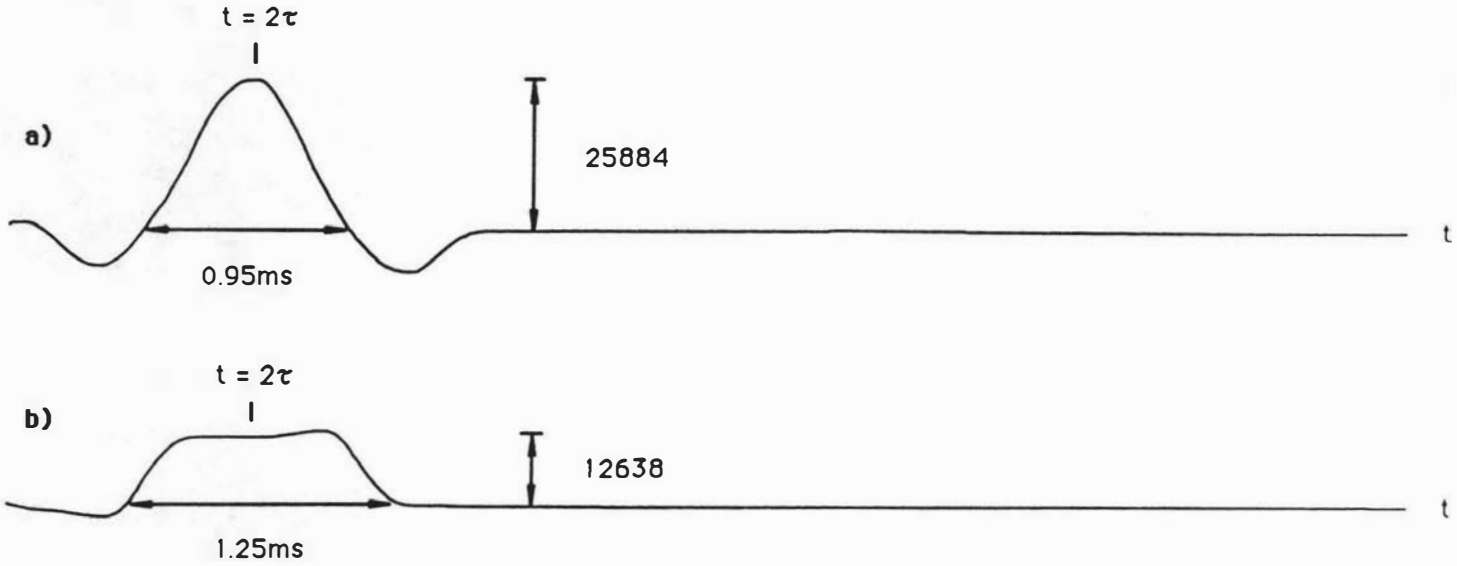

Figure 3.12 Response to a 1ms selective rf pulse using a) sinc modulation and b) rectangular modulation. To show complete echo formation the slice selection gradient has been left on during data acquisition.

4 Imaging techniques

4.1 Fourier zeugmatography

We noted earlier that the signal obtained when a uniform gradient G_z was applied after stimulating a thin transverse slice with a 90° pulse had the form

$$\xi(t) \propto \int_{-\infty}^{\infty}\int \rho(z,x)\exp(j\omega t)\,dzdx \tag{4.1}$$

where $\omega = \gamma G_z z$, in the frame of reference rotating at ω_0.

In Fourier zeugmatography a gradient G_z is applied for a time t_z and then removed and replaced by a gradient G_x for a time t_x, consequently the cumulative phase angle at point (z,x) will be

$$\varphi = \gamma(G_z z t_z + G_x x t_x) \tag{4.2}$$

and so

$$\xi(t_z t_x) \propto \int_{-\infty}^{\infty}\int \rho(z,x)\exp\{j\gamma(G_z z t_z + G_x x t_x)\}\,dzdx. \tag{4.3}$$

Dimensionally $\gamma G_z t_z$ and $\gamma G_x t_x$ have units of radians per metre and so may be replaced by the variables $2\pi k_z$ and $2\pi k_x x$, where k_z and k_x are the reciprocal space coordinates. With this substitution we identify $\xi(k_z k_x) = \xi(t_z t_x)$ as the two dimensional inverse transform of the spin density function $\rho(z,x)$.

$$\xi(k_z k_x) \propto \int_{-\infty}^{\infty}\int \rho(z,x)\exp\{j2\pi(k_z z + k_x x)\}\,dzdx. \tag{4.4}$$

If we let $k_x = 0$ we regain our original expression (equation 4.1) and as time advances we see that $\xi(t) = \xi(k_z 0)$, in other words, we are mapping k space along the positive k_z axis (see figure 4.1).

If k_x is non-zero then $\xi(t) = \xi(k_z k_x)$ will correspond to a horizontal line in k space displaced from the origin in the vertical direction by k_x (see fig. 4.2).

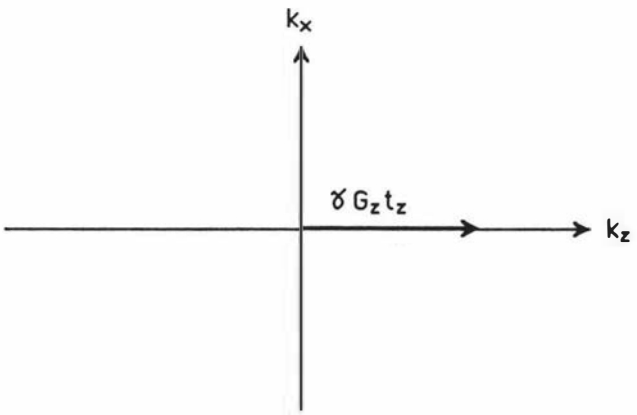

Figure 4.1 k space sampling for $t_x = 0$.

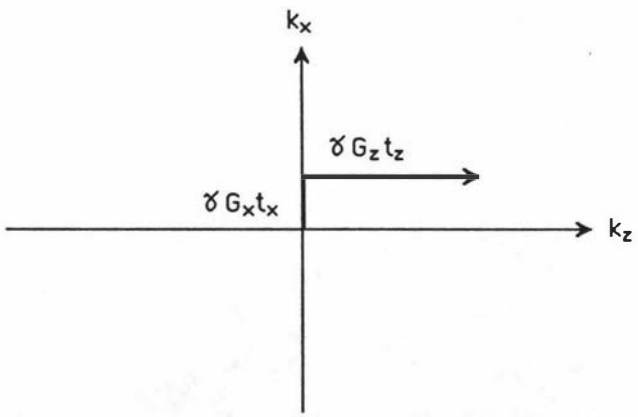

Figure 4.2 k space sampling for $t_x \neq 0$.

A number of experiments can be performed with different values of t_x (figures 4.3 and 4.4) so that the first quadrant of k space is sampled in a raster fashion, each fid being stored as a row in a matrix representing k space. A reversal of the G_x gradient allows the fourth quadrant to be mapped, while the second and third quadrants may be determined from the first and fourth using the relationship

$$\xi(-k_z,-k_x) = \xi^*(k_z,k_x) \tag{4.5}$$

where ξ^* is the complex conjugate of ξ. Note that equation 4.5 depends on the reality of $\rho(z,x)$ which means the detection phase must be set "correctly".

If the image of $\rho(z,x)$ is to contain N×N pixels a minimum of N experiments must be performed, each horizontal scan consisting of N/2 complex data points. With typical t_d values of 1 second (the time required for the nuclei to re-equilibrate) and N_{acc} accumulations per scan the total data acquistion time will be $\approx NN_{acc}$ seconds. Faster imaging times may be obtained by reducing t_d and the flip angle until an optimum signal amplitude is obtained (see section 6.9).

The technique just described was developed by Kumar et. al. in 1976[12] and is referred to as **Fourier zeugmatography.**

Variations on this technique exist - rather than varying t_x one can change the level of G_x from experiment to experiment. The technique is then referred to as spin-warp imaging[13]. This has the advantage that the time delay between excitation and sampling is kept constant and so amplitude distortion due to relaxation effects can be kept to a minimum.

4.2 Filtered back projection

Another way of mapping k space is to apply G_z and G_x simultaneously and adjust their respective magnitudes from experiment to experiment so as to sample k space in a radial fashion (see figures 4.5 and 4.6).

The net phase angle at time t of the signal arising from the point (z,x) will be

$$\varphi = \omega t = \gamma \mathbf{G}.\mathbf{r}\, t = 2\pi \mathbf{k}.\mathbf{r} \tag{4.6}$$

where

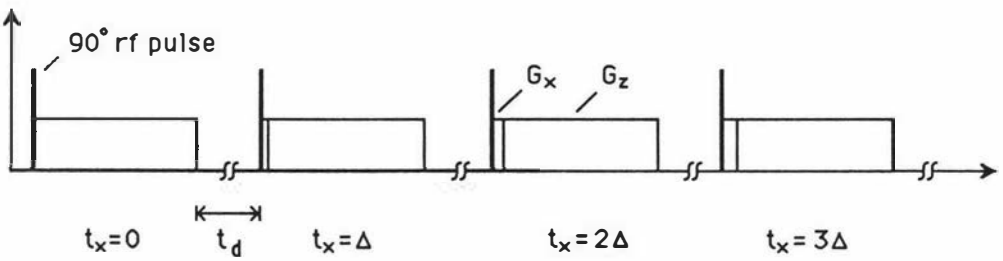

Figure 4.3 Pulse sequence for Fourier Zeugmatography.

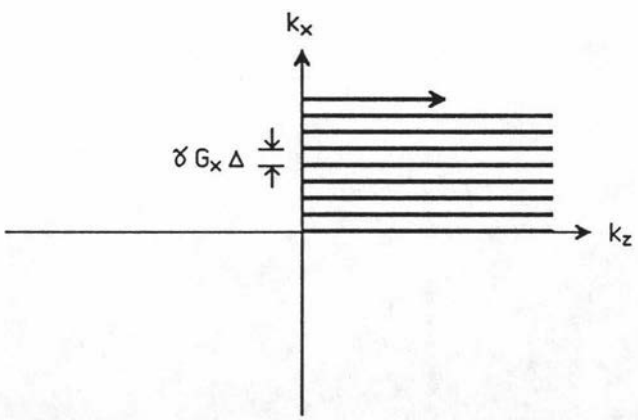

Figure 4.4 Sampling the first quadrant of k space.

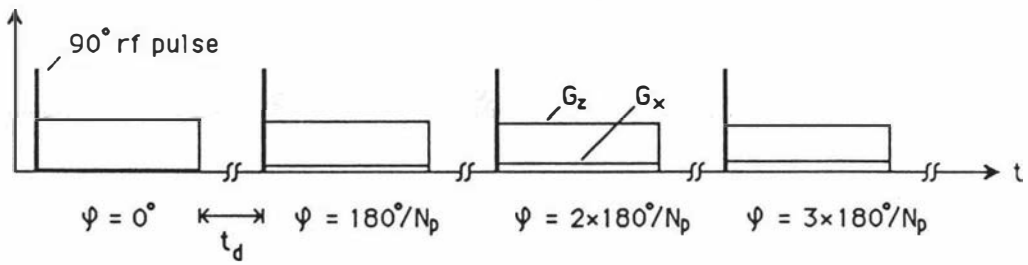

Figure 4.5 Pulse sequence for filtered back projection.

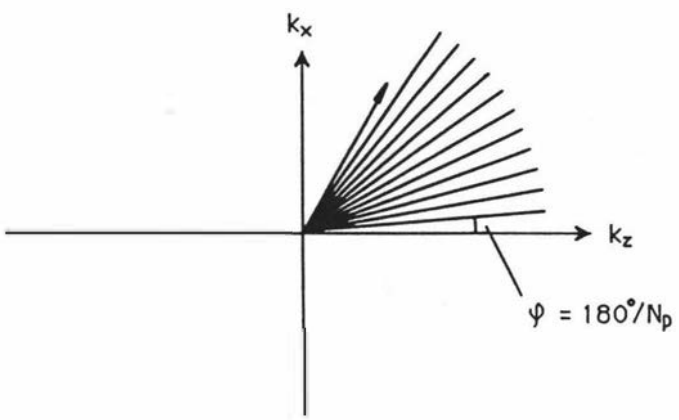

Figure 4.6 Sampling the first quadrant of k space.

$$|\mathbf{G}| = (G_z^2+G_x^2)^{1/2} \quad , \qquad \mathbf{k} = (2\pi)^{-1}\gamma \mathbf{G} t$$
$$|\mathbf{r}| = (z^2 + x^2)^{1/2} \quad , \qquad \varphi = \arctan(x/z) = \arctan(G_x/G_z). \tag{4.7}$$

From equation 4.4 we saw that we could obtain $\rho(z,x)$ by performing a two dimensional Fourier transform on $\xi(k_z,k_x)$, that is

$$\rho(z,x) \propto \int_{-\infty}^{\infty}\int \xi(k_z,k_x)\, \exp\{-j2\pi(k_z z+k_x x)\}\; dk_z dk_x. \tag{4.8}$$

An alternative expression, in polar coordinates is

$$\rho(z,x) \propto \int_{0}^{\pi}\int_{-\infty}^{\infty} \xi(k,\varphi)\, \exp\{-j2\pi \mathbf{k}.\mathbf{r}\}\; |k|\, dk\, d\varphi \tag{4.9}$$

which is equivalent to

$$\rho(z,x) \propto \int_{0}^{\pi}\int_{-\infty}^{\infty} \xi(k,\varphi)\, \exp\{-j2\pi k r'\}\; |k|\; dk\, d\varphi \tag{4.10}$$

if r' is defined as the component of $\mathbf{r}$ along the $\mathbf{k}$ vector.

The inner integral may be evaluated by multipling the nuclear signal by a ramp $|k|$ and then Fourier transforming with respect to k. The resultant function is called the filtered profile $\Psi(r',\varphi)$. Note that $\Psi(r',\varphi)$ is constant along lines perpendicular to the gradient direction.

With this substitution $\rho(z,x)$ may be re-expressed as

$$\rho(z,x) \propto \int_{0}^{\pi} \Psi(r',\varphi)\, d\varphi. \tag{4.11}$$

For a discrete Cartesian lattice this integral may be approximated by the summation

$$\rho(z,x) = \sum_{j=1}^{N_p} \Psi\{z\cos(\varphi_j) + x\sin(\varphi_j),\varphi_j\}\,\Delta\varphi \qquad (4.12)$$

since

$$\begin{aligned} \mathbf{k}.\mathbf{r} &= k_z z + k_x x \\ &= k\cos(\varphi)\, z + k\sin(\varphi)\, z \\ &= k\{z\cos(\varphi) + x\sin(\varphi)\}. \end{aligned} \qquad (4.13)$$

N_p is the total number of projections used to form the image. The process of evaluating $\Psi(r',\varphi)$ at points on the Cartesian lattice is termed backprojection - hence the name given to this technique, filtered back projection (FBP).

Total imaging time for filtered back projection is $\sim N_p N_{acc}$ where N_{acc} is the number of accumulations per projection. This can be reduced by reducing N_p, although at the expense of some loss in picture quality.

5 The signal to noise ratio in NMR

Because the S/N of an image depends so strongly on the required spatial resolution, (later in this section we shall see that S/N is proportional to Δz^{-3}), it is of great importance that the signal gathering capabilities of the spectrometer be optimized. This means maximizing the signal obtainable while keeping the noise level to a minimum. Potential noise sources within the spectrometer are numerous but in a well designed system it is the probe and the rf preamplifier which chiefly determine the overall noise figure and sensitivity of the system.

Following is an analysis which determines the expected S/N for the free induction decay obtained by stimulating a volume of water. The conditions for this analysis will be quite general. A cylindrical sample of water of volume V_s is placed inside a solenoidal coil of radius R and length ℓ, with N_t turns of wire (see figure 5.1). Hoult has indicated[15] that the highest Q is obtained when $\ell \approx 2R$ and $d \approx 3r$. The sample of water is stimulated by a 90° rf pulse applied along the y axis so that all the spins are left precessing in the x,y plane. We need to find the magnitude of the EMF induced by the precessing magnetization vector **M**. Following a 90° pulse we know that the magnitude of **M** will be

$$M_0 = N_h \gamma \hbar (P_+ - P_-)/2 \tag{5.1}$$

where N_h is the number of hydrogen nuclei per unit volume, $\gamma\hbar/2$ the proton magnetic moment component directed along the B_0 axis and $(P_+ - P_-)$ the net fraction of spins directed along this axis. Using Boltzmann statistics we know that the probability of a nuclear spin being either aligned (P_+) or antialigned (P_-) with the B_0 axis is just

$$P_\pm = \frac{\exp(-\Delta E_\pm / k_B T_s)}{\sum_\pm \exp(-\Delta E_\pm / k_B T_s)} \tag{5.2}$$

where T_s is the sample temperature in Kelvin and k_B is Boltzmann's constant. For a spin half particle $\Delta E_\pm = \pm \gamma \hbar B_0/2$, and so

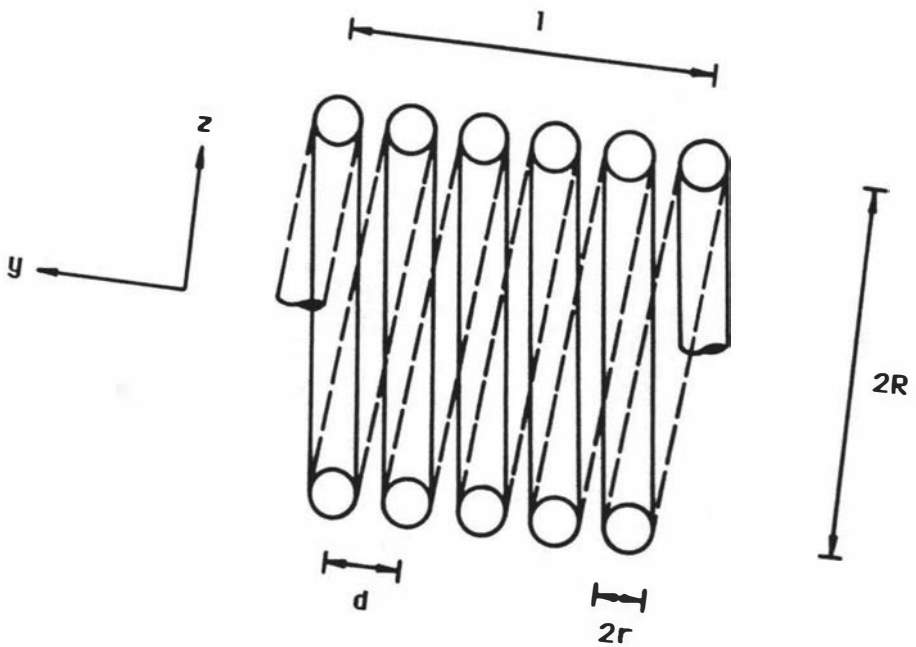

Figure 5.1 Rf coil dimensions.

$$P_{\pm} = \frac{\exp(\pm\gamma\hbar B_0/2k_BT_s)}{\exp(+\gamma\hbar B_0/2k_BT_s) + \exp(-\gamma\hbar B_0/2k_BT_s)}. \tag{5.3}$$

In the high temperature approximation ($T_s >> 0$) this simplifies to first order to give

$$P_{\pm} = (1 \pm \gamma\hbar B_0/2k_BT_s)/2 \tag{5.4}$$

and so

$$P_+ - P_- = \gamma\hbar B_0/2k_BT_s. \tag{5.5}$$

This means that

$$M_0 = N_h(\gamma\hbar)^2 B_0/(4k_BT_s). \tag{5.6}$$

In the lab frame this magnetization will precess about $\mathbf{B_0}$ at angular frequency ω_0, and so

$$M(t) = M_0 \exp(j\omega_0 t)\, \exp(j\varphi) \tag{5.7}$$

where φ is the phase angle at t=0.

From the reciprocity theorem[16] we know that the induced EMF in the coil due to a volume element dV_s in the sample is just

$$d\xi_s = -d/dt \{ B_1 M(t)/I \}\, dV_s \tag{5.8}$$

where B_1/I is the field in the volume element due to unit current flowing in the coil. For a solenoid, B_1/I is essentially uniform within the coil and may be replaced by the constant $(B_1/I)_{uy}$ where[17]

$$(B_1/I)_{uy} = \frac{\mu_0 N_t}{(4R^2 + \ell^2)^{1/2}}. \tag{5.9}$$

For the coils used in this work $\ell \approx 2R$ and so

$$(B_1/I)_{uy} = \mu_0 N_t /(\ell\sqrt{2}). \tag{5.10}$$

From section 2.3 we saw that the precessing magnetization takes the form

$$M_x(t) = M_0 \sin(\omega_0 t) \exp(-t/T_2^*) \tag{5.11}$$

and so the induced EMF due to the whole sample (which is assumed to be totally enclosed by the coil so that $(B_1/I)_{xy}$ = const.) will be

$$\xi_s(t) = \int -d/dt \{ B_1 M(t)/I \} dV_s$$

$$= \int -d/dt \{ B_1 M_0 \sin(\omega_0 t) \exp(-t/T_2^*) \} dV_s$$

$$= V_s (B_1/I)_{xy} M_0 \omega_0 \cos(\omega t) \exp(-t/T_2^*). \tag{5.12}$$

$\xi_s(t)$ is a maximum at t=0 and takes the value

$$\xi_s(0) = V_s (B_1/I)_{xy} M_0 \omega_0. \tag{5.13}$$

The noise power produced by the coil due to its resistance r_c will be $4k_B T_c \Delta f r_c$ and so the rms noise voltage will be

$$\xi_n = (4F k_B T_c r_c \Delta f)^{1/2} \tag{5.14}$$

where T_c is the coil temperature in Kelvin and F is the noise factor of the spectrometer. The resistance r_c may be re-expressed in terms of the coil Q and inductance L as

$$r_c = \omega L/Q \tag{5.15}$$

where

$$L = N (B_1/I)_{xy} A = \mu_0 N_t^2 A/(\sqrt{2}\, \ell). \tag{5.16}$$

Substituting these last two results into equation 5.14 gives an rms noise value of

$$\xi_n = \{4k_B T_c F \Delta f \omega_0 \mu_0 (N_t)^2 A/(\ell Q \sqrt{2})\}^{1/2}. \tag{5.17}$$

Combining this with equation 5.13 gives an <u>rms</u> signal to noise ratio of

$$(S/N)_{rms} = \xi_s(0)/(\xi_n\sqrt{2}) = K\,(V_s/2V_c)\,M_0\left[\frac{\mu_0 Q\omega_0 V_c}{4Fk_BT_c\Delta f}\right]^{1/2} \tag{5.18}$$

where $K = 2^{1/4}$. This is equivalent to the expression obtained by Abragam[18]. The ratio $V_s/2V_c$ is usually referred to as the filling factor η as it describes the fraction of flux due to the precessing magnetization which cuts the coil windings.

Hoult and Richards[16] have pointed out that many of the parameters in the above equation are related, so that the dependance of S/N on the various measurable parameters, such as ω_0, is not as clear as it could be. An alternative deriviation which presents S/N in terms of independent, measurable quantities is as follows. From equations 5.13 and 5.14 we have

$$(S/N)_{peak} = \frac{\omega_0(B_1)_{xy}M_0V_s}{(4Fk_BT_c\Delta f r_c)^{1/2}}. \tag{5.19}$$

Now

$$r_c = \sigma\rho L/A \tag{5.20}$$

where ρ is the resistivity, L the length and A the cross sectional area of the conductor. The factor σ takes account of the reduction in skin depth which arises from the proximity of turns in the coil. At radio frequencies $A=p\delta$ where p is the circumference of the wire and δ the skin depth which is given by

$$\delta = \left[\frac{2\rho}{\mu_r\mu_0\omega_0}\right]^{1/2}. \tag{5.21}$$

Substituting equations 5.20 and 5.21 into 5.19 and then substituting for M_0 from equation 5.6 we get

$$(S/N)_{peak} = \frac{\omega_0 V_s(B_1/I)_{xy}N_h\gamma^2\hbar^2(\omega_0/\gamma)}{4kT_s(4k_BFT_c\Delta f)^{1/2}}\left[\frac{p}{\sigma L}\right]^{1/2}\left[\frac{2}{\mu_r\mu_0\omega_0\rho}\right]^{1/4}. \tag{5.22}$$

Note that the signal to noise ratio is now expressed in terms of the peak signal rather than the rms value. Collecting terms we obtain

$$(S/N)_{peak} = \frac{V_s (B_1/I)_{xy} N_h \gamma \hbar^2 (\omega_0)^{7/4}}{6.73\ k_B T_s} \left[\frac{p}{k_B T_c \sigma L \Delta f F}\right]^{1/2} \left[\frac{1}{\mu_r \mu_0 \rho}\right]^{1/4}. \quad (5.23)$$

It is interesting to note that the signal to noise ratio depends on $(\omega_0)^{7/4}$ and not $(\omega_0)^2$ as implied by equation 5.18. This equation can be simplified if a "standard coil" configuration is used (see figure 5.1). If $2R=\ell$ then we have the following approximate relationships derived by Hoult and Richards

$$L = 6.3\, N_t R$$
$$p = 4.2\, R/N_t .$$

If we substitute these results into equation 5.23 we obtain

$$(S/N)_{peak} = \frac{(B_1/I)_{xy} V_s N_h \gamma \hbar^2 \omega_0^{7/4}}{6.73\, k_B T_s N_t} \left[\frac{2/3}{k_B T_c \sigma \Delta f F}\right]^{1/2} \left[\frac{1}{\mu_r \mu_0 \rho}\right]^{1/4}. \quad (5.24)$$

Substituting for $(B_1/I)_{xy}$ from equation 5.10 gives

$$(S/N)_{peak} = \frac{\mu_0 V_s N_h \gamma \hbar^2 \omega_0^{7/4}}{23.31\, R\, k_B T_s} \left[\frac{1}{k_B T_c \sigma \Delta f F}\right]^{1/2} \left[\frac{1}{\mu_r \mu_0 \rho}\right]^{1/4}. \quad (5.25)$$

We can now substitute for those terms which are constant. For experiments carried out on water we have:

$N_h = 6.7\times10^{28}$ nuclei m^{-3}
$T_c \approx T_s \approx 293K$
$\rho = 1.69 \times 10^{-8}\ \Omega m$
$\gamma = 2.675 \times 10^{8}\ s^{-1}T^{-1}$
$\mu_r = 1$
$\mu_0 = 4\pi \times 10^{-7}\ Hm^{-1}$
$k_B = 1.381 \times 10^{-23}\ JK^{-1}$
$\hbar = 1.054 \times 10^{-34}\ Js$.

Substituting these values into equation 5.25 gives

$$(S/N)_{peak} = 2.72\times10^{-3}\, V_s\, f^{7/4}\, R^{-1}\, \Delta f^{-1/2}\, F^{-1/2}\, \sigma^{-1/2}. \qquad (5.26)$$

Note that this result is only correct for a solenoidal coil wound with round wires. Hoult indicates that the S/N obtained using a saddle coil will be worse by a factor of ~3, thereby offsetting the advantage to be gained in high field (superconducting) systems which often use this rf coil design.

Having obtained this expression we can determine the expected S/N for a standard volume of water. 1×10^{-8} m^3 was chosen as it is typical of the sample slices imaged using this apparatus. (Typical dimensions are for a cylindrical slice 3.0mm in diameter and 1.5mm thick). From equation 5.6 we see that

$$M_0 = 6.7\times10^{28} \times (\gamma\hbar)^2/(4k_BT_s) \times B_0$$

$$= 3.35\times10^{-3} \times B_0 \quad [Am^{-1}]. \qquad (5.27)$$

To determine the proximity factor σ we note that the inductance L was measured as 0.14µH and the Q as 100. These values predict a coil resistance of 0.64Ω at 60MHz. If equation 5.20 is evaluated for the coil dimensions used we find that $r_c = 0.882\ \sigma$. Combining these two results gives a proximity factor of 7.3 . With a bandwidth of 20kHz and a coil volume $V_c = 1.47\times10^{-6}$ m^3 we therefore predict a signal to noise ratio at room temperature of

$$(S/N)_{peak} = 1040\ .$$

The observed S/N for a sample volume of this size is 515 indicating an overall noise figure + signal loss (possibly in the probe) of 6dB.

6 Signal to noise and resolution in imaging

6.1 Introduction

Having determined the parameters which affect the signal to noise ratio of the free induction decay, obtained on stimulating a known volume of water, we can now consider the S/N in the final image domain, and consider ways in which this ratio might be optimized.

Before considering any imaging process in detail we shall note some relationships between the discrete numeric data handled by the computer and the parameters which are being represented by these numbers. In section 4.1 we saw that the signals obtained in Fourier zeugmatography and filtered back projection represent spatial frequency amplitudes. The relationship between the time, t, at which data is acquired and its corresponding k space coordinate is given by

$$\mathbf{k} = (2\pi)^{-1} \gamma \mathbf{G} t \qquad (6.1)$$

where **G** is the applied gradient vector. The Fourier transform of this data is a function which depends on the spatial coordinate **r**. **k** and **r** are therefore a transform pair. Since data is handled discretely by the computer we note that

$$\text{and} \qquad \begin{aligned} |\mathbf{k}| &= 2\,n\,K/N \qquad -N/2 \le n \le N/2-1 \\ |\mathbf{r}| &= 2\,m\,R/N \qquad -N/2 \le m \le N/2-1 \end{aligned} \qquad (6.2)$$

where K is the maximum k space coordinate ($K=\gamma GT$), R is the maximum distance (or image space) coordinate, N is the total number of data points and n and m are integers representing k and r in the computer. The spatial frequency and image domain signals will be represented by the functions $S_k(n)$ and $S_r(m)$ respectively.

6.2 Signal level calculation in Fourier zeugmatography

In Fourier zeugmatography, the image data is obtained by performing a two dimensional discrete Fourier transform on the spatial frequency data. In the following analysis we shall assume that the object being imaged is cylindrical and that the imaging gradients are applied perpendicular to the cylinder's longitudinal axis (see figure 6.1). A circular image will therefore be obtained such that

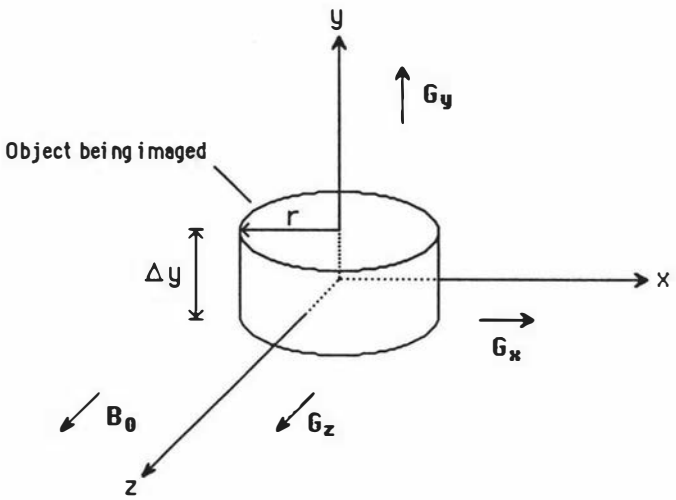

Figure 6.1 Imaging coordinate system

$$S_r(m_z,m_x) = S_r(0,0) \quad \text{for} \quad m_r \le (m_z^2+m_x^2)^{1/2}$$
$$= 0 \qquad\qquad\quad m_r > (m_z^2+m_x^2)^{1/2} \tag{6.3}$$

where m_r is the number of data points representing the radius of the cylinder. Given that we know the image amplitude we can calculate the maximum amplitude in k space (for the purposes of determining S/N) by using the inverse discrete Fourier transform (see figure 6.2)

$$S_k(n_z,n_x) = N^{-2} \sum_{m_z} \sum_{m_x} S_r(m_z,m_x) \exp(j2\pi[n_z m_z + n_x m_x]/N). \tag{6.4}$$

where all summations in this analysis range from -N/2 to N/2-1. A description of the FFT algorithm used to evaluate this summation is given in appendix B.

The maximum amplitude in k space occurs when k=0 that is, when n_z and n_x are zero

$$S_k(0,0) = N^{-2} \sum_{m_z} \sum_{m_x} S_r(m_z,m_x). \tag{6.5}$$

Using the image dimensions given in equation 6.3 we can evaluate the summation to give

$$S_k(0,0) = S_r(0,0)\,\pi m_r^2/N^2 \tag{6.6}$$

and so

$$S_r(0,0) = S_k(0,0)\,N^2/(\pi m_r^2). \tag{6.7}$$

This level may be increased by co-adding signal data such that after N_{acc} accumulations $S_r(0,0)$ takes the value

$$S_r(0,0) = N_{acc}\,S_k(0,0)\,N^2/(\pi m_r^2). \tag{6.8}$$

6.3 Calculation of the noise level in Fourier Zeugmatography

Determination of the noise level in the image domain is complicated by the filtering function which is applied to the k space data before Fourier transforming. The filtering function is

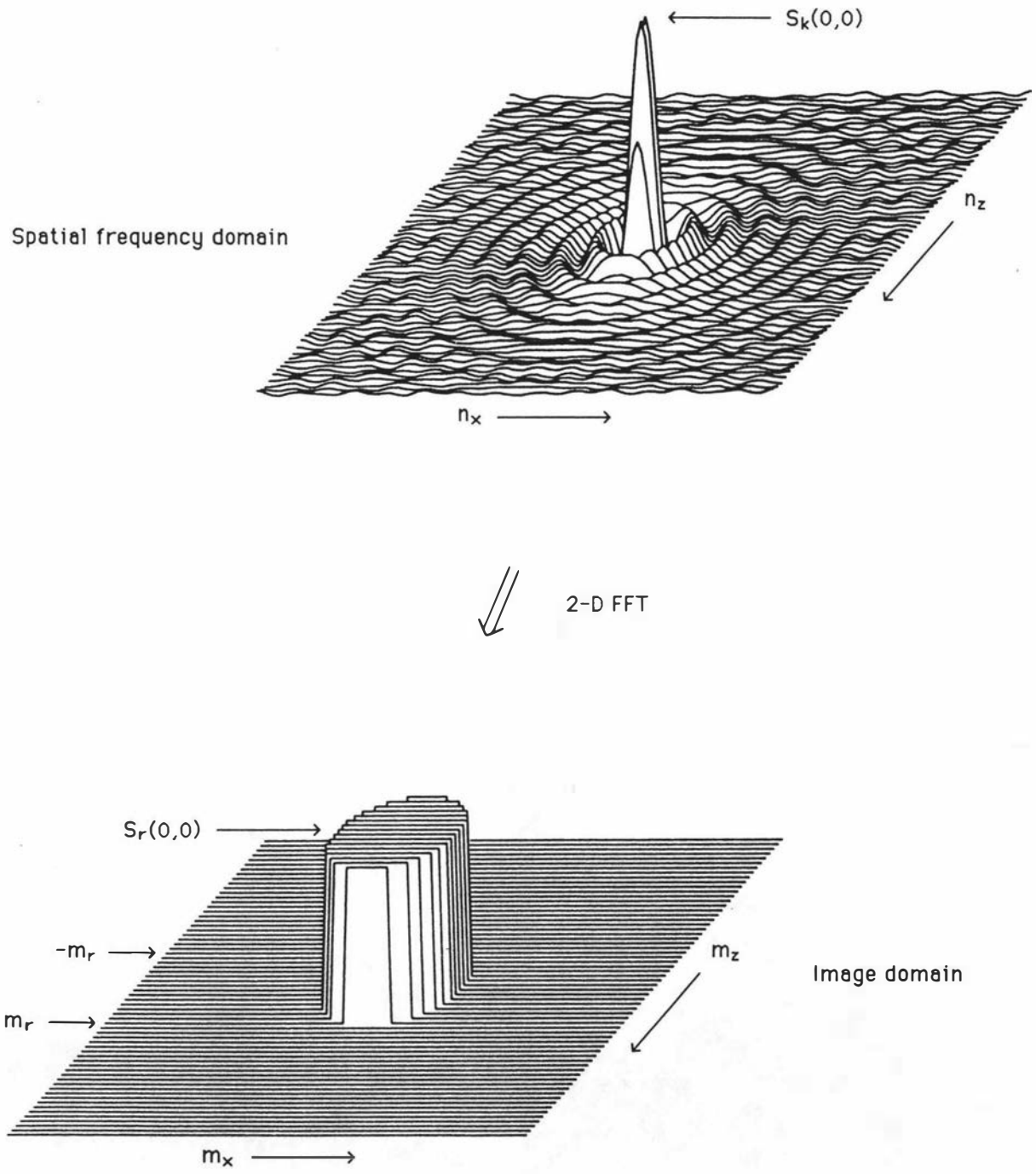

Figure 6.2 Diagram showing the 2-D F.T. process used in F.Z.

applied to optimize the signal to noise ratio. For an N×N image the maximum number of resolvable points across the image is N/2. For most purposes it isn't necessary, or possible, to have perfectly resolved points. The application of the broadening function reduces the contrast ratio, as defined in figure 6.6, but it also reduces the noise level. For the moment we shall not specify any particular form for this function but will simply represent it by F(n).

The mean squared noise level in the image may be found by evaluating the 2D discrete Fourier transform

$$\langle N_r(m_z,m_x)^2\rangle = \left\langle \left| \sum_{n_z}\sum_{n_x} N_k(n_z,n_x)\, F(n) \exp(-j2\pi[n_z m_z + n_x m_x]/N) \right|^2 \right\rangle \qquad (6.9)$$

where N_r and N_k are the noise amplitudes in the two domains. Expanding the exponential and noise signal in terms of their real and imaginary values we obtain

$$\begin{aligned} N_r(m_z,m_x) = {} & \sum_{n_z}\sum_{n_x} \mathrm{Re}\{N_k(n_z,n_x)\}\, F(n) \cos(2\pi[n_z m_z + n_x m_x]/N) \\ & - \sum_{n_z}\sum_{n_x} \mathrm{Im}\{N_k(n_z,n_x)\}\, F(n) \sin(2\pi[n_z m_z + n_x m_x]/N) \\ & + j \sum_{n_z}\sum_{n_x} \mathrm{Re}\{N_k(n_z,n_x)\}\, F(n) \sin(2\pi[n_z m_z + n_x m_x]/N) \\ & + j \sum_{n_z}\sum_{n_x} \mathrm{Im}\{N_k(n_z,n_x)\}\, F(n) \cos(2\pi[n_z m_z + n_x m_x]/N). \end{aligned} \qquad (6.10)$$

We will now evaluate $N_r(m_z,m_x)^2$ for the **real** image domain data

$$\begin{aligned} \mathrm{Re}\{N_r(m_z,m_x)\}^2 = {} & \sum_{n_z}\sum_{n_x} \mathrm{Re}\{N_k(n_z,n_x)\}^2 F(n)^2 \cos^2(2\pi[n_z m_z + n_x m_x]/N) \\ & - \sum_{n_z}\sum_{n_x} \mathrm{Im}\{N_k(n_z,n_x)\}^2\, F(n)^2 \sin^2(2\pi[n_z m_z + n_x m_x]/N) \\ & + \text{cross terms.} \end{aligned} \qquad (6.11)$$

Averaging with respect to m gives

$$\langle \mathrm{Re}\{N_r(m_z m_x)^2\}\rangle = \sum_{n_z}\sum_{n_x} \mathrm{Re}\{N_k(n_z n_x)\}^2\, F(n)^2 \langle \cos^2(2\pi[n_z m_z + n_x m_x]/N)\rangle$$
$$+ \sum_{n_z}\sum_{n_x} \mathrm{Im}\{N_k(n_z n_x)\}^2\, F(n)^2 \langle \sin^2(2\pi[n_z m_z + n_x m_x]/N)\rangle. \qquad (6.12)$$

All cross terms having vanished, since $N_k(n_z n_x)$ is a random function with mean value zero. To evaluate this equation we sum over the total number of accumulations N_{acc}, since $n_k(n)$ varies with e, the experiment number. Assuming the statistics to be ergodic (i.e. that the average of n_k over n equals the average over e) we obtain

$$\langle \mathrm{Re}\{N_r(m_z m_x)^2\}\rangle = N_{acc}\sum_{n_z}\sum_{n_x} \langle \mathrm{Re}\{N_k(n_z n_x)\}^2\rangle\, F(n)^2\, 0.5$$
$$+ N_{acc}\sum_{n_z}\sum_{n_x} \langle \mathrm{Im}\{N_k(n_z n_x)\}^2\rangle\, F(n)^2\, 0.5$$
$$= N_{acc}\langle \mathrm{Re}\{N_k(n_z n_x)^2\}\rangle \sum_{n_z}\sum_{n_x} F(n)^2. \qquad (6.13)$$

The equality $\langle \mathrm{Re}\{N_k(n_z n_x)^2\}\rangle = \langle \mathrm{Im}\{N_k(n_z n_x)^2\}\rangle$ has been assumed in the derivation of this result .

Determination of the noise level depends on our choice of filter function F(n). Conventional NMR spectroscopy techniques suggest a filter function of the form

$$F(n) = \exp\{-(n_z+n_x)/n_b\} \qquad (6.14)$$

where n_b characterises the severity of the filter function. F(n) is designed so as to have little effect at low values of reciprocal space, where most of the signal data occurs, but to significantly attenuate at high values. Since the mean squared noise level is independent of spatial frequency the application of this function will therefore result in a reduction in the noise level across the image. This particular function was originally chosen as it is easy to apply to the k space data. Each horizontal scan of k space is multiplied by $\exp(-n_z/n_b)$ and is then stored in the k space array. The function $\exp(-n_x/n_b)$ is then applied in the vertical direction. The product of this function with the k space data is equivalent to a convolution of the Fourier transform $\mathbf{F}\{F(n)\}$ and the image domain signal. Figure 6.3 illustrates F(n) in both domains for N =128 and n_b = 6. It is immediately apparent that the non-isotropic nature of this function will lead to

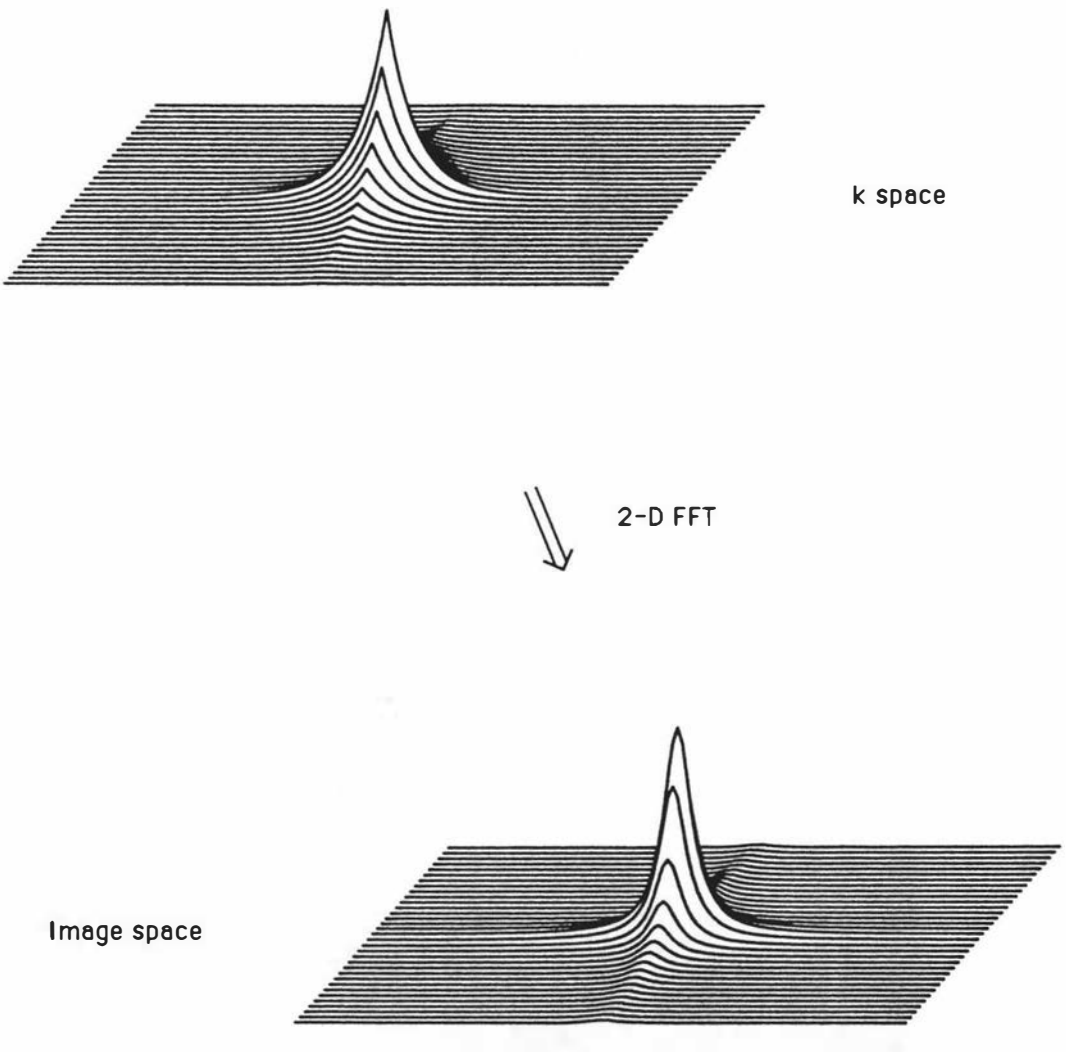

Figure 6.3 Non-ideal filter function in k space and image space.

distortions in the image; in particular the resolution Δz will now depend on the angle φ. Ideally we want a point spread function with circular symmetry so as to produce isotropic resolution in the final image. One such function is

$$F(n) = \exp(-n/n_b) \tag{6.15}$$

where $n = (n_z^2 + n_x^2)^{1/2}$. This function and its transform, are illustrated in figure 6.4. Other functions such as the Gaussian[19] could also be applied, but we will restrict ourselves in this analysis to the exponential.

Having decided on the appropriate filter function we can now substitute for F(n) in equation 6.13. The summation may be evaluated by direct integration, following transformation to polar coordinates, and for $N >> 1$ we have the result

$$\sum_{n_z} \sum_{n_x} \exp(-2n/n_b) = 0.5\pi N^2\{ (n_b/N)^2[1 - \exp(-N/n_b)] - (n_b/N) \exp(-N/n_b)\} \tag{6.16}$$

Note that this integral is obtained over a circular area in $(n_z n_x)$ space. When the actual area is square, as in FZ, the result is exact only for $n_b << N$. Combining this result with equations 6.13 and 6.8 we obtain the following

$$(S/N)_r = (S/N)_k \ (N_{acc})^{1/2} N (\pi m_r^2)^{-1} \times (0.5\pi\{ n_b^2[1 - \exp(-N/n_b)] - N n_b \exp(-N/n_b)\})^{-1/2}. \tag{6.17}$$

In the absence of any filtering, i.e. for F(n) = 1, the noise level will, from equation 6.13, be

$$(n_r)_{rms} = (n_k)_{rms} N_{acc}^{1/2} N \tag{6.18}$$

and so the signal to noise ratio becomes

$$(S/N)_r = (S/N)_k \ (N_{acc})^{1/2} N (\pi m_r^2)^{-1}. \tag{6.19}$$

We now define a smoothing factor **S**(FZ)

$$\mathbf{S}(FZ) = (0.5\pi\{ (n_b/N)^2[1 - \exp(-N/n_b)] - (n_b/N) \exp(-N/n_b)\})^{-1/2} \tag{6.20}$$

such that the signal to noise with broadening is just

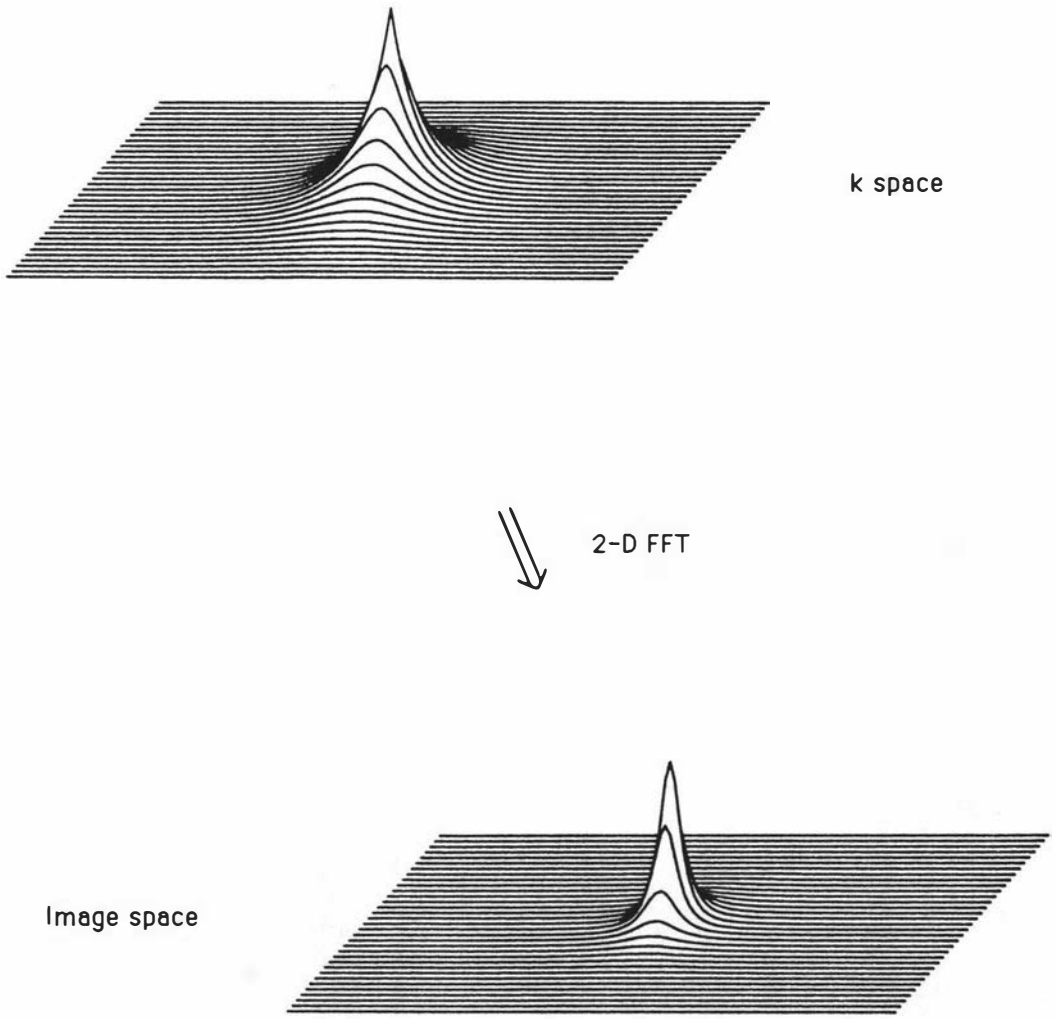

Figure 6.4 Ideal filter function in k space and image space.

$$(S/N)_r = (S/N)_k \, (N_{acc})^{1/2} \, N \, (\pi \, m_r^2)^{-1} \, \mathbf{S}(FZ). \tag{6.21}$$

$\mathbf{S}(FZ)$ is graphed as a function of N/n_b in figure 6.5. Both equation 6.20 and the exact values, obtained by direct summation of equation 6.16, have been plotted. The analytical expression is seen to provide a good approximation for all but small values of N/n_b.

The question now arises as to the optimum value of $\mathbf{S}(FZ)$ with regard to resolution. Optimum broadening occurs when next nearest neighbour pixels can just be resolved. For want of a better standard we have chosen the Rayleigh criterion, which states that two pixels will just be resolved when the contrast ratio C (as defined in figure 6.6) is 0.81. The value of N/n_b which produces this contrast ratio may be found by convoluting the Fourier transform of F(n) with two delta functions spaced two pixels apart (see figure 6.7). The results of this procedure are plotted in figure 6.8. From this figure we see that Rayleigh broadening occurs when $N/n_b = 6.4$.

Up till now we have not considered the effect that the fundamental linewidth due to T_2 broadening will have on the resolution. If we are working with a large bandwidth Δf such that T_2 broadening is much less than one pixel then the results in figure 6.5 stand. However, if the two forms of broadening are comparable we must tackle the problem in a slightly different manner. First we apply the filter

$$B(n) = \exp(n_z/p_2) \tag{6.22}$$

to the k space data to remove the effect of T_2 broadening. p_2 is chosen such that

$$p_2 = T_2 \, N/T = T_2 \, \Delta f. \tag{6.23}$$

F(n) can then be applied to produce the desired point spread function. The complete filter function is therefore given by

$$F(n)B(n) = \exp[\, n_z/p_2 - (n_z^2 + n_x^2)^{1/2}/n_b \,] \tag{6.24}$$

Figure 6.9 plots the new smoothing function $\mathbf{S}(FZ)$ obtained by evaluating the expression

$$\mathbf{S}(FZ) = N \{ \sum_{n_z n_x} \exp[\, 2n_z/p_2 - 2(n_z^2 + n_x^2)^{1/2}/n_b \,] \}^{-1/2} \tag{6.25}$$

where $n_b = N/6.4$.

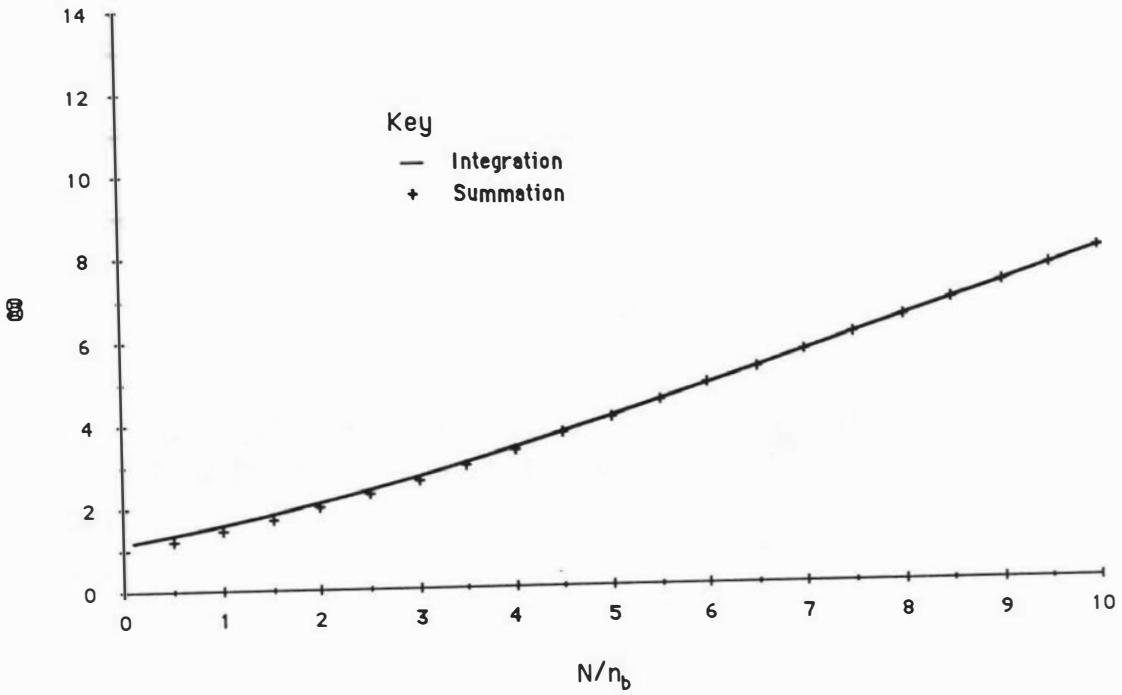

Figure 6.5 Smoothing factor vs. applied broadening for F.Z.

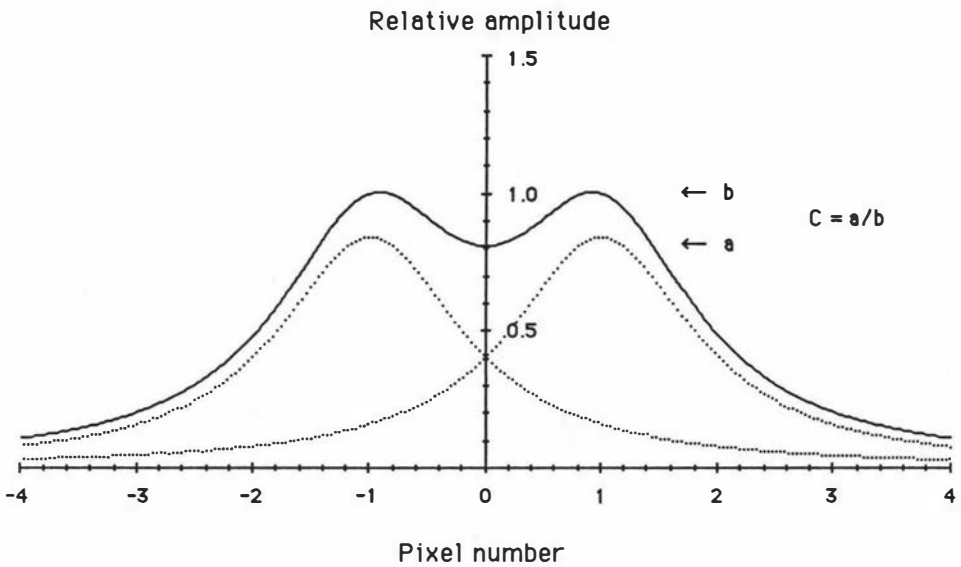

Figure 6.6 Image profile at the limit of resolution.

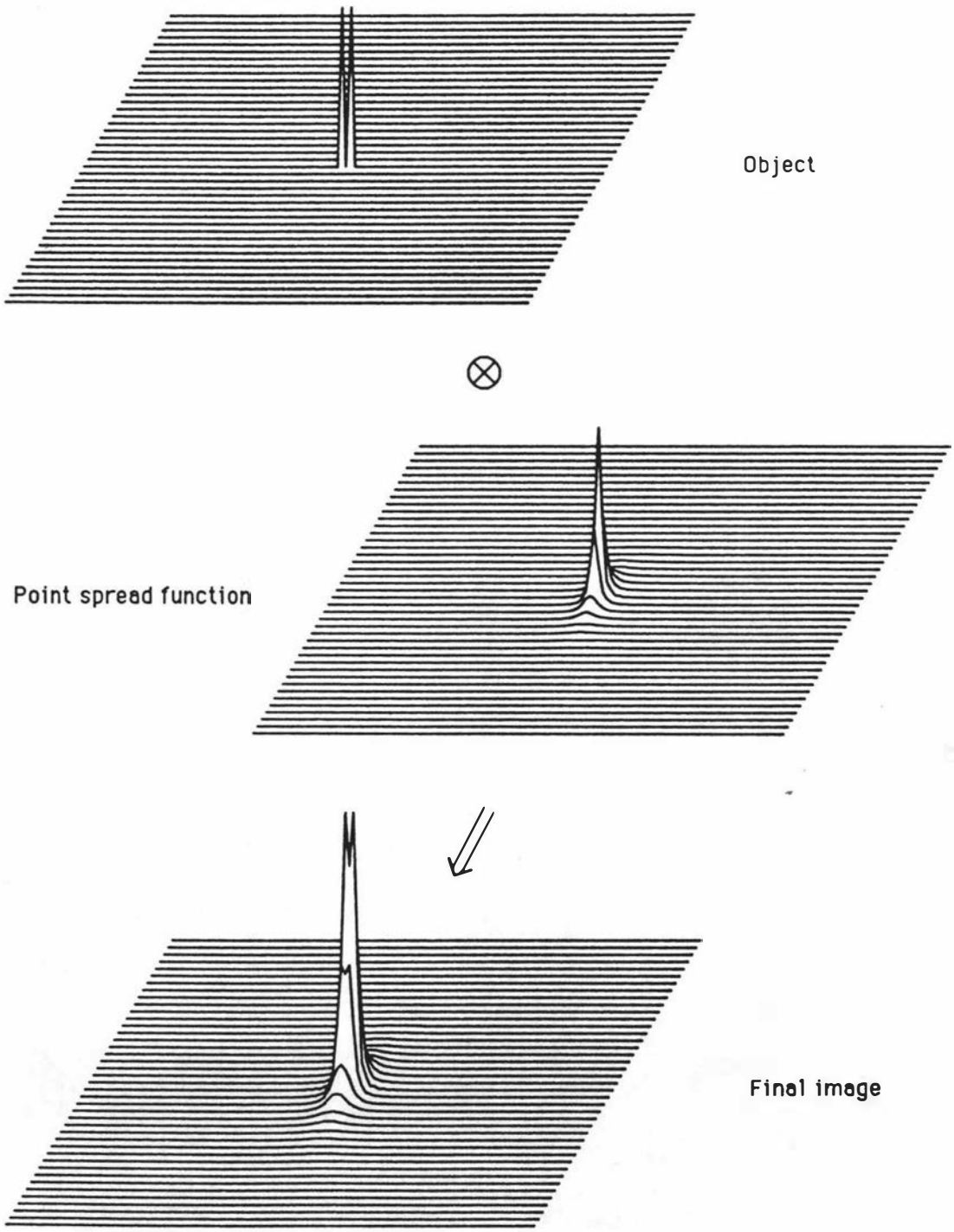

Figure 6.7 Procedure used to determine the contrast ratio

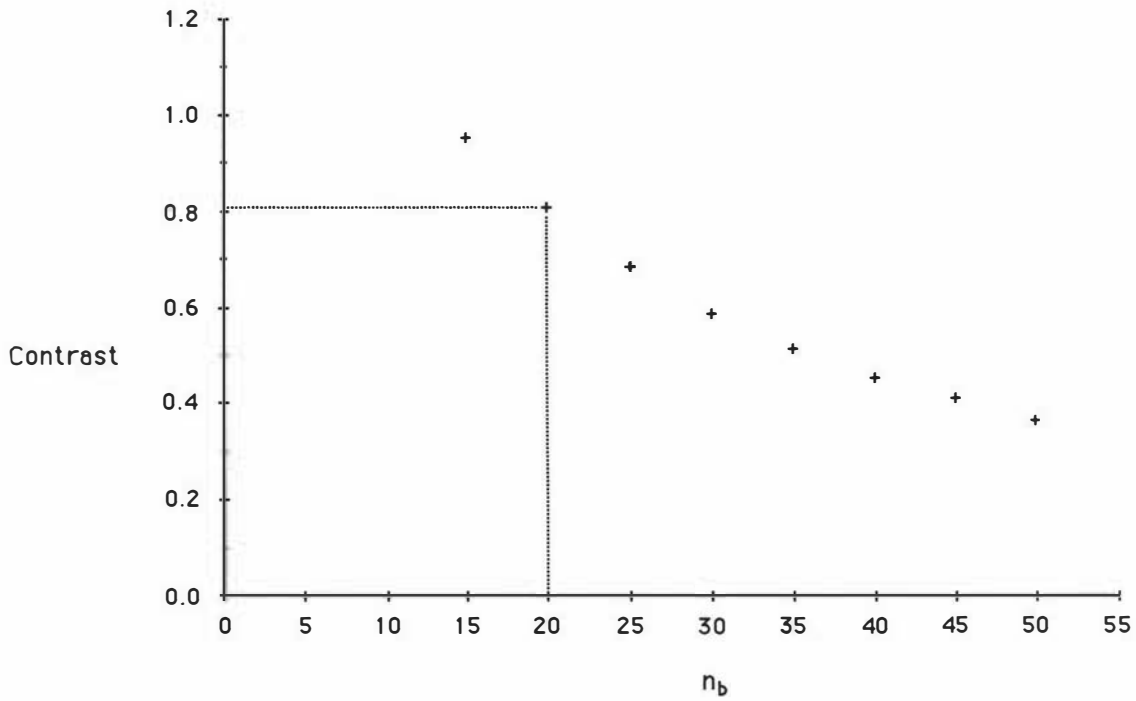

Figure 6.8 Pixel contrast as a function of filter constant for N = 128.

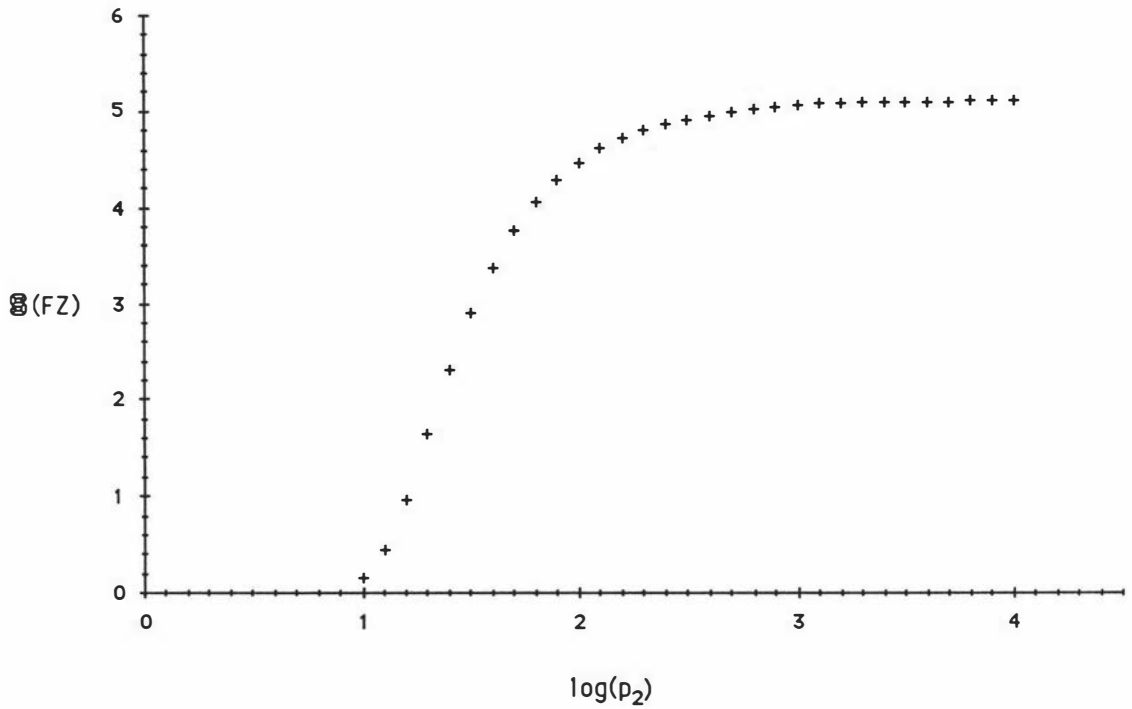

Figure 6.9 Signal to noise enhancement as a function of p_2.

6.4 Resolution in Fourier Zeugmatography

We are now in a position to evaluate an expression for the spatial resolution in the imaging microscope. From equation 5.26 we saw that the signal to noise ratio from a volume of water V_s, with dimensions defined in figure 6.1, was

$$(S/N)_k = 2.72 \times 10^{-3} V_s f^{7/4} R^{-1} (\Delta f F \sigma)^{-1/2} \quad (6.26)$$

and from 6.21 that the relationship between S/N in k space and image space was given by

$$(S/N)_r = (S/N)_k (N_{acc})^{1/2} N (\pi m_r^2)^{-1} \mathbf{S}(FZ). \quad (6.27)$$

Since next nearest neigbour pixels are resolvable we have

$$\Delta z = 2 r/m_r \quad (6.28)$$

where r is the radius of the cylinder being imaged. Substituting $(S/N)_k$ from equation 6.26 into equation 6.27 we obtain

$$(S/N)_r = 2.72 \times 10^{-3} (\pi r^2 \Delta y) f^{7/4} R^{-1} (\Delta f F \sigma)^{-1/2} (N_{acc})^{1/2} N (\pi m_r^2)^{-1} \mathbf{S}(FZ) \quad (6.29)$$

Equation 6.28 may then be applied to remove the dependence on r and m_r

$$(S/N)_r = 2.72 \times 10^{-3} (\Delta z^2 \Delta y/4) f^{7/4} R^{-1} (\Delta f F \sigma)^{-1/2} (N_{acc})^{1/2} N \mathbf{S}(FZ). \quad (6.30)$$

The resolution may then be written as

$$\Delta z = 38.34 (S/N)_r^{+1/2} \Delta y^{-1/2} f^{-7/8} R^{1/2} (\Delta f F \sigma)^{1/4} (N_{acc})^{-1/4} (N \mathbf{S}(FZ))^{-1/2}. \quad (6.31)$$

This result can be optimized by minimising $\{\mathbf{S}(FZ)^{-1/2} \Delta f^{1/4}\}$. Figure 6.10 plots this expression as a function of p_2 and T_2. The minimum occurs for $p_2 = 41.7$. It is of interest to note that the value of p_2 obtained when using a matched filter[20], that is with an applied broadening of $1/\pi T_2$, is 40.7 - very close to the observed optimum.

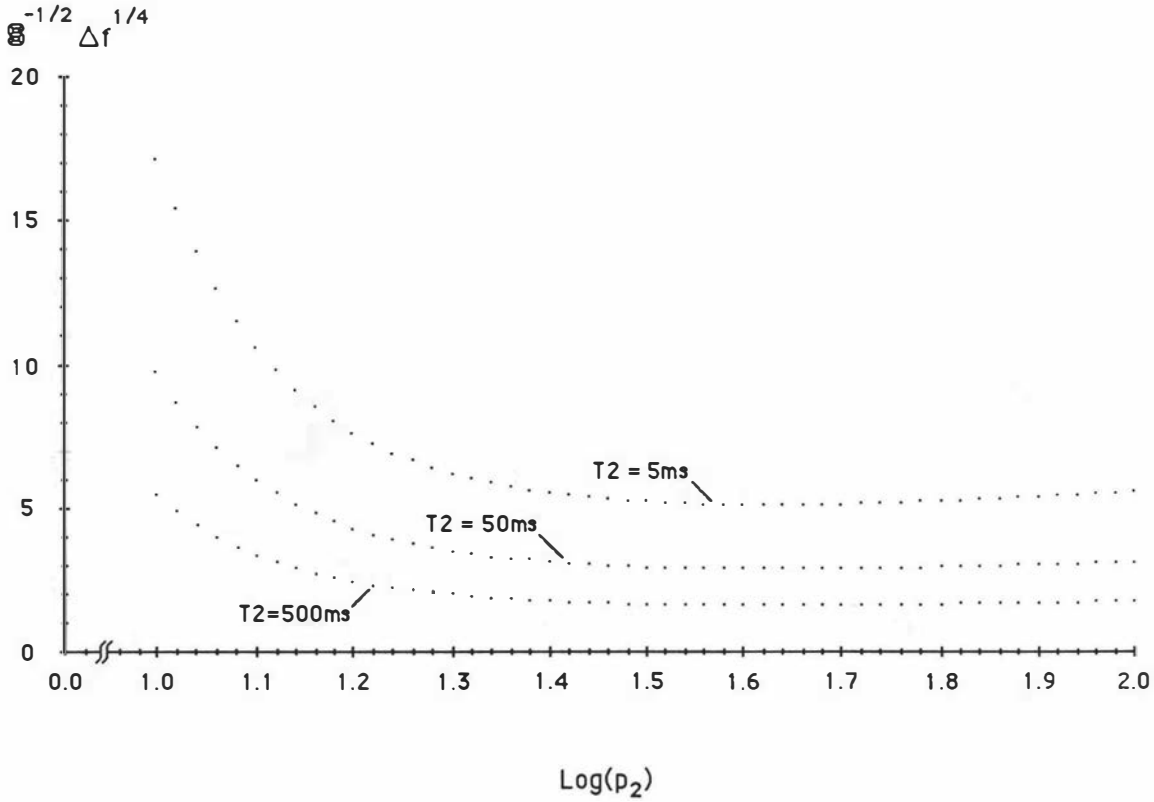

Figure 6.10 Resolution optimization in F.Z.

Δz values have been tabulated for 3 systems. For our present 60MHz system (A), for an optimized 60MHz system (B) and for a 600MHz system (C), the maximum frequency currently available in commercial spectrometers.

Table 6.1 Resolution as a function of T_2 for various imaging configurations in Fourier Zeugmatography

	System		
Parameter	**A**	**B**	**C**
f	60MHz	60MHz	600MHz
Δy	1.5mm	100μm	100μm
F	2(6dB)	1.03(0.5dB)	1.03(0.5dB)
R	2.8mm	2.0mm	2.0mm
N	256	256	256
σ	7	7	7
N_{acc}	8	8	8
S/N	40	40	40
T_2 (ms)	**Resolution (linear & voxel)** μm (μm³)		
5	19.1 (81.8)	53.0 (65.5)	7.1 (17.1)
10	16.1 (72.9)	44.6 (58.3)	5.9 (15.2)
50	10.7 (55.7)	29.8 (44.6)	4.0 (11.6)
100	9.0 (49.7)	25.1 (39.7)	3.3 (10.4)
500	6.0 (38.0)	16.8 (30.4)	2.2 (7.9)

The table assumes a repetition time of 0.5sec and a total imaging time of 2048sec (two experiments are required per complex accumulation in our system). A 2mm coil was felt to be the smallest which could be practicably made and a noise figure of 0.5dB a reasonable minimum for state of the art preamps. A 100μm slice was chosen as it is comparable with slices used in optical microscopy while a S/N of 40 was, from the experience gained in this work, considered to be the minimum required for a good quality image.

6.5 Signal level calculation in filtered back projection

The implementation of filtered backprojection is essentially a four step process. First, the time domain data is multiplied by a decaying exponential to optimize S/N for a given resolution. The data is then multiplied by a ramp $|k|$ and Fourier transformed. The resultant spectral data, or filtered profile, is then back projected onto the image plane. These four processes are then repeated for N_p projection angles ranging from 0° to 180° (see figure 6.11). The effect of each of these processes on the signal to noise ratio will now be considered.

As we find it convenient to discuss the filtered back projection process in terms of time and frequency spaces, the k and r space nomenclature developed in the last section will not be used here.

The accumulated time domain data, obtained in the presence of a linear gradient, for a cylindrical object, has the form [21]

$$S_t(t) = J_1(\gamma G r t)/(\gamma G r t) \tag{6.32}$$

where J_1 is the first order Bessel function and r the radius of the cylinder. By filtering and Fourier transforming we should be able to obtain an expression for the image space function. However due to the difficulty in handling this function analytically we have used a more indirect approach. We know from section 3.1 that the frequency domain profile for a object is just the integral of the cross section along the gradient axis. For a cylinder this takes the form (see figure 6.12)

$$\begin{aligned} Re\{S_f(f)\} &= Re\{S_f(0)\}\,[\,1-f^2/f_r^2]^{1/2} && |f| \le f_r \\ &= 0 && |f| > f_r \end{aligned} \tag{6.33}$$

where f_r is the frequency interval corresponding to the radius of the cylinder. Note that only the real data is known at this stage. $Re\{S_f(0)\}$ is related to f_r in the following manner

$$Re\{S_f(0)\} = 2\, f_r\, \rho' \tag{6.34}$$

where ρ' is directly proportional to the proton spin density function, which is assumed to be constant in this example.

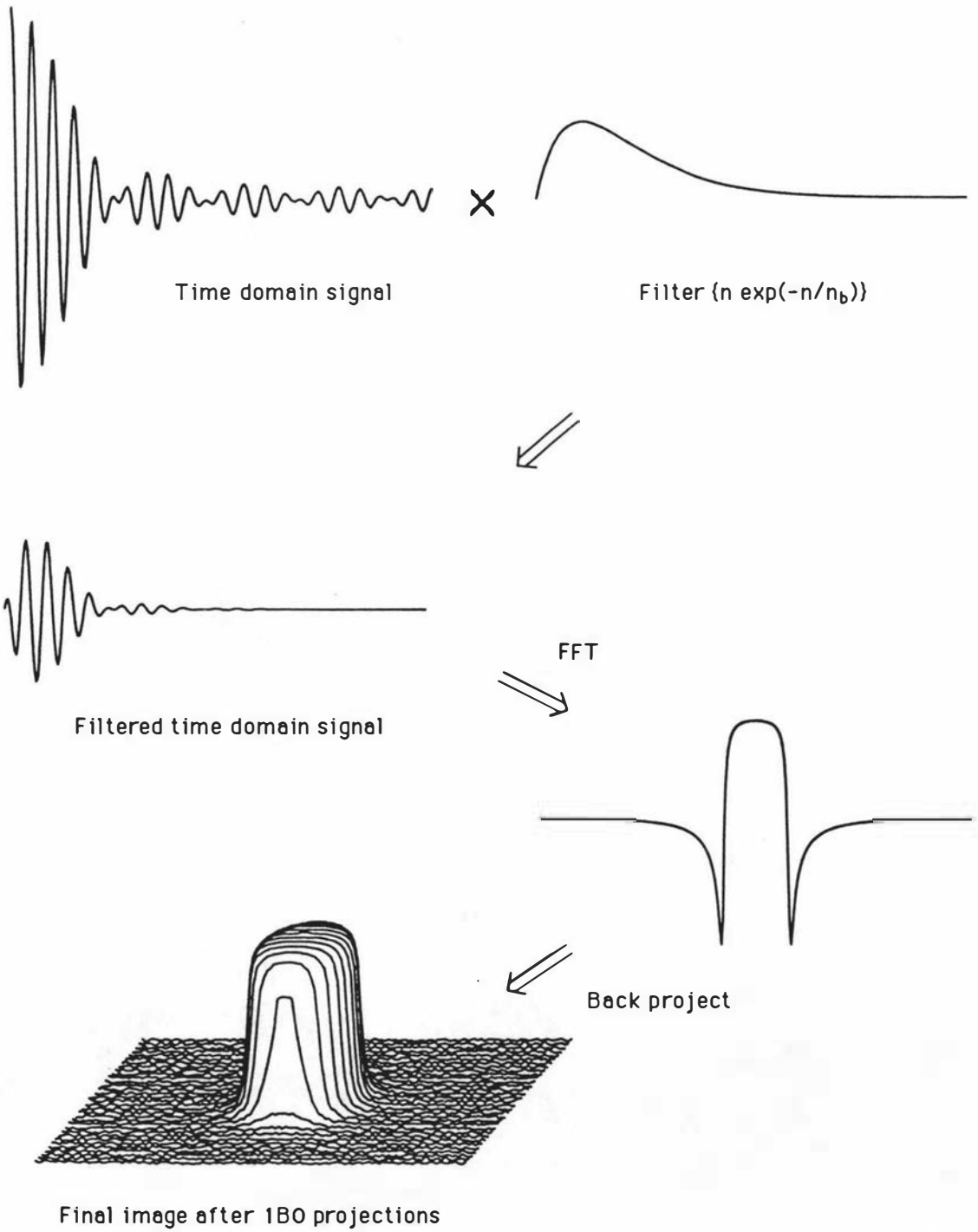

Figure 6.11 Image reconstruction in FBP.

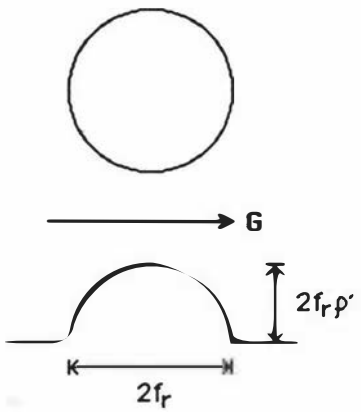

Figure 6.12 Projection profile for a cylinder.

To obtain the amplitude of the filtered transform at f=0 we note that the filtered transform is given by

$$\Psi(f) = F(f) \circledast S(f) = \int_{-\infty}^{\infty} |t|\, S(t) \exp(-j2\pi f t)\, dt \qquad (6.35)$$

where F(f) is the filter function and $\circledast$ denotes convolution. For the purposes of this analysis we shall assume that S(t) is zero for t<0 (this will halve the profile data amplitude). Equation 6.35 may then be expanded to give

$$\Psi(f) = \int_{0}^{\infty} t\, S(t) \exp(-j2\pi f t)\, dt$$

$$= \int_{0}^{\infty} t\, [\, (Re\{S(t)\} + jIm\{S(t)\})\, (\cos\{2\pi f t\} - j\sin\{2\pi f t\})\,]\, dt$$

$$= \int_{0}^{\infty} [\, t\, Re\{S(t)\} \cos(2\pi f t) + t\, Im\{S(t)\} \sin(2\pi f t)\,]\, dt$$

$$+ j \int_{0}^{\infty} [\, t\, Im\{S(t)\} \cos(2\pi f t) - t\, Re\{S(t)\} \sin(2\pi f t)\,]\, dt. \qquad (6.36)$$

Now the unfiltered imaginary domain signal is given by

$$0.5\, Im\{S_f(f)\} = \int_{0}^{\infty} [Im\{S(t)\} \cos(2\pi f t) - Re\{S(t)\} \sin(2\pi f t)\,]dt \qquad (6.37)$$

but

$$d/df\, (\, 0.5\, Im\{S_f(f)\}) = 2\pi \int_{0}^{\infty} [\, - t\, Re\{S(t)\} \cos(\omega t) - t\, Im\{S(t)\} \sin(\omega t)\,]\, dt$$

$$= -2\pi \, Re\{\Psi(f)\}. \tag{6.38}$$

Hence to calculate the filtered transform we need to know the unfiltered imaginary domain signal. Unfortunately we only know the real frequency domain data. However using the Kramers-Kronig relationship[22] we can obtain the desired result, since if

$$\chi'(f) = 0.5 \, Re\{S_f(f)\} \tag{6.39}$$

and

$$\chi''(f) = 0.5 \, Im\{S_f(f)\} \tag{6.40}$$

then

$$\chi''(f) = -\pi^{-1} \lim_{\epsilon \to 0} \int_{-\infty}^{f-\epsilon} \frac{\chi'(f) - \chi'(\infty)}{f' - f} df' - \pi^{-1} \lim_{\epsilon \to 0} \int_{f+\epsilon}^{\infty} \frac{\chi'(f) - \chi'(\infty)}{f' - f} df' \tag{6.41}$$

$$= -\pi^{-1} \, \mathbf{P} \int_{-\infty}^{\infty} \chi'(f)/(f'-f) \, df' \tag{6.42}$$

since $\chi'(\infty) = 0$ for the situations encountered in this work.

Substituting for $\chi'(f)$ and $\chi''(f)$ we obtain

$$Re\{\Psi(f)\} = (2\pi)^{-1} \, d/df \, (2\pi)^{-1} \, \mathbf{P} \int_{-f_r}^{f_r} Re\{S_f(0)\} \, [1 - f^2/f_r^2]^{1/2} \, [f'-f]^{-1} \, df'. \tag{6.43}$$

This integral may be evaluated (see appendix C) to yield, for $f < |f_r|$, the constant value

$$Re\{\Psi(f)\} = d/df \, (2\pi)^{-2} \, [\, \pi \, Re\{S_f(0)\} \, (f/f_r) \,]$$

$$= Re\{S_f(0)\}/(4\pi f_r)$$

$$= \rho'/(2\pi) \tag{6.44}$$

where the result from equation 6.34 has been used. A diagram, depicting the relationships between the time domain signal, the spectral profile and the filtered profile, is given in figure 6.13.

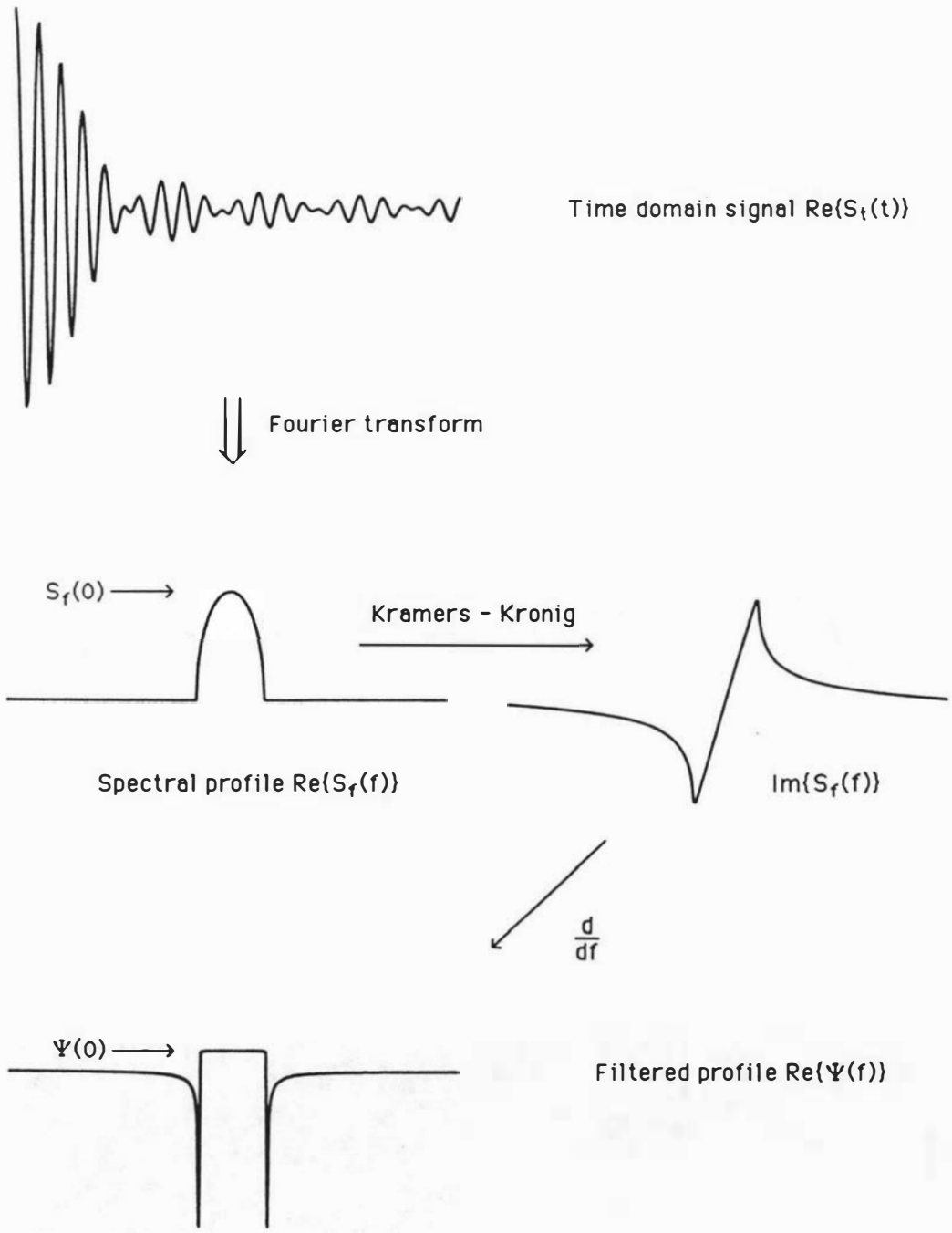

Figure 6.13 Signal processing in filtered back projection.

We now have an expression which relates the signal strength in the filtered profile with that in the unfiltered profile. To establish a relationship between the time domain data and the final image data we must express the initial time domain signal level in terms of the proton density ρ'. The time domain signal and frequency profile are related by the inverse discrete Fourier transform

$$S_t(n) = N^{-2} \sum_m [Re\{S_f(0)\} [1 - m^2/m_r^2]^{1/2} + j\, Im\{S_f(m)\}] \exp(j2\pi mn/N) \qquad (6.45)$$

where we have used m/N to represent the frequency f, and m_r/N the frequency interval f_r. The summation ranges from -N/2 to N/2-1. The initial, real, signal amplitude will therefore be

$$\begin{aligned} Re\{S_t(0)\} &= N^{-2} \sum_m Re\{S_f(0)\} [\, 1-m^2/m_r^2 \,]^{1/2} \\ &= Re\{S_f(0)\}\, m_r\pi/(2N^2). \\ &= m_r^2\, \rho'\, \pi/N^2. \end{aligned} \qquad (6.46)$$

If we compare this result with equation 6.44 we find that

$$Re\{\Psi(f)\} = 2Re\{S_t(0)\}\, N^2\, (2\pi^2\, m_r^2\,)^{-1}. \qquad (6.47)$$

The extra factor of 2 is included to correct for the assumption, made earlier in the analysis, that the time domain data is zero for t<0.

The final image is obtained by back projecting this amplitude N_p times at angles ranging from 0 to 180°. This will increase the central amplitude, and for a uniform cylinder all parts of the image, by the factor N_p

$$Re\{S_r(m_z,m_x)\} = Re\{S_t(0)\}\, N^2\, N_p\, (\pi^2\, m_r^2\,)^{-1}. \qquad m_z^2 + m_x^2 \le m_r^2 \qquad (6.48)$$

As with Fourier zeugmatography, it is normal to co-add signal data. This will increase the image amplitude by the factor N_{acc}

$$Re\{S_r(m_z,m_x)\} = N_{acc} Re\{S_t(0)\}\, N^2\, N_p\, (\pi^2\, m_r^2\,)^{-1}. \qquad m_z^2 + m_x^2 \le m_r^2 \qquad (6.49)$$

6.6 Calculation of the noise level in filtered back projection

The next step in determining the signal to noise ratio in FBP is to obtain an expression which relates the noise levels in the time and frequency (image) domains. If the noise level in the time domain is $N_t(n)$ the corresponding frequency domain function, obtained following the application of the ramp n and the smoothing filter F(n), will be

$$N_f(m) = \sum_n N_t(n)\, n\, F(n)\, \exp(-j2\pi nm/N).$$

$$= [N_{acc} \langle Re\{N_t(n)\}^2 \rangle \sum_n n^2 F(n)^2]^{1/2} \qquad (6.50)$$

where the techniques used in deriving equation 6.13 have been applied.

Application of the smoothing function is simpler in FBP than in FZ as each radial scan of k space need only be multiplied by the function

$$F(n) = \exp(-n/n_b) \qquad (6.51)$$

to obtain the desired point spread function (see figure 6.11 for example). Substituting for F(n) we obtain

$$N_f(m) = [N_{acc} N_t(n) \sum_n n^2 \exp(-2n/n_b)]^{1/2}. \qquad (6.52)$$

For large N we may evaluate this summation by a direct integration, giving

$$N_f(m) = (12)^{-1/2} (N_{acc})^{1/2} (N_t)_{rms} N^{3/2} \times [\, 6(n_b/N)^3 - \exp(-N/n_b) \{3(n_b/N) + 6(n_b/N)^2 + 6(n_b/N)^3\} \,]^{1/2} \qquad (6.53)$$

The final imaging process, back projection for angles 0 to 180° in N_p steps, will increase the noise level by a factor $N_p^{1/2}$

$$(N_r)_{rms} = (12)^{-1/2} (N_t)_{rms} (N_{acc} N_p)^{1/2} N^{3/2} \times [\, 6(n_b/N)^3 - \exp(-N/n_b) \{3(n_b/N) + 6(n_b/N)^2 + 6(n_b/N)^3\} \,]^{1/2} \qquad (6.54)$$

Combining signal and noise relationships we obtain

$$(S/N)_r = (S/N)_t \frac{(\pi^2 m_r^2)^{-1} (12\, N_{acc} N_p\, N)^{1/2}}{[\, 6(n_b/N)^3 - \exp(-N/n_b)\, \{3(n_b/N) + 6(n_b/N)^2 + 6(n_b/N)^3\}\,]^{1/2}} \qquad (6.55)$$

As in the previous section we can define a smoothing factor **S**(FBP), since the noise level in the absence of any filter is, from equation 6.50

$$(N_r)_{rms} = (12)^{-1/2} (N_{acc} N_p)^{1/2} N^{3/2} (N_t)_{rms} \qquad (6.56)$$

and the corresponding signal to noise ratio

$$(S/N)_r = ((12)^{1/2}/\pi)\, (S/N)_t\, (N_{acc} N_p\, N)^{1/2} (\pi m_r^2)^{-1}. \qquad (6.57)$$

The smoothing factor is then

$$\mathbf{S}(FBP) = [\, 6(n_b/N)^3 - \exp(-N/n_b)\, \{\, 3(n_b/N) + 6(n_b/N)^2 + 6(n_b/N)^3\}\,]^{-1/2} \qquad (6.58)$$

and so, with a filter applied, the image signal to noise ratio becomes

$$(S/N)_r = (\sqrt{12}/\pi)\, (S/N)_t\, (N_{acc} N_p\, N)^{1/2} (\pi m_r^2)^{-1}\, \mathbf{S}(FBP)\,. \qquad (6.59)$$

Equation 6.58 is plotted in figure 6.14 along with the exact values obtained by direct summation of equation 6.52.

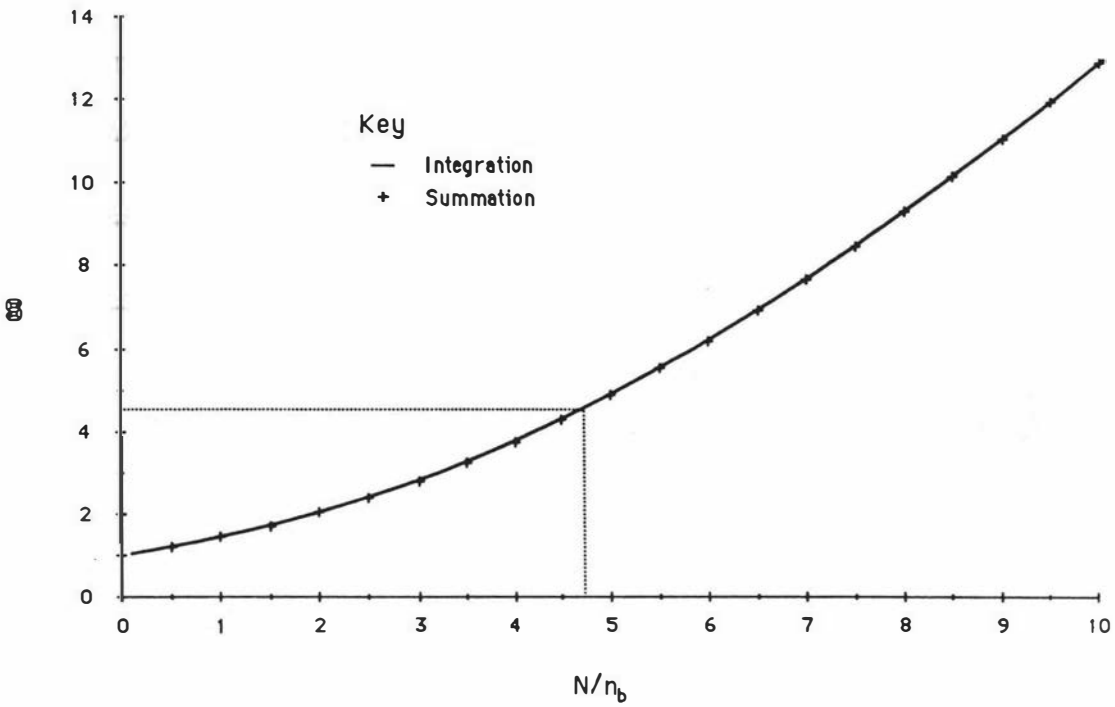

Figure 6.14 Smoothing factor vs. applied broadening for FBP.

6.7 Resolution in Filtered Back Projection

The results in section 6.6 may be used to derive an expression for spatial resolution in FBP. Combining equations 6.26, 6.28 and 6.59 we obtain

$$(S/N)_r = \sqrt{12/\pi} \times 2.72 \times 10^{-3} (\Delta z^2 \Delta y/4) f^{7/4} R^{-1} (\Delta f\, F\, \sigma)^{-1/2} (N N_p N_{acc})^{1/2}\, \mathbf{S}(FBP). \quad (6.60)$$

giving a resolution for FBP of

$$\Delta z = 36.52\, (S/N)_r^{1/2}\, \Delta y^{-1/2}\, f^{-7/8}\, R^{1/2}\, (\Delta f\, F\, \sigma)^{1/4} (N N_p N_{acc})^{-1/4}\, \mathbf{S}(FBP)^{-1/2}. \quad (6.61)$$

This expression can be minimised by adjusting the bandwidth Δf until the natural linewidth due to T_2 processes is equal to the applied broadening, in other words we apply a matched filter. The required broadening is determined by adjusting n_b until the Rayleigh criterion is satisfied. Figure 6.15 plots contrast C as a function of n_b for N = 256. From this data we see that C = 0.81 when $N/n_b = 4.74$ (since half the broadening arises from T_2 processes). The appropriate smoothing factor can then be determined from figure 6.14, as $\mathbf{S}(FBP) = 4.57$. With this result and

$$\Delta f = n_b/T_2 = 0.66N/(\pi T_2) \quad (6.62)$$

we obtain our final resolution expression

$$\Delta z = 11.58\, (S/N)_r^{1/2}\, \Delta y^{-1/2}\, f^{-7/8}\, R^{1/2}\, (F\, \sigma)^{1/4} (N_p N_{acc})^{-1/4} (T_2)^{-1/4}. \quad (6.63)$$

Δz values have been calculated using this formula for conditions identical to those used in Table 6.1. The results are listed in Table 6.2 for $N_p = N$.

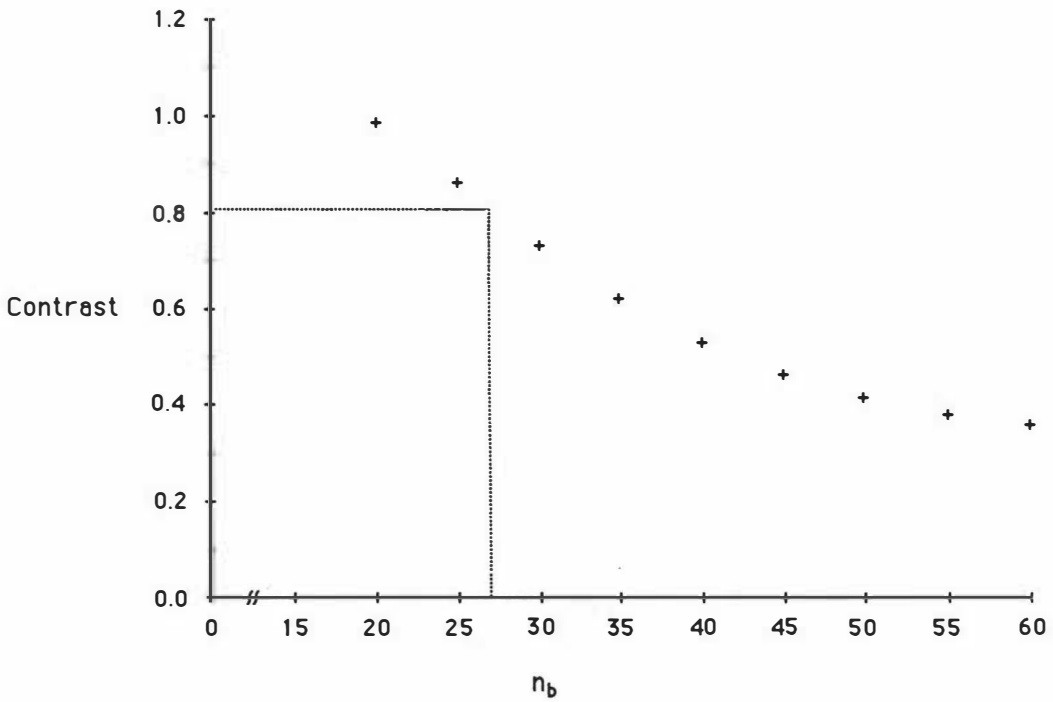

Figure 6.15 Pixel contrast as a function of filter constant for filtered back projection with N = 256.

Table 6.2 Resolution as a function of T_2 for various imaging configurations in filtered back projection

	System		
Parameter	**A**	**B**	**C**
f	60MHz	60MHz	600MHz
Δy	1.5mm	100μm	100μm
F	2(6dB)	1.03(0.5dB)	1.03(0.5dB)
R	2.8mm	2.0mm	2.0mm
N	256	256	256
σ	7	7	7
N_{acc}	8	8	8
S/N	40	40	40
T_2 (ms)	**Resolution (linear & voxel) μm (μm³)**		
5	16.9 (75.4)	46.9 (60.4)	6.3 (15.8)
10	14.2 (67.2)	39.4 (53.8)	5.3 (14.1)
50	9.5 (51.4)	26.4 (41.1)	3.5 (10.7)
100	8.0 (45.8)	22.2 (36.6)	3.0 (9.6)
500	5.4 (35.0)	14.9 (28.0)	2.0 (7.3)

6.8 Comparison of FBP and FZ

The results in equations 6.31 and 6.63 indicate that FBP is the more sensitive imaging technique. Additional sensitivity advantages arise when the sample T_2 is short, since FZ requires that k_N be established before sampling can begin.

Because of the simplicity of the FZ reconstruction process it is possible to obtain images more rapidly using this technique. With a half second repetition time, k space data for a 128×128 image can be obtained in around 2 minutes. If the first Fourier transform is performed as the data comes to hand the overall imaging time would be around 4 minutes. At present, signal to noise levels are such that the longer time required to perform FBP is not a disadvantage. Reconstruction times are currently around 36 minutes for a 256×256 image array but with 128^2 data points this could be reduced to 9 minutes. Because image reconstruction is performed while data is being acquired the FBP process is in fact faster for a given S/N ratio.

Several authors[23] have commented that FBP is particularly susceptable to image distortions caused by sample movement and gradient non-orthogonalities and we have indeed observed problems of this nature. However our few experiments with FZ have not convinced us that this technique is any better, indeed the phase distortions produced were quite severe. Initial investigations indicate that these could be caused by the poor rise times observed with small gradients (see section 8.10) which would lead to distortions in the placement of the k space data. This is not a problem in FBP as the net gradient is always the same and so the effect of the smaller gradient is swamped by the larger.

Because FZ produces both real and imaginary k space data, correct phasing is critically important if image distortions are to be kept to a minimum. Some authors[12] suggest that the absolute magnitude of the complex data be taken, but unfortunately this results in a loss of spatial resolution. Phasing problems are mimimal in FBP as the projection profile data from a single scan should always be positive (unlike the k space data obtained using FZ). A single phase adjustment at this stage is therefore all that is required to ensure the correct phasing of the final image.

6.9 Ways in which the spatial resolution might be improved

Several techniques have been suggested which might allow the resolutions predicted by equations 6.31 and 6.63 to be improved upon. The first, originally due to Waugh[24] and instigated by Hasse et al.[25], in their FLASH imaging experiment, involves reducing the excitation angle θ of the selective pulse along with the repetition time T_r. Waugh has shown that a sensitivity improvement of around 8% is obtained when θ and T_r become small. Although the signal to noise

gain from this experiment is small (despite claims to the contrary by the FLASH imaging proponents) it does allow considerable reductions in the overall imaging times if the subsequent loss in resolution and/or signal to noise can be tolerated. For example a 256×256 FZ image could be obtained in ~5s if we allocated 20ms/experiment.

In his paper on NMR sensitivity Waugh calculated that significant improvements could be made in the signal to noise ratio if the Carr-Purcell sequence shown in figure 6.16 were used and if all echoes (both forward and reverse) were co-added. Unfortunately he assumed in his analysis that $T_1 \approx T_2$ when in fact most biological tissue, and plant tissue in particular, has $T_1 >> T_2$ (see for example ref. 8 p22). The results in appendix D show that even with τ/T_2 ratios of 0.05 the improvement in S/N is only ~2.8 and since the time scale for an NMR experiment with optimum broadening is such that $N/n_b \sim 4$, little benefit is derived from applying this technique when working with optimum broadening. However for situations where the bandwidth used is much broader than optimum the improvements shown in equation D.7 could still be made. Calculations we have made[26] indicate that this allows the resolution in these cases to improved, with the limiting values being set by the optimal resolutions determined in this work.

Several papers have recently been published which promote the use of the maximum entropy method (MEM) in NMR. This technique is an iterative process which is used in place of the ordinary Fourier transform to calculate the spectral data, the constraint being that the 'entropy' defined by the function

$$S = \sum_j m_j \ln m_j \qquad (6.64)$$

is maximized, where m_j is the intensity of the jth point in the spectrum. Despite several claims[27] of considerable improvements in S/N it would appear that the optimum S/N, consistent with minimum base line distortion, is not better than that obtained using the more conventional approach of applying an optimum filter[28] to the fid and then Fourier transforming. However whereas the application of the optimum filter doubles the spectral linewidth the MEM leaves it unchanged and so a potential doubling of the spectral resolution is feasible. Although this could sigificantly improve the resolution in imaging it would be difficult to implement on a small system because of the large number of computations required when applying the MEM to two dimensional data.

With the above comments in mind it would therefore seem that the data in table 6.2 provides a maximum limit for resolution on our system (column B) and for systems in general (column C).

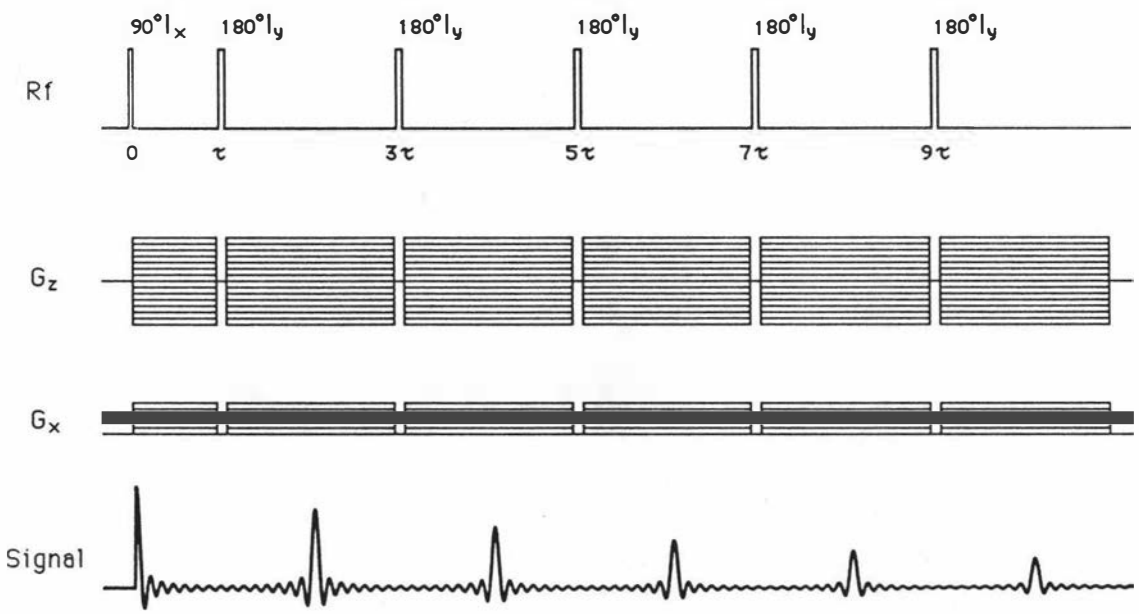

Figure 6.16 Carr-Purcell pulse sequence used to enhance the sensitivity of the FBP imaging experiment. The echoes may be coadded to improve the signal to noise ratio.

7 The FX60 spectrometer

Having considered the imaging process in some detail we can now move on and look at some of the practical aspects of microscopic imaging. The following chapter looks briefly at the existing spectrometer - a Jeol FX60. This machine is a multinuclear instrument which uses pulsed Fourier transform techniques to obtain NMR spectra. A block diagram showing the essential components of the system is given in figure 7.1.

The operating procedure for producing a free induction decay is as follows. Upon instruction by the computer the rf transmitter will produce the short $\pi/2$ pulse which is channelled by the duplexor to the probe tank circuit. The probe resonantly excites the nuclei which subsequently precess in a plane transverse to the main field. Once the transmitter pulse has been removed the nuclear signal is free to pass to a low noise preamplifier and high gain receiver. The voltage generated by the receiver is then digitized and transferred to the computer for spectral analysis.

7.1 RF probe

The commercial Jeol rf probes are rather elaborate items (see figure 8.2), since each unit has a full set of shim coils which allow the field inhomogeneity to be reduced to within a few parts in 10^8 (corresponding to a line width of a few hertz). The probe is of a solid copper construction plated with silver for good conduction. The shim coils are mounted on the sides of the probe which are constructed from fibreglass pcb (also silver plated). The entire construction of the probe has been designed to promote maximum shielding from outside rf interference. To eliminate any possibility of field distortions non-ferrous metals are used throughout - even down to the bolts which are made from copper (as brass contains ferrous impurities).

The electronics in the standard probe tend to be fairly complicated since the main rf coil must perform two functions. It must be able to stimulate the desired nuclei with a pulse of rf, observe the response, and simultaneously irradiate a second nuclear species so a lock signal can be generated to prevent the main field from drifting. When both the nuclei under investigation and lock nuclei are present in the same sample we are said to be using an internal lock. When it is undesirable to contaminate the sample with the lock nucleus (as in this work) an external lock may be used. This consists of a small rf coil and lock sample which are placed in close proximity to the NMR tube containing the nuclei of interest. In this case the rf electronics is quite separate for both systems.

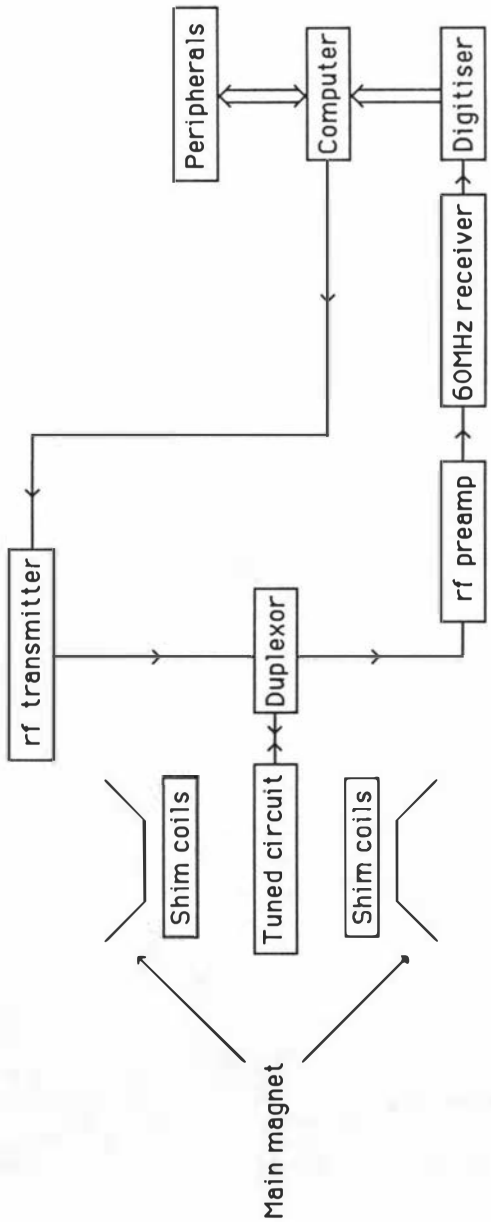

Figure 7.1 Block diagram of the FX-60 spectrometer.

7.2 Lock system

Since the resonant frequency of interest depends on the strength of the applied magnetic field it is important that this field be as stable as possible.

The lock system is basically a continuous wave spectrometer. When setting up the lock the main field is swept, by means of a set of Helmholtz coils wound on the outside of the probe, through the lock resonance. This causes a change in the impedance of the detection tank circuit (see figure 7.2a) which results in a change in the rf voltage level at point a. The phase shift in the detection system is adjusted until the response has a dispersion like form. The main field is then adjusted manually until (with the sweep now disconnected) we are exactly on resonance (i.e. at f_0). Any deviations from resonance (due to drift in the system) will produce a non-zero signal which is detected by the error detection circuitry and fed, with an appropriate sign change to the Helmholtz coils so as to correct the drift.

Since some frequencies may be more susceptible to interference than others it is normal to modulate the lock oscillator with a square wave so that a variety of lock frequencies are produced (figure 7.2b).

7.3 Duplexor

To achieve short 90° and 180° pulse times it is necessary to irradiate the sample with a large rf voltage - typically 60V p-p in the Jeol system. To protect the rf preamplifier from this large voltage (since it is designed to detect signals in the μV range) it is necessary to have some form of switch, or duplexor, which selects the signal path (see figures 7.3a and 7.3b).

During the transmit phase, diodes D_1 to D_4 may be replaced by short circuits since their forward conduction threshold is ~0.6V. Since a shorted $\lambda/4$ line looks like an open circuit a direct path exists from transmitter to sample coil. In the receive phase a small fid with an amplitude very much less than 0.6V is generated across the tank circuit. Diodes D_1 to D_4 now look like open circuits and so a direct path exists from the sample coil to the rf preamplifier.

The $\lambda/4$ line tends to be rather cumbersome and is really only useful at one frequency. The Jeol system (fig. 7.4) uses a lumped circuit which achieves the same result although at the expense of greater complexity and some signal loss.

The complex tapping arrangment in the sample tank circuit is a form of impedance matching. The network inside the dotted rectangle takes the place of the quarter wave line. During the transmit pulse diode pairs $D_{5,6}$ and $D_{7,8}$ act as short circuits. The parallel combination L_2,C_5 is tuned to the

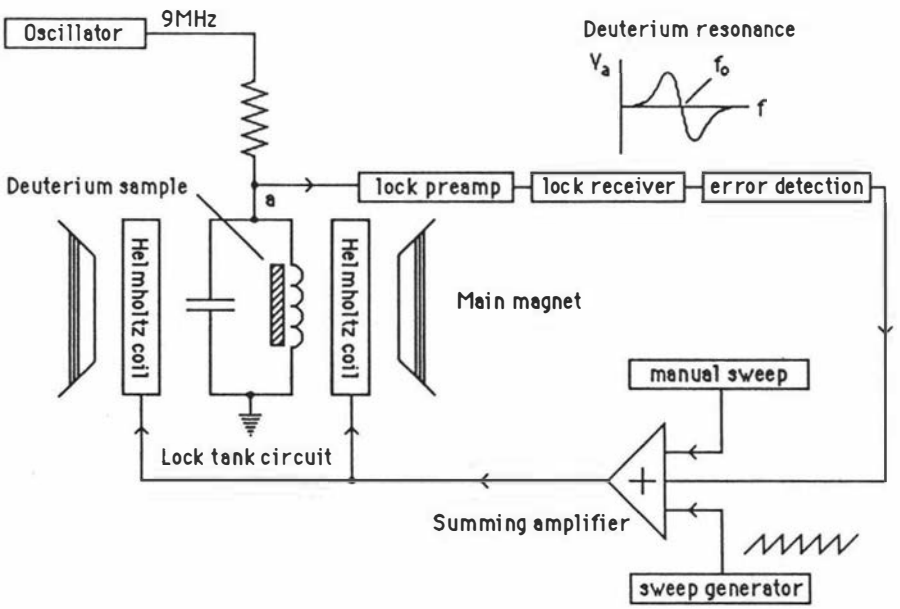

Figure 7.2a Block diagram of the lock system.

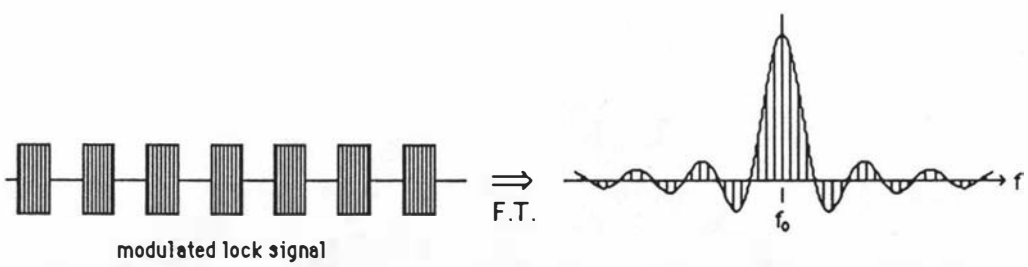

Figure 7.2b Lock modulation.

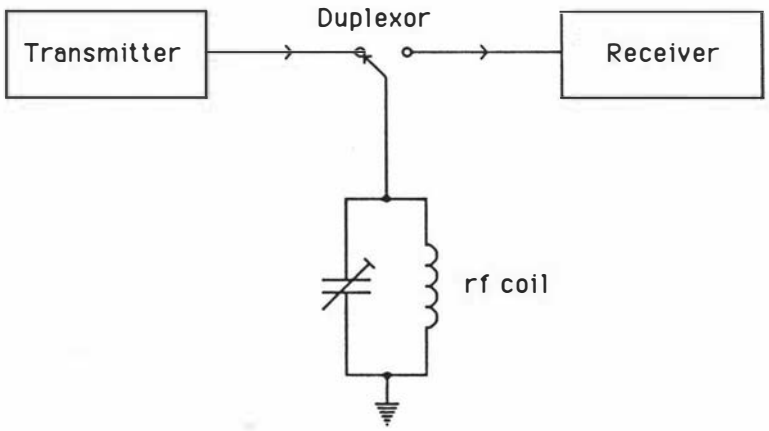

Figure 7.3a The ideal duplexor.

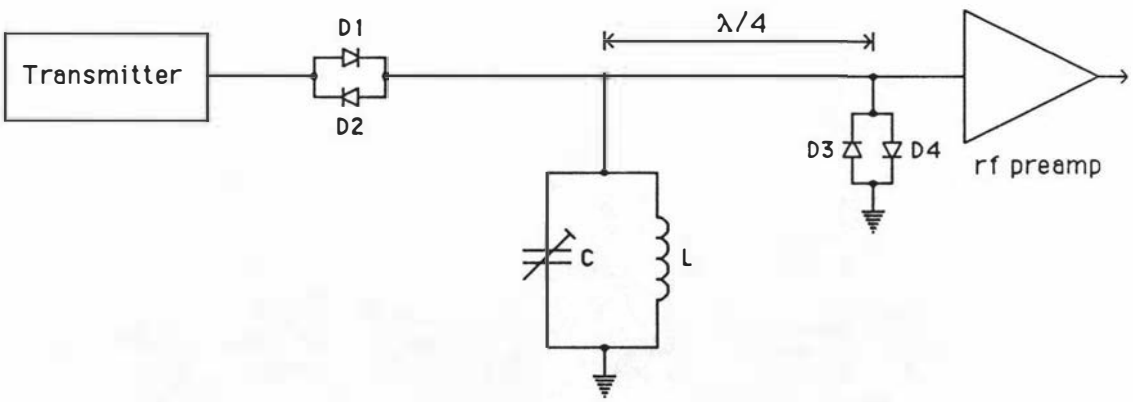

Figure 7.3b A practical duplexor.

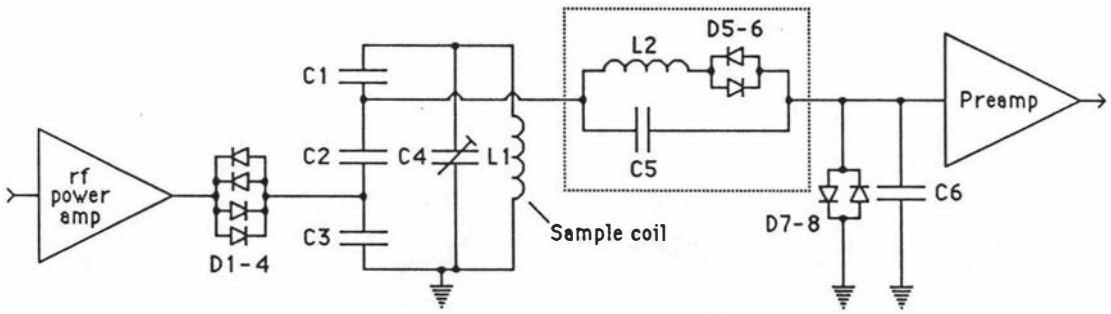

Figure 7.4 Schematic of JEOL duplexor.

resonant frequency ω_0 and so will look like an open circuit, effectively isolating the preamp from the transmitter. In the receive mode all crossed diodes appear as open circuits leaving a direct path via capacitor C_5 from sample to preamp.

7.4 60MHz Receiver

After passing through the rf preamplifier the NMR signal undergoes further amplification and is then detected by a fairly conventional fixed frequency, single conversion, superheterodyne receiver (see figure 7.5).

A single stage rf amplifier (at 60MHz) is followed by a mixer stage which produces an 11MHz signal. This is then amplified by two MC1350 based intermediate frequency stages. A second mixer stage - operating as a phase sensitive detector (i.e. local oscillator frequency = incoming carrier frequency) produces an audio signal which is amplified by a variable gain 741 opamp. The output from this amplifier feeds a two stage active filter which has a bandwidth equal to that defined by the subsequent digitizing stage (so as to prevent noise aliasing). This is based around a 12 bit device with sampling intervals ranging from 20μs to 5ms (i.e. filter bandwidths from ±25kHz to ±100Hz). The digitised signal is read by a TI-980A computer and stored in memory for later analysis.

7.5 TI-980A computer

The Texas Instruments 980A computer is a 16 bit machine with 32k words of memory and an average execution time of ~1μs per instruction. The 980A can drive a number of peripherals including an oscilloscope for data display, light pen for interactive experiment design and data analysis, a plotter for producing hardcopy of the free induction decay or corresponding spectra and a digital cassette recorder for program and data storage.

An extensive software package is supplied with the machine and includes the following features.

1) The selection of a 1 or 2 pulse irradiation sequence with control over all aspects of pulse timing and rf phase.

2) A data averaging algorithm allowing the accumulation of data over long time periods for the purpose of improving the signal to noise ratio.

3) A fast Fourier transform allowing rapid (5s for an 8k transform) generation of frequency domain data.

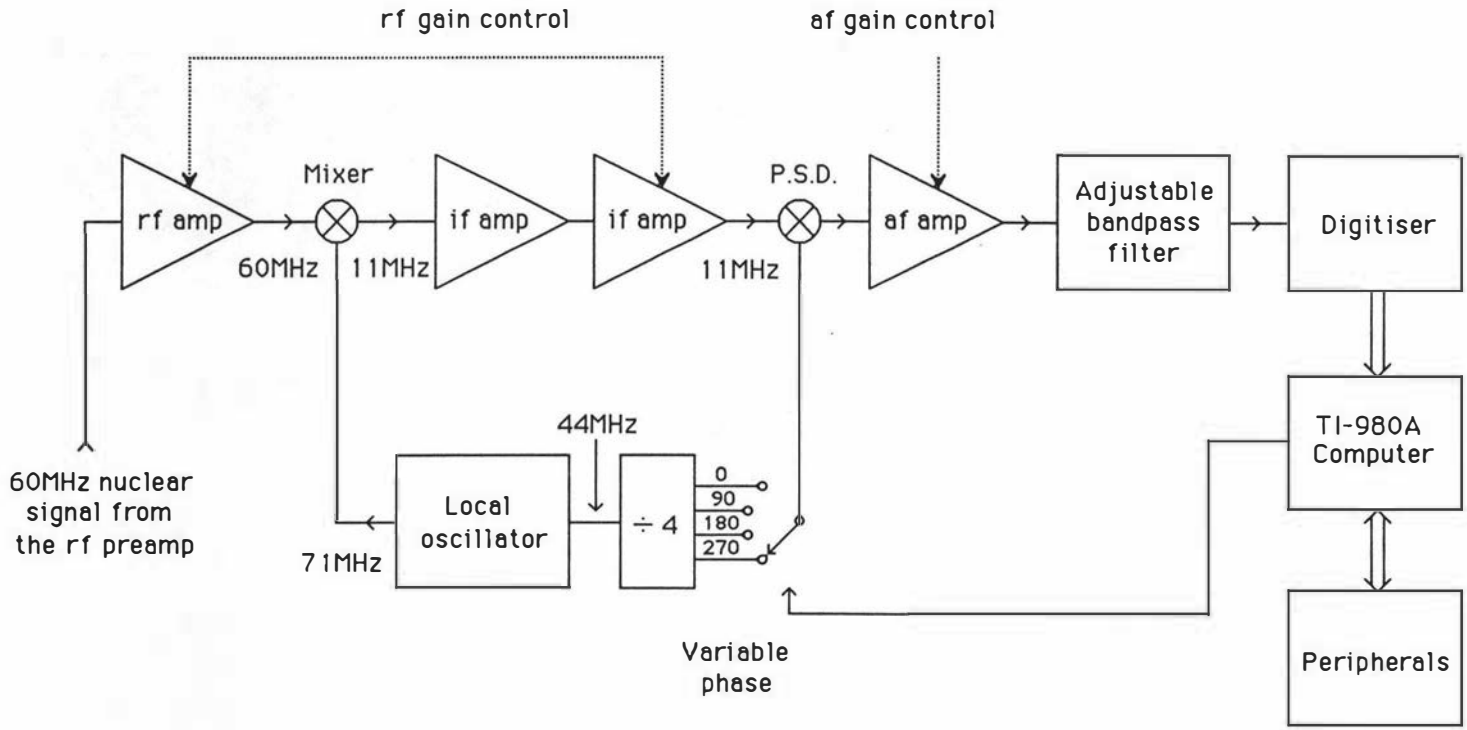

Figure 7.5 FX-60 receiver and data acquisition block diagram.

4) A versatile data smoothing procedure which when used in conjunction with the FFT leads to an improvement in S/N in the frequency domain.

5) A procedure for analysing the frequency domain data which includes an integration routine for finding the area under a peak.

All processes are activated using a menu based system - interaction with the software being via the light pen.

8 Imaging Hardware

During the development of the imaging system it was necessary to make various alterations and additions to the apparatus described in the previous section. A block diagram of the complete imaging system is given in figure 8.1. Those items enclosed by a dotted line are new and are described in detail in the following sections.

8.1 Rf probe

The rf detection circuitry used in the imaging system is housed in a modified ^{13}C Jeol probe (see figure 8.2). The rf coil, which is used to supply the rf pulse and detect the nuclear signal is the most important part of the probe. Because spatial resolution varies as the square root of the coil radius (eq. 6.63) it is important that the coil be as small as possible for a given sample size. For this reason the coil can be unplugged and other coils selected to match the size of the specimen being imaging. Two coils are presently available and have the following characteristics (see also fig. 8.3).

Table 8.1 Rf coil characteristics

Parameter	Large coil	Small coil
diameter	13mm	5.8mm
length	11mm	5.8mm
wire diameter	shim	0.76mm
inductance	0.15µH	0.17µH
unloaded Q	100	100
No. of turns	3	6
90° pulse time	11.5µs	3.5µs

Copper shim (dimensions 0.08×3mm) was used in the larger coil since round wire of sufficient diameter would have prevented insertion of the rf coil into the narrow confines of the probe. Since the tank circuit must be matched to an equivalent impedance for maximum power transfer the Q measured in situ will be half that obtained in the unloaded configuration. Loaded Q was therefore 50 giving rise to a bandwidth of 1.2MHz. The shorter 90° pulse time in the smaller coil

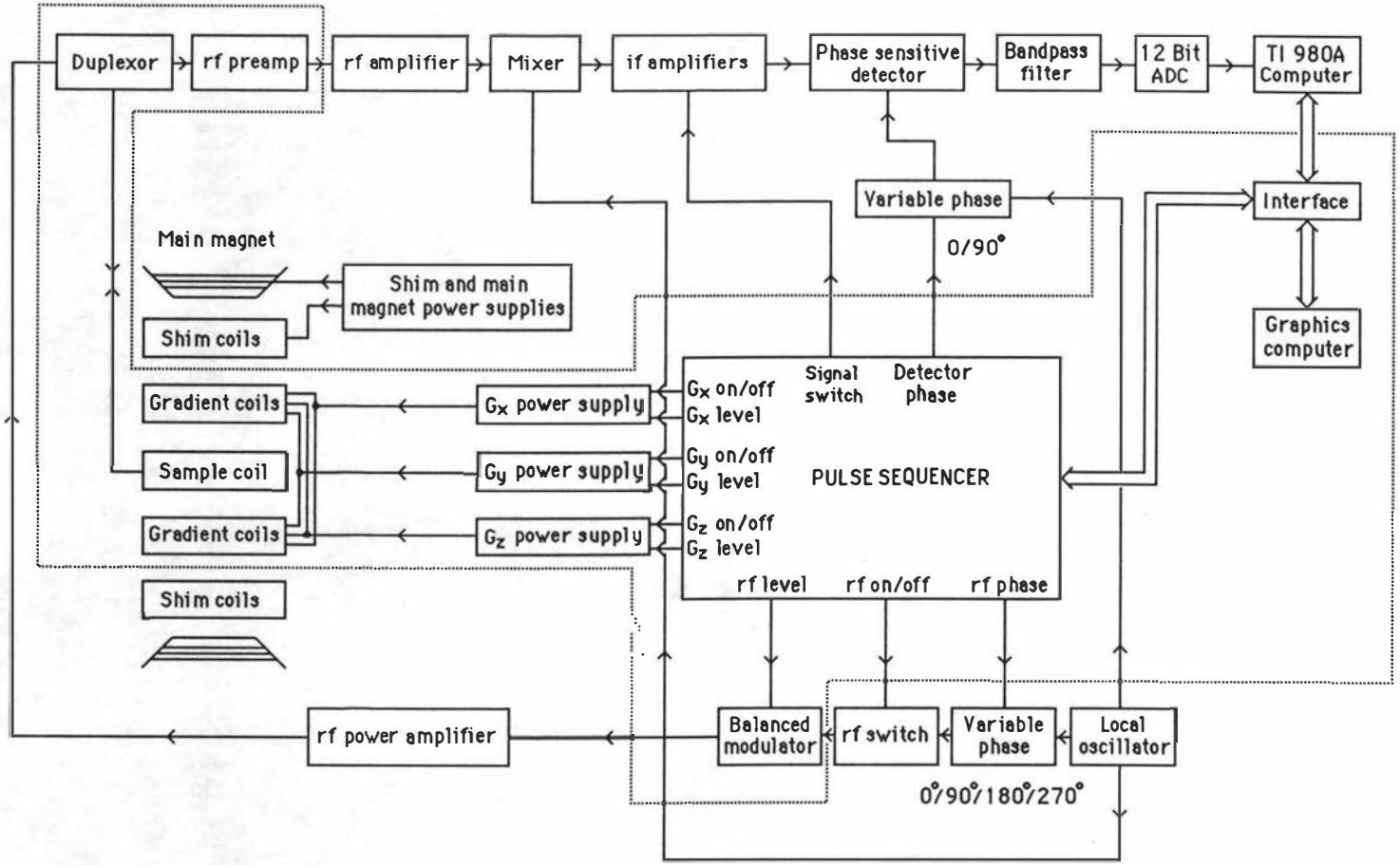

Figure 8.1 Block diagram of the imaging system.

Figure 8.2 *(top)* The modified ^{13}C probe used to perform imaging experiments.

Figure 8.3 *(bottom)* The rf coils used in this work.

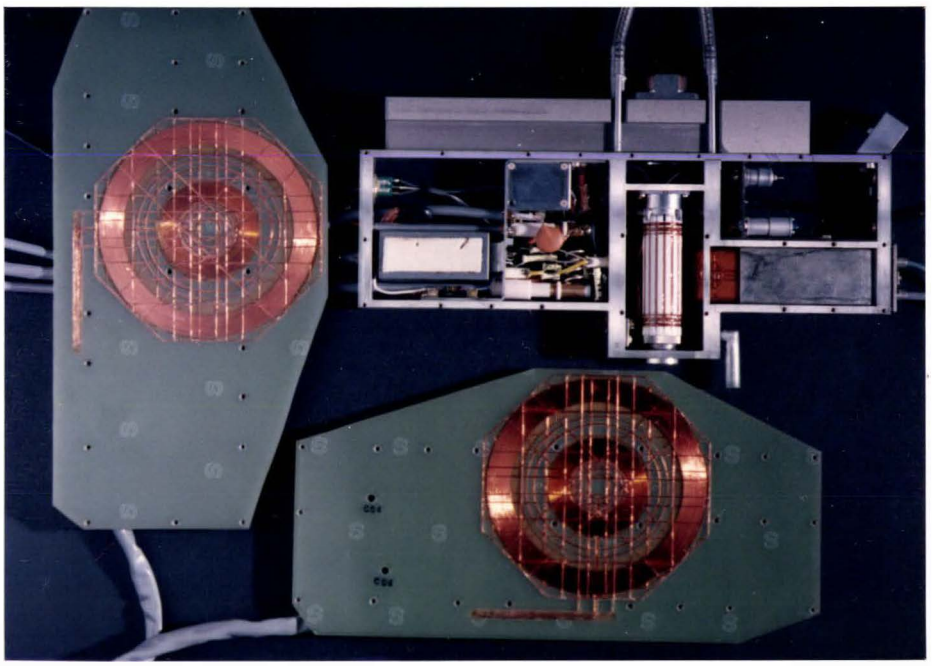

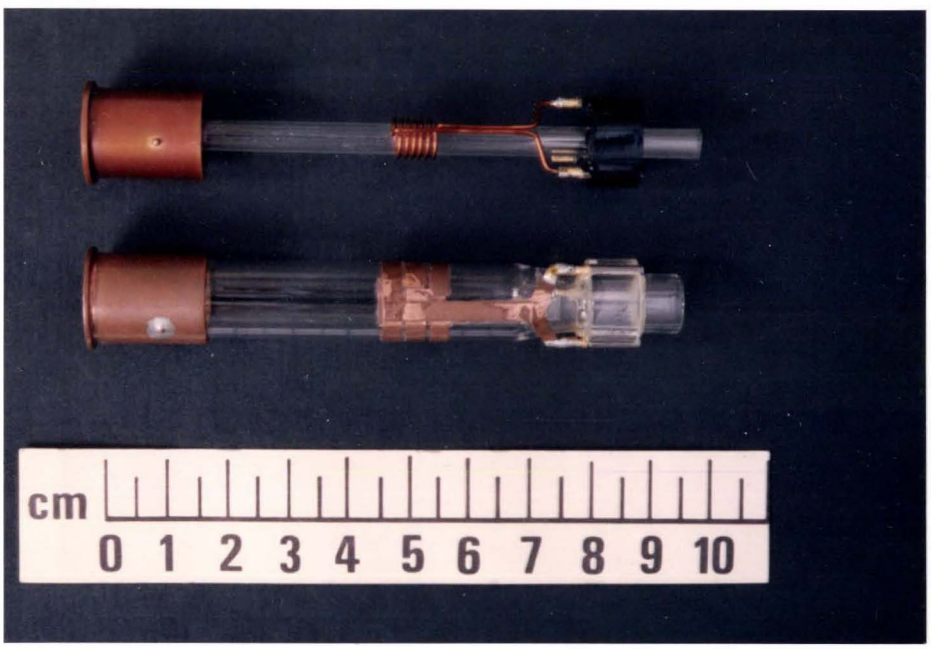
cm
0 1 2 3 4 5 6 7 8 9 10

is due to the more intense field it produces. From the dimensions given above one would expect a four fold reduction (c.f. equation 5.9).

The function of the rf probe is two fold. Firstly it must transfer a high level (~60Vp-p) rf pulse of variable duration, from the spectrometer to the nuclear system in an efficient manner. Secondly it must be able to pass with little loss in signal strength the induced nuclear signal from rf coil to preamp .

For single coil systems (as used in this work) the sensitive rf preamp must be electrically isolated from the rf pulse during the transmit phase. The lumped circuitry used in the existing duplexor, as described in section 7.3, was removed in favour of the simpler arrangement, due to Hoult[15], also described in section 7.3 and redrawn, in more detail, in figure 8.4.

The tank circuit includes an impedance matching transformer which is necessary to prevent severe damping of the circuit Q. The circuit acts much like an auto transformer - a small voltage across C_1 appearing as a much larger voltage across L. Capacitors C_1 and C_2 are selected so that the tank circuit presents a 50Ω impedance to the transmission lines. (See appendix E for a detailed discussion of impedance matching circuits).

Unlike the duplexor depicted in figure 7.3a, the diode duplexor is not ideal. At 60MHz most diodes have a significant capacitance when not conducting[16]. During the receive phase this can lead to increases in noise levels due to coupling with the transmitter. Significant improvements may be obtained by replacing each diode with two diodes in series. This reduces the capacitance by a factor of 2. The subsequent increase in conduction voltage (0.6V to 1.2V) which arises from this configuration of diodes was not found to present any major difficulties.

To achieve maximum power transfer it was necessary to match all impedances to 50Ω. Tank circuit tuning was achieved using an rf bridge (see figure 8.5). The tank circuit was placed in one arm of the bridge which was driven by a 60MHz signal generator. C_1 and C_2 were then adjusted until a null was obtained on the oscilloscope. The correct length for the $\lambda/4$ line was determined by connecting it to the output of a signal generator which was being monitored at the source by an oscilloscope. Since an open ended $\lambda/4$ line acts as a short circuit, correct cable length was found by reducing the length until a null was observed on the oscilloscope.

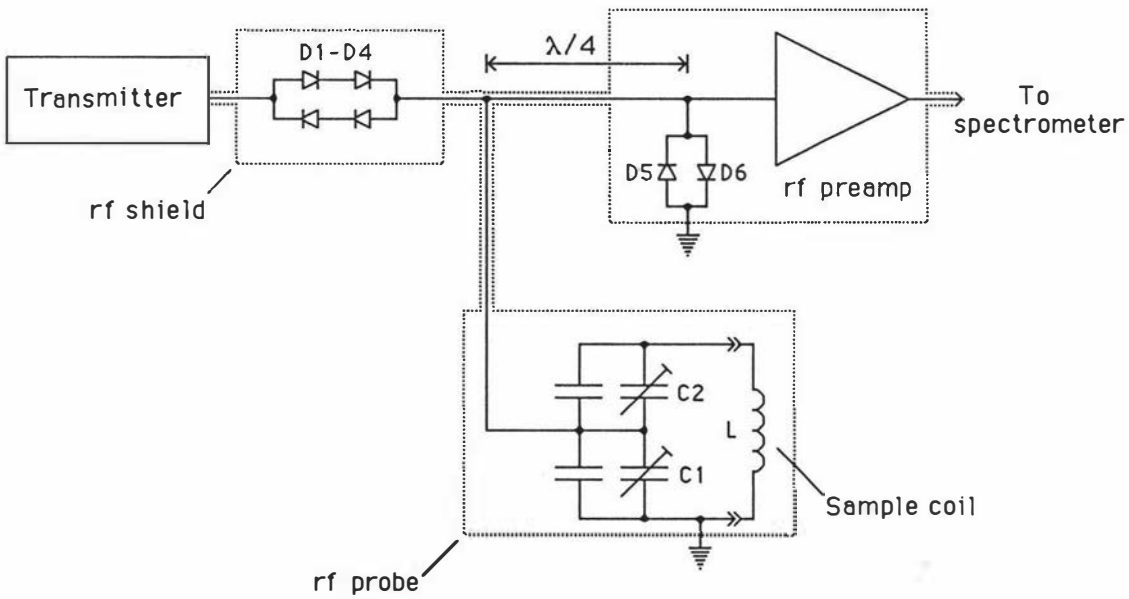

Figure 8.4 Schematic of the rf probe and duplexor used in the imaging system.

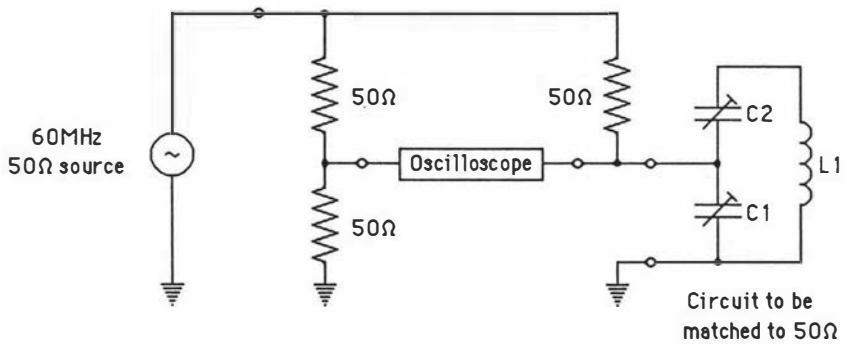

Figure 8.5 Schematic of rf bridge.

8.2 The Radio Frequency Preamplifer

From the point of view of optimizing the signal to noise ratio the most important part of the detection system in an NMR spectrometer is the rf preamplifier. If the preamp has reasonable gain its noise figure will largely determine the noise figure of the complete system. The noise figure of the spectrometer alone is poor as can be seen from following table.

Table 8.2 Noise figure of the spectrometer as a function of rf gain

RF gain	System gain	Noise level[1]	Equiv. input noise	Noise fig.[2]
1	0.95	0.18mV	190μV	63
2	4.13	0.18	44	51
3	50.9	0.76	15	41
4	1000	0.81	0.8	16
5	5438	1.70	0.3	8

Notes.

1) Rms noise level measured directly after the filter unit (BW 20kHz) with 50Ω resistor connected to the input.

2) Noise figure = 20 Log_{10} (Equivalent input noise/rms noise level due to a 50Ω resistor over a 20kHz BW).

If a preamplifier with a voltage gain of say 15 and a noise figure of 0.8db were connected to the input of the system the noise level would be reduced in the following manner.

$$N_T = [\ (N_p\ G_p\ G_s)^2 + (N_s\ G_s)^2\ ]^{1/2} \qquad (8.1)$$

where N_T is the rms equivalent input noise of the complete system, N_p is the equivalent input noise for the preamp, N_s is the equivalent input noise for the spectrometer, G_p is the preamp gain and G_s is the spectrometer gain.

Using the gain and noise figures of table 8.1 we would obtain:

Table 8.3 Noise figure as a function of rf gain setting

Rf gain	G_pG_s	N_T	Noise figure
1	14	12.70μV	40
2	62	2.84	27
3	764	0.90	17
4	15000	0.15	1.4
5	81570	0.14	1.0

A noise figure of 1db corresponds to a 12% increase in the noise voltage due to noise sources within the system. For most purposes this is more than adequate. Unfortunately with a gain of 81570 the noise level would be ~11mV rms and since the maximum signal before overload, for this gain setting, is ~200mV rms the maximum signal to noise ratio possible would be ~26 (peak/rms). This is clearly insufficient. The solution to this problem was to attach a high gain, low noise preamp to the front end of the system and image with the rf gain set to 1. The preamp used is based on broadband (300MHz) Plessey amplifiers (see figure 8.6).

The tapping on inductor L was adjusted so as to present a 50Ω impedance to the driving source and 200Ω (the optimum for noise figure purposes) to the preamp. The voltage gain for the amplifier was measured as 900±50 (output into 50Ω /unloaded input). The noise figure was determined to be

$$NF = 10 \log \{(N_p^2 + N_{50}^2)/N_{50}^2\} = 1.9 \pm 0.4 dB \qquad (8.2)$$

where N_p is the equivalent input noise voltage for the amplifier. The observed p-p noise voltage on the output was 30±2mV (measured with a 100MHz BW oscilloscope) and so N_p = 6.0±0.4mV/900±50 = 6.7±0.8μV rms. Note that because of the bandpass filter on the input the noise due to the source can be ignored. N_{50} is the noise produced by a 50Ω resistor over a 100MHz BW which is just 9μV rms.

With the preamp in place the following measurements were made:

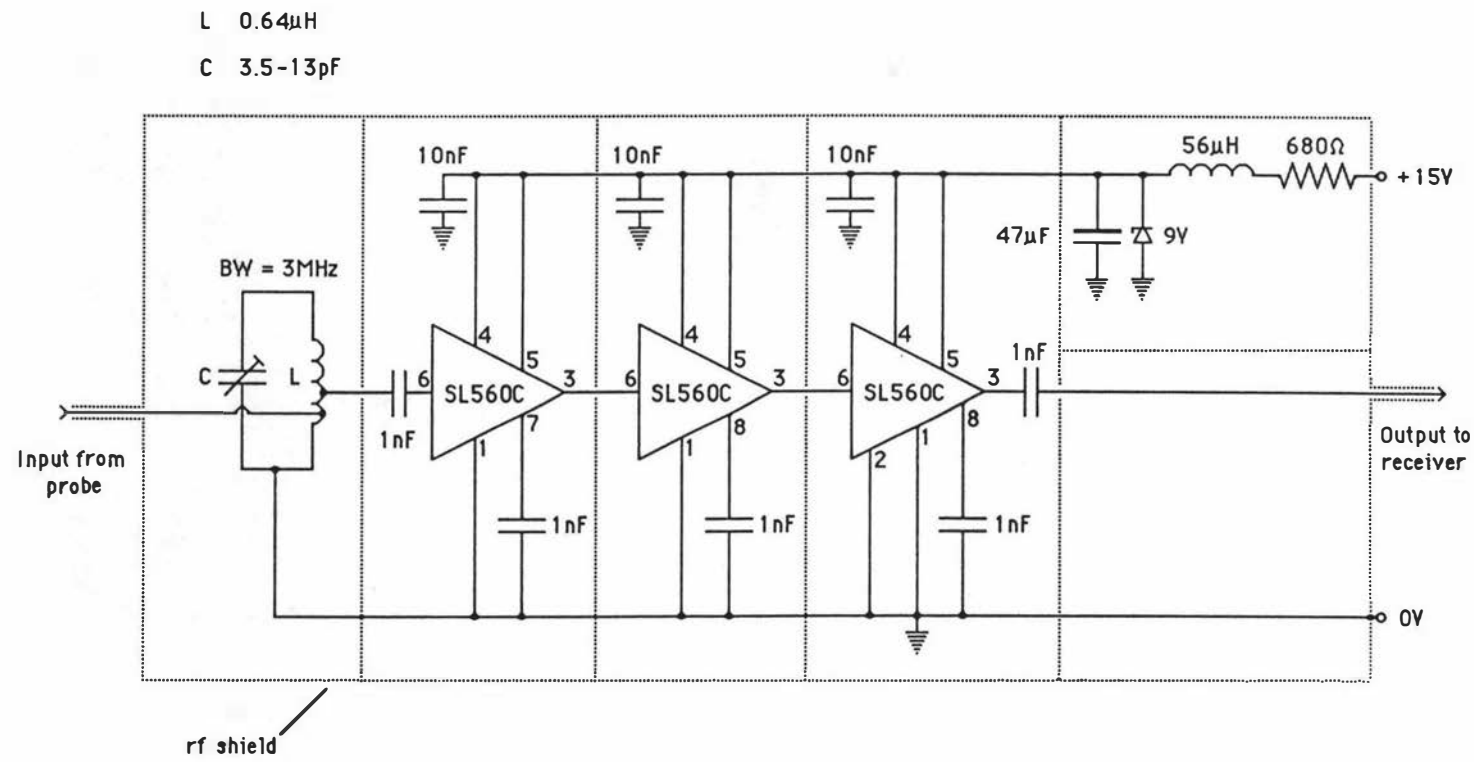

Figure 8.6 Schematic of rf preamplifier

Table 8.4 Noise figure of the spectrometer and preamp as a function of rf gain

RF gain	Noise level	System gain	Noise figure
1	0.54mV	2830	3.4dB
2	2.35	10800	4.5
3	30.0	111000	6.4

Maximum signal to noise with this system (before overload) is 520.

It is evident from this data and that in table 8.2 that these results are inconsistent with previous gain and noise figure measurements. Investigations soon revealed a plethora of impedance mismatches, and instabilities within the spectrometer. The input impedance of the first rf stage (after the preamp) was observed to vary from 57 to 86Ω depending on the rf gain setting while the output impedance of the preamp was only 18Ω - far from the 50Ω suggested in the application notes. Attempts to match the output impedance of the preamp to 50Ω (without significant loss) ended in failure because of the resulting instabilities. In addition it was found that the observed noise level was critically dependent on the mixer offset frequency (which can be adjusted manually over a 100kHz range). Interference from the digital circuitry in the spectrometer seemed to be the culprit. State of the art Jeol spectrometers no longer suffer from this problem as the digital and rf sections are electrically isolated, with optical fibres being the sole means of communication.

At this stage it was concluded that successful rf engineering required a certain familiarity with the black arts and that time would be better spent on more tractable aspects of the project. Despite these misgivings the dynamic range was markedly better than it had been, while the noise figure was considered adequate for most imaging tasks.

8.3 Rf Modulation

In section 3.2 we found it was necessary to apply a sinc modulated rf pulse to the nuclear spin system if selective spatial excitation was to be carried out effectively.

From figure 8.7 we see that amplitude modulation is incapable of producing the correct excitation spectrum because of the large frequency component at ω_c. What is required is some form of carrier suppressed modulation - either double sideband suppressed carrier (DSB) or, ideally, single side band suppressed carrier (SSB). A SSB signal is normally generated from a DSB signal and so we will consider DSB modulation first.

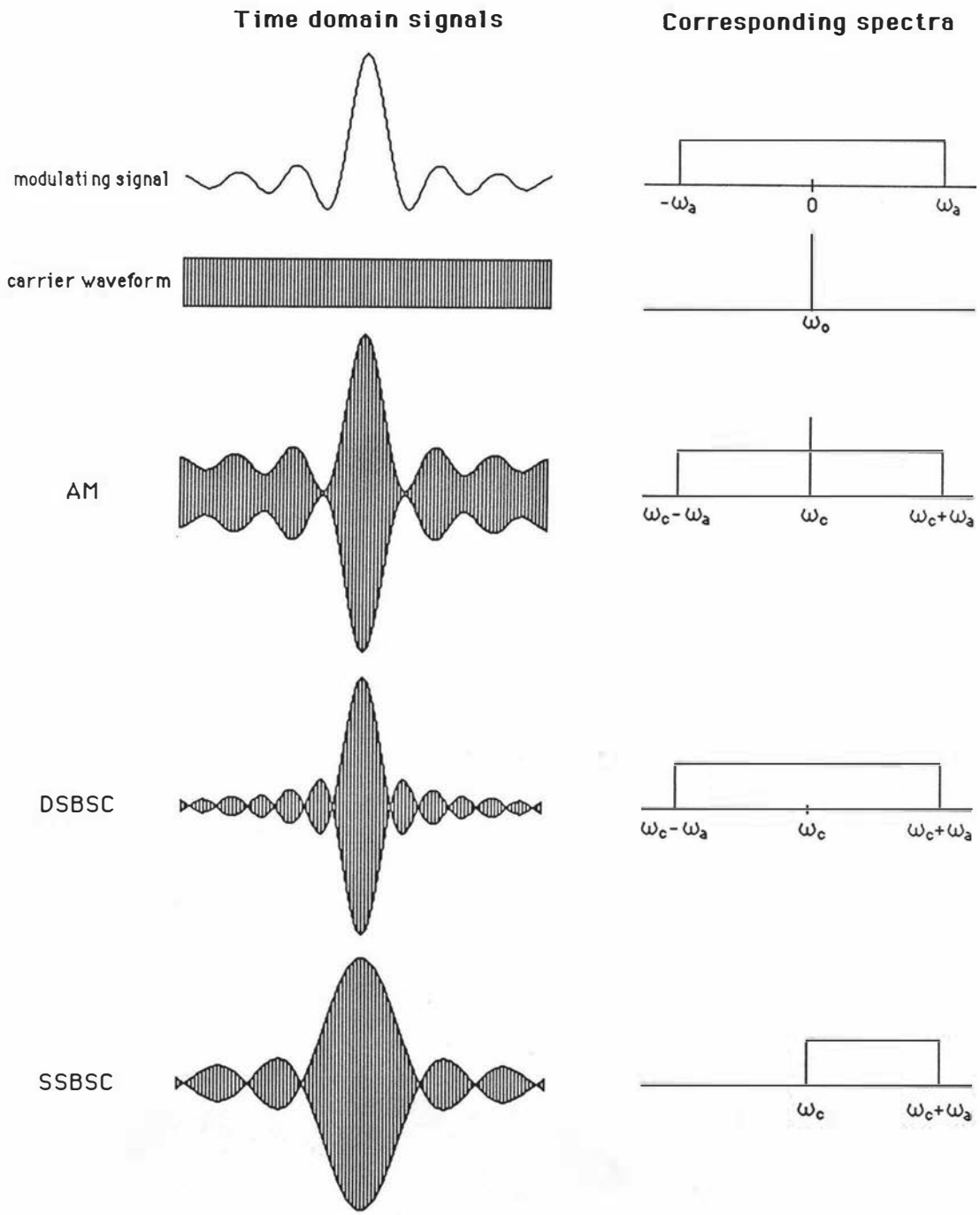

Figure 8.7 Modulation techniques

The difference between AM and DSB modulation is that the modulation coefficient is always positive for AM but may take either sign for DSB modulation. AM may therefore be simply implemented with some form of attenuation mechanism. With DSB modulation it is necessary to perform a proper multiplication between carrier and modulation functions. The multiplication process produces sum and difference frequencies so if

$$V_c(t) = V_c(0)\cos(\omega_c t)$$
$$V_m(t) = V_m(0)\cos(\omega_m t) \qquad (8.3)$$

then

$$V_c(t)V_m(t) = 0.5\, V_c(0)\, V_m(0)\{\cos(\omega_c + \omega_m)t + \cos(\omega_c - \omega_m)t\} \qquad (8.4)$$

For the case where $V_m(t)$ is a sinc function we have

$$V_c(t)V_m(t) = V_c(0)\cos(\omega_c t)\int_{-\omega_a}^{\omega_a}\cos(\omega_m t)\, d\omega_m$$
$$= V_c(0)\int_{-\omega_a}^{\omega_a}\cos(\omega_c t)\cos(\omega_m t)\, d\omega_m$$
$$= 0.5\, V_c(0)\int_{-\omega_a}^{\omega_a}\cos(\omega_c + \omega_m)t\, d\omega_m + 0.5\, V_c(0)\int_{-\omega_a}^{\omega_a}\cos(\omega_c - \omega_m)t\, d\omega_m \qquad (8.5)$$

In the frequency domain this corresponds to irradiating with a rectangular function of frequencies centered at ω_c (see figure 8.7). The device used to perform this multiplication process is called a double balanced modulator and is commonly used in communications equipment. Aside from performing either AM, DSB or SSB modulation it can also be used as a mixer or phase sensitive detector.

A block diagram showing how the modulator fits in with the rest of the system is given in figure 8.8. The carrier signal is derived from a 10.65MHz digital source which can have its phase set under pulse sequencer control. It then passes through an rf switch. This switch is normally used by the 980A to define the width of the rf pulses. In the imaging system the rf level is switched

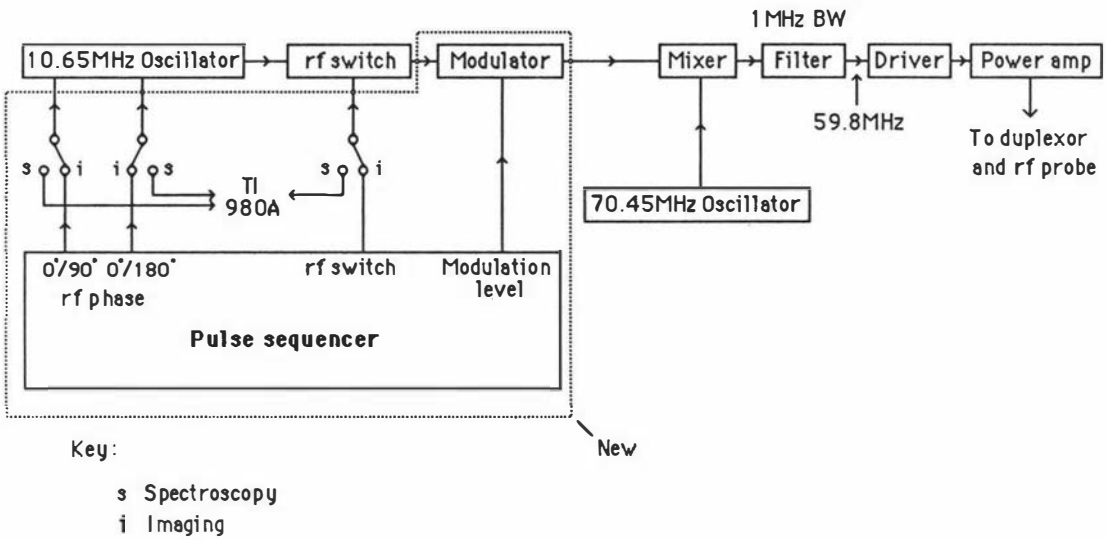

Figure 8.8 The rf modulator and associated components.

off until just before it is required since a reset to the pulse sequencer switches the modulator hard on (see below for reason).

The DBM used in this work is a Motorola IC, the MC1496. The schematic for this device is given in figure 8.9a. The device has two modes of operation - we will initially consider the situation where the carrier amplitude V_c is large. In this mode the device uses switching to periodically reverse the modulating signal polarity, effectively multiplying the signal by a square wave. An analysis of circuit operation (from Roddy and Coolen[29]) is given below.

The carrier may be considered to be a switching voltage which alternately switches transistors Q_1,Q_4 and Q_2,Q_3 on and off, each pair being switched together. Figure 8.9b shows the circuit condition when the carrier has switched Q_2,Q_3 on and Q_1,Q_4 off. If we assume that the base currents are negligible (i.e. β is large) then

$$\begin{aligned} I_2 &= I + i_e \text{ at junction A} \\ I_1 &= I - i_e \text{ at junction B.} \end{aligned} \tag{8.6}$$

The output voltage is

$$V_o = V_2 - V_1 = R(I_2 - I_1) = 2Ri_e. \tag{8.7}$$

Applying Kirchoff's voltage law to the loop containing V_m and R_e gives

$$V_m = R_e i_e - (V_{be})_6 + (V_{be})_5 \tag{8.8}$$

but the circuit is normally operated with $I \gg i_e$ and so $(V_{be})_6 \approx (V_{be})_5$. Hence,

$$V_m \approx V_e \tag{8.9}$$

which means that

$$i_e = V_e/R_e = V_m/R_e \tag{8.10}$$

where V_m is the modulating signal. Therefore

$$V_o = 2Ri_e = 2RV_m/R_e. \tag{8.11}$$

When the carrier signal input changes polarity, transistors Q_1 and Q_4 are switched on while Q_2 and Q_3 are now off (fig. 8.9c). The output voltage is then $V_1 - V_2$ and so

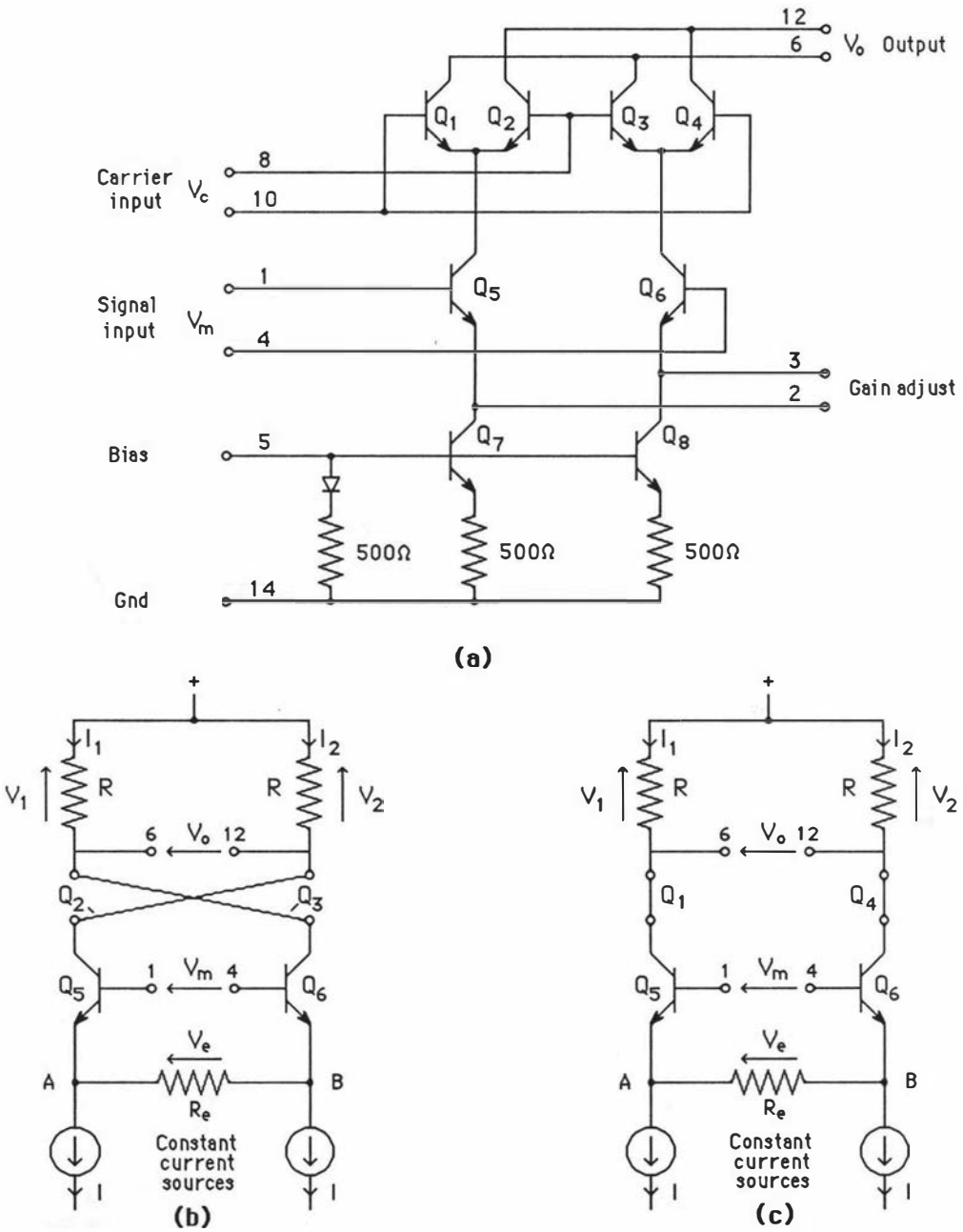

Figure 8.9 The MC1496P balanced modulator.

$$V_o = -2RV_m/R_e. \tag{8.12}$$

Thus the action of the carrier is to switch V_o at carrier frequency, between $\pm 2RV_m/R_e$. If we represent the switching action by a square wave function p(t) at the carrier frequency then

$$V_o = -2RV_m p(t)/R_e. \tag{8.13}$$

A square wave can be represented by a Fourier series and so

$$p(t) = \sin(\omega_c t) - 1/3\sin(3\omega_c t) + 1/5\sin(5\omega_c t) + \ldots \tag{8.14}$$

We see from this result that the output voltage will contain a product term $V_m \sin(\omega_c t)$. For sinusoid modulation we then have

$$V_o = (-R/R_e)\, V_m [\cos(\omega_c t - \omega_m t) - \cos(\omega_c t + \omega_m t)] + \text{higher terms} \tag{8.15}$$

The higher terms may be filtered out or more simply we can reduce the level of V_c until the carrier acts as a sinusoid (i.e. we are no longer driving the transistors to saturation and cutoff). In this case the higher terms vanish leaving us with

$$V_o \propto (-R/R_e) V_m V_c [\cos(\omega_c t - \omega_m t) - \cos(\omega_c t + \omega_m t)] \tag{8.16}$$

The disadvantage of this technique is that the output voltage level is no longer independent of the carrier level.

Figure 8.10 is the schematic diagram for the rf modulator. Pin 8 of the DBM accepts the carrier signal (at 10.65 MHz) while the modulating signal is applied to pin 1, via a CA3140 opamp. This device performs 4 functions, it inverts the negative going signal produced by the DAC. It also allows the amplitude of the modulated signal to be varied by adjusting VR1. Carrier suppression is obtained by adjusting VR2 which adds an offset voltage to the signal being applied to pin 1. The offset available by adjusting VR2 also allows digital inputs of less than 128 to be interpreted as negative allowing a modulation range of -128 to +127. (Hence the reason for the rf switch).

Although some carrier feedthrough is inevitable (the specifications for this device indicate a carrier suppression -40db at 10MHz) this was in fact not found to be a problem because of the non-linear characteristics of the final power amplifier (see section 8.5).

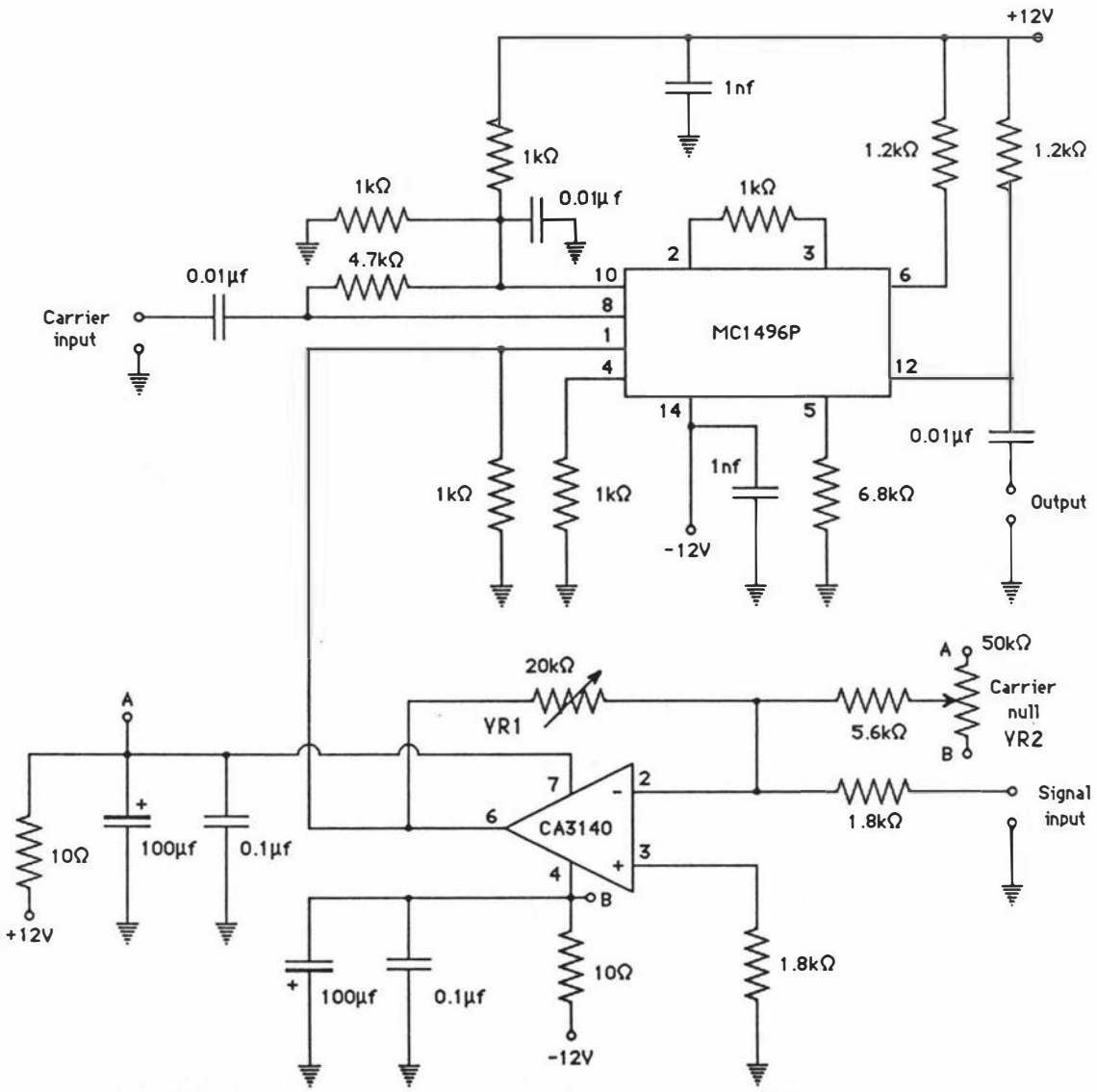

Figure 8.10 Schematic of the rf modulator.

8.4 Single sideband modulation

A disadvantage of the DSB form of modulation is that it doesn't allow the slice selected to be moved up or down the y axis. Ideally one should be able to select the y coordinate of interest and image a slice at that level. This can be achieved by changing the Larmor frequency, either through the use of a frequency synthesiser or by suitably modifying the modulation function so as to shift the block of exciting frequencies away from resonance. However since both sum and difference frequencies will be produced in the DBM an equivalent block of frequencies will be produced on the other side of resonance. Since both will selectively excite a slice of spins a good deal of confusion could result in the final image.

Two methods have been devised which remove one of the sidebands - the first is commonly used in SSB communication systems. The DSB signal is fed through a narrow bandpass filter leaving only one sideband. The filter center frequency and bandwidth are usually fixed and although this is quite adequate for communications it would be a severe limitation in an imaging system since a range of frequencies above and below ω_0 should be accessable.

The alternative technique is rather more complicated in that it requires two double balanced modulators. The required excitation spectrum is first Fourier transformed. The real and imaginary time domain signals are then applied to 2 DBM (see figure 8.11) which are driven by carrier signals with quadrature phase. The resultant signals are then added leaving only one sideband.

One disadvantage of this technique is that it requires 2 eight bit registers and 2 DACs to supply the real and imaginary signals. In addition there is an inherent delay of 2µs between any two DAC level changes which could give rise to imperfect sideband suppression. At present only a single DBM is used and different slices are obtained by physically moving the sample along the y axis.

8.5 RF Transmitter Response

Ideally the rf modulation at the nucleus should be the same as that generated by the modulator. However the rf power amplifier response was found to be very non-linear and it was necessary to determine its transfer function before accurate selective pulses could be generated.

The system was calibrated by observing the nuclear tip angle as a function of the modulation amplitude for a fixed pulse width. This is chosen to be around 1ms corresponding to a bandwidth of about 1kHz. This time interval is considered a minimum appropriate to narrow excitation but without significant T_2 relaxation. Because the selective excitation pulse sequence includes a 180° pulse it was necessary to calibrate the system for tip angles ranging from 0° to 180°.

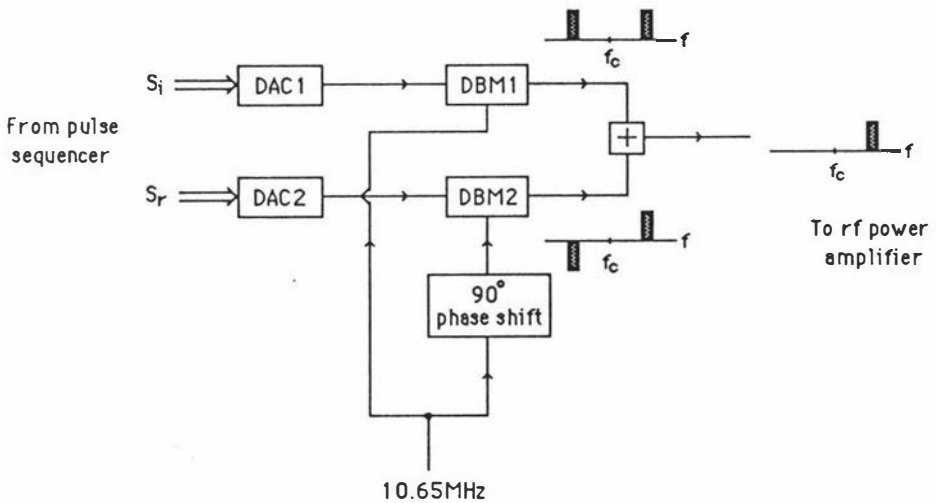

Figure 8.11 Block diagram of a single sideband rf modulator.

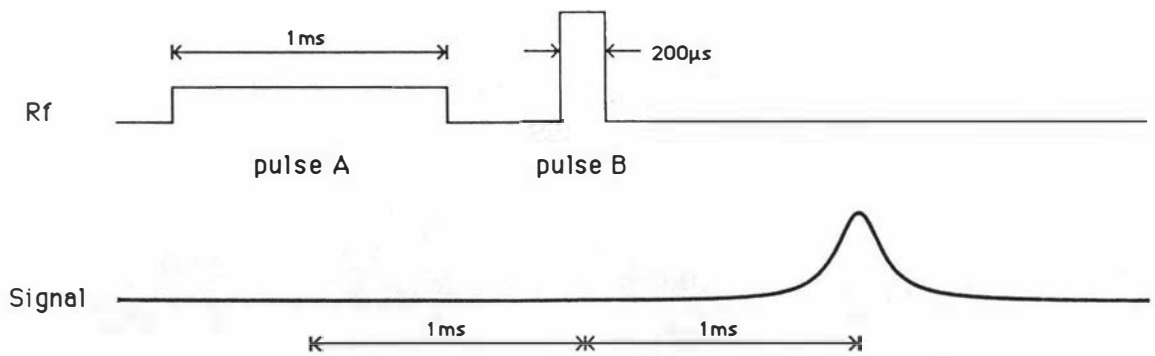

Figure 8.12 Pulse sequence used to calibrate the modulator.

The calibration procedure (see figure 8.12) starts by setting the DAC level for pulse B to the maximum value of 127 and then manually adjusting the gain of the modulator (VR1 in figure 8.10) until a null is obtained directly following pulse B (pulse A having been set to zero amplitude). Pulse B is then a 180° pulse (it is important that this adjustment be made from minimum gain and that the first null be selected - otherwise we might be seeing a 360° pulse). The width of the 180° pulse is chosen so that the 90° pulse uses digital values in the mid to upper range. Once the rf level for the 180° pulse has been determined the amplitude of pulse A is increased until a maximum echo amplitude is obtained - this corresponds to a 90° pulse. By recording intermediate values of echo amplitude it is then possible to determine tip angle as a function of DAC input for that particular setting of VR1, since

$$\theta = \arcsin(A_e/A_{90}). \qquad (8.17)$$

Typical results for values of θ from 0° to 90° are listed in table 8.5 and plotted in figure 8.13.

Table 8.5 Tip angles as a function of modulator input

A_{DAC}	A_e	θ	A_{DAC}	A_e	θ
110	2297	90.0	86	652	16.5
108	2288	84.9	84	540	13.6
106	2206	73.8	82	433	10.9
104	2098	66.0	80	358	9.0
102	1923	56.8	78	266	6.6
100	1739	49.2	76	209	5.2
98	1578	43.4	74	131	3.3
96	1439	38.8	72	109	2.7
94	1302	34.5	70	70	1.7
92	1046	27.1	68	3.2	0.8
90	915	23.5	66	23	0.6
88	755	19.2	64	0	0

Nb.

1) Rf DAC levels range from -128 to 127

2) Results are symmetrical i.e. $\theta(A_{DAC}) = \theta(-A_{DAC})$

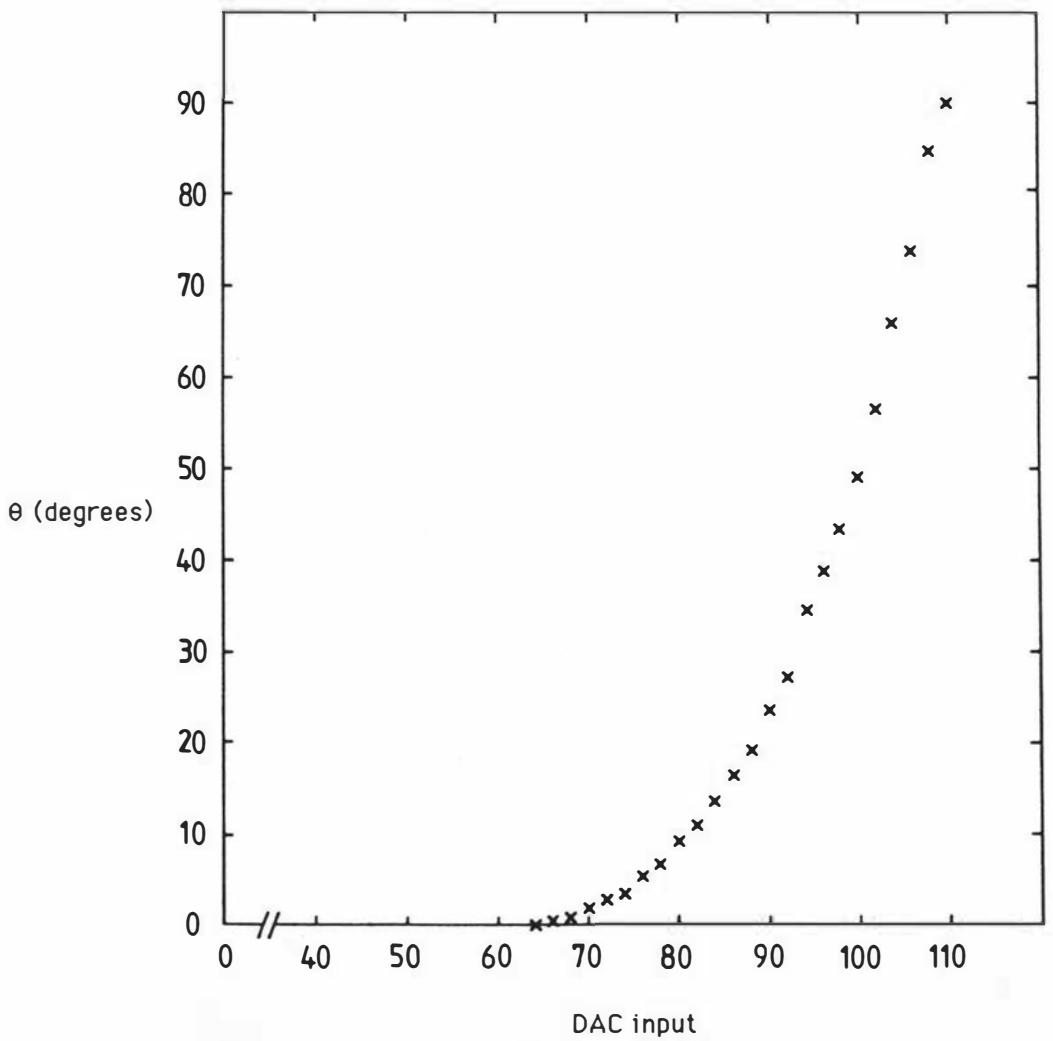

Figure 8.13 Tip angle θ as a function of applied DAC input.

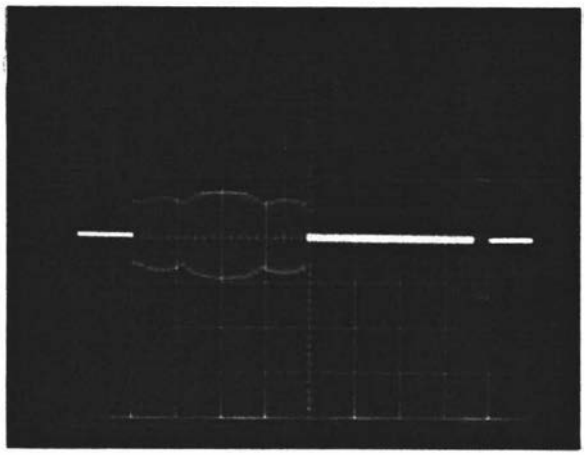

Figure 8.14 Output waveform from the rf modulator required for selective excitation [timebase, 500μs/div; vertical scale, 0.5V/div].

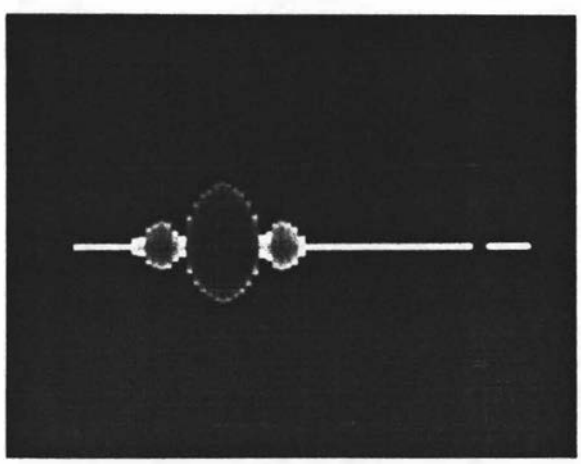

Figure 8.15 Output waveform from the rf transmitter due to the application of the waveform in Fig. 8.14 [timebase, 500μs/div; vertical scale, 0.5V/div].

Once these results are obtained it is a simple matter to determine the required modulation levels for any selective excitation function. The effectiveness of this procedure may be seen in figures 8.14 and 8.15 which show the modulator and transmitter waveforms for a sinc modulated rf pulse.

8.6 The imaging gradients ; an introduction

To perform NMR imaging it is necessary to have three orthogonal linear magnetic field gradients at ones disposal. The gradients are perhaps the most important part of an imaging system as their characteristics determine the quality of the images produced. A set of fairly stringent conditions must be met if image distortion is to be kept to a minimum.

1) The 3 gradients must be highly orthogonal. Non-orthogonalites lead to a range of distortions - the particular type depending on the imaging technique being used.

2) The gradients must be highly linear. Linearity requirements depend on the number of resolvable pixels to be displayed in the final image - a 256×256 image would require a linearity of better than 1 part in 256 if distortions due to non-linearities are to be negligible.

3) Gradient switching must be fast - ideally one should be able to switch a gradient on or off in less than one sampling interval (20μs for 50kHz BW).

4) The spatial resolution in the final image depends on the applied gradient magnitude. To perform imaging in the microscopic regime requires gradient strengths greater than $10Gcm^{-1}$. An additional requirement in our system was the ability to perform diffusion measurments using pulsed field gradient NMR. This technique requires gradients of a least $100Gcm^{-1}$. By contrast, typical medical imaging systems use field gradients of less than $1Gcm^{-1}$.

If the main field B_0 is directed along the z axis then the gradients required are $\partial B_z/\partial x$, $\partial B_z/\partial y$, and $\partial B_z/\partial z$. Gradients with respect to any other field component would have negligible effect due to the magnitude of B_0. For example a 100G field directed along the x axis would result in a frequency shift of $\sim 3\times10^{-5}\omega_0$ while if directed along the z axis the frequency shift would be $\sim 7\times10^{-3}\omega_0$.

A variety of coil configurations have been developed to generate linear field gradients including the Maxwell pair, the planar shim coil due to Anderson[30] and the quadrupolar coil developed by Webster and Marsden[31].

Of these the Maxwell pair is perhaps the simplest to construct giving highly linear gradients of large magnitude (see Callaghan et al.[32]). Unfortunately it has a fairly high inductance for a given gradient and tends to be rather bulky, not lending itself to the generation of orthogonal gradients.

The planar shim coil design is compact (at least in one dimension) but large inductances are required to provide gradients of reasonable magnitude leading to long rise times (t_r >100μs). Deviations from linearity are also significant, 1 to 5% being typical.

The quadrupolar coil was determined to be the most suitable since it is compact and is capable of producing highly linear field gradients of large magnitude with low inductance coils. Unfortunately the design is only capable of producing gradients in the x and z directions and so the third gradient - directed along the y axis, is generated by a set of planar shim coils mounted on the outside of the probe. The poorer linearity is not a problem as this gradient is usually only required for slice selection.

8.7 X and Z gradient coil design

Webster[31] indicates that the optimum design for a gradient coil is produced by distributing the current, I, on the surface of a cylinder such that

$$I = I_0 \cos 2\theta \qquad (8.18)$$

A continuous current distribution of this nature would be difficult to produce and so Webster suggests that bundles of wires be placed around the circumference such that the above condition is approximated.

The design used in this work consisted of 3 groups of windings per quadrant (see figures 8.16 and 8.17) with turns ratio N_1/N_0 = 7/10 (G_z coil) and N_1/N_0 = 14/10 (G_x coil). Each group of windings is separated by an angle of 22.5° thereby closely approximating the required cos(2θ) relationship. The two gradient coils are wound on a common former (they are shown separated in figure 8.16 for clarity) with a 45° rotation between the two sets of turns. The G_x and G_z designations are presently tentative, being based on simple hand drawn field distributions. Justification will be found in the evaluation of the orthogonal gradients which are negligible by comparison.

To determine the gradient field strengths and uniformity the magnetic field due to each wire element is considered. From figure 8.18 the field at point (x_1,y_1,z_1) due to current I flowing in the vertical wires is given by the Biot-Savart law[17] as

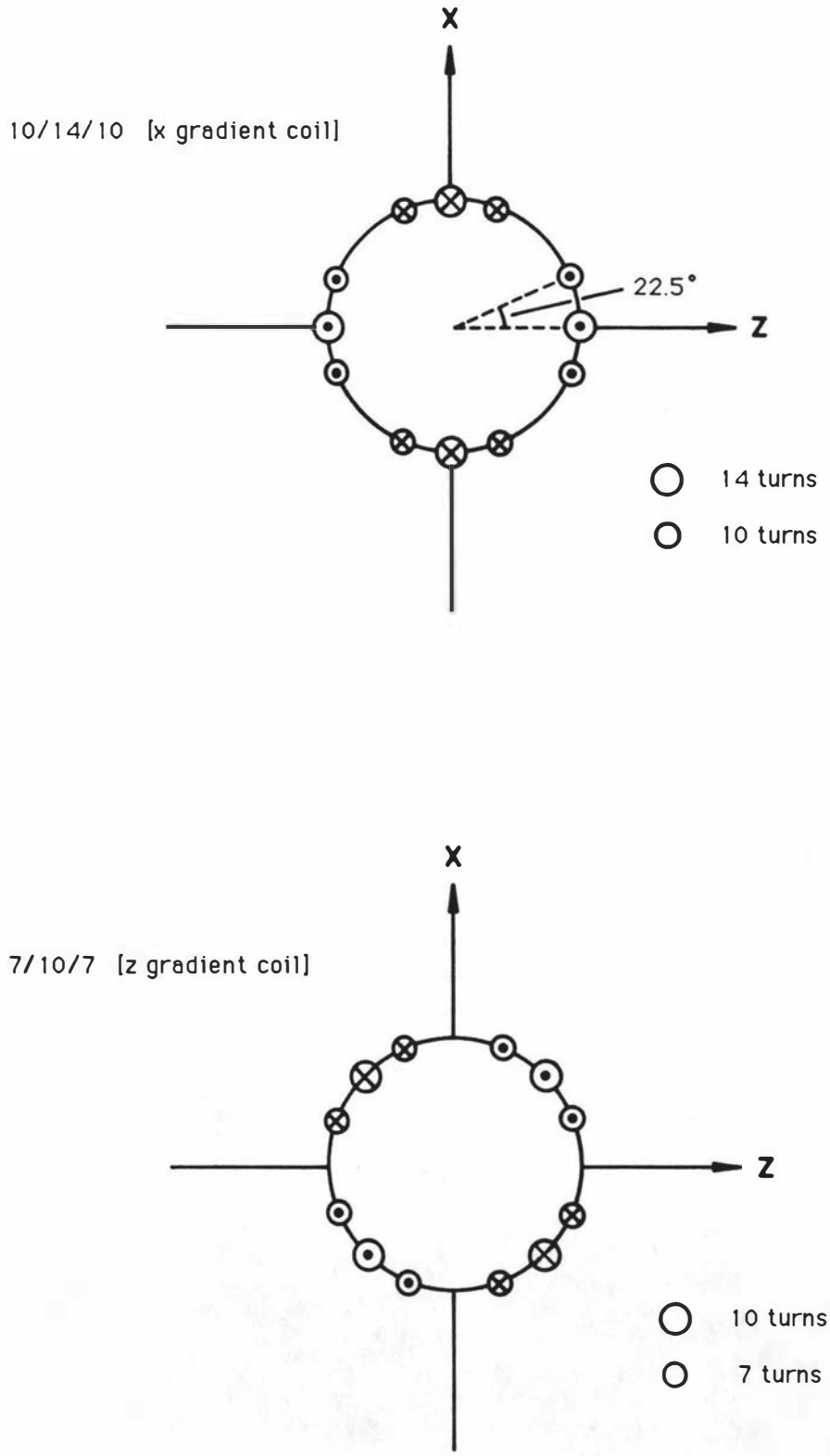

Figure 8.16 A plan view of the G_x and G_z quadrupolar coils showing the distribution of turns and current direction.

Figure 8.17 Photograph of the quadrupolar coil used to generate the G_x and G_z gradients. The coils are wound on a slotted teflon former of diameter 20mm and length 50mm and are held in place with epoxy resin.

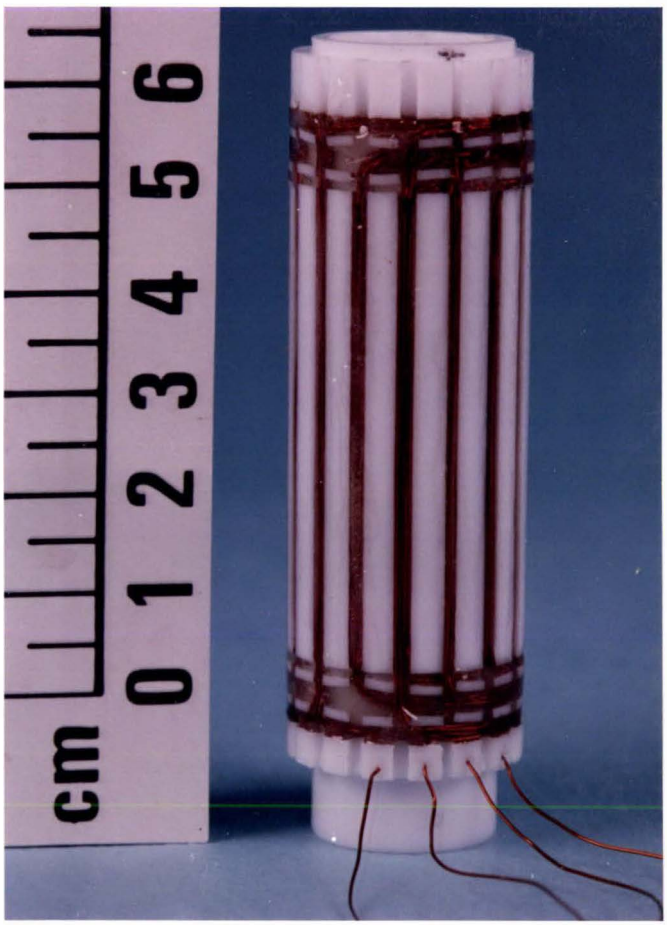
cm
0 1 2 3 4 5 6

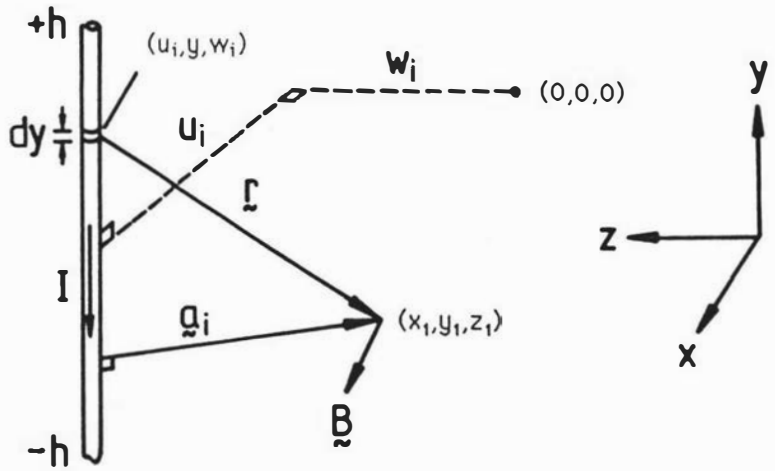

Figure 8.18 Geometry for finding the field at point (x_1, y_1, z_1) due to current I flowing parallel to the y axis in wire i.

$$\mathbf{B} = \frac{\mu_0 I}{4\pi} \int \frac{d\mathbf{l} \times \mathbf{r}}{r^3}. \tag{8.19}$$

The z component of this field (which is of interest) may be obtained by expanding the cross-product

$$B_z = \frac{\mu_0 I}{4\pi} \int \frac{dx\, r_y - dy\, r_x}{r^3}. \tag{8.20}$$

For the case where the wires are parallel to the y axis, dx=0 and so we have

$$B_z = -\frac{\mu_0 I}{4\pi} \int_{-h}^{h} \frac{dy\, r_x}{r^3}. \tag{8.21}$$

From figure 8.18 we have that

$$r_x = x_1 - u_i \tag{8.22}$$

and

$$r = \{ (u_i - x_1)^2 + (y-y_1)^2 + (w_i - z_1)^2 \}^{1/2} \tag{8.23}$$

where u_i and w_i are the x and z coordinates of the ith wire.

Substituting equations 8.22 and 8.23 into 8.21 we obtain

$$B_z = \frac{\mu_0 I}{4\pi} \int_{-h}^{h} \frac{(u_i - x_1)\, dy}{\{ a_i^2 + (y-y_1)^2 \}^{3/2}}. \tag{8.24}$$

where

$$a_i^2 = (u_i - x_1)^2 + (w_i - z_1)^2.$$

On evaluating this integral we obtain

$$B_z = \frac{\mu_0 I}{4\pi}\left[\frac{(y-y_1)(u_i-x_1)}{a_i^2\{(y-y_1)^2 + a_i^2\}^{1/2}}\right]_{-h}^{+h}$$

$$= \frac{\mu_0 I}{4\pi}\left[\frac{h-y_1}{\{(h-y_1)^2 + a_i^2\}^{1/2}} + \frac{h+y_1}{\{(h+y_1)^2 + a_i^2\}^{1/2}}\right]\frac{(u_i-x_1)}{a_i^2}. \qquad (8.25)$$

The return paths for the vertical wires are unfortunately curved, and so evaluation of their contribution to the net field is difficult. However the analysis is simplified if the return paths are approximated by straight wires (see figure 8.19a). In that case we have for the z gradient coil

$$B_z = \frac{\mu_0 I}{4\pi}\int_{-d_j}^{d_j}\frac{r_y\,dx}{r^3} \qquad (8.26)$$

but

$$r_y = (y_1 - v_j) \qquad (8.27)$$

and

$$r = [(x-x_1)^2 + (v_j - y_1)^2 + (w_j - z_1)^2]^{1/2} \qquad (8.28)$$

and so

$$B_z = \frac{\mu_0 I}{4\pi}\int_{-d_j}^{d_j}\frac{(y_1 - v_j)dx}{[a_j^2 + (x-x_1)^2]^{3/2}} \qquad (8.29)$$

where

$$a_j^2 = (v_j - y_1)^2 + (w_j - z_1)^2. \qquad (8.30)$$

Evaluating equation 8.30 gives

$$B_z = \frac{\mu_0 I_j}{4\pi}\left[\frac{d_j-x_1}{\{(d_j-x_1)^2 + a_j^2\}^{1/2}} + \frac{d_j+x_1}{\{(d_j-x_1)^2 + a_j^2\}^{1/2}}\right]\cdot\frac{(y_1 - v_j)}{a_j^2} \qquad (8.31)$$

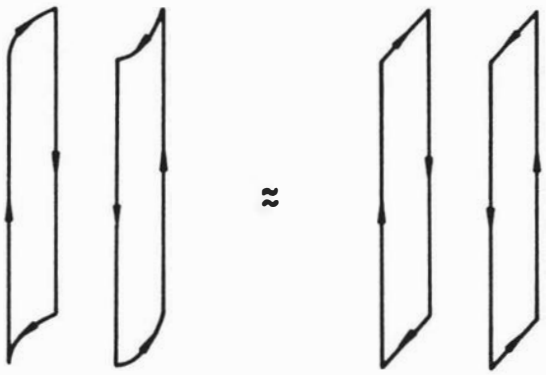

Figure 8.19a Return path approximation used in this analysis.

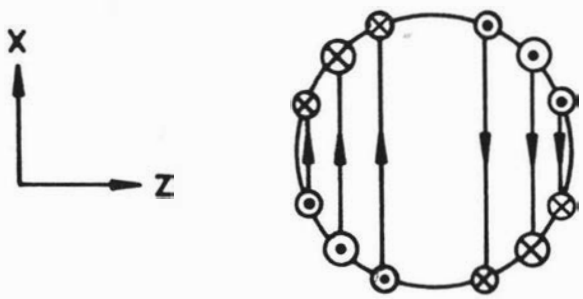

Figure 8.19b Plan view of the z gradient coil return paths.

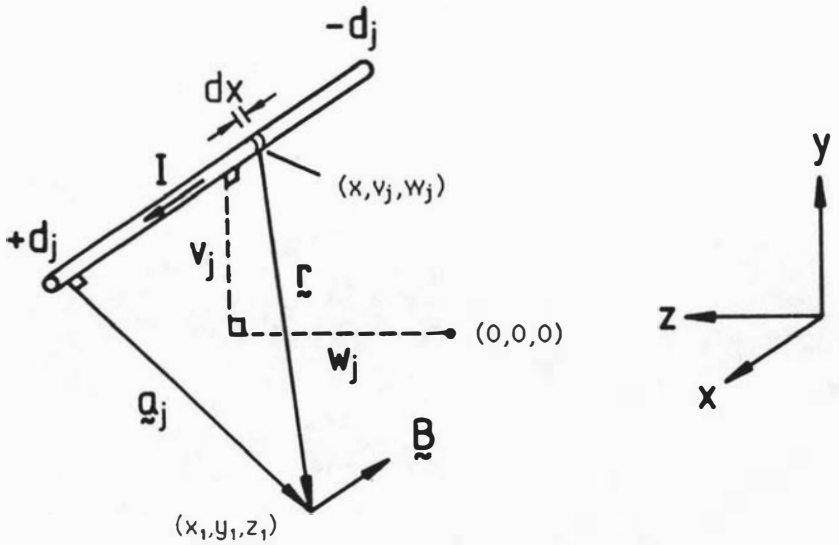

Figure 8.19c Geometry for finding the field at point (x_1, y_1, z_1) due to current I flowing parallel to the x axis in wire j.

The return paths for the x gradient coil are inclined at 45° to the z axis (see fig. 8.20a). The analysis for the wires is simplified by rotating the coil through 45° and evaluating B_z in this rotated frame (see fig. 8.20b).

In this case

$$B_z = \mathbf{B} \cdot \mathbf{k} = (B_{x'}\,\mathbf{i}' + B_{y'}\,\mathbf{j}' + B_{z'}\,\mathbf{k}') \cdot \mathbf{k}$$

$$= (B_{x'} + B_{z'})/\sqrt{2} \tag{8.32}$$

We already have an expression for $B_{z'}$ (equation 8.31). In a like manner we can derive an expression for $B_{x'}$ as

$$B_{x'} = \frac{\mu_0 I}{4\pi} \int_{-d_j}^{d_j} \frac{r_z\,dy' - r_y\,dz'}{r^3} = 0 \tag{8.33}$$

and so

$$B_z = B_{z'}/\sqrt{2}. \tag{8.34}$$

By differentiating the results in equations 8.25, 8.31 and 8.34 with respect to the appropriate variable and summing the contributions for each wire, we obtain expressions for the field gradient as a function of position. Starting with the z gradient we have that

$$G_z(x_1,y_1,z_1) = \frac{\partial B_z(x_1,y_1,z_1)}{\partial z_1}$$

$$= \frac{\partial}{\partial z_1} \sum_I \frac{\mu_0 I_i}{4\pi} \left[\frac{(h-y_1)}{\{(h-y_1)^2 + a_i^2\}^{1/2}} + \frac{(h+y_1)}{\{(h+y_1)^2 + a_i^2\}^{1/2}} \right] \frac{(u_i - x_1)}{a_i^2}$$

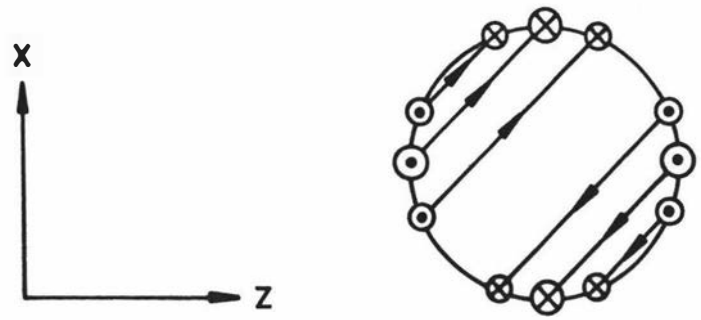

Top view of x gradient coil.

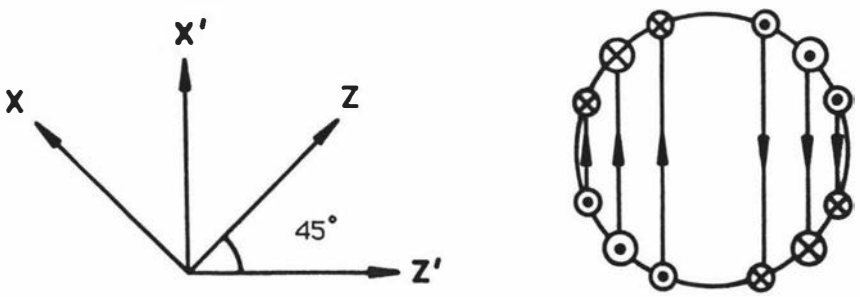

Figure 8.20 Rotation of the x gradient coil required to simplify the calculation of B_z.

$$+ \frac{\partial}{\partial z_1} \sum_j \frac{\mu_0 I}{4\pi} \left[\frac{(d_j - x_1)}{\{(d_j - x_1)^2 + a_j^2\}^{1/2}} + \frac{(d_j + x_1)}{\{(d_j + x_1)^2 + a_j^2\}^{1/2}} \right] \frac{(y_1 - v_j)}{a_j^2} \qquad (8.35)$$

where

$$a_i^2 = (u_i - x_1)^2 + (w_i - z_1)^2$$

and

$$a_j^2 = (v_j - y_1)^2 + (w_j - z_1)^2.$$

Evaluation of this derivative gives

$$\begin{aligned} G_Z(x_1,y_1,z_1) = & \sum_i \frac{\mu_0 I_i}{2\pi} \left[\frac{(h - y_1)}{\{(h - y_1)^2 + a_i^2\}^{1/2}} + \frac{(h + y_1)}{\{(h + y_1)^2 + a_i^2\}^{1/2}} \right] \frac{(u_i - x_1)(w_i - z_1)}{a_i^4} \\ & + \sum_i \frac{\mu_0 I_i}{4\pi} \left[\frac{(h - y_1)}{\{(h - y_1)^2 + a_i^2\}^{3/2}} + \frac{(h + y_1)}{\{(h + y_1)^2 + a_i^2\}^{3/2}} \right] \frac{(u_i - x_1)(w_i - z_1)}{a_i^2} \\ & + \sum_j \frac{\mu_0 I_j}{2\pi} \left[\frac{(d_j - x_1)}{\{(d_j - x_1)^2 + a_j^2\}^{1/2}} + \frac{(d_j + x_1)}{\{(d_j + x_1)^2 + a_j^2\}^{1/2}} \right] \frac{(y_1 - v_j)(w_j - z_1)}{a_j^4} \\ & + \sum_j \frac{\mu_0 I_j}{4\pi} \left[\frac{(d_j - x_1)}{\{(d_j - x_1)^2 + a_j^2\}^{3/2}} + \frac{(d_j + x_1)}{\{(d_j + x_1)^2 + a_j^2\}^{3/2}} \right] \frac{(y_1 - v_j)(w_j - z_1)}{a_j^2}. \end{aligned} \qquad (8.36)$$

The x gradient, for the x gradient coil, may be found in a similar manner since

$$\begin{aligned} G_X(x_1,y_1,z_1) &= \{G_X(x_1,y_1,z_1)\}_m + \{G_{X'}(x_1',y_1',z_1')\ \mathbf{i}'.\mathbf{i} + G_{Z'}(x_1',y_1',z_1')\ \mathbf{k}'.\mathbf{i}\}_r \\ &= \{G_X(x_1,y_1,z_1)\}_m \\ &\quad + \partial/\partial x' \{B_{Z'}(x_1',y_1',z_1')/\sqrt{2}\} - \partial/\partial z' \{B_{Z'}(x_1',y_1',z_1')/\sqrt{2}\} \end{aligned} \qquad (8.37)$$

where the term subscripted m is due to the main coil (wire parallel with the y axis), while the remaining terms, labelled r are due to the return paths. Using the results in equations 8.25 and 8.31 we obtain

$$
\begin{aligned}
G_x(x_1,y_1,z_1) = & \frac{\partial}{\partial x}\sum_i \frac{\mu_0 I_i}{4\pi}\left[\frac{(h-y_1)}{\{(h-y_1)^2+a_i^2\}^{1/2}} + \frac{(h+y_1)}{\{(h-y_1)^2+a_j'^2\}^{1/2}}\right]\frac{(u_i - x_1')}{a_j'^2} \\
& + \frac{\partial}{\partial x'}\sum_j \frac{\mu_0 I_j}{4\pi}\left[\frac{(d_j-x_1')}{\{(d_j-x_1')^2+a_j'^2\}^{1/2}} + \frac{(d_j+x_1')}{\{(d_j-x_1')^2+a_j'^2\}^{1/2}}\right]\frac{(y_1'- v_j)}{2\,a_j'^2} \\
& - \frac{\partial}{\partial z'}\sum_j \frac{\mu_0 I_j}{4\pi}\left[\frac{(d_j-x_1')}{\{(d_j-x_1')^2+a_j'^2\}^{1/2}} + \frac{(d_l+x_1')}{\{(d_j-x_1')^2+a_j'^2\}^{1/2}}\right]\frac{(y_1'- v_j)}{2\,a_j'^2}.
\end{aligned}
\tag{8.38}
$$

Evaluating equation 8.37 gives

$$
\begin{aligned}
G_x(x_1,y_1,z_1) = & \sum_i \frac{\mu_0 I_i}{2\pi}\left[\frac{(h-y_1)}{\{(h-y_1)^2+a_i^2\}^{1/2}} + \frac{(h+y_1)}{\{(h+y_1)^2+a_i^2\}^{1/2}}\right]\left[\frac{(u_i - x_1)^2}{a_i^4} - \frac{1}{2a_i^2}\right] \\
& + \sum_i \frac{\mu_0 I_i}{2\pi}\left[\frac{(h-y_1)}{\{(h-y_1)^2+a_i^2\}^{3/2}} + \frac{(h+y_1)}{\{(h+y_1)^2+a_i^2\}^{3/2}}\right]\frac{(u_i - x_1)}{a_i^2} \\
& + \sum_j \frac{\mu_0 I_j}{4\pi}\left[\frac{1}{\{(d_j+x_1')^2+a_j'^2\}^{1/2}} - \frac{1}{\{(d_j-x_1')^2+a_j'^2\}^{1/2}}\right]\frac{(y_1 - v_j)}{2a_j^2}
\end{aligned}
\tag{8.39}
$$

$$+ \sum_j \frac{\mu_0 I_j}{4\pi}\left[\frac{(d_j-x_1')^2}{\{(d_j-x_1')^2 + a_j'^2\}^{3/2}} - \frac{(d_j+x_1')^2}{\{(d_j+x_1')^2 + a_j'^2\}^{3/2}}\right]\frac{(y_1 - v_j)}{2a_j'}$$

$$- \sum_j \frac{\mu_0 I_j}{2\pi}\left[\frac{(d_j-x_1')}{\{(d_j-x_1')^2 + a_j'^2\}^{1/2}} + \frac{(d_j+x_1')}{\{(d_j+x_1')^2 + a_j'^2\}^{1/2}}\right]\frac{(y_1 - v_j)(w_j - z_1')}{2a_j^4}$$

$$- \sum_j \frac{\mu_0 I_j}{4\pi}\left[\frac{(d_j-x_1')}{\{(d_j-x_1')^2 + a_j'^2\}^{3/2}} + \frac{(d_j+x_1')}{\{(d_j+x_1')^2 + a_j'^2\}^{3/2}}\right]\frac{(y_1 - v_j)(w_j - z_1')}{2a_j^2}.$$

where

$$x_1' = z_1/\sqrt{2} + x_1/\sqrt{2}$$
$$z_1' = z_1/\sqrt{2} - x_1/\sqrt{2}. \qquad (8.40)$$

8.8 Y gradient coil design

The third and final gradient is directed along the y (i.e. the vertical) axis. Due to the limited clearance between the probe and magnet pole faces (~1mm either side) it was necessary to use the existing y gradient planar shim coil mounted on the outside of the probe. The dimensions and orientation of this coil are given in figure 8.21.

As in the case of the quadrupolar coil, we shall consider the field due to each wire separately. Using the results from the previous section we see that the net field at point (x_1,y_1,z_1) will be

$$B_z(x_1,y_1,z_1) = \sum_i \frac{\mu_0 I_i}{4\pi}\left[\frac{(c_i-y_1)}{\{(c_i-x_1)^2 + a_i^2\}^{1/2}} + \frac{(y_1-e_i)}{\{(y_1-e_i)^2 + a_i^2\}^{1/2}}\right]\frac{(u_i - x_1)}{a_i^2}$$

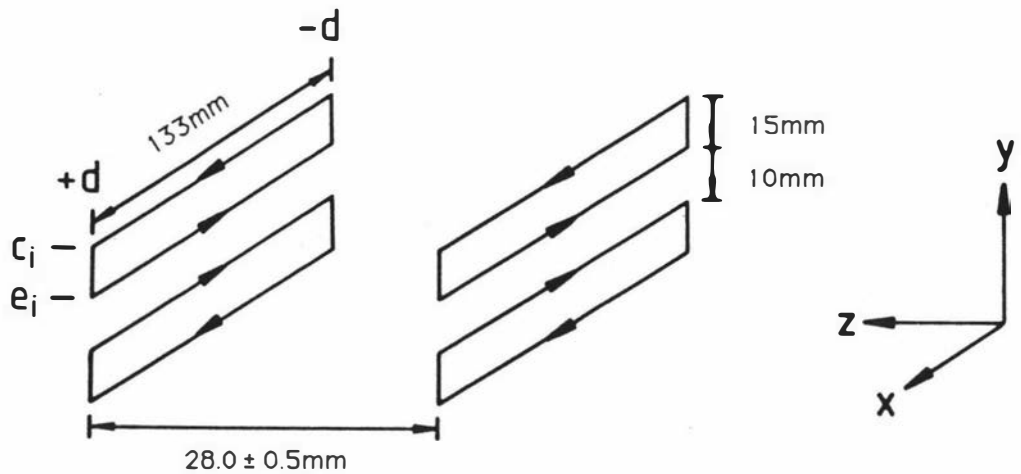

Figure 8.21 Y gradient shim coil, configuration and dimensions.

$$\sum_j \frac{\mu_0 I_j}{4\pi}\left[\frac{(d_j-x_1)}{\{(d_j-x_1)^2+a_j^2\}^{1/2}} + \frac{(d_j+x_1)}{\{(d_j-x_1)^2+a_j^2\}^{1/2}}\right]\frac{(y_1-v_j)}{a_j^2} \quad (8.41)$$

Differentiating with respect to y gives

$$\begin{aligned} G_y(x_1,y_1,z_1) = & \sum_i \frac{\mu_0 I_i}{4\pi}\left[\frac{1}{\{(y_1-e_i)^2+a_i^2\}^{1/2}} - \frac{1}{\{(c_i-y_1)^2+a_i^2\}^{1/2}}\right]\frac{(u_i-x_1)}{a_i^2} \\ & + \sum_i \frac{\mu_0 I_i}{4\pi}\left[\frac{(c_i-y_1)^2}{\{(y_1-e_i)^2+a_i^2\}^{3/2}} - \frac{(y_1-e_i)^2}{\{(c_i-y_1)^2+a_i^2\}^{3/2}}\right]\frac{(u_i-x_1)}{a_i^2} \\ & + \sum_j \frac{\mu_0 I_j}{4\pi}\left[\frac{(d_j-x_1)}{\{(d_j-x_1)^2+a_j^2\}^{1/2}} + \frac{(d_j+x_1)}{\{(d_j+x_1)^2+a_j^2\}^{1/2}}\right]\left[\frac{2(y_1-v_j)^2}{a_j^4} - \frac{1}{a_j^2}\right] \\ & + \sum_j \frac{\mu_0 I_j}{4\pi}\left[\frac{(d_j-x_1)}{\{(d_j-x_1)^2+a_j^2\}^{3/2}} + \frac{(d_j+x_1)}{\{(d_j+x_1)^2+a_j^2\}^{3/2}}\right]\frac{(y_1-v_j)^2}{a_j^2} \end{aligned} \quad (8.42)$$

where the summation over i corresponds to the return paths which are parallel to the y axis and those over j to the main elements parallel to the x axis.

Computer programs has been written which use equations 8.36, 8.39, 8.42 and the data in figures 8.17 and 8.21 to determine G_x, G_y and G_z as a function of position. The orthogonal gradients have also been calculated for each coil and have been determined at the origin and at x=y=z=6mm. These results may be used as an indicator of the size of the undesirable gradient components.

Table 8.6 Calculated gradients

coil	desired gradients	orthogonal gradients	
10/14/10	G_x = (21±4)	$G_y = 3\times10^{-7}$ [0.14]	G_z = 0.3 [0.4]
shim	G_y = (1.63±0.09)	$G_x = 5\times10^{-10}$ [2×10^{-9}]	$G_z = 6\times10^{-9}$ [0.9]
7/10/7	G_z = (15±3)	$G_x = 3\times10^{-6}$ [0.1]	G_y = 0 [0.07]

Notes

1) All gradients are in $Gcm^{-1}A^{-1}$.
2) The desired gradients are determined at x=y=z=0.
3) The orthogonal gradients are determined at the origin and at x=y=z=6mm (those terms in square brackets).
4) The errors in the desired gradients arise from the uncertainty in the coil dimensions.

As expected the orthogonal gradients are negligible, apart from the G_z gradient in the 10/14/10 coil which is due to the return wires.

Contour plots showing predicted percentage deviations of the desired gradients from the above values are given in figures 8.22 and 8.23. These results indicate that a 7mm diameter object could be accomodated within the 0.4% (1/256) contour, thereby satisfying condition 2. The poor linearity of the shim coil is apparent from the contour plot in figures 8.24a and b. If the coil had been wound using the optimum parameters[30] $w/z_0=1.55$ and $y_c=1.19z_0$ then the gradient linearity would have been much improved (see figure 8.24c). The non-linearity of the shim coil results in a non-uniform slice. This will produce an uncertainty in the proton density of ~±5% for a 7mm diameter object. However the information in figure 8.24a could be used to correct for this distortion.

The above simulations do not take into account the effect of image currents generated within the pole pieces of the main magnet. Calculations along these lines may be performed by considering the gradient due to the coil configuration depicted in figure 8.25. The calculations assume a medium with infinite permeability and so represent an extreme case. The predicted central gradient is $(16\pm3)Gcm^{-1}A^{-1}$, approximately 7% higher than that obtained when the image gradients are ignored. Because of the difficulty in accessing the actual magnitude of the image gradients the contour plot in figure 8.26 should not be taken as an accurate representation of the gradient uniformity but only as an illustration of the effect image gradients could have on the position of the contours. In this particular case the 0.4% contour is now positioned so that a 5mm object could be accomodated with negligible image distortion.

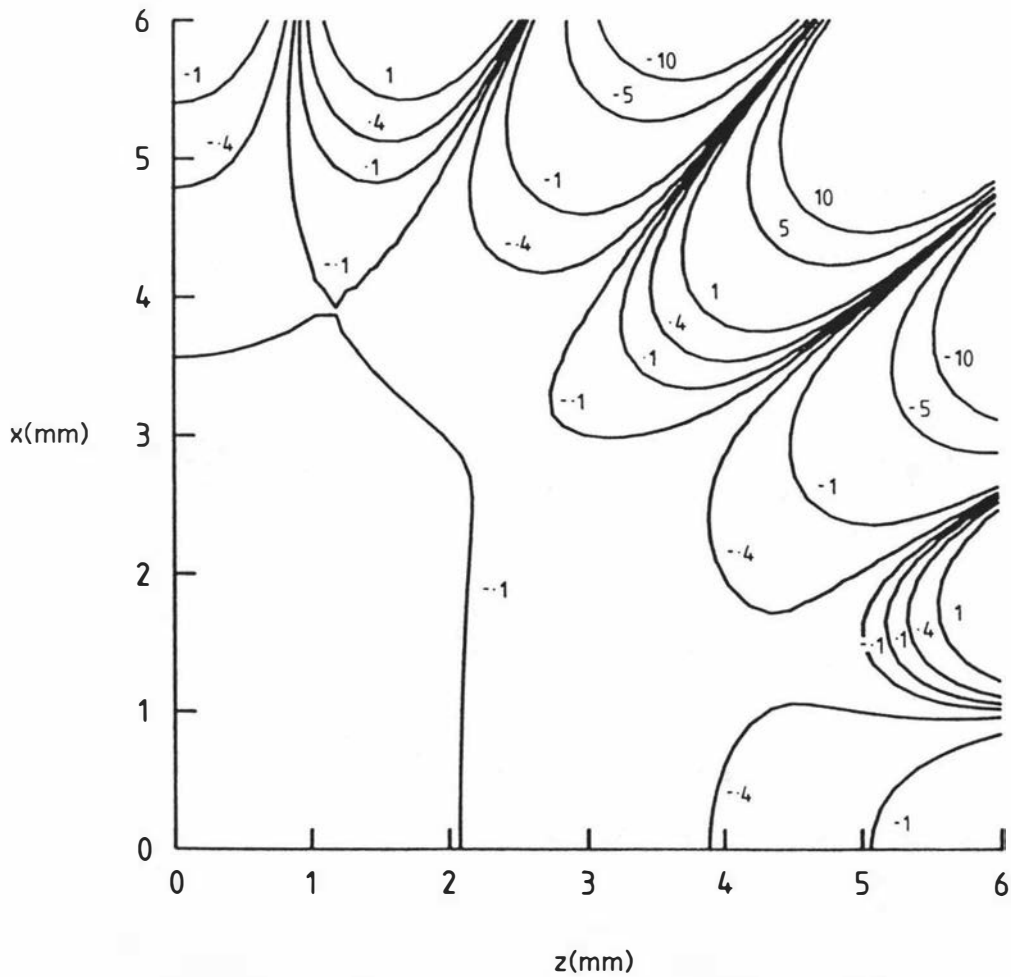

Figure 8.22a Percentage variation in the z gradient for the 7/10/7 coil at y=0mm.

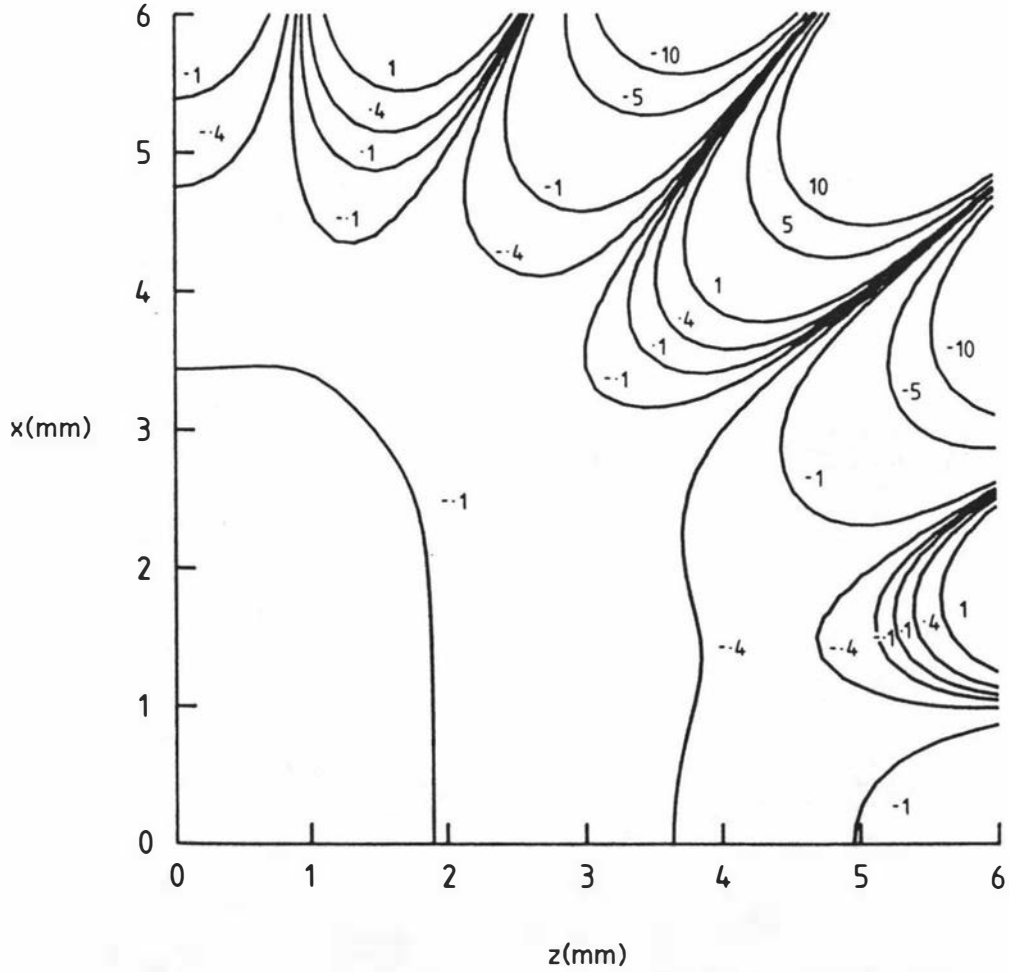

Figure 8.22b Percentage variation in the z gradient for the 7/10/7 coil at y=3mm.

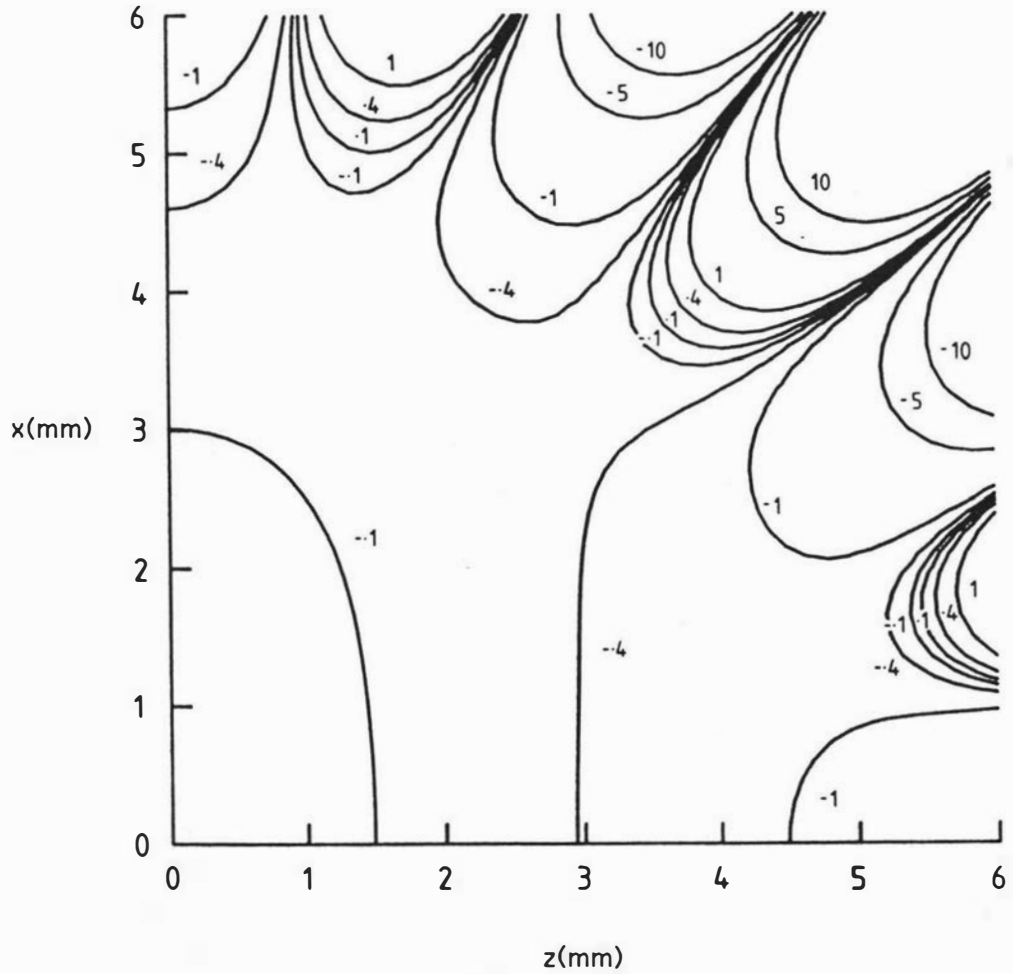

Figure 8.22c Percentage variation in the z gradient for the 7/10/7 coil at y=6mm.

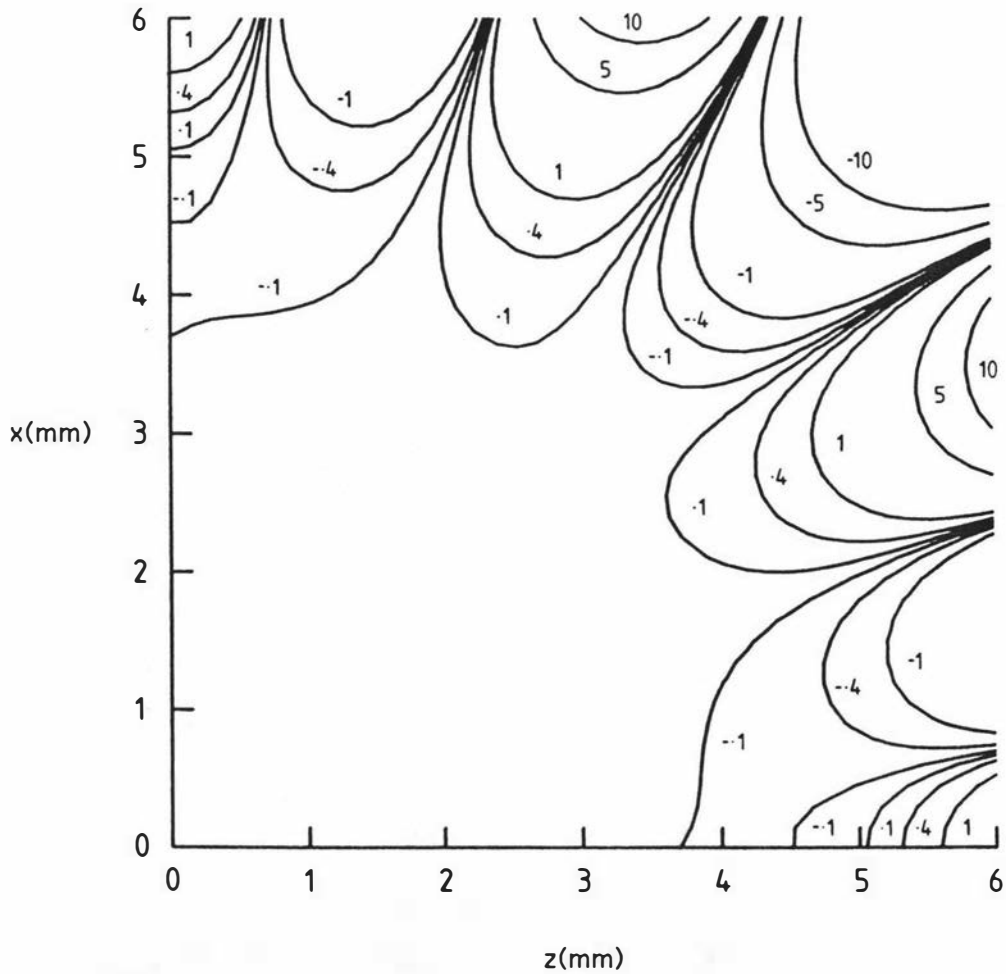

Figure 8.23a Percentage variation in the x gradient for the 10/14/10 coil at y=0mm.

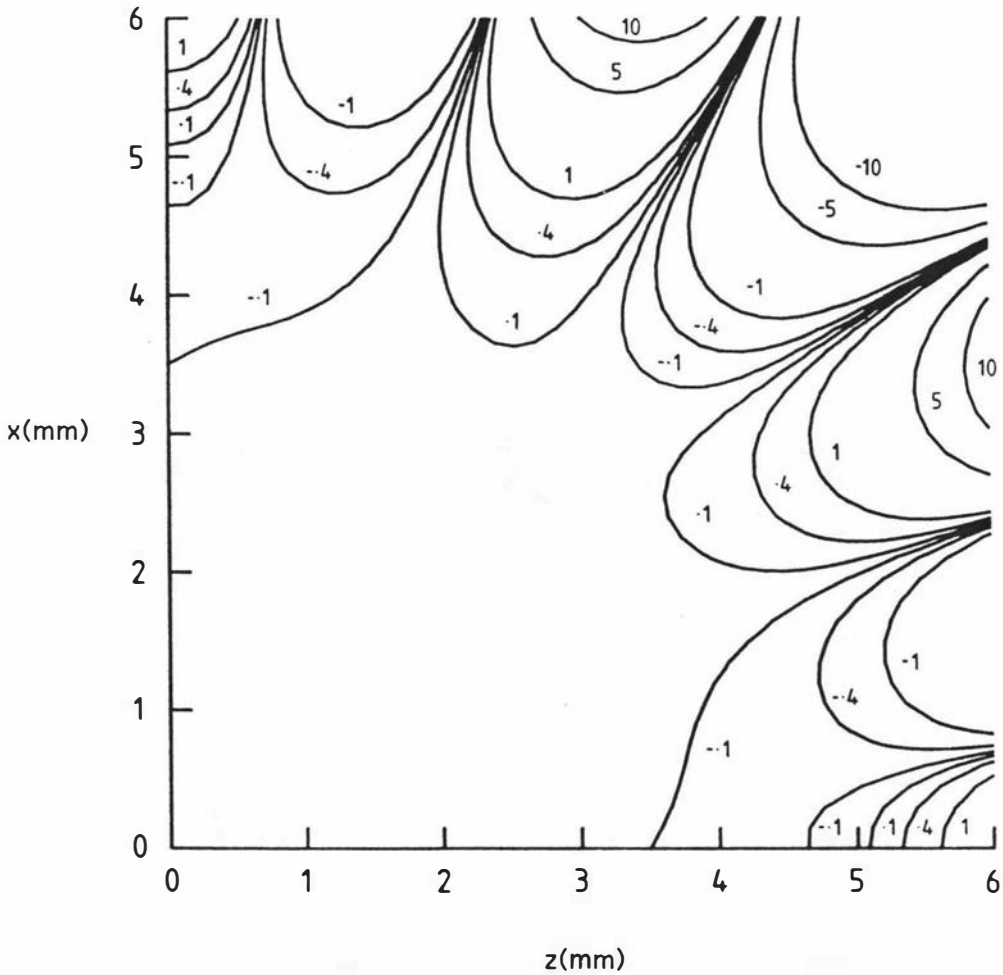

Figure 8.23b Percentage variation in the x gradient for the 10/14/10 coil at y=3mm.

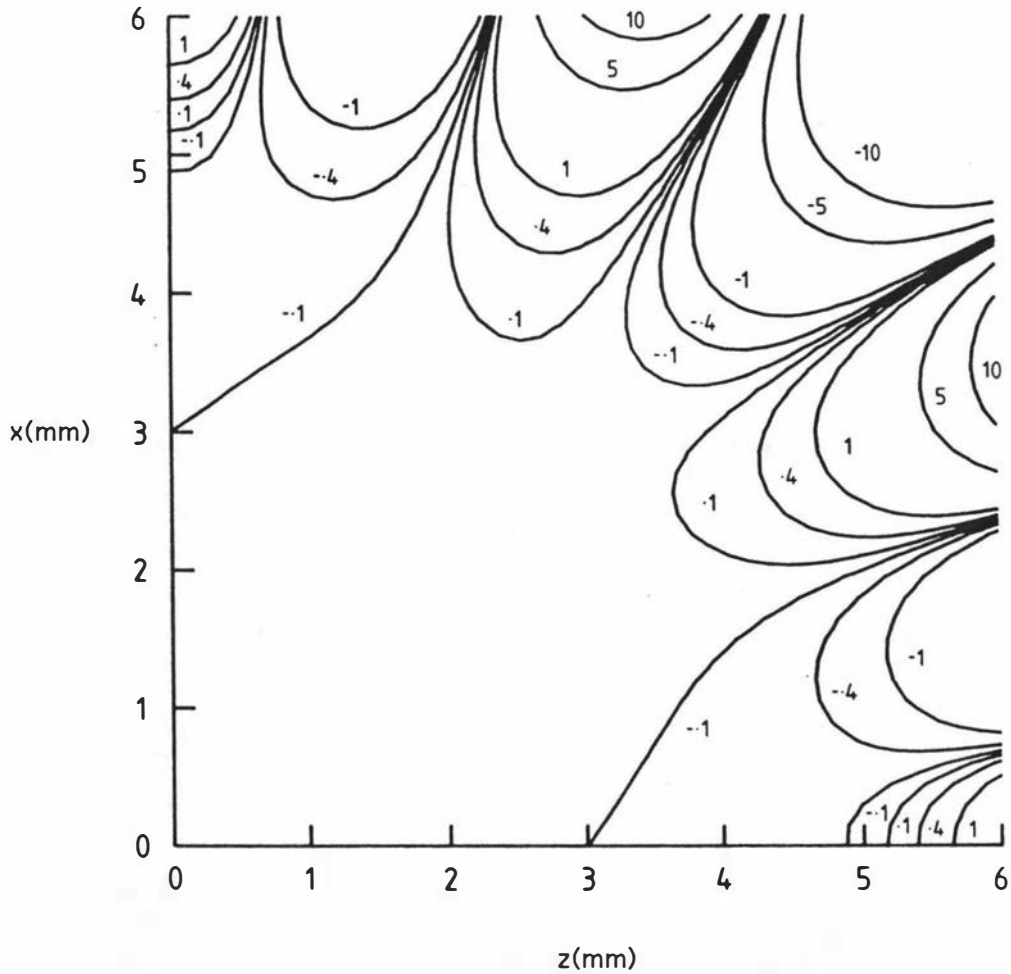

Figure 8.23c Percentage variation in the x gradient for the 10/14/10 coil at y=6mm.

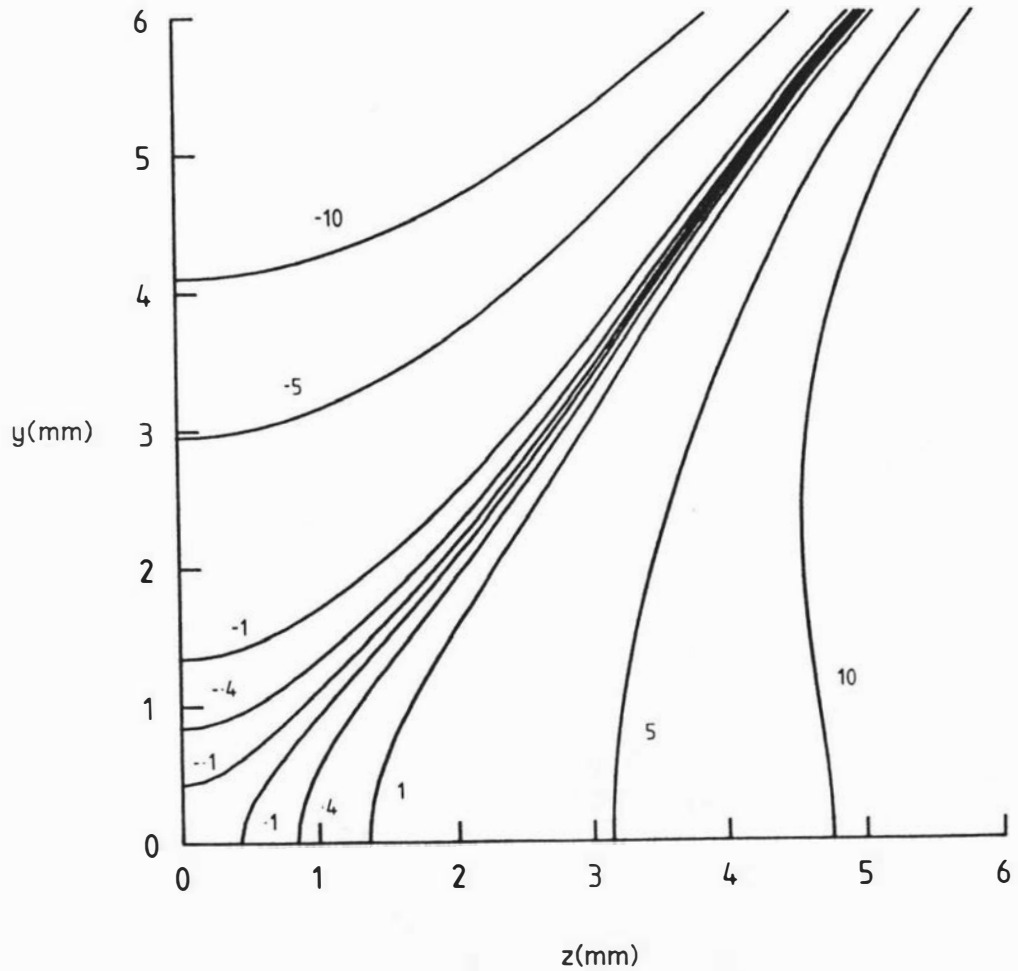

Figure 8.24a Percentage variation in the y gradient for the planar shim coil at x=0mm.

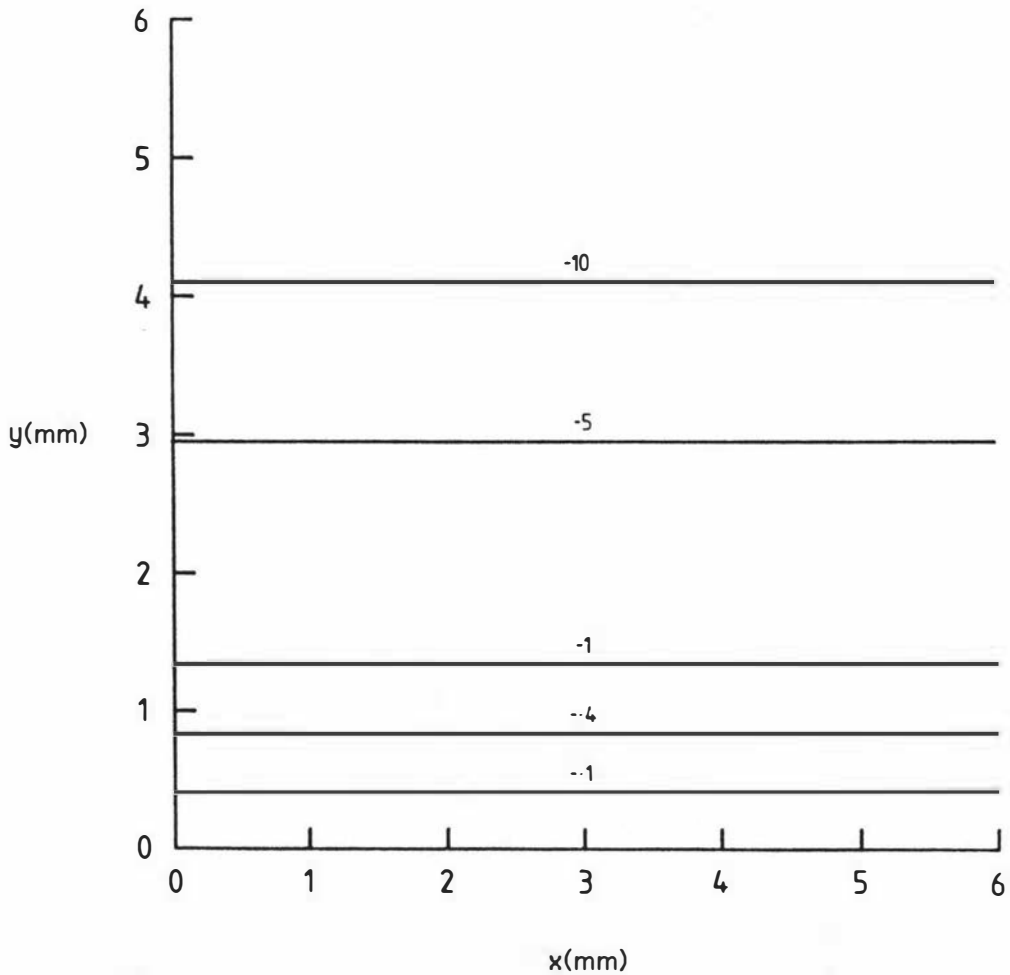

Figure 8.24b Percentage variation in the y gradient for the planar shim coil at z=0mm.

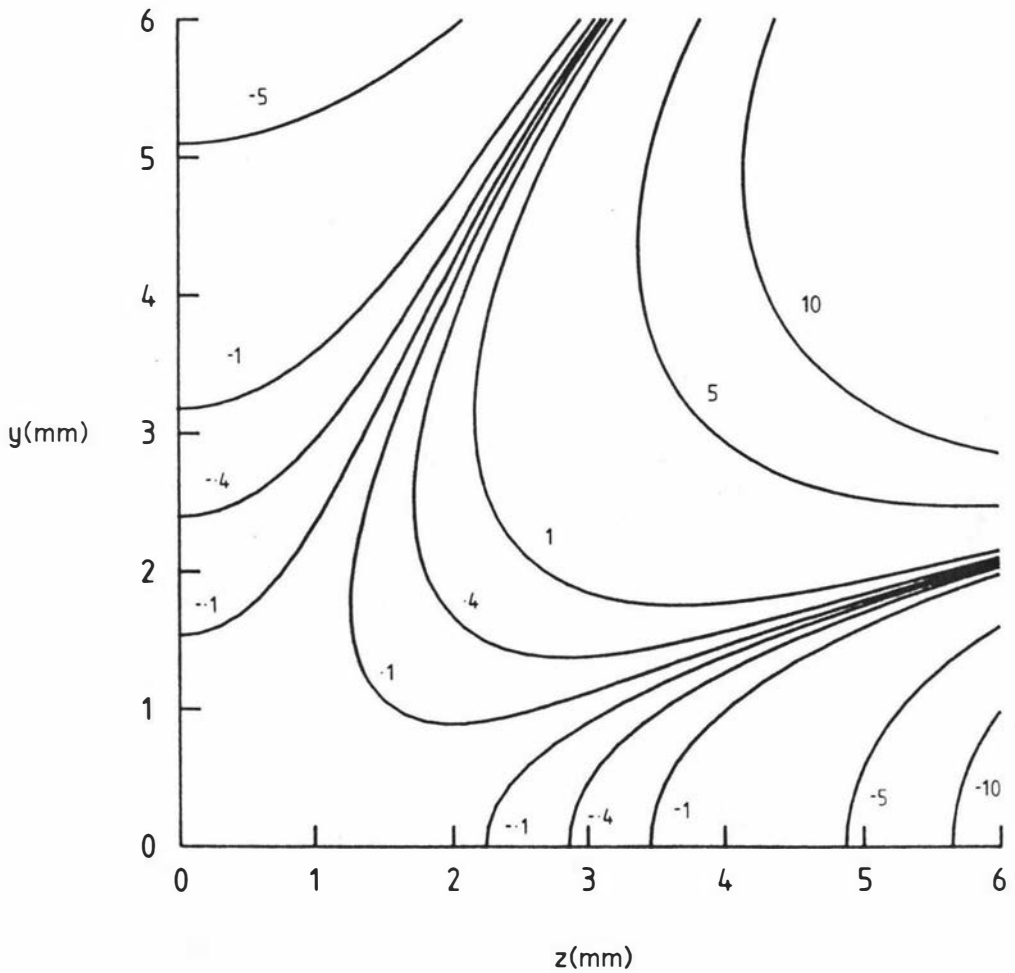

Figure 8.24c Percentage variation in the y gradient for the planar shim coil at x=0mm using optimized coil dimensions.

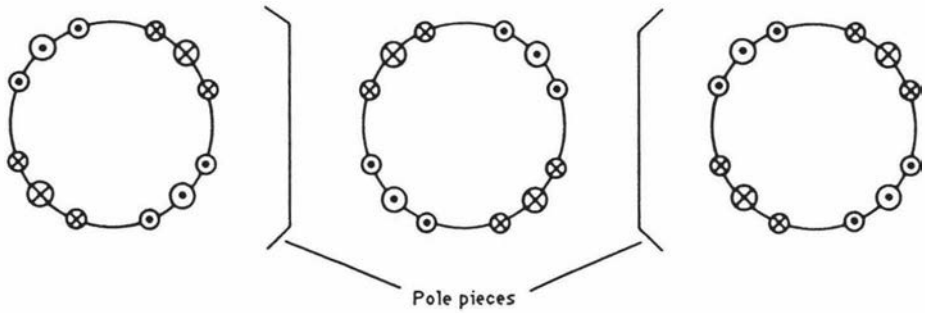

Figure 8.25 Effective image currents produced within the main magnet pole pieces by the z gradient coil.

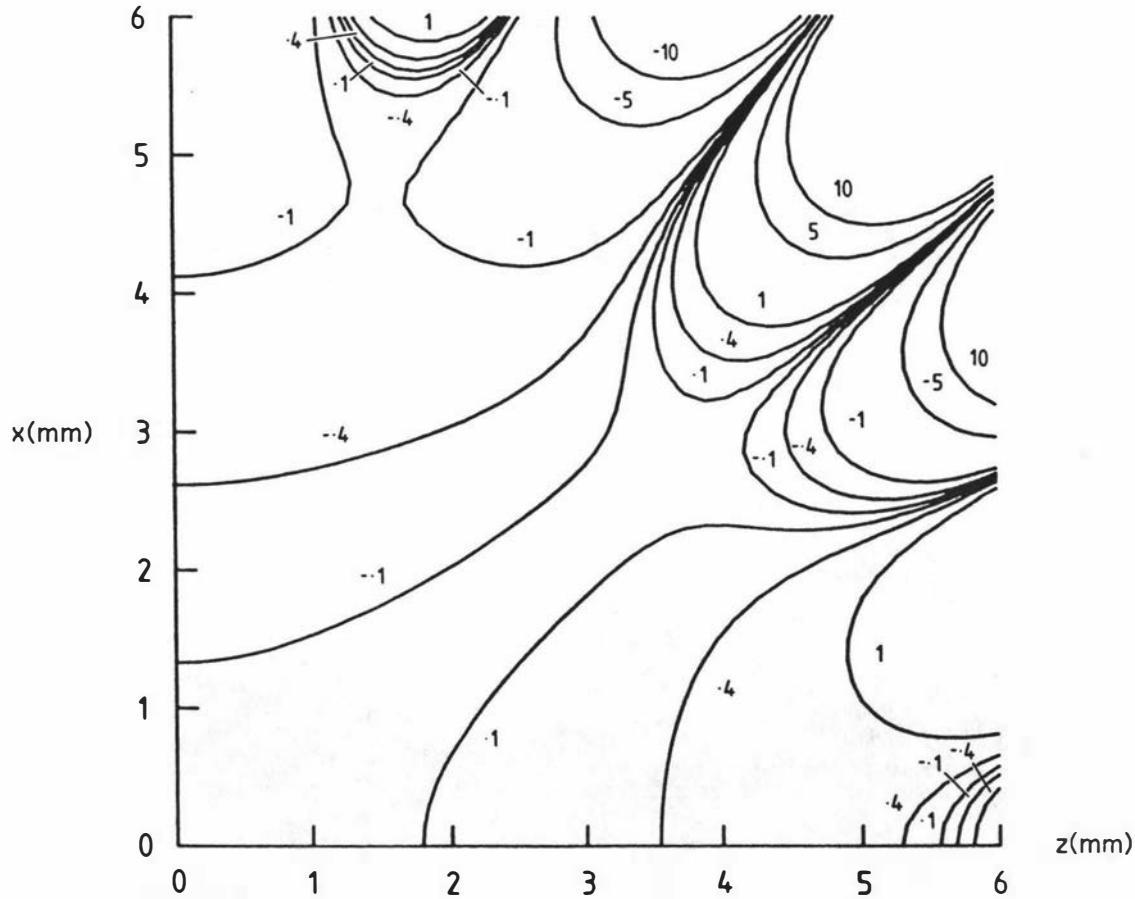

Figure 8.26 Percentage variation in the z field gradient for the 7/10/7 coil at y=0mm when image gradients are considered.

The gradients have been indirectly measured in two ways. Using standard pulsed field gradient spin echo techniques (see section 9.2) we obtain gradients (23.74 ± 0.06) $Gcm^{-1}A^{-1}$ and (14.89 ± 0.09) $Gcm^{-1}A^{-1}$ for G_x and G_z. By performing a 1-D imaging experiment with a cylindrical sample of water of known diameter we can infer the gradient magnitude from the frequency width of the profile. This experiment gave G_x = (22.8 ± 0.8)$Gcm^{-1}A^{-1}$, G_z = (14.6 ± 0.5)$Gcm^{-1}A^{-1}$ and G_y = (1.58±0.06) $Gcm^{-1}A^{-1}$.

8.9 Controller for the imaging gradients

The current supplies and controller required for each gradient are based on the design of Callaghan[32] et al. who used this system successfully in their work with pulsed field gradient NMR. The gradient coils are driven by 3 Kepco power supplies operating in a constant current mode. To improve gradient pulse rise times and completely isolate the coils when not required (found to be advantageous in PFG work) a series of high power switching transistors are connected between the Kepco psu and the gradient coils. Controlling logic routes the current to ground when not required.

A complete schematic of the gradient controller is given in figure 8.27. The switching transistors operate in a Darlington configuration providing very high current gains. Switching times for the TIP36C are ~1µs, more than adequate for this task.

In a typical pulse sequence the first instruction switches the gradient off by closing SW2 and opening SW1. The required current level is then applied to the Kepco power supply. A delay of several 100µs is then required to ensure the supply current has settled. When the gradient is required a TTL 'on' signal is applied via the optocoupler (providing a further stage of isolation) which switches SW2 off and SW1 on, allowing current to pass through the gradient coils. When the supply is subsequently switched off the back EMF generated in L_1 is shunted to ground via diodes D_1 to D_4, protecting the transistors and hastening the fall time of the pulse. Four diodes were found to be necessary to remove all traces of the ringing present in the coil circuit. This ringing appears to be of mechanical origin since it is not present when the main field is switched off. The extra diodes prevent current from flowing unless the voltage is greater than ~2.8V. Whether the inclusion of the extra diodes actually improves the fall time of the gradient field is debatable.

Because the gradient pulses are generally quite short (<40ms) with a duty cycle in an imaging experiment of at worst 1:5, average power dissipation in the gradient coils is generally low (several watts at the most). However in the event of a program error it is quite likely that a continuous 10A current might be passed throught the coil with a resultant power dissipation of

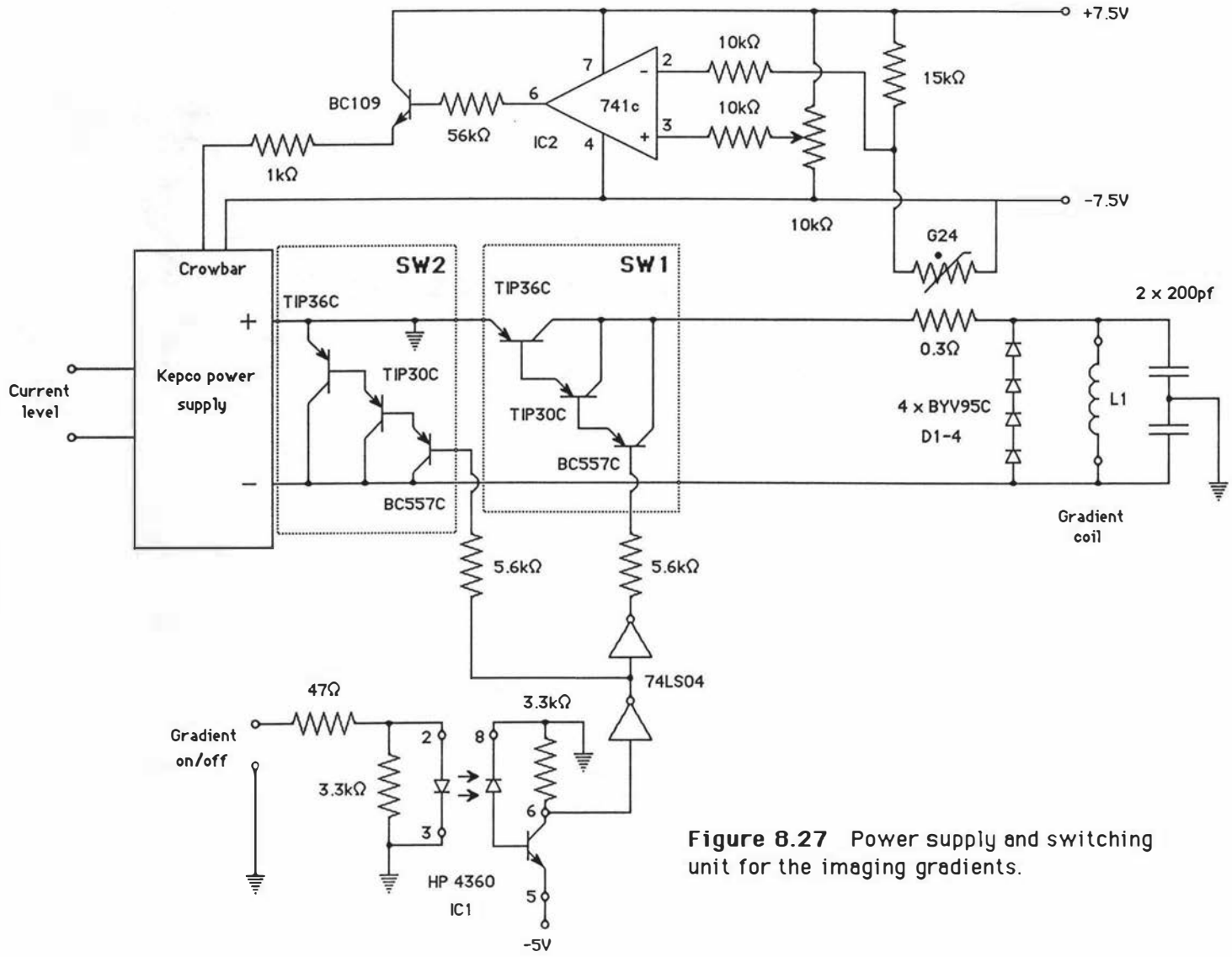

Figure 8.27 Power supply and switching unit for the imaging gradients.

several hundred watts. Such action would rapidly ruin the coils. To prevent such an event from occuring a small I^2R sensor is included in the current path. This consists of 3 turns of nichrome wire wound about a thermistor. Good thermal contact is maintained with silicon grease. If the power dissipated in the gradient coil becomes excessive the corresponding temperature rise in the nichrome coil will be such as to cause IC2 to change state, throwing the crowbar on the Kepco, thereby cutting power to the coil. This feature has proved to be very useful in the development of the system, providing a rapid indication that all is not well.

8.10 Gradient pulse response times

It was noted at the beginning of this chapter that gradient switching times should be short, ideally less than one sampling interval, to reduce image distortions and imaging times. Gradient switching times depend largely on the ability of the Kepco power supplies to keep the current level constant. Since the coil is a reactive load it presents a fairly high impedance when first switched on. To achieve fast rise times the Kepco must be able to supply high voltages to the coil to keep the current constant. In practice the maximum voltage available from the Kepco is ~25V.

The resistance and inductance for the gradient coils are listed below

Table 8.7 Gradient coil inductance and resistance

Coil	x	y	z
Gradient ($Gcm^{-1}A^{-1}$)	23.74±0.06	1.58±0.06	14.89±0.09
Inductance (μH)	83±2	30±2	43±2
Resistance (Ω)	2.56±0.02	11.5±0.1	1.93±0.02

From this data we can predict the minimum rise times for the coils with a 25V power supply. The x gradient coil is driven by a 4A Kepco unit. 10 to 90% rise times for this coil can be calculated as follows.

The current through the coil will be

$$i(t) = V_m/R_x \ [1-\exp(-R_x t/L_x)] \tag{8.43}$$

$$\Rightarrow \ t = -L_x/R_x \ln[1-R_x \ i(t)/V_m] \tag{8.44}$$

where V_m is 25V. Substituting for R, V and i(t) we obtain

$$t_{10\%} = -L_x/R_x \ \ln[1-0.4R_x/V_m] = 1.4\mu s \quad (8.45)$$
$$t_{90\%} = -L_x/R_x \ \ln[1-3.6R_x/V_m] = 14.9\mu s \quad (8.46)$$

and so a rise time of 13.5 µs is predicted. For the y gradient coil the maximum current is 25/11.5 = 2.17A and so

$$t_{10\%} = -L_y/R_y \ln[1-0.217R_y/V_m] = 0.3\mu s \quad (8.47)$$
$$t_{90\%} = -L_y/R_y \ \ln[1-1.953R_y/V_m] = 6.0\mu s \quad (8.48)$$

giving a rise time of 5.7µs. For the z gradient coil the maximum current is 10A so

$$t_{10\%} = -L_z/R_z \ln[1-1.0R_z/V_m] = 1.8\mu s \quad (8.49)$$
$$t_{90\%} = -L_z/R_z \ \ln[1-9.0R_z/V_m] = 26.4\mu s \quad (8.50)$$

giving a rise time of 24.6µs.

In practice the rise times are rather larger being around 30 to 40µs for the x and z coils and 100µs for the y coil. The extra delay in the x and z coils seems to be caused by the limited BW of the Kepco (this would seem to be the case as the rise times for purely resistive loads are about the same), while the large mutual inductance between the various shim coils might explain the long y coil rise time.

8.11 Pulse Sequencer

Precise timing is important in all NMR experiments. Timing errors associated with the rf pulse or gradient switching could produce phase shifts leading to a variety of imaging distortions.

Because of the range of experiments envisaged in the imaging field it was necessary to consider the implementation of a fairly versatile pulse controller. It would be required to perform a number of operations - the main features being to:

1) Provide analogue control of the rf level.
2) Provide analogue control of the gradient levels.
3) Provide digital switching for a variety of units.

Since frequencies up to 25kHz are detected by the NMR spectrometer it is essential that timing be accurate to within a fraction of the period of this maximum frequency if phase errors are to be keep to a minimum. Since one cycle takes 40µs at 25kHz, a phase error of one degree (really quite small) would require a timing accuracy of ~100ns. A series of switches and digital to analogue converters controlled directly by the 980A computer would clearly have no chance of achieving this sort of timing precision. In addition a great deal of work would be required to obtain software delays of the required lengths. A further disadvantage of using direct software control would be the minimum delay required between level changes. Even with the most efficient output instruction the 980A is incapable of switching levels closer than ~10µs apart - a clear disadvantage when a 90° rf pulse lasts 4µs. However the requirement that a variety of pulse sequences be available requires some sort of software control - a dedicated microprocessor system might be able to achieve this, but not without some sort of external interrupt timing circuitry to achieve pulse timing accuracy which would add considerably to the overall complexity of the unit.

After considering such an option it was decided that a flexible hardware based system which could be programmed to produce a series of accurately timed pulses would be more suitable. A block diagram of the system eventually designed to achieve this function is given in figure 8.28. The system is based around 5 byte control words which are transferred from the 980A to the 4k bytes of RAM in the pulse sequencer before the experiment begins. These words contain the following information :

Table 8.8 Pulse sequencer register functions

Byte	Function	Register
1	destination of data level	mode register
2	data byte	data register
3→5	time in µs	timing registers

Before the experiment is started the required pulse sequence is analysed by the Hitachi software (see volume 2) which generates a series of these words, one for each level change. This data is then transferred to the 980A which passes it to the 4k bytes of RAM in the pulse programmer via the input registers. This allows a total of 819 level changes in any pulse sequence.

On receiving a start pulse from the 980A the first 5 bytes of memory are transferred from the RAM into 5, eight bit registers (see above). The start pulse also starts a 24 bit decade counter which counts in 1µs steps from 0 to 999999µs.

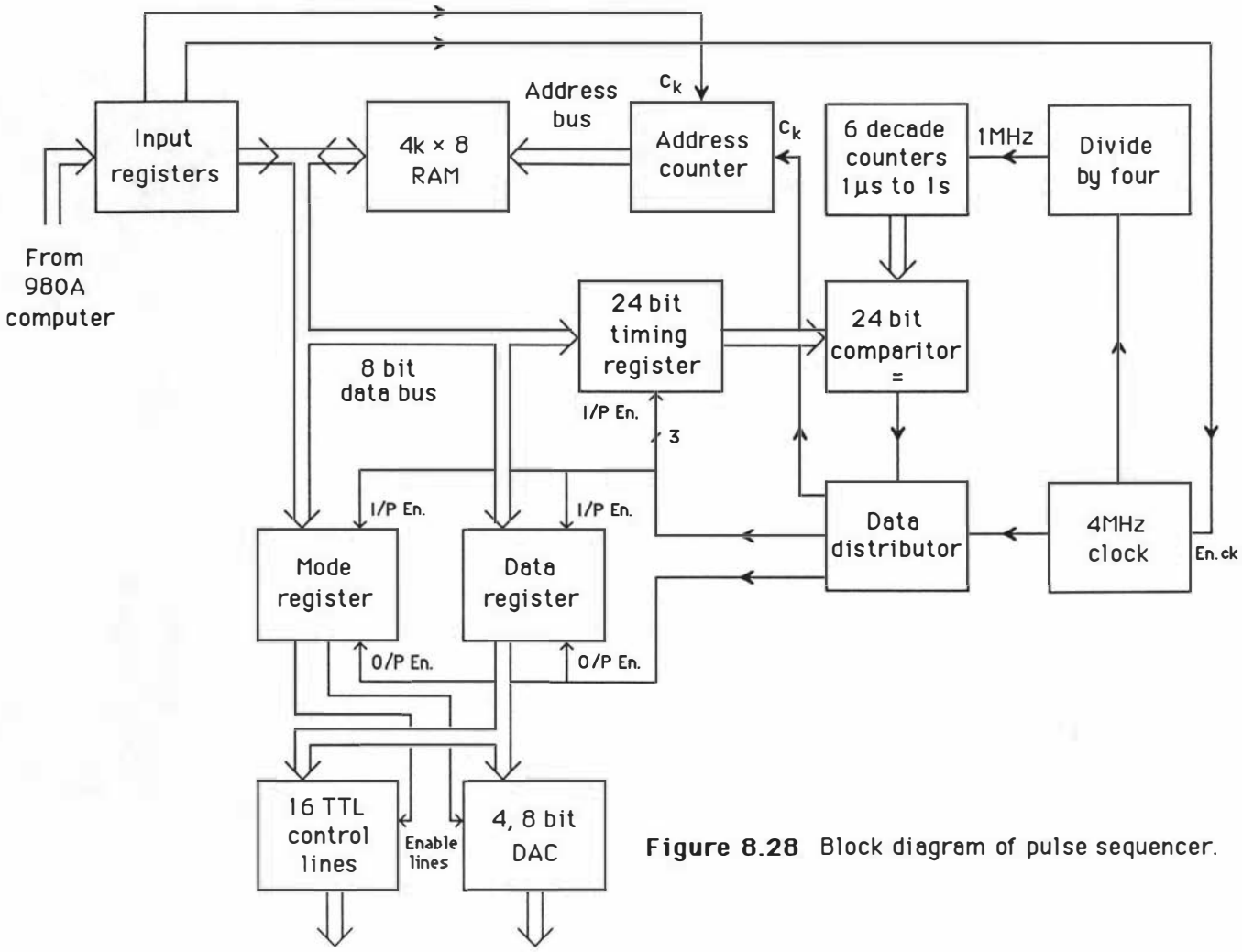

Figure 8.28 Block diagram of pulse sequencer.

The data in the timing registers is continually compared with the output of the decade counters and when equal a pulse is produced which transfers the contents of the mode and data registers to a further series of buffer registers whose outputs control the experiment, either via a series of TTL buffers or digital to analogue converters.

The equality pulse also initiates the transfer of the next 5 bytes of information from data RAM. Since the timing counter is uninterrupted during this process the output levels will change at the required times with an uncertainty determined by the various delays in the circuitry and the variability in the clock frequency.

Due to limitations in the memory read/write times (nominally 150ns for the devices used) a certain delay is necessary while data is transferred from RAM to the data registers. A 4MHz clock (period 250ns) controls this data transfer and so 1.25µs is required. Because of this delay adjacent levels may not be changed unless they are 2µs or more apart. An increase in clock frequency to perhaps 8MHz would allow levels to be changed when only 1µs apart but because the R/W period would now be 125ns the reliability of the RAM devices might become questionable. In any case it has been found that a 1µs pulse is not required in any of our experiments.

The following outputs are available from the pulse sequencer - the corresponding control word is given on the right.

Table 8.9 Pulse sequencer outputs

Function	Control code
G_x level (0→255)	40[1],level[2],time[3]
G_y level (0→255)	20,level,time
G_z level (0→255)	01,level,time
rf level (-128→127)	80,level,time
G_x on/off	08,01,time
G_y on/off	08,04,time
G_z on/off	08,80,time
rf on/off	08,40,time
rf phase 0°/90°	04,20,time
rf phase 0°/180°	04,04,time

980A sampling interrupt	08,08,time
rf signal switch	08,20,time
Pulse sequencer reset	08,02,time

Notes

1) The first byte refers to the register to which the data is to be sent.

2) The second byte determines which digital lines will be set.

3) Time at which data is to be transferred. Data is coded in BCD and stored in three bytes.

Eight registers are capable of being accessed with this code but due to pcb size constraints only 6 registers are made available (01,04,08,20,40,80). This gives four, eight bit DAC levels and sixteen TTL levels which are used for control purposes. Only 9 are used at present.

Appendix F looks at the pulse sequencer design in more detail giving schematics of each pcb and a description of their function.

Table 8.10 gives an example of the code produced for a typical pulse sequence; a standard spin-echo 1-D imaging experiment (see figure 8.29 for the corresponding pulse sequence).

Table 8.10 Pulse sequence code

Address	Control word			Comments
0000[1]	08	00	000100	Reset all control lines at 100µs
0005[2]	01	FF	000102	Set G_z level to 255 at 102µs
000A	80	FF	000104	Set rf level to 127 at 104µs
000F[3]	08	80	001100	G_z on at 1.1ms
0014	08	00	001102	G_z off at 1.102ms
0019	01	20	001104	Set G_z level to 20_{16} at 1.104ms
001E[4]	04	00	008080	Set rf phase to 0° at 8.08ms
0023[5]	08	40	008100	Switch rf on at 8.1ms (90° pulse)
0028	08	00	008104	Switch rf off at 8.104ms
002D	04	20	009080	Set rf phase to 90° at 9.08 ms
0032	08	40	009100	Switch rf on at 9.100ms (180° pulse)

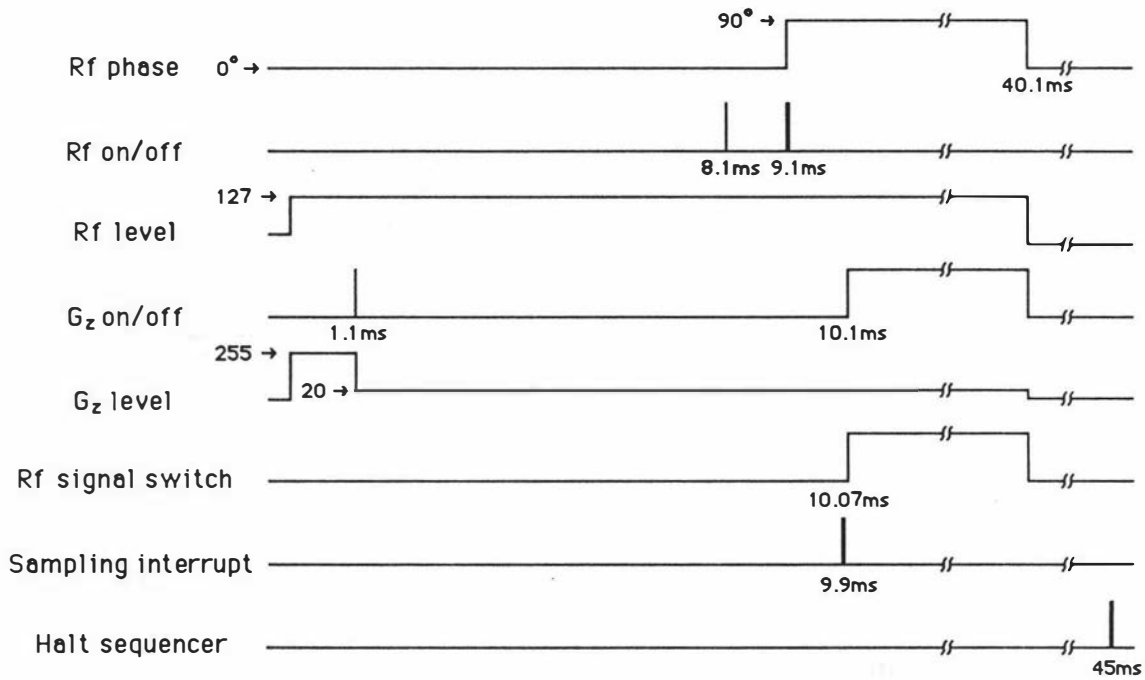

Figure 8.29 Timing diagram for a 1-D imaging experiment.

0037	08	00	009108	Switch on rf off at 9.108 ms
003C[6]	08	08	009900	Switch on sampling interrupt at 9.9ms
0041	08	00	009930	Switch off sampling interrupt at 9.93ms
0046[7]	08	20	010070	Switch rf signal on at 10.07ms
004B	08	A0	010100	Switch G_z on at 10.1ms
0050	08	00	040100	Switch everything off at 40.1ms
0055[8]	08	02	045130	Halt pulse sequencer at 45.1ms

Notes

1) 100μs is added to all times to allow for initial data loading (this time is arbitrary - anything greater than 2μs would do).

2) All data levels are set up well in advance to allow for the appropriate device to respond (this isn't a problem with the modulator but is important in the case of the gradients).

3) The gradient level is initally pulsed so that the response times are improved in the latter part of the sequence . A 2μs pulse is chosen so to have no effect on the NMR system (since the gradient rise times ~50μs)

4) The rf phase must be set up at least 20μs before it is required to allow the phasing circuitry to stabilise.

5) The rf level is switched, rather than just having its level changed, to prevent carrier feed-through when the pulse is not required.

6) The delay between the interrupt pulse and the desired sampling time is introduced to match software delays in the 980A which occur between reception of the interrupt pulse and the onset of sampling.

7) The rf signal switch is switched 30μs before it is required to give it time to respond (see comment in section 8.13).

8) A complete pulse sequence halt (i.e. the clock is stopped) is necessary to prevent spurious pulse switching from occuring after the end of the pulse sequence due to random data in the pulse sequencer memory.

All the required delays are transparent to the user who enters an idealised pulse sequence (see volume 2 for a description of the pulse sequencer software).

8.12 Quadrature detection

In the original NMR system the free induction decay corresponded to a projection of the magnetization vector **M** onto the y axis. Since the x axis projection M_x was unavailable it wasn't possible to determine whether the magnetization was rotating clockwise or counter-clockwise, i.e. above or below the resonant frequency. For this reason it was necessary to adjust the offset frequency so that all frequencies of interest lay above or below resonance. If this wasn't done aliasing occurred. While this did not present a problem in routine spectroscopy, such an affect is highly undesirable in imaging where DSBSC selective excitation requires that the slice Larmor frequency be close to the carrier. Furthermore, for the purposes of image reconstruction it would be useful to work exactly on resonance as this simplifies the mathematics.

For this reason a small circuit was added to the spectrometer which allowed M_x to be detected as well. With both M_x and M_y available it is possible to work right on resonance without aliasing, with the additional benefit of a doubled bandwidth.

Most systems which allow detection of the quadrature signal component $\xi_x(t) \propto M_x$ (such as the Jeol FX90Q), do so by having 2 completely separate digitising systems. The advantage of this arrangment is that it allows simultaneous acquisition of both in phase and quadrature signals. Unfortunately since each signal must pass through a separate af amplifier and digitiser, the chances of a gain mismatch are quite high. This will lead to the production of ghost lines in the frequency domain.

In our system we have achieved quadrature detection by detecting ξ_x and ξ_y at different times, this has the disadvantage of requiring twice as long as the previous method but since both signals pass through identical circuitry, amplitude mismatches (at least from this source) are not a problem.

From figure 8.30 we see that

$$\xi_y = \xi_0 \cos(\Delta\omega + \omega_0)t \text{ and } \xi_x = \xi_0 \sin(\Delta\omega + \omega_0)t \qquad (8.51)$$

where $\Delta\omega$ is the frequency offset from resonance.

In the detection procedure (phase sensitive detection) one multiplies the NMR signal by a local oscillator at the resonant frequency i.e.

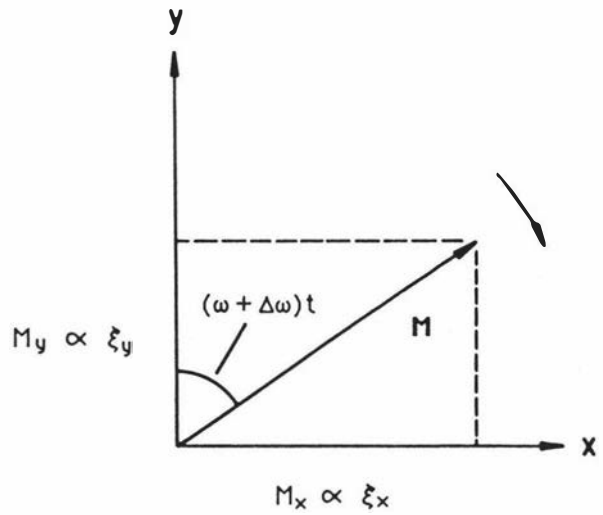

Figure 8.30 Components of the magnetization vector in the lab frame.

$$\xi(t) = \xi_0 \cos(\Delta\omega + \omega_0)t \cos \omega_0 t$$

$$= 0.5\, \xi_0 [\cos(\Delta\omega + 2\omega_0)t + \cos \Delta\omega t] \quad (8.52)$$

where relaxation effects have been ignored. The high frequency component is filtered out leaving

$$\xi(t) = 0.5\, \xi_0 \cos \Delta\omega t \quad (8.53)$$

which is a direct measurement of M_y in the rotating frame.

If instead of multiplying by $\cos\omega_0 t$ in the detector we multiply by $-\sin\omega_0 t$ we obtain

$$\xi(t) = -\xi_0 \cos(\Delta\omega + \omega_0)t \sin \omega_0 t$$

$$= 0.5\, \xi_0 [\sin(\Delta\omega + 2\omega_0)t + \sin \Delta\omega t]. \quad (8.54)$$

Low pass filtering will now give the quadrature signal

$$\xi(t) = 0.5\, \xi_0 \sin \Delta\omega t \propto M_y \quad (8.55)$$

It is therefore apparent that the local oscillator phase must be altered by 90° if we are to detect the quadrature signal.

In the FX60 the local oscillator is generated digitally with a variety of phases being made available (clearly with quadrature detection in mind). It was therefore simply a matter of adding a logic switch to allow selection of the 0° or 90° local oscillator phase. The schematic for this alteration may be found in figure 8.31. To reduce the effects of hardware gain drift, in phase and quadrature signals are accumulated alternately.

Once accumulated the two time domain signals must be Fourier transformed to obtain the spectral density function. Normally this would be done with a full Cooley-Tukey complex fast Fourier transform, with

$$\xi(t) = \xi_y(t) + j\xi_x(t) \quad (8.56)$$

Unfortunately the supplied FFT is based on the Bergland transform[33] which performs a FFT on real data only (allowing reduction in memory space and computation time). However, it is quite a straightforward procedure to implement a full complex FFT using the available algorithm since

$$F\{\xi(t)\} = F\{\xi_y(t) + j\xi_x(t)\}$$

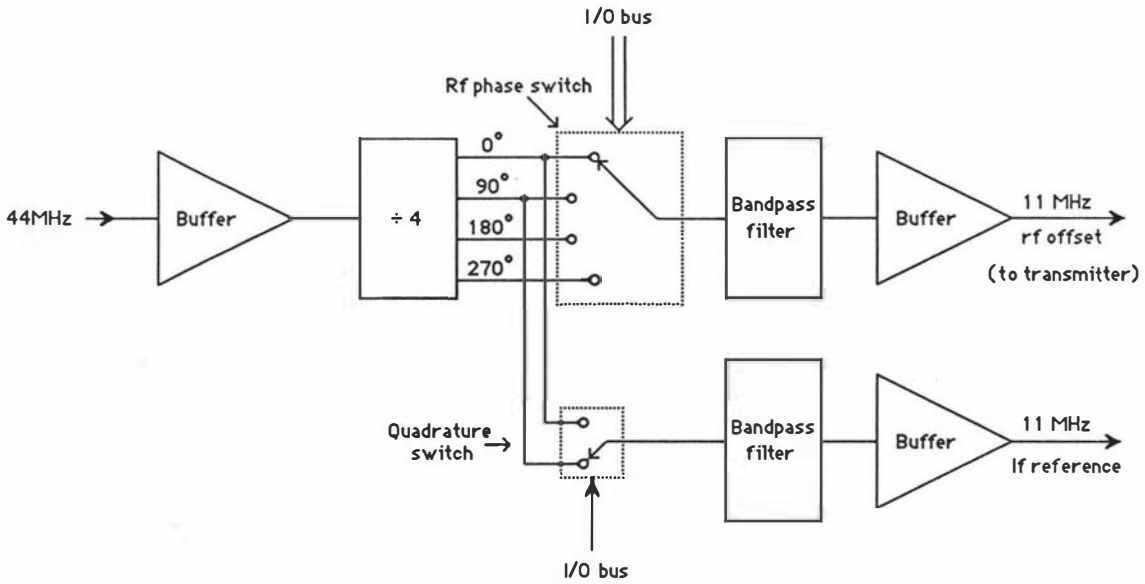

Figure 8.31a Block diagram of the 4 phase generator.

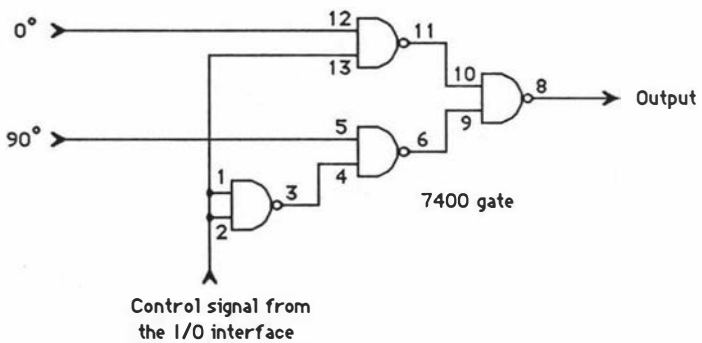

Figure 8.31b Schematic of quadrature switch.

$$= \int_{-\infty}^{\infty} \{\xi_y(t) + j\xi_x(t)\}\{\cos\omega t + j\sin\omega t\}\, dt$$

$$= [\, F_C\{\xi_y(t)\} - F_S\{\xi_x(t)\}\,] + j[\, F_C\{\xi_x(t)\} + F_S\{\xi_y(t)\}\,]. \qquad (8.57)$$

Given a function $\xi(t)$ the Bergland FFT will produce $F_C\{\xi(t)\}$ and $F_S\{\xi(t)\}$. It is therefore a simple matter to generate the above function by Fourier transforming ξ_x and ξ_y individually.

8.13 Rf signal switching

After a few 1-D imaging tests had been performed it was clear that working on resonance (i.e. $\Delta\omega=0$) was going to cause problems. The projection profile (see section 3.1) of a tube of water had a large spike at zero frequency (resonance) - see figure 8.32. The size of the spike was seen to diminish as one went off resonance. It was also dependent on the phase setting and pulse sequence used. For example pulse sequence A (fig. 8.33) which used a spin echo to generate a nuclear signal produced a marked spike while the profile due to sequence B was practically spike free.

From this information it became apparent that the problem was due to the ac capacitive coupling used in the af amplifiers of the spectrometer. The dc level present before the G_z gradient comes on in sequence A causes this capacitance to charge up. When the gradient is applied the system responds by producing a rapidly changing initial signal followed by a slow decay. When Fourier transformed this decay manifests itself as a narrow spike at zero frequency.

The improvements observed when operating off resonance were simply due to the fact that the signal was no longer at zero frequency and so little or no charge was built up. Critical phase adjustments reduced the glitch if the signal level was set to zero directly before the G_z pulse was switched on.

The solution to this problem was simply to ground the signal until it was required. In this way there would be no time for a charge to build up. The signal was effectively grounded by reducing the gain of the IF stage until sampling was due to start. No modification to the system was necessary as signal switching was already used in the original system, possibly to prevent overload during rf transmission since one would never have worked on resonance. A simple mechanical switch was used to select rf signal switching under spectrometer control (for normal NMR) or pulse sequencer control (for imaging) - as shown in figure 8.34. A short delay between

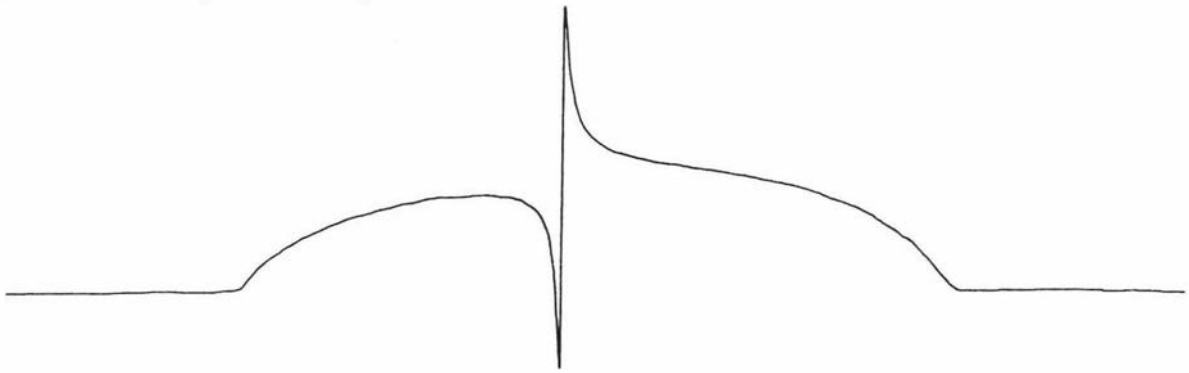

Figure 8.32 Projection profile of a tube of water showing the large spike at zero frequency caused by ac coupling within the spectrometer.

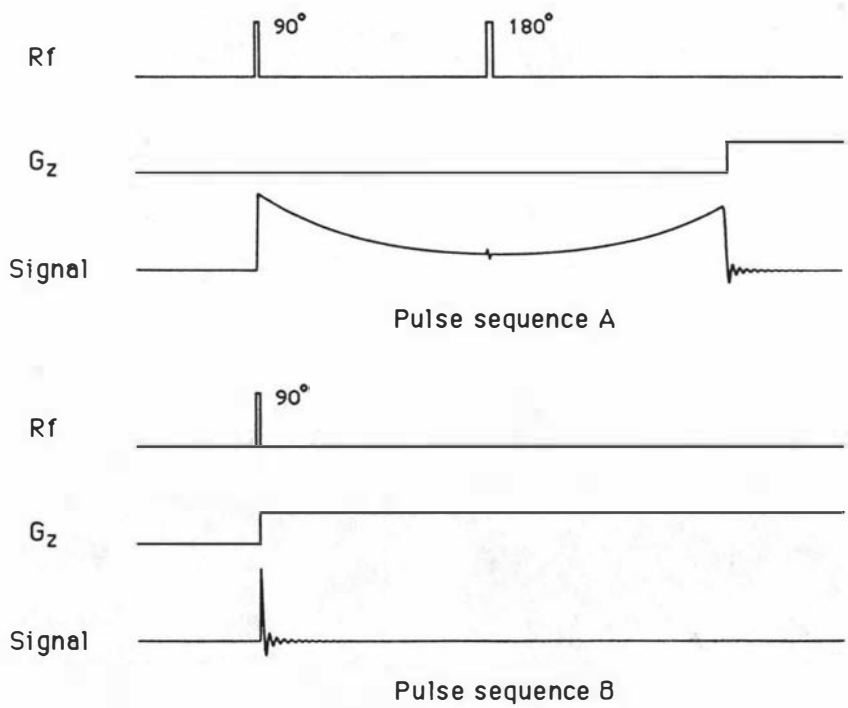

Figure 8.33 Pulse sequence used to observe the zero frequency glitch.

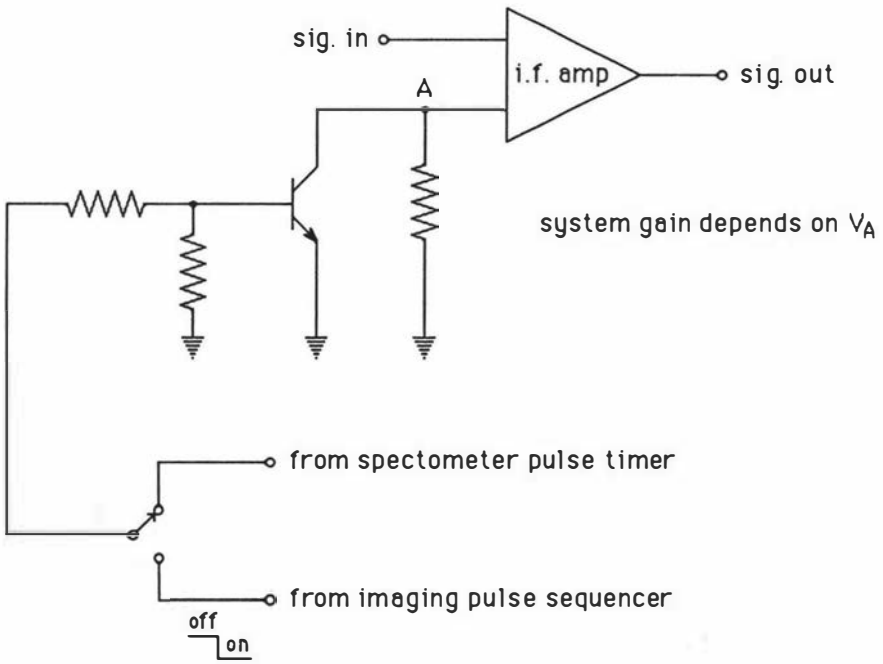

Figure 8.34 Rf signal switch.

signal switching and sampling was necessary to allow the system to respond; 30µs was found to be about optimum (see figure 8.35). The effect of this switch is dramatic as can be seen in figure 8.36.

Unfortunately it was discovered that this switching had only partially solved the problem. When an exponential window was applied before the FFT the glitch was seen to return. After investigating the software in some detail the problem was traced to the way in which the baseline correction was performed. Before the exponential window is applied a baseline correction is performed which subtracts the average data value from all data points. If the signal is asymmetric this results in a DC offset. Normally this wouldn't be seen in the frequency domain as the DC point is thrown away before display. However when an exponential filter is applied the DC level is converted to an exponential decay which again manifests itself as a low frequency glitch in the frequency domain (see figure 8.37).

This problem was solved by rewriting the baseline correction routine so that only the average of the last half of the data points was subtracted, since these points usually have much the same value, due to the rapid decay of the signal. The improvement obtained is significant (fig. 8.38).

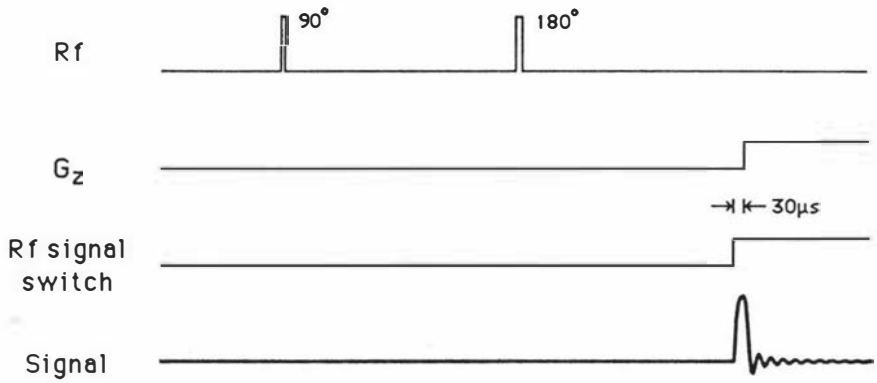

Figure 8.35 Pulse sequence incorporating the rf signal switch.

Figure 8.36 Improved projection profile obtained when rf signal switching is used.

Figure 8.37 Zero frequency glitch returns when exponential filtering is applied.

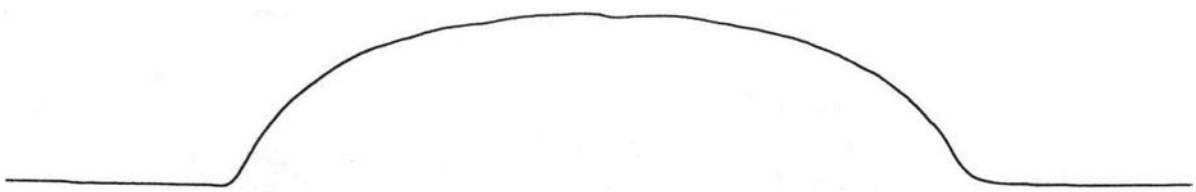

Figure 8.38 Improved result obtained by modifying the baseline correction routine.

8.14 The graphics computer

Initially it was proposed that the proton density data would be displayed on the oscilloscope interfaced to the TI-980A computer. However the data memory available (4k words) limited the image size which could be displayed to a 64×64 array. Image quality was also poor due to the flicker produced by low screen refresh rates.

The limited memory and poor image quality prompted the purchase of an independent graphics computer. This machine, an Hitachi MB16000, is based on the 8088 microprocessor and is supplied with MSDOS. Currently it is configured with 256kbytes of main memory, two 320kbyte disk drives and 192kbytes of graphics memory. The latter allows the display of 640×400 pixels in 8 colours as well as 16 pages of 16 colour text.

Image reconstruction is currently performed using both computers. The TI-980A collects the k space data, applies a filter and then obtains the Fourier transform. The resultant filtered profile is then transferred to the Hitachi pc via the parallel interface described in appendix F. Once in the Hitachi the data is backprojected onto the image plane. The back projection process is fairly slow requiring ~24s per projection. At present this poses few problems as large numbers of accumulations are required to provide sufficient signal to noise ratios in the final image. The image data is stored in the upper 128kbytes of memory as a 256×256 image with 16 bits per data point.

8 colours were considered to be insufficient for the signal to noise ratios expected (10→20) and so the screen resolution was reduced to 320×200 so that 4 screen pixels could be used to represent each data point. To reduce image flicker, pixels in the same column were set to the same colour while those in the same row were allowed to differ. With this restriction 36 different colour combinations were possible of which 16 were chosen to form a scale which could be used to represent proton density (see, for example, figure 9.2). The choice of colours was necessarily arbitrary, but an attempt was made to provide a scale which ranged from dark to light. An alternative scale was also produced so that image data could be displayed on a monochrome monitor (see figure 8.39).

Once obtained, images are stored on disk as two 64kbyte data files. Hardcopy may be obtained in the form of a dot matrix screen dump with images displayed as an array of 213×256 dots in up to 10 shades, as in figure 9.20, or by directly photographing the screen. Sections through the image can be displayed so that signal to noise measurements and amplitude data can be obtained (see figure 8.40). Software listings of the routines used to generate these functions may be found in volume 2.

Figure 8.39 *(top)* Monochrome image of a section through an Aralia stem.

Figure 8.40 *(bottom)* A horizontal amplitude profile taken through the "10 tubes" image, figure 9.13. (See section 9.1 for imaging details).

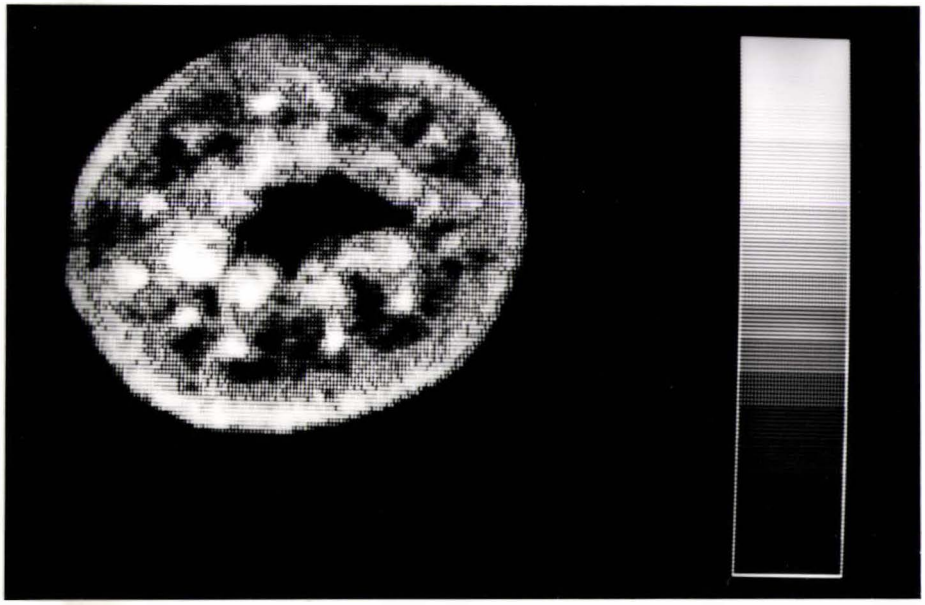

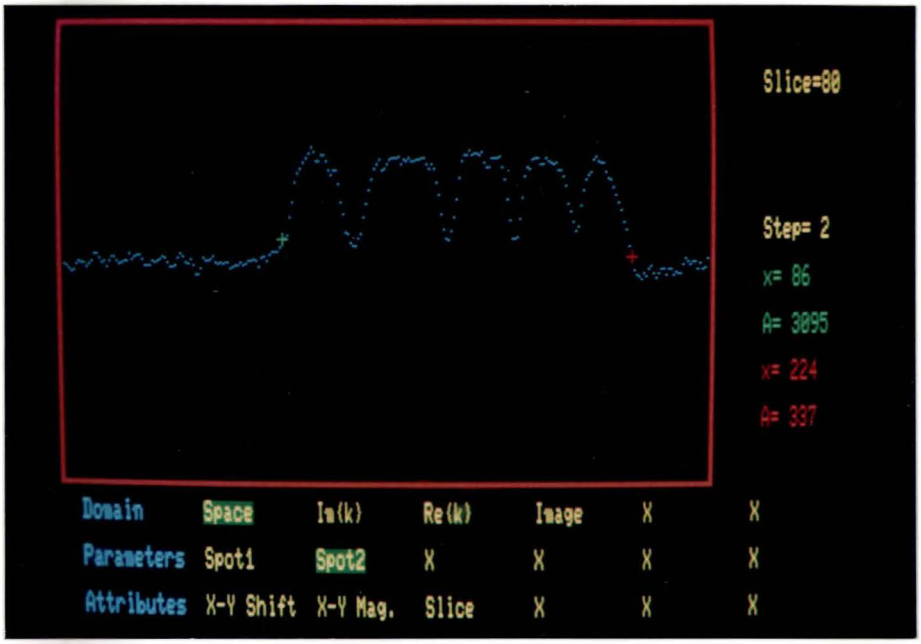
Slice=80
Step= 2
x= 86
A= 3095
x= 224
A= 337
Domain Space Im(k) Re(k) Image X X
Parameters Spot1 Spot2 X X X X
Attributes X-Y Shift X-Y Mag. Slice X X X

9 IMAGING EXPERIMENTS

9.1 Proton density imaging

Proton density imaging is the simplest imaging technique and has already been described in some detail in chapter 4. The pulse sequence used to produce images which are functions of proton density is given in figure 9.1.

The short 2μs gradient pulses are used to prepare the Kepco power supplies so that gradient rise times are as short as possible. The G_y and rf pulse sequences selectively excite a slice of spins along the y axis. Data acquisition is initiated with the application of the x and z imaging gradients and continues for a time $T=N/\Delta f$ where N is the number of data points and Δf the bandwidth. Alternate experiments change the phase of the 90° pulse by 180° for coherent noise cancellation purposes, while every second pair of experiments changes the local oscillator phase used in phase sensitive detection, thereby producing the quadrature signal. After four such experiments have been carried out (and the real and imaginary time domain signals stored) the process is repeated until N_{acc} accumulations have been obtained.

When the time domain data has been accumulated it is filtered to improve the frequency domain signal to noise ratio, and then multiplied by a ramp in preparation for backprojection. A quadrature FFT is then performed, with the resultant phased data

$$f_p(k) = f_r(k)\cos\alpha + f_i(k)\sin\alpha \qquad (9.1)$$

being transferred to the Hitachi for backprojection and display. A preparatory experiment is normally performed before imaging begins which adjusts α so that the phased data has a flat baseline.

Once the filtered projection has been transferred to the Hitachi p.c., new gradient parameters are transferred to the pulse sequencer and the process is repeated for the next projection angle φ. The required gradient values are generated by the Hitachi when the pulse sequence is written and are stored in the TI-980A memory throughout the experiment. When φ has reached 90° the x gradient must be reversed (this is done manually at present) to allow the second and third quadrants of k space to be mapped.

Initial experiments were carried out without the assistance of a y gradient coil and so it was necessary to physically cut the samples to prevent image confusion due to overlying structures. Because the sensitivity of the system was initially rather poor, fairly thick slices were required and so the resolution was low. Plant stems were therefore obvious imaging candidates as their

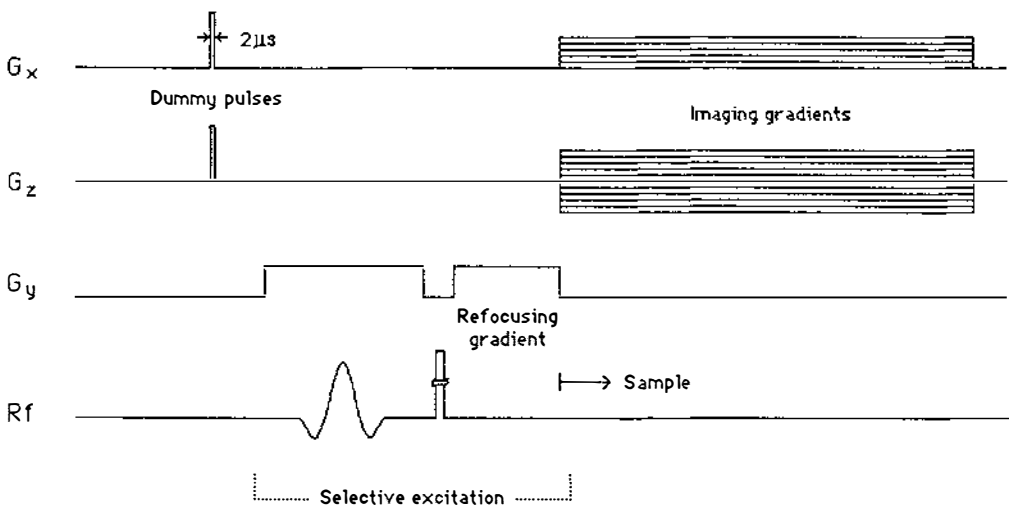

Figure 9.1 FBP pulse sequence for proton density imaging with slice selection.

structure varies little along the longitudinal axis. The imaging parameters and observed resolutions for the images presented in this section are listed in table 9.1

Table 9.1 Imaging parameters

Sample	Δy	Δz_{max}	f_b[1]	N_{acc}	t_{rep}	Δf	res1[2]	res2	S/N[3]
Hydrangea	9mm	6mm	smot 9	20	1s	50kHz	250µm	220µm	50
Parsnip	7mm	4.5mm	smot 9	20	1s	50kHz	250µm	220µm	40
10mm tube	2mm	10mm	smot 3	40	0.5s	50kHz	330µm	200µm	50
Rye grass	6mm	2mm	284Hz	50	0.4	20kHz	90µm	50µm	55
Wheat grain	2mm	3.5mm	384Hz	24	0.5	50kHz	180µm	60µm	38
Aralia	1.1mm	2.4mm	300Hz	24	0.5s	20kHz	120µm	52µm	32
2 tubes	1.5mm	3.2mm	156Hz	60	0.2s	20kHz	140µm	47µm	38
10 tubes	1.5mm	1.3mm	350Hz	60	0.2s	20kHz	45µm	36µm	34
A. Tenium	1.5mm	1mm	350Hz	24	0.5s	20kHz	45µm	35µm	38

Notes

1) The first 4 images were obtained before the zero frequency glitch problem was solved (see section 8.13) and so, rather than applying an exponential window, a smoothing routine was used on the spectral profile data. Smot 9 means that 4 points on either side of each data point are averaged; an equivalent exponential broadening would be around 1.7kHz in this case. The rye grass image used a combination of exponential broadening and smoothing to reduce the size of the zero frequency glitch; smot=3 in this instance (the quoted figure is the total broadening).

2) Resolution was measured from a cross section of the image data. The rate at which the signal dropped away at the edge of the image was used as a measure of the resolution. This result will tend to be larger than the calculated resolution (res2), which is based on the applied broadening and uses the Rayleigh criterion, because of the non-discontinuous changes in proton density at the edge of the sample.

3) The signal to noise ratio is measured from the cross section data and is defined as peak signal height/rms noise level. The rms noise level is approximated as peak-to-peak noise/5[20].

Figure 9.2 is a light micrograph of a section through an Hydrangea stem. This plant is a dicot which means that the vascular bundles are spread around the periphery of the stem (although their

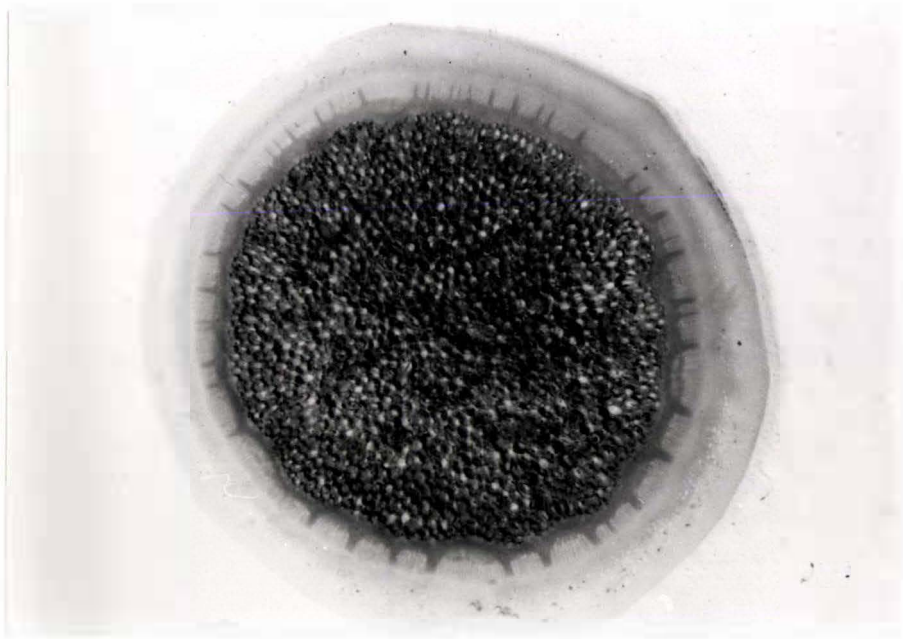

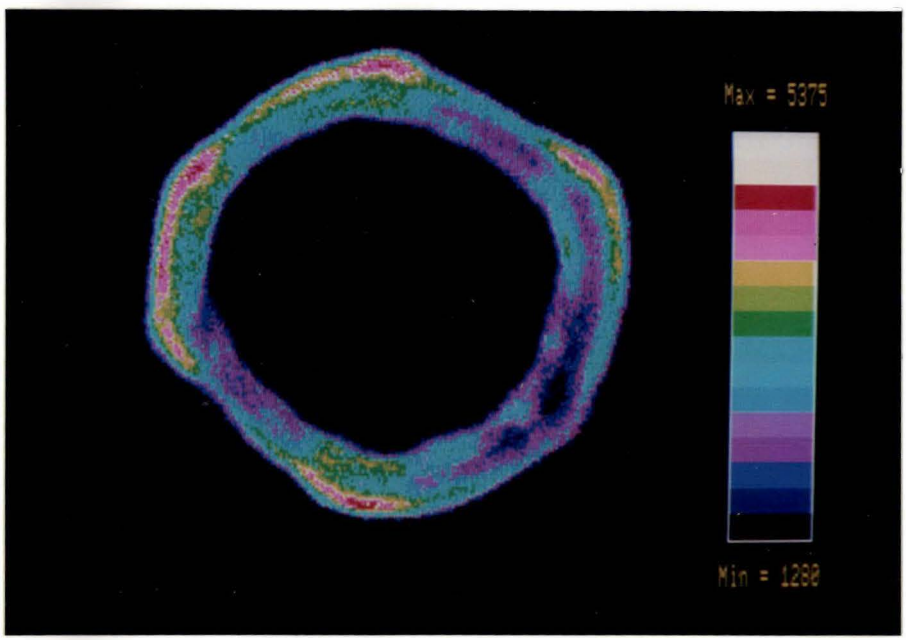
Max = 5375
Min = 1260

presence is not obvious from this photograph). The central region is composed chiefly of collenchyma tissue which contains large quantities of cellulose. The corresponding NMR image, figure 9.3, shows a marked contrast between the outer regions of the stem, which were green and moist in the original plant, presumably containing the vascular bundles, and the central pulpy region which was quite dry. This illustrates the important point that only hydrogen nuclei which are not significantly bound to surfaces, or attached to rigid macromolecules, will produce narrow NMR spectral lines suitable for imaging purposes. The water protons in the vascular bundles fall into this category. The spectral lines from nuclei which are fixed and unable to move relative to one another, such as those in the cellulose of the collenchyma tissue, will be significantly broadened due to dipolar interactions between neighbouring nuclei. These signals will go undetected by the imaging system due to its limited bandwidth and so this region of the plant appears black.

The second micrograph, figure 9.4, is of a thin section through a parsnip stem. This plant is clearly a monocot (i.e. vascular bundles distributed throughout the stem) and again the surrounding collenchyma tissue is quite prominent. The vascular bundles are quite obvious in the corresponding NMR image, figure 9.5, as regions of high intensity indicating high levels of mobile hydrogen nuclei, probably in the form of water. Because of the thick slices used in these experiments individual cells are not visible. In fact the largest cellular structure in these micrographs is about 50μm in diameter, which is less than the transverse resolution applicable in this experiment.

The next micrograph, figure 9.6, is of a thin section through a rye grass stem. Again the vascular bundles are obvious as is the surrounding collenchyma tissue. The rye grass stem used in the imaging experiment, figure 9.7, was different from that shown in figure 9.5. This section was taken from higher up in the stem. The dry outer sheath of the grass is visible as a region of lower intensity while only 3 vascular bundles are visible. It has been suggested that this might reflect the trigonal leaf structure of this plant, other non-active bundles being invisible. However more samples would need to be studied before a definitive statement could be made. The rye grass stem was left standing in a weak copper sulphate solution prior to imaging to reduce T_1, thereby allowing a reduction in the repetition time t_{rep}.

The next image, figure 9.8, is of water in a 10mm diameter flat bottomed sample tube. The water just covers the bottom of tube and the image exhibits a meniscus effect with the water around the edges of the tube some 2mm deep while that at the centre is somewhat less than 1mm. The slight irregularity in the shape of this image suggests a non-uniformity in the x and/or z gradients.

The removal of the zero frequency glitch, described in section 8.13, enabled exponential filtering to be used. Additional S/N improvements were also obtained by replacing the rf preamplifier and

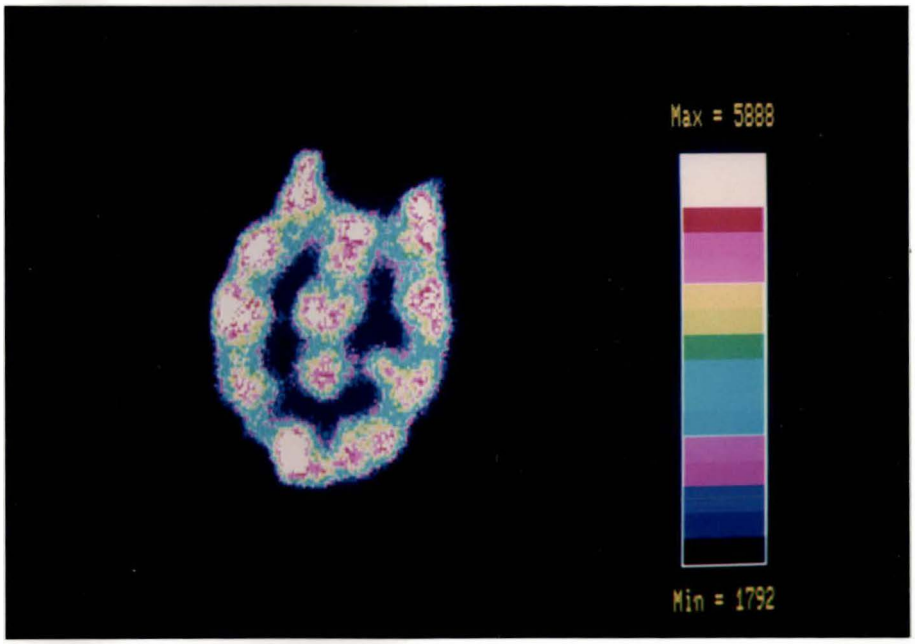
Max = 5888
Min = 1792

Figure 9.6 *(top)* Light micrograph of a thin section through a rye grass stem.

Figure 9.7 *(bottom)* The NMR image of a 6mm slice through a rye grass stem which was 2mm in diameter. The particular slice imaged was different from that used to obtain the light micrograph having had a hole in the centre and being surrounded by a dry outer sheath (the purple and blue regions in the image).

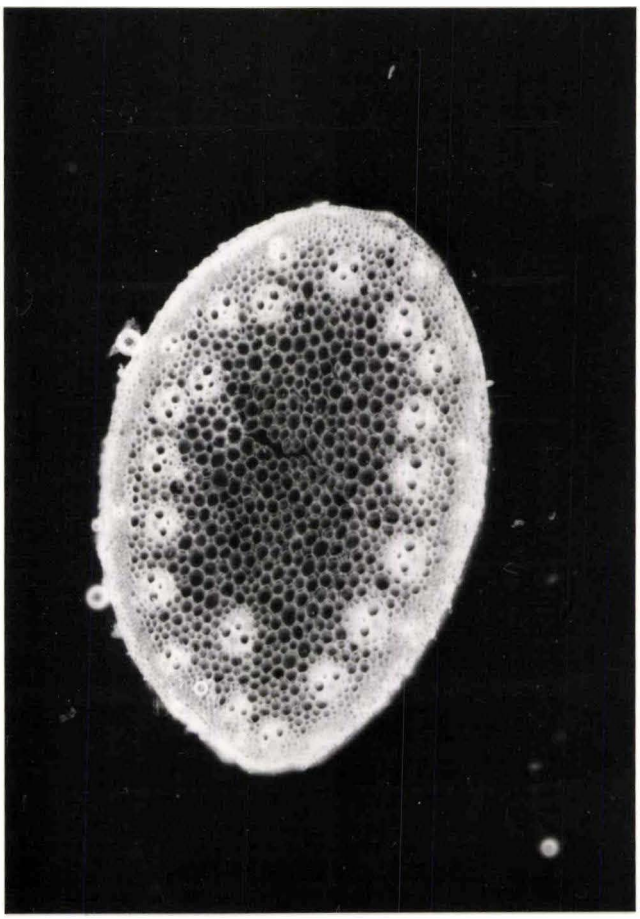

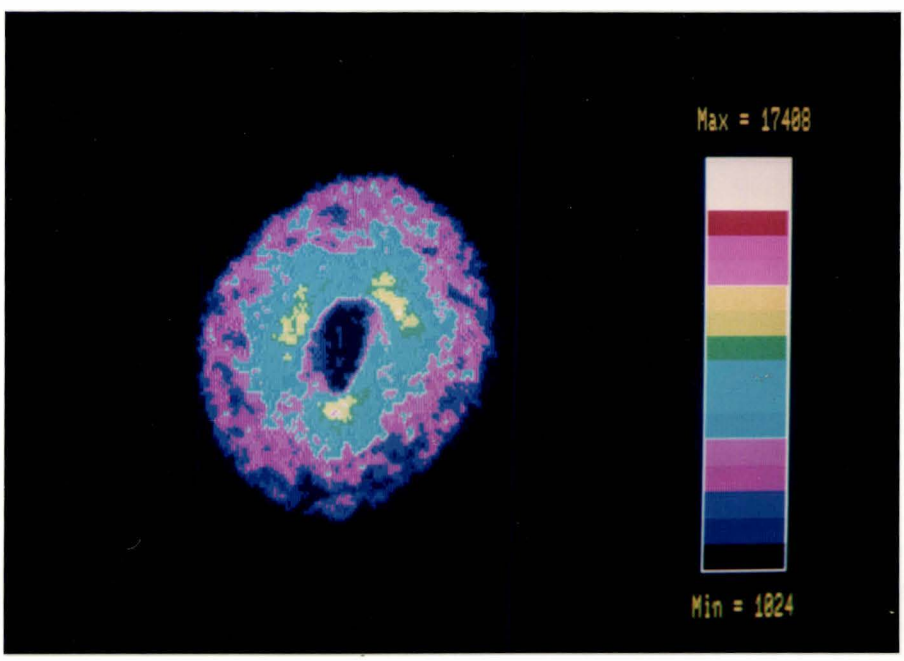
Max = 17408
Min = 1024

Figure 9.8 *(top)* The NMR image of water in a flat bottomed, 10mm diameter, NMR tube. The water has formed a meniscus which is clearly visible in the image. Note the non-circular nature of the image - possibly caused by gradient nonlinearities.

Figure 9.9 *(centre)* The NMR image of a 2mm transverse section through a 3.5mm wide wheat grain. No base line correction has been applied to this image and so background noise is visible.

Figure 9.10 *(bottom)* The major anatomical features of the wheat grain.

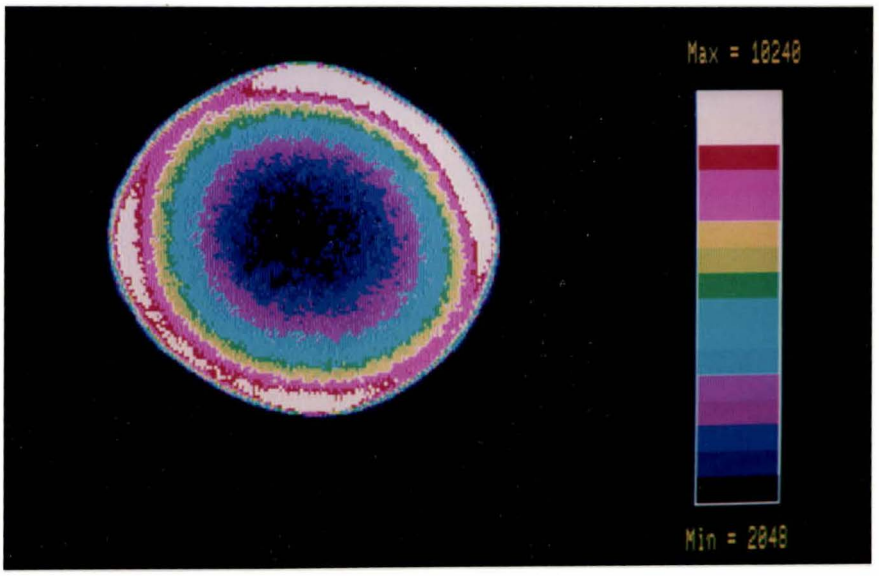
Max = 10240
Min = 2048

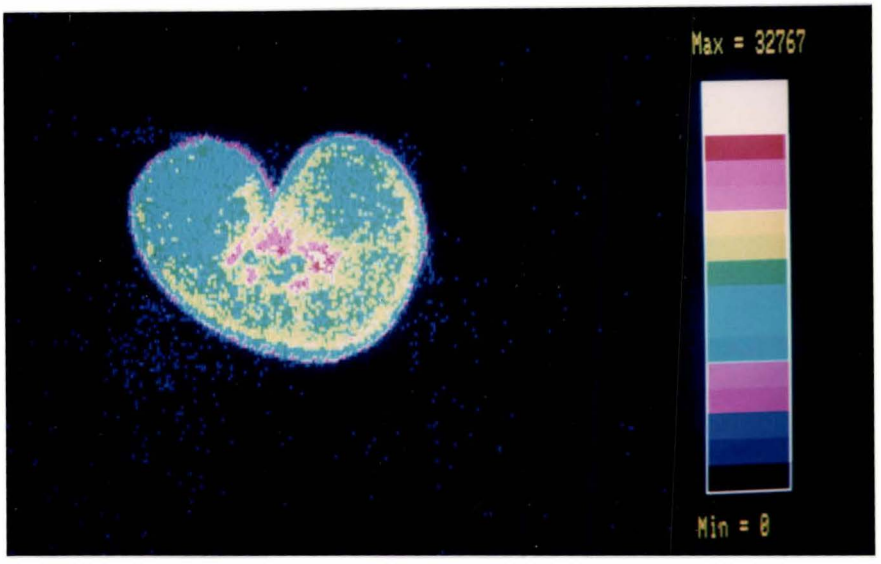
Max = 32767
Min = 0

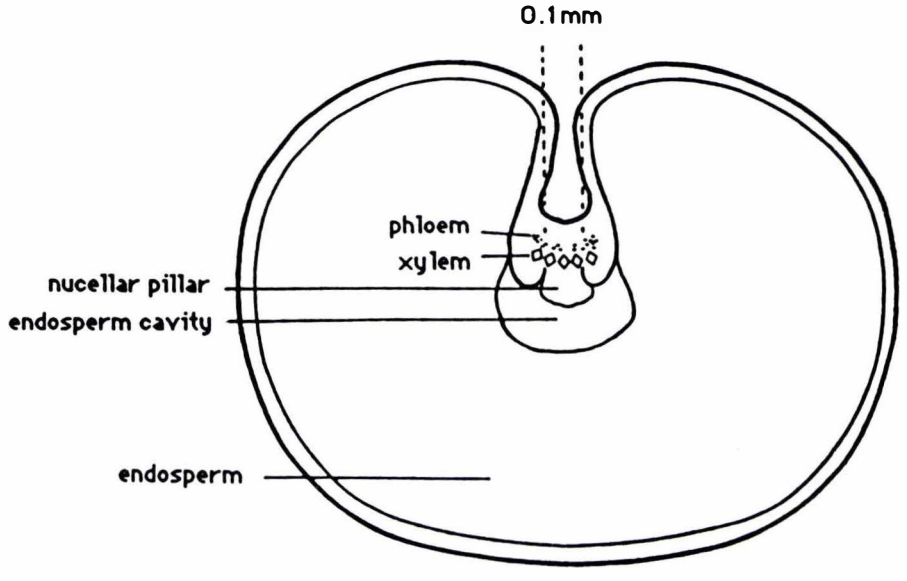
0.1mm
phloem
xylem
nucellar pillar
endosperm cavity
endosperm

associated circuitry with the improved apparatus described in section 8.2. The following images are representative of those obtained after these modifications had been made.

Figure 9.9 is an image of a 2mm transverse slice taken through a wheat grain. Figure 9.10 is a diagram showing the major anatomical details within the grain. The vascular bundles again stand out as regions of high proton density as does the thin aleurone layer covering the grain, while the starchy endosperm tissue has an intermediate density.

Further resolution enhancements were obtained by reducing the size of the rf coil from 12 to 5.6mm. At this stage electronic slice selection, as opposed in physical slice selection, was achieved, allowing intact specimens to be imaged in a non-invasive fashion. The following images were obtained using the small rf coil and the slice selection procedure discussed in section 3.2, apart from the Aralia stem, which was cut.

Figure 9.11 is an image of a thin section through an Aralia stem. This was the thinnest section used in these experiments and shows the increased amount of detail which becomes visible as the slice thickness is reduced. Vascular bundles with diameters ranging from 100 to 600μm are again clearly differentiated.

To obtain figure 9.12 a 1mm i.d. pasteur pipette was placed inside a 3.2mm i.d. NMR tube and then immersed in doped water. Several features are notable - the low filter constant (close to optimal) resulted in an essentially uniform proton density, except for some artifacts which seem to be caused by gradient non-orthogonality. A minor software error in the backprojection routine which has since been corrected may also have contributed to this effect.

Ten glass capillary tubes were drawn under a flame, filled with doped water, the ends sealed, and were then mounted in two groups of 5 either side of a sheet of paper of thickness 80μm. The resultant image, displayed in figure 9.13 again shows artifacts due to gradient non-orthogonality, and the large applied broadening which has resulted in a non-uniform intensity across the tubes. Despite these problems the tubes, which have internal diameters ranging from 130 to 280μm, are clearly differentiated.

A micrograph of a section through the stem of Alyssum Tenium is shown in figure 9.14. An NMR image through a similar stem, figure 9.15, shows remarkable similarities with the two rings of vascular bundles, ranging in width from 50 to 130μm, being prominently displayed.

Having obtained proton density images, it is of interest to see how the observed resolution compares with the expected resolution as determined by equation 6.63. The imaging technique used in these experiments differs slightly from that described in section 6.5 in that only half of k space is sampled. Because of this the signal amplitude in image space will be halved. The noise

Figure 9.11 *(top)* The NMR image of a 1.1mm transverse section through an aralia stem which was 2.4mm in diameter. The vascular bundles are visible as regions of high intensity.

Figure 9.12 *(centre)* The NMR image of doped water in a 3.2mm i.d. glass tube. The stem of a 1mm Pasteur pipette has been introduced to highlight the image distortions caused by gradient nonlinearities and inaccurate backprojection.

Figure 9.13 *(bottom)* The NMR image of doped water in 10 capillary tubes which ranged from 130 to 280μm in diameter. Selective excitation was used to ensure that only a 1.5mm slice of spins were stimulated.

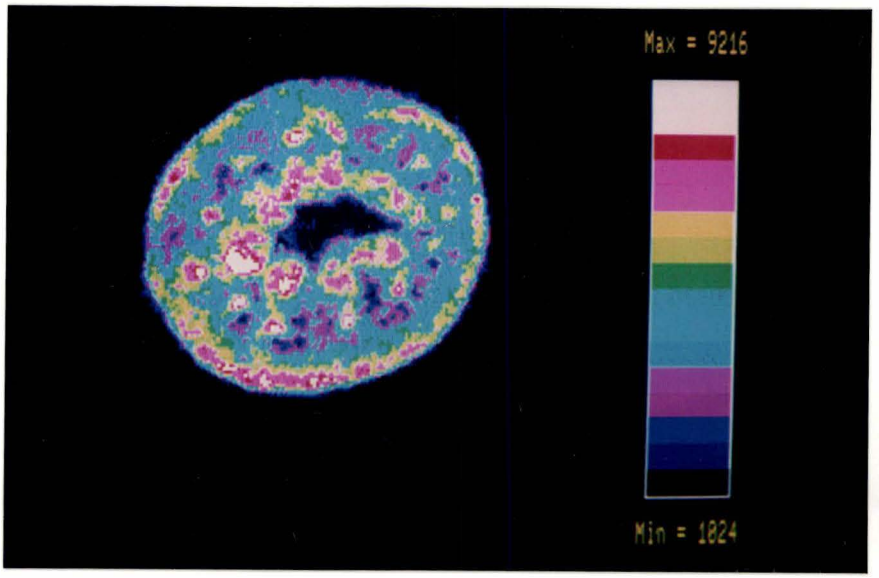
Max = 9216
Min = 1024

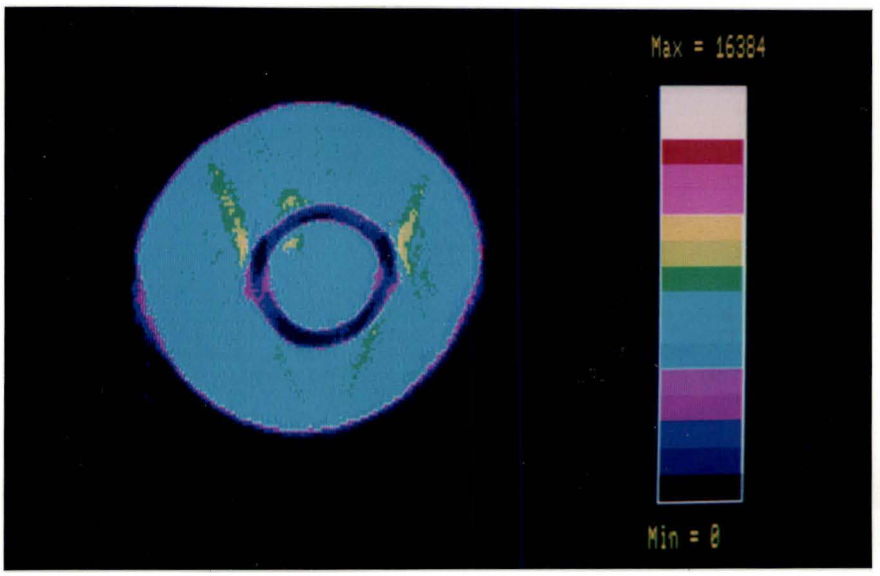
Max = 16384
Min = 0

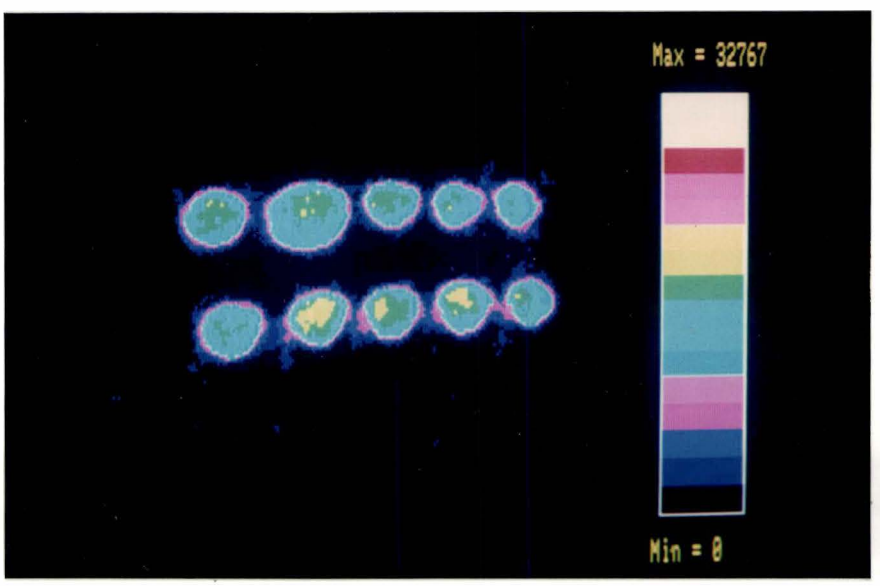
Max = 32767
Min = 0

Figure 9.14 *(top)* Light micrograph of a thin section through the stem of Alyssum Tenium.

Figure 9.15 *(bottom)* The NMR image of a 1.5mm (stimulated) transverse slice through a 1mm diameter Alyssum Tenium stem. Note the two rings of vascular bundles which have been clearly differentiated.

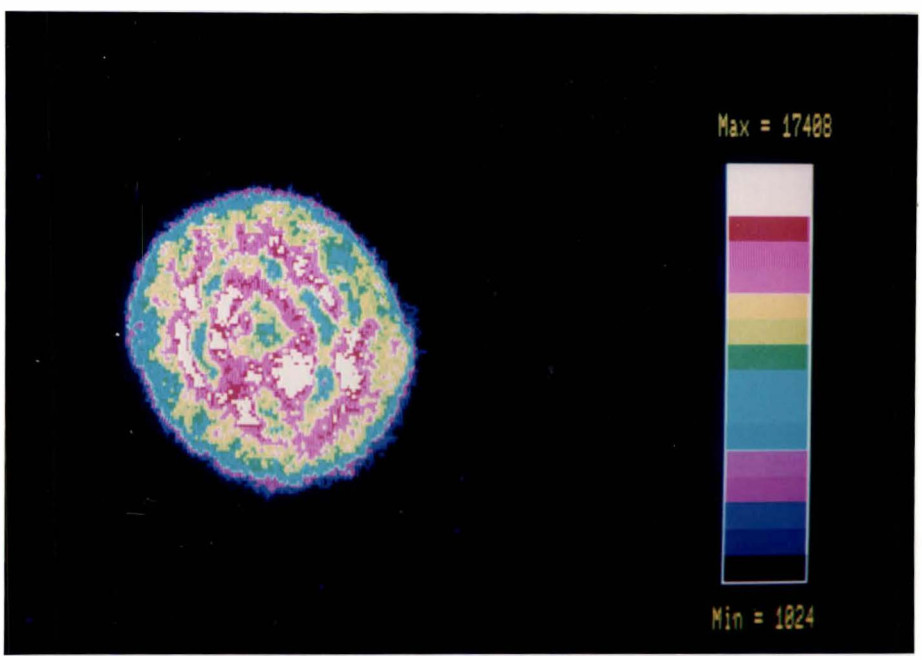
Max = 17408
Min = 1024

level will also be altered. If equation 6.50 is re-evaluated for n=0→N rather than for -N/2→N/2 we find the noise level is decreased by a factor of $1/\sqrt{2}$. The overall S/N therefore decreases by a factor of $2^{-1/2}$. A number of the parameters in equation 6.63 have also been altered. In the 10 tube image the number of complex accumulations has increased from 8 to 60, the observed signal to noise is 34 not 40 and 90 rather than 256 projections are performed. The short T_2 of the $CuSO_4$ doped sample (5.8ms) resulted in a significant attenuation in the observed signal. The delay between initial excitation and application of the imaging gradients was 6ms. This resulted in an attenuation of exp(-6/5.8) = 0.355. The selective pulse used to excite the nuclei was not 100% efficient - not all spins were excited by 90°. A signal to noise experiment conducted using a selective pulse showed an efficiency of ~68% when compared with a non-selective pulse. With all these factors combined we find a net resolution of

$$\Delta x_{new} = \Delta x_{old} \, (8/60)^{1/4} \, (34/40)^{1/2} \, (2)^{1/4} \, (0.355)^{-1/2} \, (256/90)^{1/4} \, (0.68)^{-1/2}$$

$$= \Delta x_{old} \times 1.75 \; . \qquad (9.2)$$

Using the result in column A of Table 6.2 for T_2 = 5ms we find an expected resolution of 16.9 × 1.75 = 29.6μm. Note that this is the resolution using optimal broadening. From equation 6.62 we see this corresponds to a 9.3kHz B.W. and an applied broadening of 53Hz. In this particular experiment a 350Hz broadening was used to improve the S/N. As a first approximation we might expect a decrease in resolution of (106/403) = 0.26. A more detailed analysis, obtained by simulating the effect on a computer shows a resolution drop of ~1/4.5 - points are resolved when 2 pixels apart if the optimum filter is used and 9 apart with the 350Hz filter. The effect of adding the filter is to improve the S/N by the ratio $(350/53)^{3/2}$ (obtained using equation 6.58, modified for n=0→N), while the increase in bandwidth from 9.3 to 20kHz results in a reduction of $(9.3/20)^{1/2}$ = 0.68 in signal to noise. Combining these factors we obtain a final resolution of

$$\Delta x_{new} = 29.6\mu m \times (53/350)^{3/4} \, (20/9.3)^{1/4} \, 4.5$$

$$= 39\mu m \qquad (9.3)$$

close to the observed value of 36μm.

9.2 Diffusion contrast imaging

A knowledge of molecular self diffusion coefficients enables one to directly probe dynamical processes within a system. Pulsed gradient, spin echo NMR (PGSE NMR) is one of only a few techniques which allow non-invasive measurement of molecular diffusion in systems undergoing Brownian motion. The technique makes measurements on the time scale of tens of milliseconds

and allows self diffusion coefficents as low as $10^{-14}m^2s^{-1}$ to be measured. This corresponds to displacements of around 100nm.

The pulse sequence used to perform PGSE NMR is given in figure 9.16. The 90 and 180° pulses produce a conventional spin echo, the 180° pulse reversing the dephasing of the magnetic moments caused by inhomogeneities in the main field. The addition of the two gradient pulses cause an attenuation in the echo if the nuclei have moved in the time Δ. This arises because rephasing occurs in a different magnetic environment and so is incomplete. The attenuation of the echo may be related to the self diffusion coefficients of the nuclei, and therefore to the molecules they are part of, by using the Stejskal-Tanner equation[34] (see appendix G)

$$A/A_0 = \exp[-\gamma^2G^2D\delta^2(\Delta-\delta/3)] \qquad (9.4)$$

where D is the self diffusion coefficient and G the applied gradient magnitude. By performing a number of experiments with different values of G (or Δ) it is therefore possible to obtain a value for the self diffusion coefficient D. When D is known, as is the case with water[35], this technique may be used to calibrate the applied gradient. This has been done for the x and z imaging gradients. The results are plotted in figure 9.17. The y gradient must be measured using a different technique (described in section 8.8) as it produces insufficient echo attenuation.

In a conventional PGSE NMR experiment the diffusion of a bulk sample is measured. It is implicity assumed that the diffusion coefficient is constant throughout the sample. When dealing with naturally occuring samples, such as plant stems, this is no longer the case as the variety of physical and chemical environments within the sample lead to a range of diffusion coefficients. Normally it would be necessary to remove the region of interest and study it separately. This is necessarily a rather invasive techique and so as an alternative we can perform an imaging experiment on the magnetization in the sample at the time 2τ (figure 9.18a), thereby obtaining a 2-D distribution of attenuations which can be directly related to the spatially dependent self diffusion coefficient function D(x,z).

In its simplest form, such an experiment would require obtaining a number of images with different values of G and then calculating D(x,z) from the attenuation data. Figures 9.19, 9.20, 9.21 and table 9.2 illustrate the results of such an experiment performed on cut slices of wheat grain 1.25mm thick. Selective excitation wasn't available at the time this experiment was carried out, although the pulse sequence in figure 9.18b could now be used. Diffusion was measured along the grain's longitudinal axis, in order to make a comparison with data obtained using radioactive tracer methods[36]. Since the y gradient cannot be used as a diffusion sensing gradient (because of its limited magnitude) it was necessary to mount the grain slice vertically as shown in figure 9.22 and use the z gradient. This meant using the G_y gradient as one of the imaging gradients. The rather odd image shape (when compared to that in figure 9.9) is a

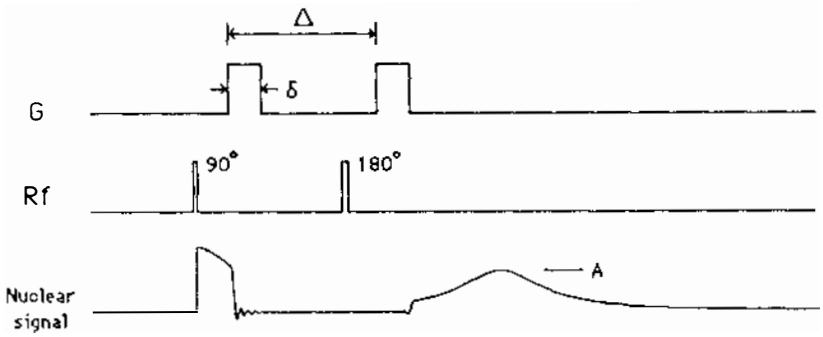

Figure 9.16 Pulse sequence for measuring self diffusion.

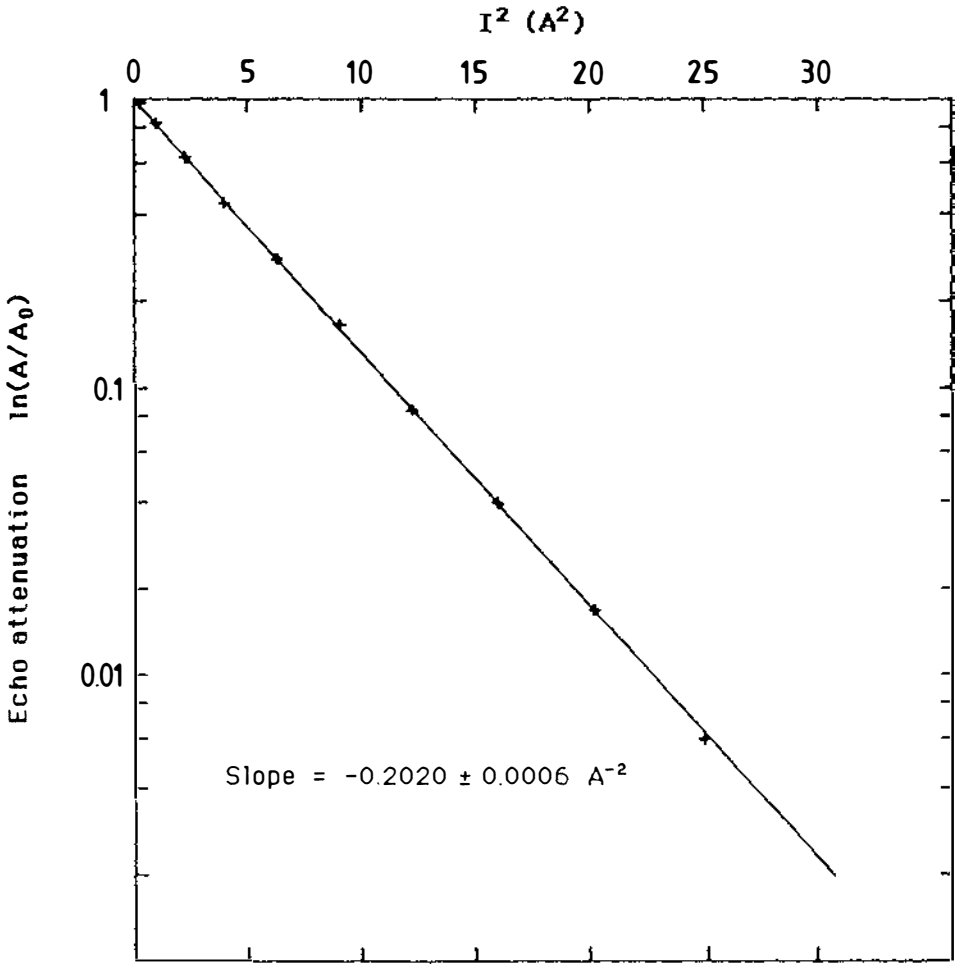

Figure 9.17a Echo attenuation plot for a $CuSO_4$ doped water sample at 29°C using the G_x gradient coil and experimental parameters of $\Delta = 20ms$ and $\delta = 1ms$. The diffusion coefficient of water at 29°C, $(2.547 \pm 0.004) \times 10^{-9}\ m^2 s^{-1}$, has been used with the above attenuation data and equation 9.4 to obtain a value for the applied gradient of $(23.74 \pm 0.06)\ G\ cm^{-1} A^{-1}$.

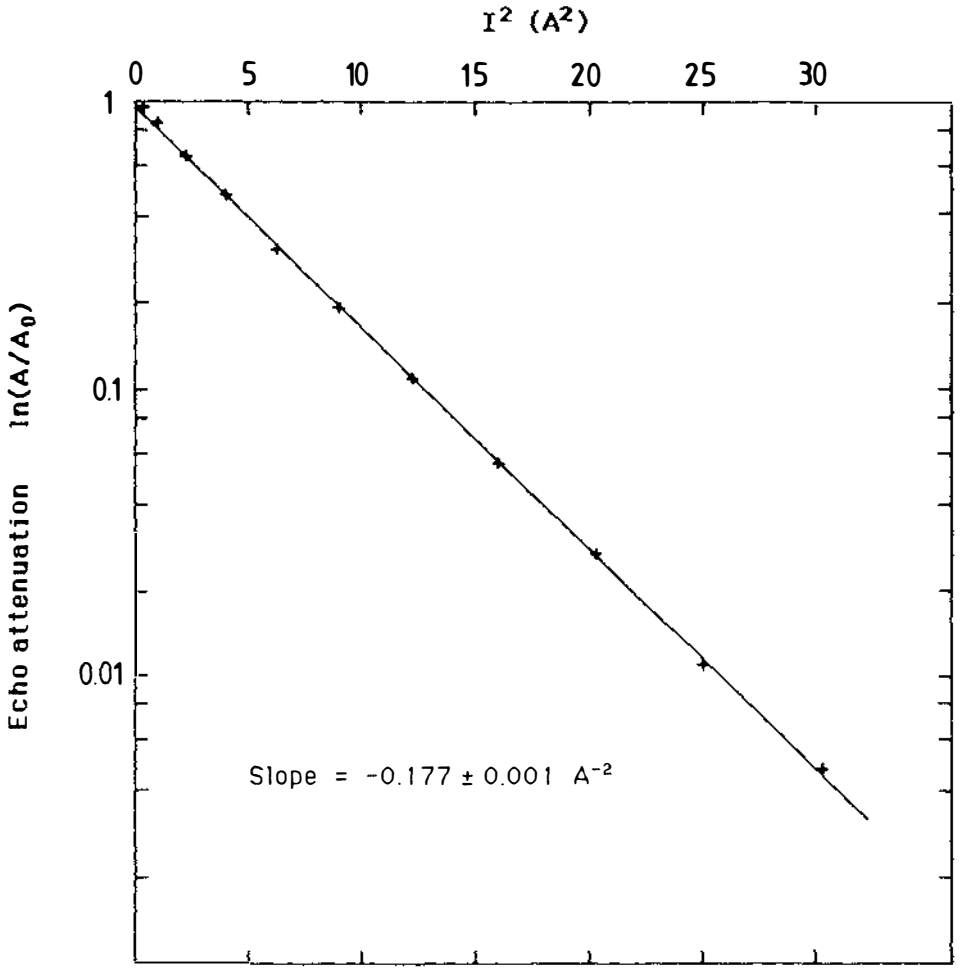

Figure 9.17b Echo attenuation plot for a $CuSO_4$ doped water sample at 29°C using the G_z gradient coil and experimental parameters of $\Delta = 20$ms and $\delta = 1.5$ms. The diffusion coefficient of water at 29°C, $(2.547 \pm 0.004) \times 10^{-9}\ m^2 s^{-1}$, has been used with the above attenuation data and equation 9.4 to obtain a value for the applied gradient of $(14.89 \pm 0.09)\ G\ cm^{-1} A^{-1}$.

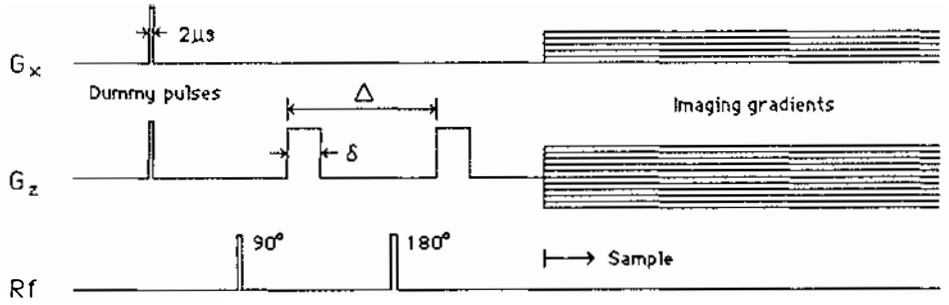

Figure 9.18a Pulse sequence used to perform diffusion contrast imaging.

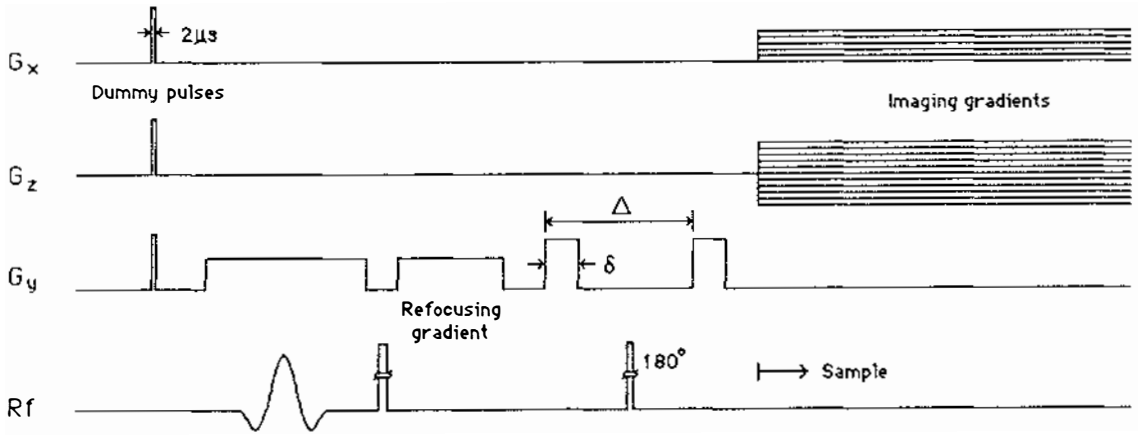

Figure 9.18b Diffusion contrast imaging with slice selection.

Figure 9.19 The NMR image of a transverse section through a wheat grain illustrating the influence of the pulsed gradient sequence given in figure 9.18a. As the magnitude of the gradient pulses are increased, the spin echo amplitude decreases at a rate determined by the local water diffusion rate. Z gradient current values are, from top to bottom, a) $3A^2$; b) $6A^2$; c) $12A^2$; d) $18A^2$.

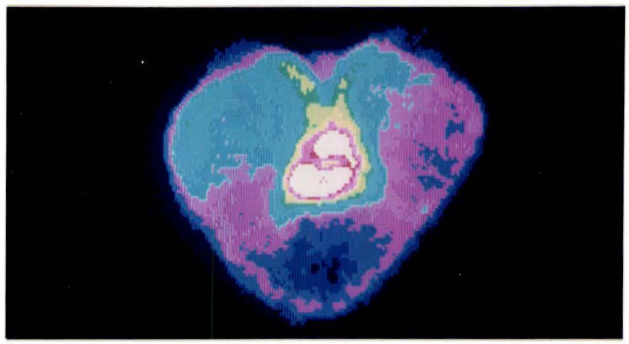

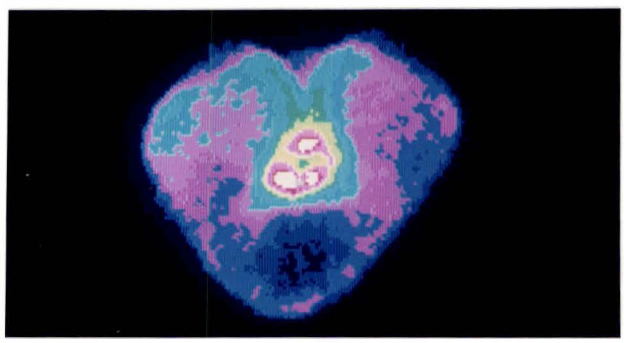

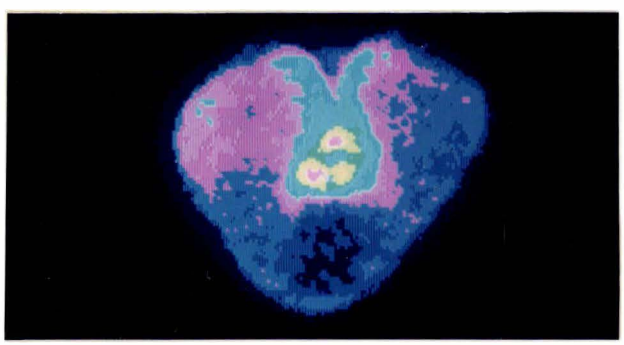

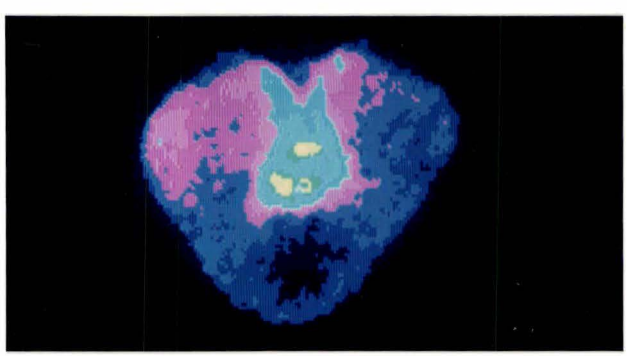

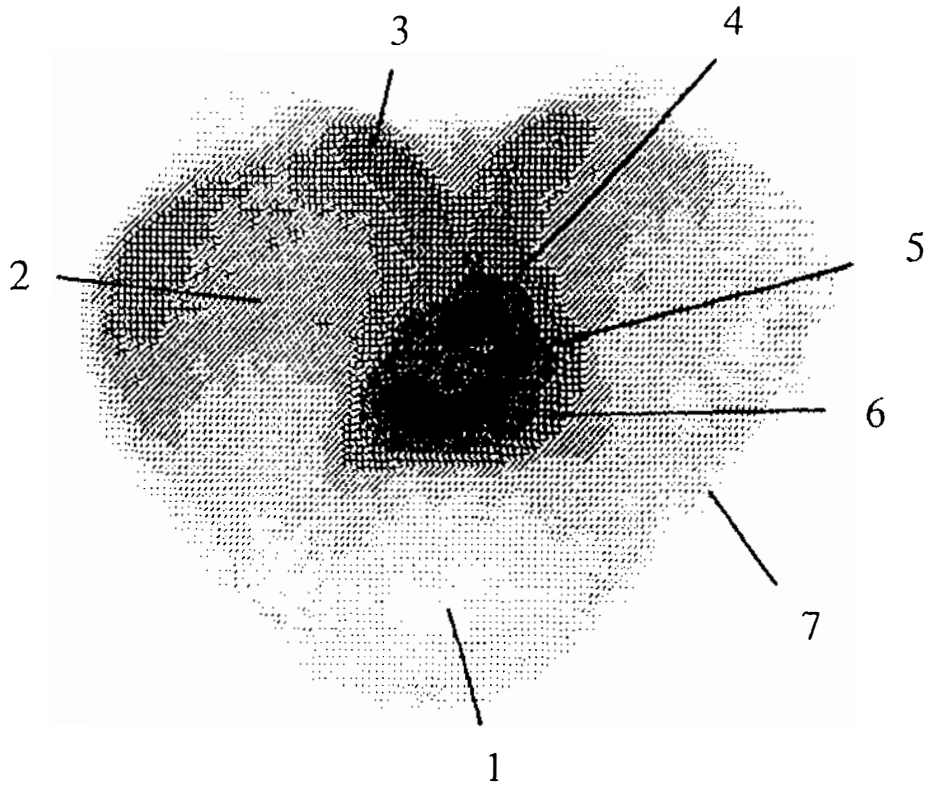

Figure 9.20 Dot matrix image of figure 9.19 indicating the location of those features which have been examined to determine the local diffusion coefficients.

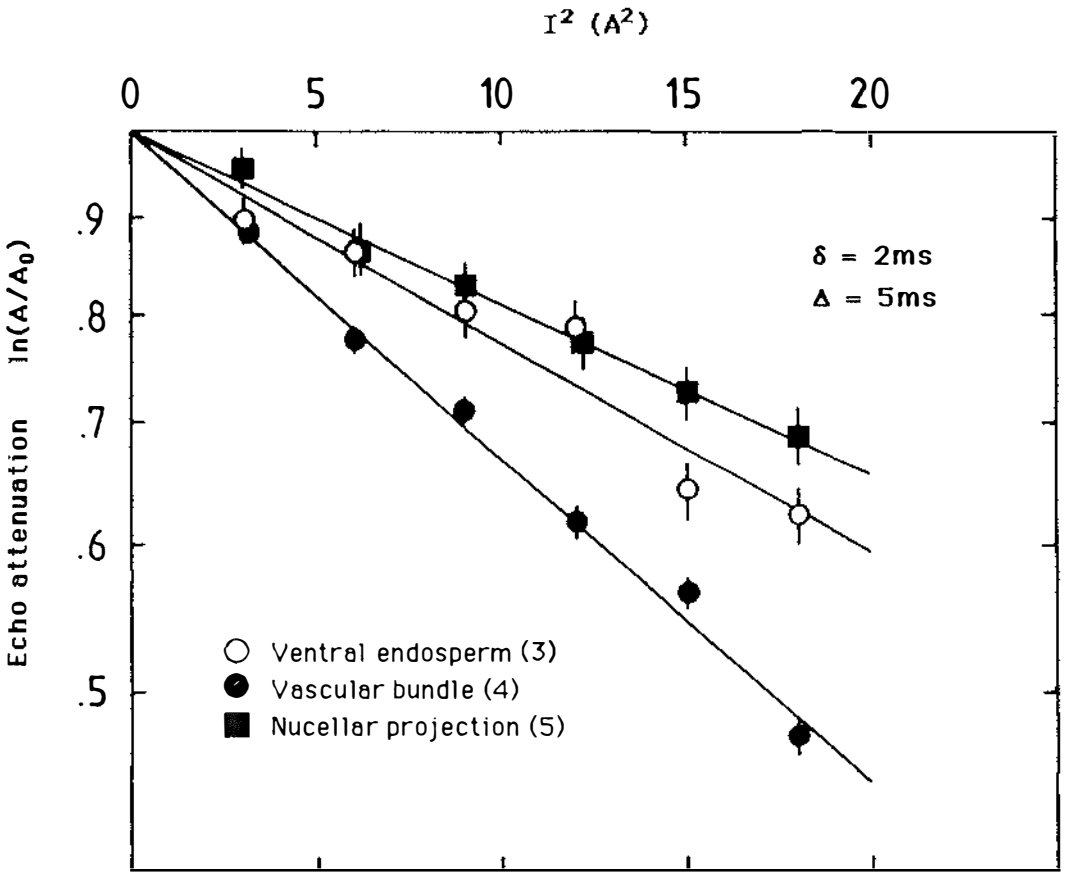

Figure 9.21 Spin echo attenuation plots for regions 3, 4 and 5 showing the exponential dependence of image amplitude on G^2 in accordance with equation 9.4. The self diffusion coefficients obtained are given in table 9.2.

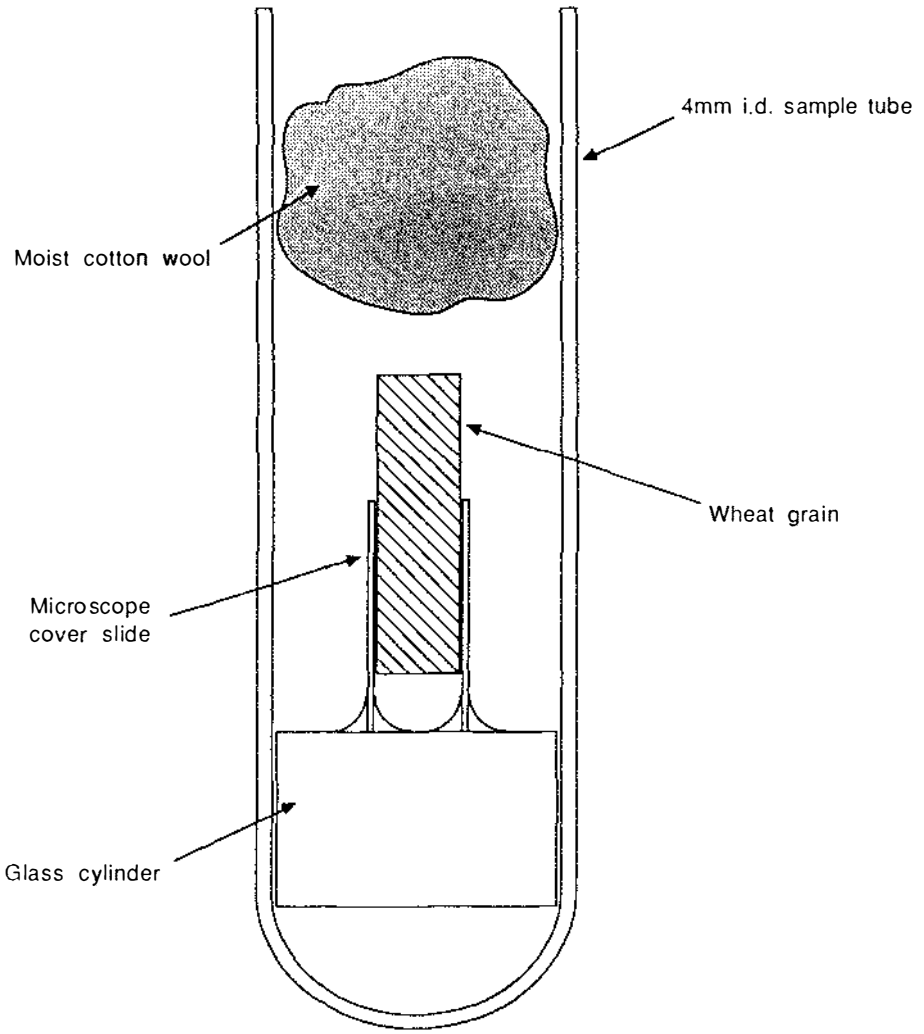

Figure 9.22 Wheat grain mount for diffusion contrast experiment.

consequence of imaging with this rather non-linear gradient. Difficulties were also encountered because of the long rise time of this gradient. This was alleviated to some extent by using a 10kHz bandwidth with a consequent 100μs sampling interval. Despite the narrower bandwidth it was still necessary to switch G_y on 50μs before G_x in order to mimimize phase distortion in the filtered profile.

Even with the enhanced signal to noise ratio obtained by working with a reduced bandwith it was still necessary to image for an hour to offset the insensitivity of the 10mm rf coil used at the time. The total experiment was therefore rather long, taking 4-5 hours to obtain sufficient data from which to calculate diffusion coefficients. The long imaging period proved to be a problem as the cut sample invariably changed shape (due to dehydration), leading to anomalous diffusion coefficients in regions of small area, such as the vascular bundles. This effect was reduced by placing a small piece of cotton wool, saturated with water, above the sample to keep it moist for the duration of the experiment.

Clearly improvements would be seen if a larger, more linear, y gradient were available and if the 5mm rf coil were used. Despite the limitations of these experiments the results shown in table 9.2 are consistent with the average of 6 to $7\times10^{-10}m^2s^{-1}$ obtained by other methods[37] and indicate the potential of this technique for the investigation of spatially dependent self diffusion coefficients.

Table 9.2 Localized water self-diffusion within the wheat grain

Region[1]	Identification[2]	D (10^{-10} m^2 s^{-1})
1	Dorsal endosperm	5±3
2	Cheek endosperm	7.0±0.5
3	Ventral endosperm	7±1
4	Vascular bundle + chalaza	10.1±0.5
5	Nucellar projection	5±2
6	Endosperm cavity	10.6±0.8
7	Aleurone layer + testa + pericarp[3]	9±3

Notes

1) See figure 9.20.

2) The endosperm (regions 1, 2 and 3) is the organ in which starch is deposited; at this stage of development starch comprises about 80% of the wheat grain's dry weight. The outer layer of the endosperm (the aleurone layer), the seed coat (testa) and the wall of the fruit (pericarp) are not resolved and together correspond to region 7. Longitudinal transport of water and solutions of nutrients is provided by the xylem and phloem vessels in vascular bundles scattered through region 4. Nutrients travel from the vascular bundles into the endosperm via the chalaza and nucellar projection (region 5) and through a liquid filled cavity occupying part of region 6.

3) The data corresponding to region 7 is subject to errors associated with defining a consistent region close to the image boundary.

9.3 Restricted diffusion

When the motion of a molecule is restricted by the presence of some solid barrier, such as a cell wall, equation 9.4 no longer holds. As the time scale of the experiment is increased the $\ln(A/A_0)$ vs Δ plot will become non-linear. A simple example of this effect may be seen in figure 9.23 which shows resticted diffusion in a parsnip stem. As Δ is increased a fairly even attenuation is seen across the image, but when Δ becomes large the attenuation of the echo signal in the regions around the edge of the stem exceeds that in the rest of the image. It is clear from this data that the water in the central vascular bundles is suffering restricted diffusion when Δ is greater than ~5ms. Using the Einstein relationship (equation G.11) and a diffusion coefficient of $\sim 10^{-9} m^2 s^{-1}$ it may be deduced that the water molecules giving rise to these signals are trapped within structures of ~5μm in diameter. Measurements of restricted diffusion therefore allow an indirect probe of structure an order of magnitude smaller than those directly visible using the imaging process.

9.4 Relaxation contrast imaging

Aside from proton density and diffusion coefficients there are a variety of other parameters which can be imaged using the NMR technique. Of particular interest in the medical field are those images which contain relaxation information. Quite often images which have little contrast in straight spin density show considerable detail when spin relaxation is used as an imaging parameter. In its simplest form relaxation contrast may be obtained by using a long

Figure 9.23 A series of images showing the effects of restricted diffusion in the parsnip stem. PGSE parameters are, from top to bottom a) Δ=2ms, δ=0ms ; b) Δ=2ms, δ=1ms ; c) Δ=8ms, δ=1ms. Note the minimal attenuation in the central vascular bundles which occurs as Δ is increased. If we assume that the diffusion coefficients of the water in these vascular bundles is similar to those around the periphery then this implies that spins in this region have their motion restricted.

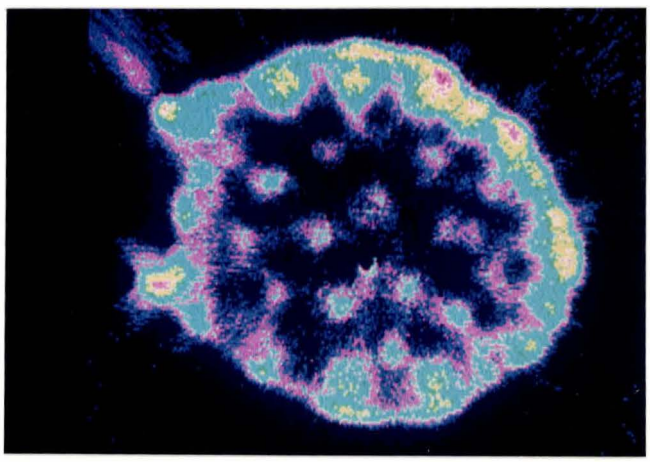

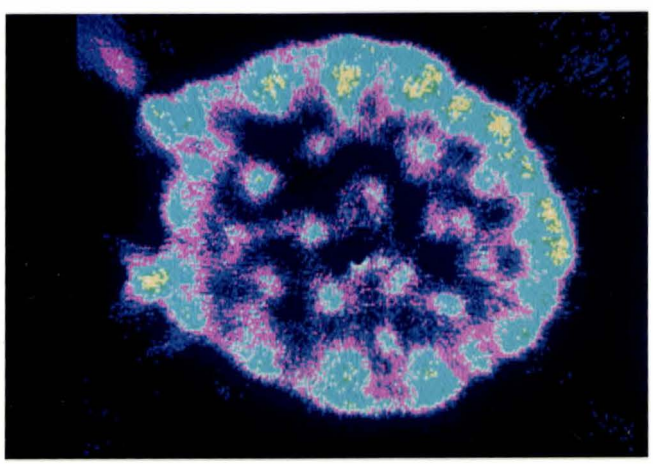

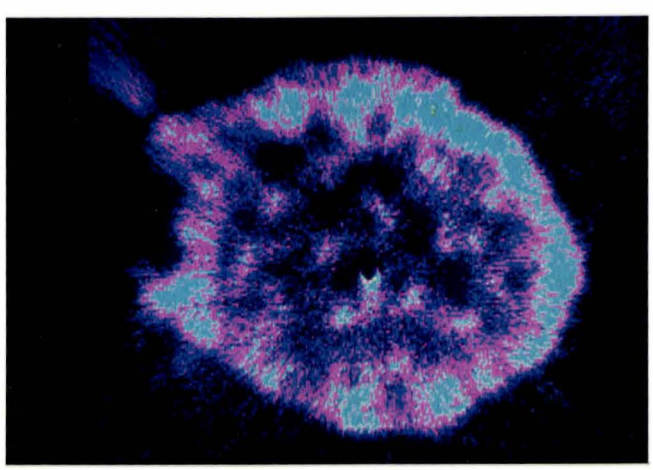

delay between the selective 90° pulse and the refocussing 180° pulse. Those parts of the image with short spin-spin relaxation times will be attenuated with respect to those with longer T_2 values (see figure 9.24 for an example of this technique). More quantitative results may be obtained by performing a series of experiments, in a manner akin to that used in diffusion contrast imaging, from which the attenuation data may be used to determine T_2 as a function of position.

T_1 contrast may be obtained by reducing the experiment repetition time so that those areas with long relaxation times will be selectively attenuated. More quantitative data may be obtained by performing a conventional $180°|_{\pi} - \tau - 90°|_{\pi}$ inversion recovery pulse sequence and imaging after the 90° pulse (see figure 9.25). However, both pulses would have to be spatially selective if slice selection was desired. The relaxation time could again be obtained by analysing attenuations as a function of τ and position.

Figure 9.24 *(top)* The spin echo image (τ=2ms) of a cube of eraser rubber with a 2mm hole drilled through the centre. *(bottom)* A repeat of the above experiment but with the hole filled with water. The water produces a more intense signal because of its longer spin-spin relaxation time.

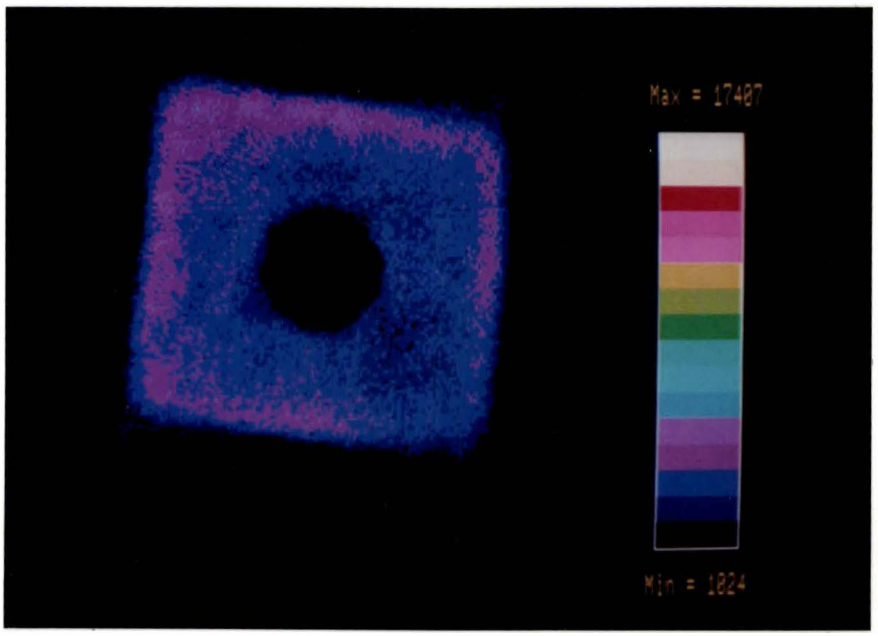
Max = 17407
Min = 1024

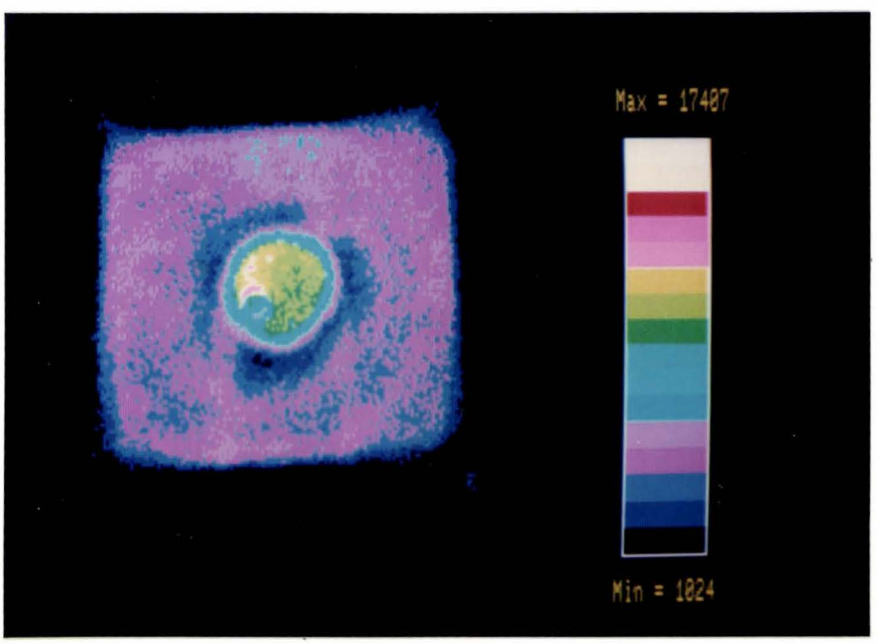
Max = 17407
Min = 1024

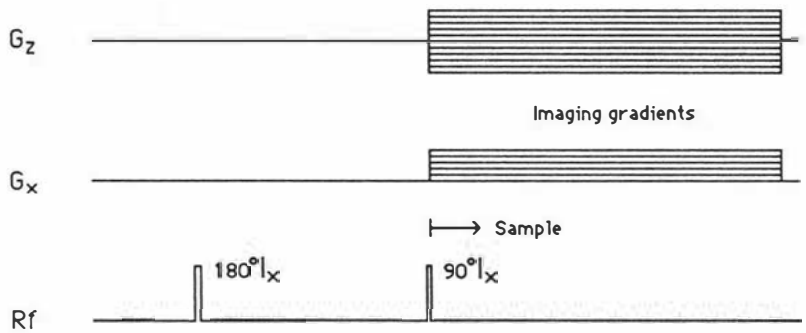

Figure 9.25 T_1 contrast imaging pulse sequence

10 PROPOSED IMAGING EXPERIMENTS

10.1 Flow imaging

Of interest in the microscopic regime is the possibility of imaging bulk fluid flow. This could give valuable information concerning transport processes in plants, which at present can only be studied by means of radioactive labelling techniques. The potential of high spatial resolution combined with completely non-invasive measurement provides a strong incentive for the development this technique.

In its most straightforward implementation, NMR flow imaging would observe the motion of protons - usually those in water. More complex experiments which would allow one to selectively observe the motion of particular molecular species can also be envisaged using excitation techniques discussed in the next section.

The first treatment of flow using PGSE NMR techniques was due to Stejskal[38] who extended the treatment of diffusion measurement to include effects due to bulk transport of matter. The evolution of the self correlation function[39] $P_s(\mathbf{r_0}\,|\,\mathbf{r},t)$ under diffusion and flow is given by

$$\partial P_s/\partial t = \nabla.\mathbf{D}.\nabla P_s - \nabla.\mathbf{v}\,P_s \,. \qquad (10.1)$$

The first term is a more general case of equation 9.4 and includes the possibility of non-isotropic diffusion. $\mathbf{D}$ is the diffusion tensor and has components D_{ij} which take account of diffusion along the i axis due to gradients in P_s along the j axis. The second term is simply an expression of the continuity equation for fluid flow and gives the probability per unit time that a nucleus will pass through unit volume.

For the case of uniform, constant diffusion and a spatially uniform, but time dependent flow, equation 10.1 has the following solution[38]

$$P_s(r_0\,|\,r,t) = (64\pi^3\, D_{xx}\, D_{yy}\, D_{zz}\, t^3)^{-1/2}$$

$$\times \exp\{(x-x_0-S_x)^2/4D_{xx} - (y-y_0-S_y)^2/4D_{yy} - (z-z_0-S_z)^2/4D_{zz}\} \qquad (10.2)$$

where S_x , S_y , and S_z are the components of the fluid displacement vector $\mathbf{S}$. Substituting into equation G.7 Stejskal obtains, in the narrow gradient pulse approximation

$$R(G,\Delta,\delta) = \exp\{ - \gamma^2\delta^2\, \mathbf{G}.\mathbf{D}.\mathbf{G}\,\Delta - j\gamma\delta\mathbf{G}.\mathbf{v}\Delta \}$$

$$= \exp\{ - \gamma^2\delta^2 \mathbf{G.D.G}\,\Delta \}\{\cos(\gamma\delta\mathbf{G.v}\Delta) - j\sin(\gamma\delta\mathbf{G.v}\Delta) \}. \qquad (10.3)$$

It can be seen that in addition to the real attenuation (which for isotropic diffusion is identical to equation 9.4) we also have a complex oscillatory term which depends on the nuclear velocity.

Since the signal is a complex quantity the observed echo amplitude will be

$$\xi = \{M_y - jM_x\}\, R(G,\Delta,\delta) \qquad (10.4)$$

For a correctly phased spectrometer and a $90°|_x - \tau - 180°|_y$ spin echo, M_x will be zero and so our signal will have the peak value

$$\xi = M_y \exp\{ - \gamma^2\delta^2 \mathbf{G.D.G}\,\Delta \}\{ \cos(\gamma\delta\mathbf{G.v}\Delta) - j\sin(\gamma\delta\mathbf{G.v}\Delta) \}$$

The echo amplitude should therefore look something like figure 10.1 when plotted against Δ. It is clear from equation 10.5 that if diffusion produces a significant attenuation then a series of experiments which vary Δ rather than G will provide a more accurate assessment of **v**.

A flow imaging experiment would work along the same lines as that used in the diffusion work, except that more experiments would have to be performed to unambiguously determine the flow velocity, due to the sinusoidal nature of the attenuation function. The most accurate way of determining the magnitude of **v** would be to Fourier transform the attenuation function with respect to Δ. A peak would then be observed at the frequency $\gamma\delta\mathbf{G.v}/2\pi$ with a broadening determined by the self diffusive motion.

All the imaging techniques described so far (relaxation, diffusion and flow) require that a number of images be produced from which the required data can be extracted. Due to memory limitation in the graphics computer it is currently necessary to do this extraction by hand. Clearly it would be more efficient if an image of the appropriate parameter could be produced in one experiment.

10.2 Chemical shift imaging

It was mentioned in chapter 1 that the resonant frequency of a nucleus is modified by its local chemical environment. The spectra from even moderately complex molecules contain a wealth of information which can give insights into the overall electronic configuration of a molecule. On a more mundane level chemical shift information can be used as a "finger print" for identification purposes.

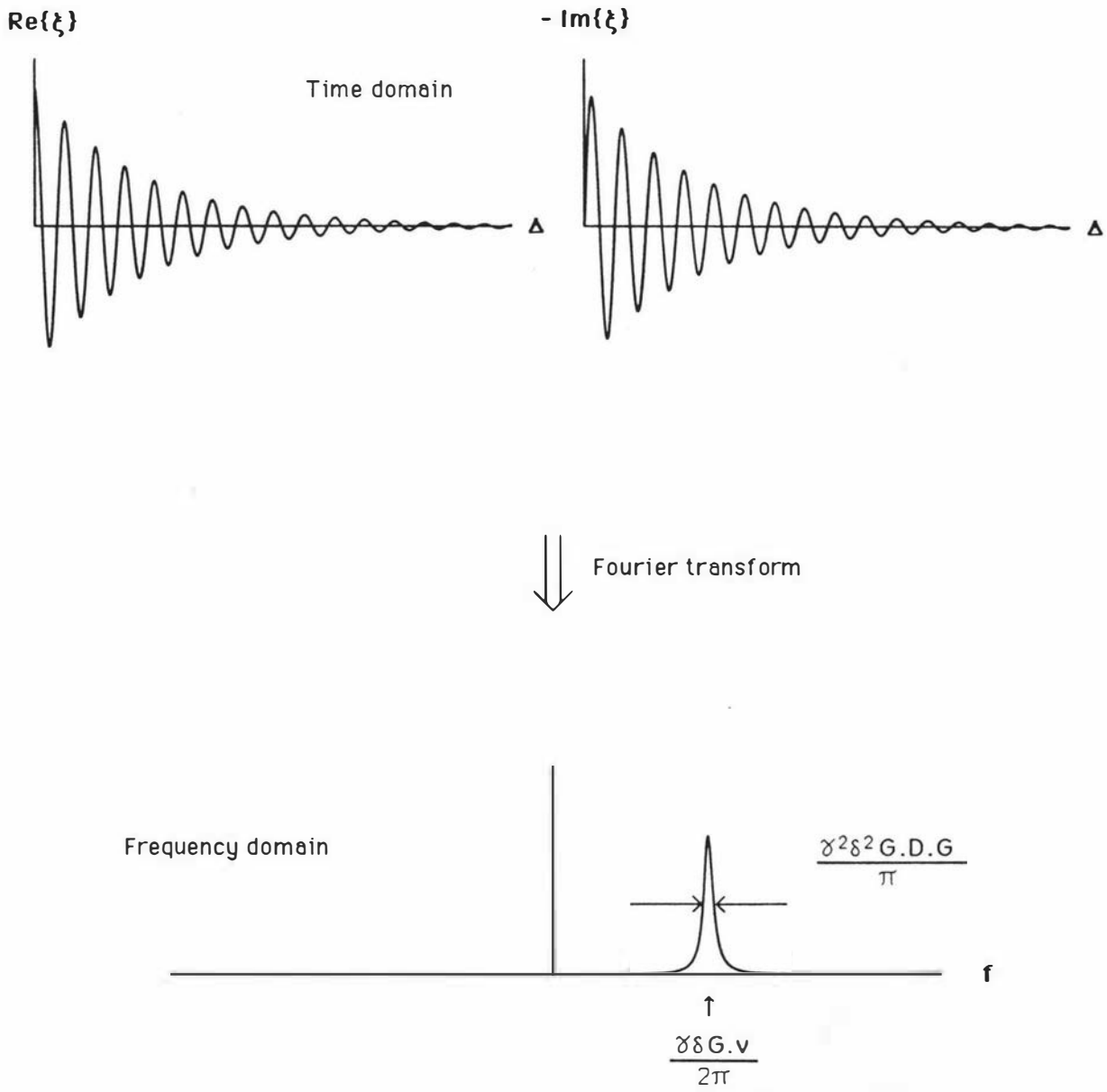

Figure 10.1 Fluid flow velocity measurment using the PGSE technique.

Normal spectroscopy obtains the data from the bulk sample - no spatial differentiation is obtained. An imaging technique which could produce spectroscopic data as a function of position would be very useful. A variety of methods have been suggested, and a few demonstrated, which would allow chemical shift information to be imaged. They fall into three catagories . In the first, termed selective volume excitation spectroscopy[40], a small volume within the sample is selectively excited. The subsequent nuclear signal is observed in the absence of a gradient and so can be used to obtain high resolution spectra. Although not really an imaging technique in the normal sense it does have the advantage that sophisticated data analysis is unecessary and results can be obtained rapidly.

The second technique - often called four dimensional imaging, is due to Hall et al. [41], and uses the pulse sequence in figure 10.2. During the experiment the gradients are adjusted so as to sample a lattice of points in k space. Each experiment produces a free induction decay, for times greater than τ, which can be Fourier transformed to produce a high resolution spectrum. The signal obtained has the form (for $t>\tau$)

$$\xi(t,\mathbf{G}) = \int_V \rho(\mathbf{r}) \exp(-\gamma \mathbf{G}.\mathbf{r}\, t) \int_{-\infty}^{\infty} g(\nu,\mathbf{r}) \exp(-j2\pi\nu t)\, d\nu\, dV \qquad (10.6)$$

where $g(\nu,\mathbf{r})$ is the spectral profile for the free induction decay produced by the molecules at point $\mathbf{r}$ and $\mathbf{G}$ is the net gradient vector applied during the time $0\rightarrow\tau$.

The first step in reconstruction is to Fourier transform this signal with respect to t to obtain

$$\xi(\nu,\mathbf{G}) = \int_V \rho(\mathbf{r}) \exp(-\gamma \mathbf{G}.\mathbf{r}\, t)\; g(\nu,\mathbf{r})\, dV. \qquad (10.7)$$

When k space has been completely sampled, data with constant frequency offsets ν can be Fourier transformed with respect to $\mathbf{r}$ to obtain

$$\xi(\nu,\mathbf{r}) = \rho(\mathbf{r})\; g(\nu,\mathbf{r}) \qquad (10.8)$$

which is the desired function. The disadvantage of this technique is the time required to obtain the data and the amount of memory space required to store it. A 128×128 image with 128 points in the frequency domain per positional coordinate would require 128^3 words of memory and several hours of data accumulation time[41] (at the very least).

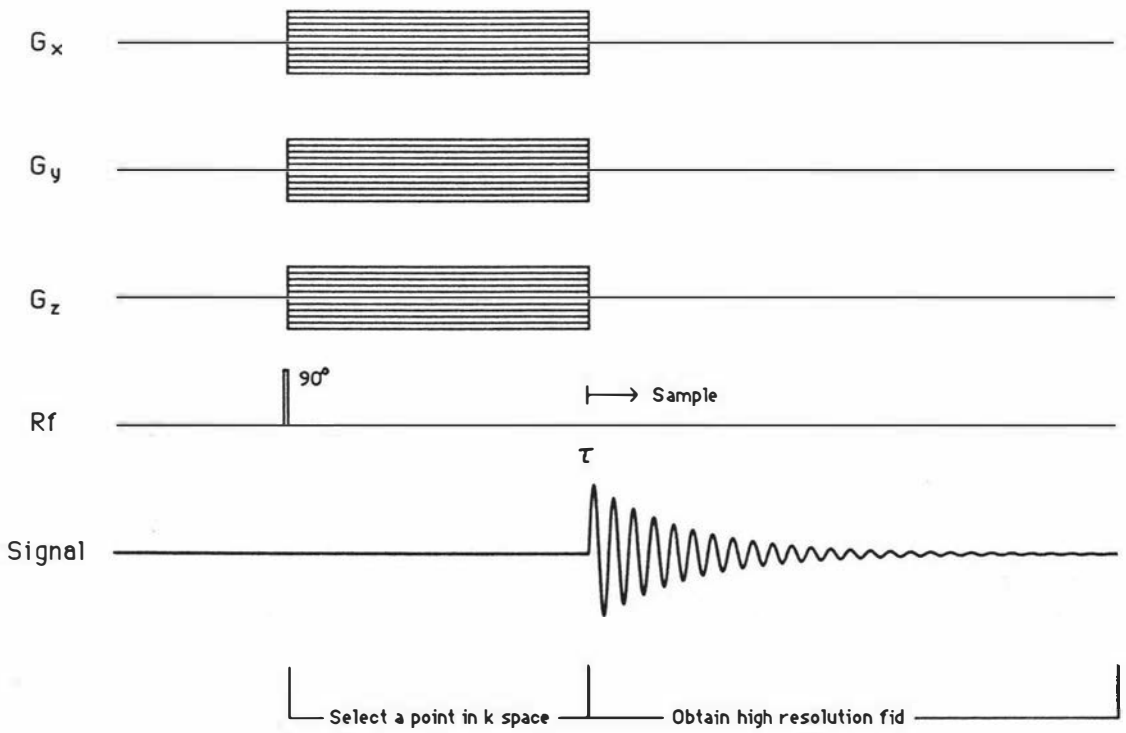

Figure 10.2 4-D chemical shift imaging pulse sequence used by Hall. If only 2-D spatial information is required G_y can be used to selectively excite a slice of spins in the usual manner.

The third technique, frequency selective excitation, is attractive when differentiation of only a few spectral lines is required (typically the case in medical imaging). Selective excitation is achieved by the application of a broad ("soft") 90° pulse at the resonant frequency of the line of interest. Various, rather complicated pulse schemes, such as STEAM[42], have been invented to allow simultaneous slice and frequency selection. One advantage of these techniques is that data from more than one spectral profile can be obtained in a single repetition time since different nuclei are being stimulated in each case.

Alternatively one can perform selective saturation experiments[43] in which certain spectral lines are excited with a soft 90° pulse and then allowed to dephase. The line of interest is left unaffected by this process (see figure 10.3). This technique can only look at one line at a time since it is necessary to wait times of order T_1 to allow the saturated spins in re-equillibrate.

10.3 Imaging of the self correlation function $P_s(r,r_0)$

In many complex molecular systems it would be of interest to directly measure the function $P_s(\mathbf{r}\,|\,\mathbf{r_0},\Delta)$ - particulary in those cases where it is suspected that Gaussian statistics can no longer be assumed, e.g. when a particle is undergoing restricted diffusion. We see from equation G.7 that the attenuation of the PGSE is given by the Fourier transform of P_s . To obtain P_s we therefore need to sample k space so as to obtain an attenuation $R(\mathbf{G},\delta,\Delta)\equiv R(\mathbf{k},\Delta)$ for each point. A two dimensional Fourier transform can then be applied to produce $P_s(\mathbf{r}\,|\,\mathbf{r_0},\Delta)$. Since only one point in k space is determined per experiment it would be necessary to limit the number of points in the final image to perhaps 32^2.

By varying Δ between successive experiments it would be possible to see P_s develop with time. For example, if our sample consisted of a thin film of water between two lamellar boundaries, we would expect a narrow Gaussian for short times Δ, which became progressively broader as Δ was increased. As Δ became very large the sides would flatten and for $\Delta\rightarrow\infty$ we would have a triangular function.

The advantage of this sort of experiment over the normal method described in section 9.2 is that it gives a two dimensional picture of the diffusion process and so is not limited by assumptions made concerning the statistics of the molecular motion.

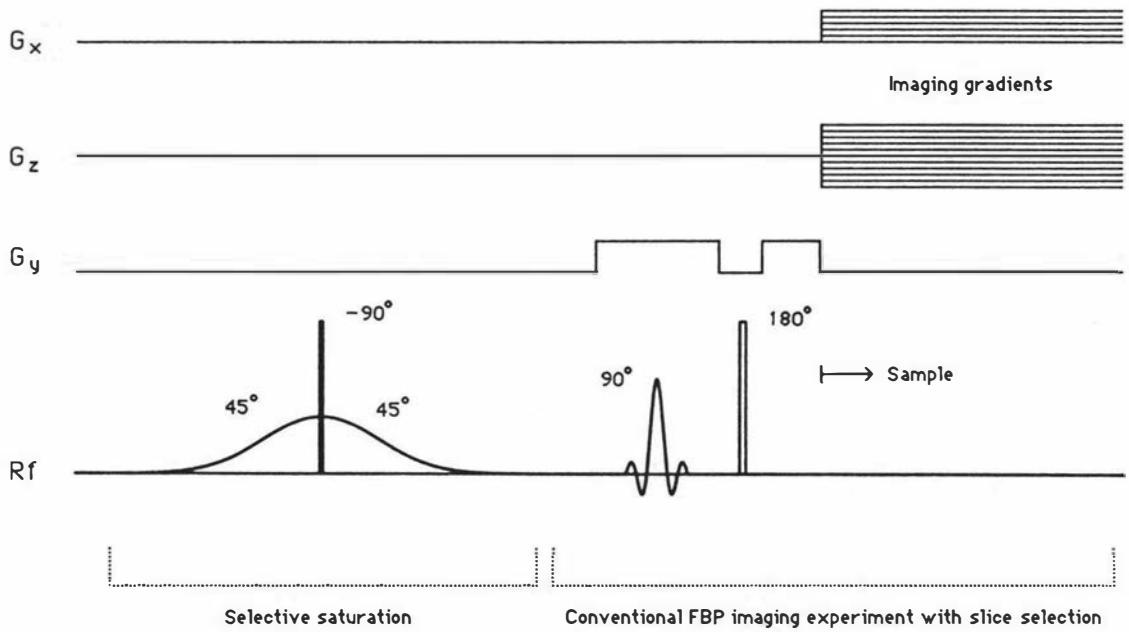

Figure 10.3 A modification of Axel and Dougherty's selective saturation experiment which performs chemical shift imaging using FBP. The composite selective saturation pulse leaves the spins producing the desired spectral line unaffected whilst tipping all others through 90°. By the time the imaging experiment starts the magnetization due to these spins will have completely dephased and so only those nuclei resonating at the desired frequency will be imaged.

11 SUMMARY AND CONCLUSIONS

This work has described the modification of a commercial NMR spectrometer to perform high spatial resolution NMR imaging on samples smaller than 10mm. Voxel resolutions of around 120μm have been reported while theoretical calculations indicate that this could be reduced to ~50μm in the ideal case.

An analysis of the two most commonly used imaging techniques show that filtered back projection is more sensitive than Fourier zeugmatography, particulary when dealing with samples having short T_2 values.

A fundamental limitation to the resolution is the available signal to noise ratio. Beyond optimizing the detection system, this can only be improved by employing higher Larmor frequencies. The present work was performed on a 60MHz (1.4T magnet) apparatus and when first reported[44] (see appendix I) in June 1986, represented an improvement of a factor of 5 over previously published voxel resolutions[5]. In July 1986 Aguayo et al.[45] reported a voxel resolution of 30μm obtained using a 400MHz machine.

Despite the limitations of the magnetic field, the present work has established the potential of NMR microscopy and quantified the factors which determine resolution. The demonstration of diffusion contrast microscopy is novel and illustrates the potential of NMR microscopy, even at low fields, in the measurment of local molecular dynamics. The wheat grain study has clearly demonstrated the application of the method in plant physiology. The potential of the technique to measure both diffusion and flow of water and nutrients in intact plant tissue is apparent.

APPENDIX A

A Runge-Kutta algorithm for solving the Bloch equations

We need an algorithm which can solve the coupled partial differential equations

$$\begin{aligned} \partial M_x/\partial t &= \gamma\{M_y B_z - M_z B_y\} - M_x/T_2 \\ \partial M_y/\partial t &= \gamma\{M_z B_x - M_x B_z\} - M_y/T_2 \\ \partial M_z/\partial t &= \gamma\{M_x B_y - M_y B_x\} - (M_z - M_0)/T_1 \end{aligned} \qquad (A.1)$$

using numerical techniques. Given an initial magnetization vector **M** at time t we wish to determine its magnitude and direction at time t+Δt. This process may then be iteratively applied to determine the function **M**(t) for all times of interest.

The procedure on which the following program is based is the fourth order Runge-Kutta algorithm which is normally presented in the following form:

Given an initial value problem $y' = f(x,y)$, $y(x_0) = y_0$ find y for $x > x_0$. Given the initial value y_n we calculate the four auxillary quantities A_n, B_n, C_n, D_n to find the new value y_{n+1}, where

$$\begin{aligned} A_n &= h\, f(x_n, y_n) \\ B_n &= h\, f(x_n + 0.5h,\ y_n + 0.5\, A_n) \\ C_n &= h\, f(x_n + 0.5h,\ y_n + 0.5\, B_n) \\ D_n &= h\, f(x_n + h,\ y_n + C_n) \end{aligned} \qquad (A.2)$$

and

$$y_{n+1} = y_n + (A_n + 2B_n + 2C_n + D_n)/6$$

y_{n+1} is then an approximation of $y(x_{n+1})$ where $x_{n+1} = x_0 + (n+1)h$. This algorithm can be modified to solve equation A.1 by noting that A.1 has the form $\partial M_i/\partial t = f_i(M_x, M_y, M_z)$. A.2 therefore becomes

$$\begin{aligned} A_{in} &= h\, f_i(M_x, M_y, M_z) \\ B_{in} &= h\, f_i(M_x + 0.5A_{xn},\ M_y + 0.5A_{yn},\ M_z + 0.5A_{zn}) \\ C_{in} &= h\, f_i(M_x + 0.5B_{xn},\ M_y + 0.5B_{yn},\ M_z + 0.5B_{zn}) \\ D_{in} &= h\, f_i(M_x + C_{xn},\ M_y + C_{yn},\ M_z + C_{zn}) \end{aligned} \qquad (A.3)$$

and

$$M_{i(n+1)} = M_{i(n)} + (A_{in} + 2B_{in} + 2C_{in} + D_{in})/6$$

where i can be x, y or z and h is the step interval for time t i.e. $t_{n+1} = t_0 + (n+1)h$.

Table A.1 is a listing of this algorithm which has been coded in BASIC. This particular version determines the response to a 90° rf pulse. Line 280 initialises the magnetization components to their equilibrium values while line 290 sets the B_x (B_1) field to a value which gives a 20μs 90° pulse. Line 300 sets T_1 = 1s, T_2=80μs and h, the time step, to 1μs. The main program, lines 310→410 calculates the new values of M_x, M_y and M_z for each step in time by calling the Runge-Kutta algorithm on lines 1000→1370. This process is then repeated with the results of each intermediate step being recorded in the arrays MXA, MYA, MZA. This data may then be plotted to produce the result shown in figure A.1. More complex pulse sequences (such as those used to generate the data in section 3.2) may be obtained by rewriting the main program to follow the various gradient and rf level changes (see table A.2). The routine in table A.3 simulates spin echo formation by following the motion of a large number of spins each of which experience a slightly different local field. Results are presented in figure A.2 for a $90°|_x - 180°|_y$ pulse sequence.

Table A.1

```
100 '
110 ' Program to simulate the response of a group of spins
120 ' to a 90 degree, 20us, rf pulse. (T1=1s, T2=80us).
130 '
140 DIM MXA(1000),MYA(1000),MZA(1000)

150 '
160 ' Bloch equations
170 '
180 DEF FNFX(MX,MY,MZ)=GAMMA*(MY*BZ-MZ*BY)-MX/T2
190 DEF FNFY(MX,MY,MZ)=GAMMA*(MZ*BX-MX*BZ)-MY/T2
200 DEF FNFZ(MX,MY,MZ)=GAMMA*(MX*BY-MY*BX)-(MZ-M0)/T1

210 '
220 ' Constants
230 '
240 GAMMA=2.6752E+08
250 '
260 '  Initialise variables
270 '
280 MX=0:MY=0:MZ=1:N=0
290 BX=2.935848E-04:BY=0:BZ=0
300 T1=1:T2=.00008:H=.000001

310 '
320 ' Main program
330 '
340 FOR T=0 TO .0005 STEP H
350    IF T>.00002 THEN BX=0
360    MXA(N)=MX:MYA(N)=MY:MZA(N)=MZ
370    N=N+1
380    GOSUB 1000:' Runge-Kutta
390 NEXT T
400 GOSUB 2000:' Plot data
410 END

1000 '
1010 ' Runge-Kutta Algorithm
1020 '
1030 ANX=FNFX(MX,MY,MZ)
1040 ANY=FNFY(MX,MY,MZ)
1050 ANZ=FNFZ(MX,MY,MZ)
1060 '
1070 XARG=MX+.5*H*ANX
1080 YARG=MY+.5*H*ANY
1090 ZARG=MZ+.5*H*ANZ
1100 '
1110 BNX=FNFX(XARG,YARG,ZARG)
1120 BNY=FNFY(XARG,YARG,ZARG)
1130 BNZ=FNFZ(XARG,YARG,ZARG)
```

```
1140 '
1150 XARG=MX+.5*H*BNX
1160 YARG=MY+.5*H*BNY
1170 ZARG=MZ+.5*H*BNZ
1180 '
1190 CNX=FNFX(XARG,YARG,ZARG)
1200 CNY=FNFY(XARG,YARG,ZARG)
1210 CNZ=FNFZ(XARG,YARG,ZARG)
1220 '
1230 XARG=MX+H*CNX
1240 YARG=MY+H*CNY
1250 ZARG=MZ+H*CNZ
1260 '
1270 DNX=FNFX(XARG,YARG,ZARG)
1280 DNY=FNFY(XARG,YARG,ZARG)
1290 DNZ=FNFZ(XARG,YARG,ZARG)
1300 '
1310 MXN=MX+H*(ANX+2*BNX+2*CNX+DNX)/6
1320 MYN=MY+H*(ANY+2*BNY+2*CNY+DNY)/6
1330 MZN=MZ+H*(ANZ+2*BNZ+2*CNZ+DNZ)/6
1340 '
1350 MX=MXN:MY=MYN:MZ=MZN
1360 '
1370 RETURN
```

Table A.2

```
100 '
110 ' Program to determine the motion of the y magnetization
120 ' vector following a 30 degree selective sinc pulse.
130 '
140 DIM MXA(1000),MYA(1000),MZA(1000)

150 '
160 ' Bloch equations
170 '
180 DEF FNFX(MX,MY,MZ)=GAMMA*(MY*BZ-MZ*BY)-MX/T2
190 DEF FNFY(MX,MY,MZ)=GAMMA*(MZ*BX-MX*BZ)-MY/T2
200 DEF FNFZ(MX,MY,MZ)=GAMMA*(MX*BY-MY*BX)-(MZ-M0)/T1

210 '
220 ' Constants
230 '
240 GAMMA=2.6752E+08:PI=3.1415927#
250 '
260 '  Initialise variables
270 '
280 TAU=.0015:H=.000005:DEL=1E-09
290 MX=0:MY=0:MZ=1
```

```
300 '
310 ' Main program
320 '
330 FOR Z=.00026 TO .004 STEP .00002
340    FOR T=0 TO .003-H  STEP H
350       BX=.000003671464#*SIN(3*PI*(T-TAU+DEL)/TAU)/(3*PI*(T-TAU+DEL)/TAU)
360       BY=0:BZ=.02844*Z
370       GOSUB 1000:' Runge-Kutta
380    NEXT T
390    FOR T=.003 TO .0045-H STEP H
400       BX=0:BY=0:BZ=-.02844*Z
410       GOSUB 1000:' Runge-Kutta
420    NEXT T
430    MXA(N)=MX:MYA(N)=MY:MZA(N)=MZ
440    N=N+1
450 NEXT Z
460 GOSUB 2000:' Plot data
470 END
```

Table A.3

```
100 '
110 ' Program to simulate the formation of a spin echo by coadding the response
120 ' of 500 spins, each of which experiences a slightly different main field.
130 '
140 DIM MXA(1000),MYA(1000),MZA(1000),IBZ(500)

150 '
160 ' Bloch equations
170 '
180 DEF FNFX(MX,MY,MZ)=GAMMA*(MY*BZ-MZ*BY)-MX/T2
190 DEF FNFY(MX,MY,MZ)=GAMMA*(MZ*BX-MX*BZ)-MY/T2
200 DEF FNFZ(MX,MY,MZ)=GAMMA*(MX*BY-MY*BX)-(MZ-M0)/T1

210 '
220 ' Constants
230 '
240 GAMMA=2.6752E+08
250 GOSUB 800: ' Define inhomogeneous field
260 '
270 '  Initialise variables
280 '
290 BX=2.935848E-04:BY=0:BZ=0

300 '
310 ' Main program
320 '
330 FOR SPIN=1 TO 500
340 MX=0:MY=0:MZ=1:N=0
350    FOR T=0 TO .0004 STEP H
360       IF N<5 THEN BX=1.174339E-03  ELSE BX=0
370       IF N>=100 AND N<110 THEN BY=1.174339E-03  ELSE BY=0
```

```
380        IF N<5 OR (N>=100 AND N<110) THEN BZ=0 ELSE BZ=IBZ(SPIN)
390        MYA(N)=MY+MYA(N)
400        N=N+1
410        GOSUB 1000:' Runge-Kutta
420     NEXT T
430 NEXT SPIN
440 GOSUB 2000:' Plot data
450 END

800 '
810 ' Generate an array of random numbers having
820 ' a Gaussian probability distribution
830 '
840 INPUT"Enter standard deviation of inhomgeneity (in Tesla)";SD
850 RANDOMIZE
860 FOR I=0 TO 500
870     AMP=-SD*LOG(RND(1)+9.999999E-21)
880     IF INT(RND(1)+.5)=1 THEN SIGN=1 ELSE SIGN=-1
890     IBZ(I)=AMP*SIGN
900 NEXT I
910 RETURN
```

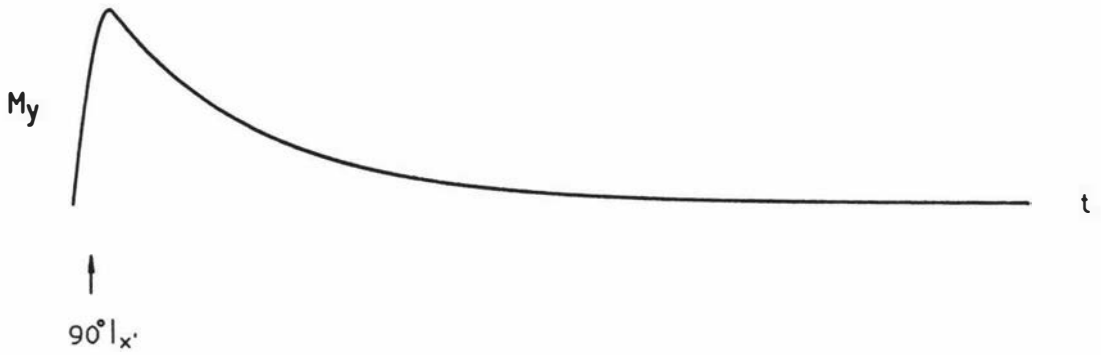

Figure A.1 The simulated response to a 90° rf pulse obtained as a result of running the program in table A.1

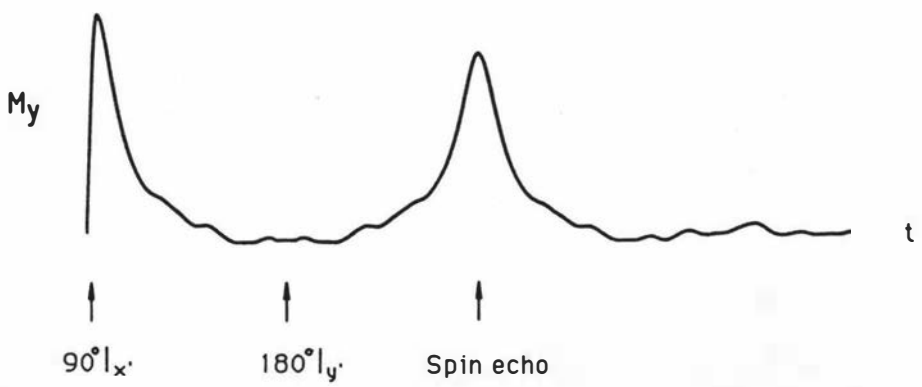

Figure A.2 The simulated response of 500 spins to a $90°I_x - \tau - 180°I_y$ pulse sequence. The decay is caused by inhomogeneities in the main field. Refer to table A.2 for details.

APPENDIX B

THE FAST FOURIER TRANSFORM

Many of the image reconstruction techniques discussed in this work make use of the fast Fourier transform. A description of this algorithm will now be presented.

First we must consider the relationship between the continuous Fourier transform and the corresponding transform obtained using discrete time and frequency intervals - the discrete Fourier transform. First we have the continuous transform

$$S_f(f) = \int_{-\infty}^{\infty} S_t(t) \exp(-j2\pi ft)dt \qquad (B.1)$$

where S_t and S_f represent time and frequency domain data respectively.

To obtain the discrete Fourier transform we make the following substitutions

$$t = n\delta t \qquad 0 \le n < N$$
$$f = m\delta f \qquad 0 \le m < N$$
$$T = N\delta t$$
$$\Delta f = N\delta f$$

where N is the total number of data points in the two domains, T the total sampling time and Δf the frequency bandwidth.

If the integral in equation B.1 is replaced by a summation these relationships may be used to obtain the following expression

$$S_f(m\delta f) = \sum_{n=0}^{N-1} S_t(n\delta t) \exp\{-j2\pi nm\delta t\delta f\} \delta t. \qquad (B.2)$$

If we arbitrarily set $\delta t=1$ then we have

$$S_f(m/N) = \sum_{n=0}^{N-1} S_t(n)\ \exp\{-j2\pi nm/N\} \qquad (B.3)$$

since $\Delta f = 1/\delta t = 1$.

The inverse discrete Fourier transform may be obtained in the following manner. First we multiply both sides of equation B.3 by the function $\exp\{j2\pi n'm/N\}$ to give

$$S_f(m/N)\exp\{j2\pi n'm/N\} = \sum_{n=0}^{N-1} S_t(n)\ \exp\{j2\pi(n'-n)m/N\}. \qquad (B.4)$$

Summing both sides with respect to m we obtain

$$\sum_{m=0}^{N-1} S_f(m/N)\exp\{j2\pi n'm/N\} = \sum_{m=0}^{N-1}\sum_{n=0}^{N-1} S_t(n)\ \exp\{j2\pi(n'-n)m/N\}.$$

$$= \sum_{n=0}^{N-1} S_t(n)\,\delta_{n'n}\,N$$

$$= S_t(n')\,N. \qquad (B.5)$$

Or

$$S_t(n) = N^{-1}\sum_{m=0}^{N-1} S_f(m/N)\exp\{j2\pi nm/N\} \qquad (B.6)$$

which is the desired result.

Equation B.3 may be expanded giving

$$S_f(m/N) = \sum_{n=0}^{N-1} [\, Re\{S_t(n)\} \cos(2\pi nm/N) + Im\{S_t(n)\} \sin(2\pi nm/N)]$$

$$+ j \sum_{n=0}^{N-1} [\, Im\{S_t(n) \cos(2\pi nm/N) - Re\{S_t(n)\} \sin(2\pi nm/N)]. \qquad (B.7)$$

To obtain this result requires $4N^2$ multiplications, $2N^2$ additions and $2N^2$ trig. function calculations (usually obtained from a look-up table). Of these the multiplications dominate the computation time and so we have a computation time t_c where

$$t_c \approx 4N^2 t_x \qquad (B.8)$$

t_x being the time required to perform a multiplication.

For large values of N the computation time will become very long and for small personal computers, it becomes time consuming to calculate the DFT for N greater than about 64. (for example it takes the Hitachi p.c. ~20 seconds to evaluate the DFT in equation B.7 when N=256).

The Cooley-Tukey algorithm[46] reduces the amount of computational effort required by factoring equation B.3. Using this method the computation time becomes

$$t_c \approx N \log_2 N \, t_x \qquad (B.9)$$

which results in a substantial reduction in computation times for large N.

The Cooley-Tukey algorithm

Let us represent $\exp(-j2\pi nm/N)$ as $W(nm)$. Equation B.3 may then be reexpressed as

$$S_f(m/N) = \sum_{n=0}^{N-1} S_t(n)\, W(nm). \qquad (B.10)$$

Let us suppose that N is some power of 2 i.e.

$$N = 2^p \qquad (B.11)$$

Then the summation can be rewritten as

$$S_f(m/N) = \sum_{n_0=0}^{1} \sum_{n_1=0}^{1} \sum_{n_2=0}^{1} \ldots \sum_{n_{p-1}=0}^{1} S_t(n)\, W(nm) \qquad (B.12)$$

where n and m are now represented by the binary numbers

$$n = n_{p-1}\, 2^{p-1} + n_{p-2}\, 2^{p-2} + n_{p-3}\, 2^{p-3} + \ldots + n_0$$

and (B.13)

$$m = m_{p-1}\, 2^{p-1} + m_{p-2}\, 2^{p-2} + m_{p-3}\, 2^{p-3} + \ldots + m_0.$$

If we expand W(nm) in terms of these variables we obtain

$$W(nm) = W\{m(n_{p-1}\, 2^{p-1} + n_{p-2}\, 2^{p-2} + \ldots + n_0)\}$$

$$= W\{m\, n_{p-1}\, 2^{p-1}\}\; W\{m(n_{p-2}\, 2^{p-2} + \ldots + n_0)\}. \qquad (B.14)$$

But

$$m\, 2^{p-1} = m_{p-1}\, 2^{2p-2} + m_{p-2}\, 2^{2p-3} + m_{p-3}\, 2^{2p-4} + \ldots + m_0\, 2^{p-1} \qquad (B.15)$$

and since all terms from 2^{2p-2} to 2^p are multiples of 2^p (=N) we have that

$$W\{m\, n_{p-1}\, 2^{p-1}\} = W\{m_0\, n_{p-1}\, 2^{p-1}\}. \qquad (B.16)$$

With this simplification equation B.12 becomes

$$S_f(m/N) = \sum_{n_0=0}^{1} \sum_{n_1=0}^{1} \ldots [\sum_{n_{p-1}=0}^{1} S_t(n)\, W(m_0\, n_{p-1}\, 2^{p-1})]\, W\{m(n_{p-2}\, 2^{p-2} + \ldots + n_0)\}. \qquad (B.17)$$

The term in square brackets will be written as $S_t^1(m_0, n_{p-2}, n_{p-1}, \ldots, n_0)$, m_0 having replaced n_{p-1}.

The simplification process depicted in this equation may then be repeated, with S_t^1 in place of $S_t(n)$. In general at the ith step, the function

$$S^i(m_0,m_1,\ldots,m_{i-1},n_{p-i-1},n_{p-i-2},\ldots,n_0) =$$

$$\sum_{n_{p-1}=0}^{1} S^{i-1}(m_0,m_1,\ldots,m_{i-2},n_{p-i},n_{p-i+1},\ldots,n_0) \times W\left([m_0+2m_1+\ldots+m_{i-1}2^{i-1}]2^{p-i}\, n_{p-i} \right). \quad (B.18)$$

Note that the subscript t has been dropped as the intermediate steps no longer represent time domain data.

Expanding the summation we obtain

$$S^i(m_0,m_1,\ldots,m_{i-1},n_{p-i-1},\ldots,n_0) = S^{i-1}(m_0,m_1,\ldots,m_{i-2},1,n_{p-i-1},\ldots,n_0)$$

$$+ S^{i-1}(m_0,m_1,\ldots,m_{i-2},0,n_{p-i-1},\ldots,n_0)\ W([m_0+2m_1+\ldots+m_{i-1}2^{i-1}]2^{p-i}). \quad (B.19)$$

We therefore have a relationship between between time and frequency domain data in terms of an iterative expression. To evaluate equation B.19 we first note that the argument, $(m_0,m_1,\ldots,m_{i-1},n_{p-i-1},n_{p-i-2},\ldots,n_0)$, is a binary number consisting of p bits. We can therefore replace it with a binary number ℓ where $0 \le \ell \le N-1$ i.e.

$$S^i(\ell) = S^{i-1}(\ell') + S^{i-1}(\ell'')\ W(d) \quad (B.20)$$

where ℓ' has $m_{i-1} = 0$, ℓ'' has $m_{i-1} = 1$ and d takes the value

$$d = [m_0+2m_1+\ldots+m_{i-1}2^{i-1}]2^{p-i}. \quad (B.21)$$

Note that $\ell'' = \ell' + 2^{p-i} = \ell' + N/2^i$ and so equation B.19 becomes

$$S^i(\ell) = S^{i-1}(\ell') + S^{i-1}(\ell' + N/2^i)\ W(d). \quad (B.22)$$

Consider the special case when $\ell = \ell'$. Then $m_{i-1} = 1$ and equation B.19 becomes

$$S^i(\ell') = S^{i-1}(\ell') + S^{i-1}(\ell' + N/2^i)\ W(d') \quad (B.23)$$

the other special case is $\ell = \ell''$ in which case $m_{i-1} = 0$ and equation B.19 gives

$$S^i(\ell' + N/2^i) = S^{i-1}(\ell') + S^{i-1}(\ell' + N/2^i)\ W(d'') \tag{B.24}$$

where

$$\begin{aligned} d' &= [m_0+2m_1+ \ldots + 2^{i-1}\ ]\ 2^{p-i} \\ d'' &= [m_0+2m_1+ \ldots +m_{i-2}\ 2^{i-2}\ ]\ 2^{p-i} \end{aligned} \tag{B.25}$$

and so

$$W(d'') = W(d')\ W(2^{p-1}) = W(d')\ W(N/2) = -W(d'). \tag{B.26}$$

Removing all primes from equations B.23 and B.24 and using the result from equation B.26 we obtain the so called "butterfly operations"

$$S^i(\ell) = S^{i-1}(\ell) + S^{i-1}(\ell + N/2^i)\ W(d) \tag{B.27}$$

$$S^i(\ell + N/2^i) = S^{i-1}(\ell) - S^{i-1}(\ell + N/2^i)\ W(d) \tag{B.28}$$

where we have redefined ℓ and d as

$$\begin{aligned} \ell &= (m_0,m_1, \ldots ,m_{i-2},0,n_{p-i-1},n_{p-i-2}, \ldots ,n_0) \\ d &= [m_0+2m_1+ \ldots +m_{i-2}\ 2^{i-2}\ ]\ 2^{p-i}. \end{aligned} \tag{B.29}$$

Since the input $\{ S^{i-1}(\ell), S^{i-1}(\ell + N/2^i) \}$ and the output $\{ (S^i(\ell), S^i(\ell + N/2^i) \}$ have the same argument indices, the computation may be executed in place, by writing the output results over the input data, for each stage ℓ. A pictorial example of the above calculations is illustrated in figure B.1 for N=8.

Each node represents a variable while the arrow implies an additive contribution from two previous nodes. Multiplications by a constant are represented by a number written near the arrowhead.

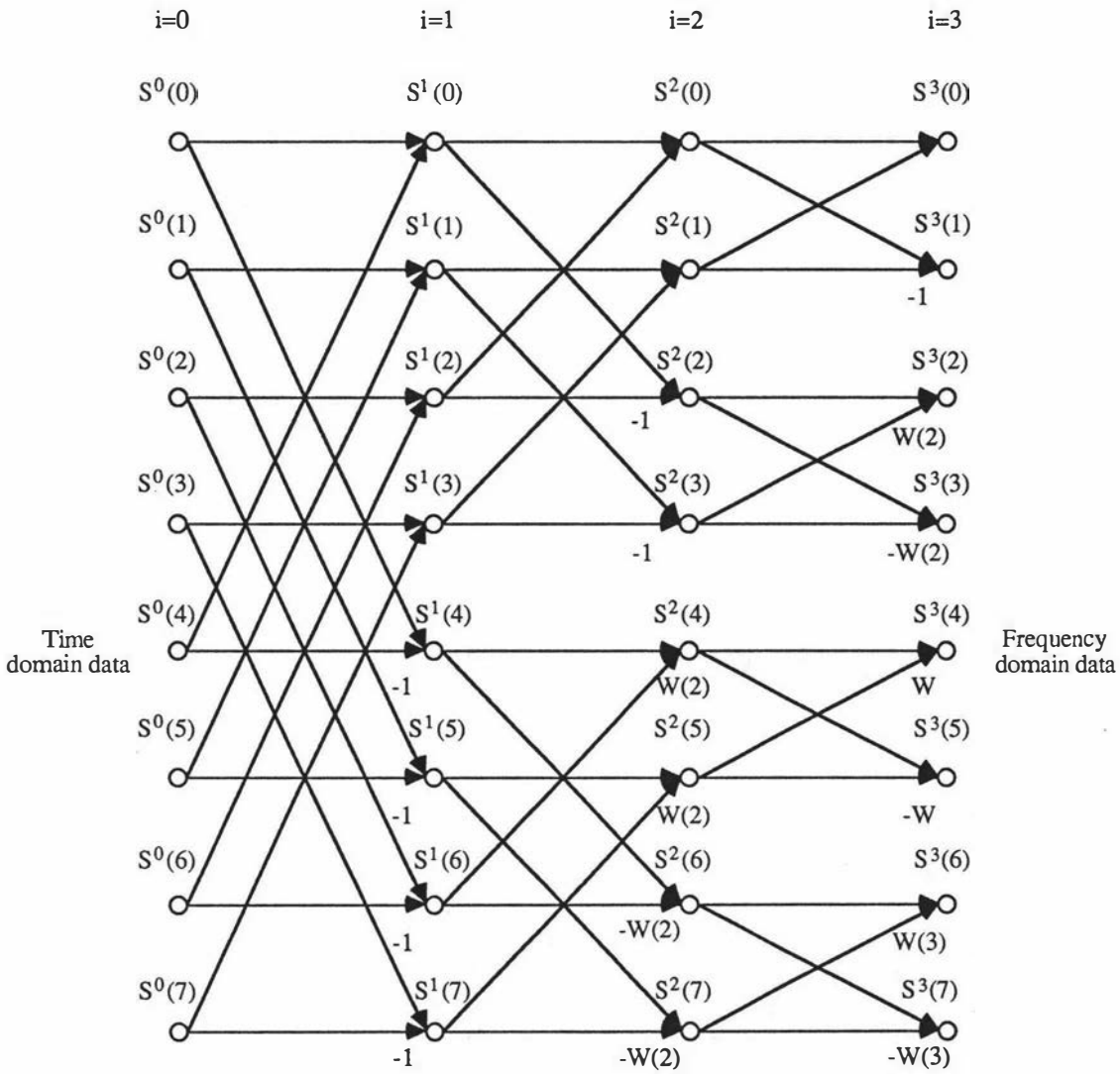

Figure B.1 "Butterfly diagram" showing the sequence of events which occur in the Radix 2 fast Fourier transform algorithm for N=8. Each node represents a variable and each arrow the additive contribution from two previous nodes. Multiplications by a constant are represented by a value written near the arrowhead.

Note from this diagram and equation B.29 that the index of the final result has its bits in reverse order

$$S_f(m_0,m_1,\ldots,m_{p-1}) = S_t(n_{p-1},n_{p-2},\ldots n_0). \tag{B.30}$$

It is therefore necessary to perform a bit reversal before the frequency domain data can be used.

From equation B.29 we see that d may be obtained from ℓ by dividing by 2^{p-i} followed by a bit reversal i.e.

$$\begin{aligned} d &= \text{B.R.}\{\ell/2^{p-i}\} \\ &= \text{B.R.}\{0,0,0,\ldots,0,m_0,m_1,\ldots,m_{l-2},0) \\ &= \{0,m_{i-2},m_{i-3},\ldots,m_1,m_0,0,0,0,\ldots,0) \\ &= \{0,m_{i-2},m_{i-3},\ldots,m_1,m_0\}\ 2^{p-i} \end{aligned} \tag{B.31}$$

which is just equation B.29.

Since $S_t(n)$ and $W(d)$ are complex functions, equations B.27 and B.28 must be expanded in terms of the real and imaginary parts of these variables, that is

$$S(n) = \text{Re}\{S(n)\} + \text{Im}\{S(n)\}$$

$$W(d) = \cos(2\pi d/N) - j\sin(2\pi d/N)$$

and so equation B.27 becomes

$$\text{Re}\{S^i(\ell)\} = \text{Re}\{S^{i-1}(\ell)\} + \text{Re}\{S^{i-1}(\ell)\}\cos\{2\pi d/N\} + \text{Im}\{S^{i-1}(\ell)\}\sin\{2\pi d/N\}$$

(B.32)

$$\text{Im}\{S^i(\ell)\} = \text{Im}\{S^{i-1}(\ell)\} + \text{Im}\{S^{i-1}(\ell)\}\cos\{2\pi d/N\} - \text{Re}\{S^{i-1}(\ell)\}\sin\{2\pi d/N\}$$

and equation B.28

$$\text{Re}\{S^i(q)\} = \text{Re}\{S^{i-1}(\ell)\} - \text{Re}\{S^{i-1}(q)\}\cos\{2\pi d/N\} + \text{Im}\{S^{i-1}(q)\}\sin\{2\pi d/N\}$$

(B.33)

$$Im\{S^i(q)\} = Im\{S^{i-1}(\ell)\} - Im\{S^{i-1}(q)\}\cos\{2\pi d/N\} - Re\{S^{i-1}(q)\}\sin\{2\pi d/N\}$$

where $q = \ell + N/2^i$ and both real and imaginary domains have N data points.

The computation of $\cos\{2\pi d/N\}$ and $\sin\{2\pi d/N\}$ is simplified as d has only N discrete values which can be stored in a look up table. Since second, third, and fourth quadrant data can be calculated from first quadrant values it is only necessary to store the N/4+1 values

$$\alpha(\sigma) = \sin\{2\pi\sigma/N\} \qquad \sigma \in \{0,1,2, \ldots ,N/4\} \qquad (B.34)$$

from which

$$\begin{aligned} W(d) &= \alpha(N/4-d) + j\alpha(d) && \sigma \in \{0\rightarrow N/4\} \\ &= -\alpha(d-N/4) + j\alpha(N/2 - d) && \sigma \in \{N/4\rightarrow N/2\} \\ &= -W(d-N/2) && \sigma \in \{N/2\rightarrow N\}. \end{aligned} \qquad (B.35)$$

The assembly listing for the N point FFT used in this work is given in volume 2.

APPENDIX C

Derivation of equation 6.44

$$\mathrm{Re}\{\Psi(f)\} = (2\pi)^{-1}\, d/df\, [\,(2\pi)^{-1}\, \mathbf{P} \int_{-f_r}^{f_r} \mathrm{Re}\{S_f(0)\}\ (1-f^2/f_r^2)^{1/2}\,(f'-f)^{-1}\, df'\,]. \quad (C.1)$$

The term in the square brackets may be written

$$(2\pi)^{-1}\, \mathbf{P} \int_{-f_r-f}^{f_r-f} (a + bx + cx^2)^{1/2}\, x^{-1}\, dx \quad (C.2)$$

where

$$x = f' - f$$
$$a = f_s^2 - f^2$$
$$b = -2f$$
$$c = -1$$

C.2 is a standard integral[47] given for $-f_r < f < f_r$ by

$$\frac{1}{2\pi f_r}\ \mathbf{P} \left[(a + bx + cx^2)^{1/2} + \frac{b}{2\sqrt{(-c)}} \sin^{-1}\left(\frac{(2cx - b)}{(b^2 - 4ac)^{1/2}}\right) - \sqrt{a}\, \ln\left(\frac{(a + bx + cx^2)^{1/2} + a^2}{x} + \frac{b}{2\sqrt{a}}\right) \right]_{-f_r - f}^{f_r - f} \quad (C.3)$$

Evaluating the principle part and substituting back in C.1 yields

$$\mathrm{Re}\{\Psi(f)\} = d/df\, (2\pi)^{-2}\, [\,\pi\, \mathrm{Re}\{S_f(0)\}\, (f/f_r)\,] \quad (C.4)$$

which is the desired result.

APPENDIX D

Sensitivity enhancement using multiple spin echo summation

By recalling the nuclear signal using 180° rf pulses it is possible to increase the signal strength and so improve the signal to noise ratio. The degree to which the S/N ratio can be improved depends on the T_2 for the sample, since eventually the recalled signal is lost in the noise.

It is of interest then to determine the optimum number of recalled echoes and the consequent improvement in the signal to noise ratio, for a given T_2. The pulse sequence for imaging with echo summation is given in figure 6.16. We shall presume that both sides of the echo are summed to maximize the S/N enhancement and that one side of the echo has much the same form as the other. Let the 180° pulses be applied at intervals of 2τ seconds. The signal level after summing m echoes will then be

$$\begin{aligned} S_m &= [\, 1 + 2\exp(-2\tau/T_2) + 2\exp(-4\tau/T_2) + \ldots + 2\exp(-2m\tau/T_2) \,]\, S_0 \\ &= [\, 1 + \sum_{n=1}^{m} 2\exp(-2n\tau/T_2) \,]\, S_0 \end{aligned} \qquad (D.1)$$

where S_0 is the signal level for a single fid.

The noise level also increases, but less rapidly because of its random nature

$$N_m = (2m + 1)^{1/2}\, N_0 \qquad (D.2)$$

N_0 is the noise level for a single fid. The final signal to noise ratio after m echoes have been summed is therefore given by

$$(S/N)_m = (S/N)_0\, [\, 1 + \sum_{n=1}^{m} 2\exp(-2n\tau/T_2) \,]\, (2m + 1)^{1/2} \qquad (D.3)$$

The optimum number of echos can be found by maximizing the enhancement factor m, that is finding m such that

$$\frac{d}{dm}\left[\left[1+\sum_{n=1}^{m}2\exp(-2n\tau/T_2)\right](2m+1)^{-1/2}\right] = 0. \qquad (D.4)$$

We first note the series sum

$$\sum_{n=0}^{k-1} a^n = (1-a^k)/(1-a). \qquad (D.5)$$

With $k = m + 1$ and $a = \exp(-2\tau/T_2)$ we find that

$$2\sum_{n=1}^{m}2\exp(-2n\tau/T_2) = \frac{2\,[1-\exp(-2(m+1)\tau/T_2)]}{[1-\exp(-2\tau/T_2)]} - 2$$

$$= \frac{2\exp(-2\tau/T_2)\,[1-\exp(-2m\tau/T_2)]}{[1-\exp(-2\tau/T_2)]}$$

$$= \frac{2\,[1-\exp(-2m\tau/T_2)]}{[\exp(-2\tau/T_2)-1]} \qquad (D.6)$$

and so

$$(S/N)_m = (S/N)_0\,[1+2(1-\exp\{-2m\tau/T_2\})\,(\exp\{2\tau/T_2\}-1)^{-1}]\,[2m+1]^{-1/2} \qquad (D.7)$$

Although equation D.4 can be evaluated[26] it is more straightforward to calculate the enhancement factor for a range of m values and look for a maximum. The results of such a calculation are given in table D.1.

Table D.1 S/N enhancement and optimum echo number as a function of τ/T_2

τ/T_2	optimum m	S/N enhancement
1	0	1
0.5	1	1.002
0.2	3	1.452
0.1	6	2.028
0.05	12	2.858

APPENDIX E

Impedance matching

It is important when working with low level rf signals to ensure that each successive stage in a system is efficiently matched to the subsequent circuit. For maximum power transfer this implies that the output impedance of one stage be equal to the input impedance of the next. However for the case of noise matching it may be necessary to use non-optimal power matching to obtain the best noise figure[15].

The various interconnections between successive rf stages in the imaging system are made using 50Ω coaxial cable. Since the resonant circuits and amplifiers invariably have impedances which differ from this value it is frequently necessary to transform impedances to achieve optimal matching. A variety of circuits are available which achieve this purpose but 2 are of particular interest in this work.

The first (see figure E.1) is used to couple both the transmitter and receiver to the rf coil for maximum power transfer. At resonance the equivalent parallel resistance of this circuit is quite high and, for large quality factors, is given by $R = Q^2r$ where r is the coil resistance. R is about 5kΩ for the rf coil used in this work. As the circuit is tuned above resonance the resistance R is reduced and the combination C_2-L begins to look inductive. Capacitor C_1 may be adjusted (without significantly altering the tuning since $C_1 >> C_2$) until this inductive component is tuned out. In this way the circuit can be made to look resistive with any value of resistance less than the maximum of 5KΩ. For particular values of L, and NMR resonant frequency ω_0, we obtain values for C_1 and C_2 using the following technique.

First it is necessary to obtain an expression for the equivalent parallel resistance of an inductor i.e. to show that $R=Q^2r$. The impedance of the r-L combination in figure E.1b is just

$$Z = r + j\omega L \tag{E.1}$$

and from figure E.1c

$$Z = \frac{j\omega LR}{j\omega L + R} = \frac{\omega^2L^2R + j\omega LR^2}{R^2 + \omega^2L^2}. \tag{E.2}$$

Equating real and imaginary parts in equations E.1 and E.2 we obtain

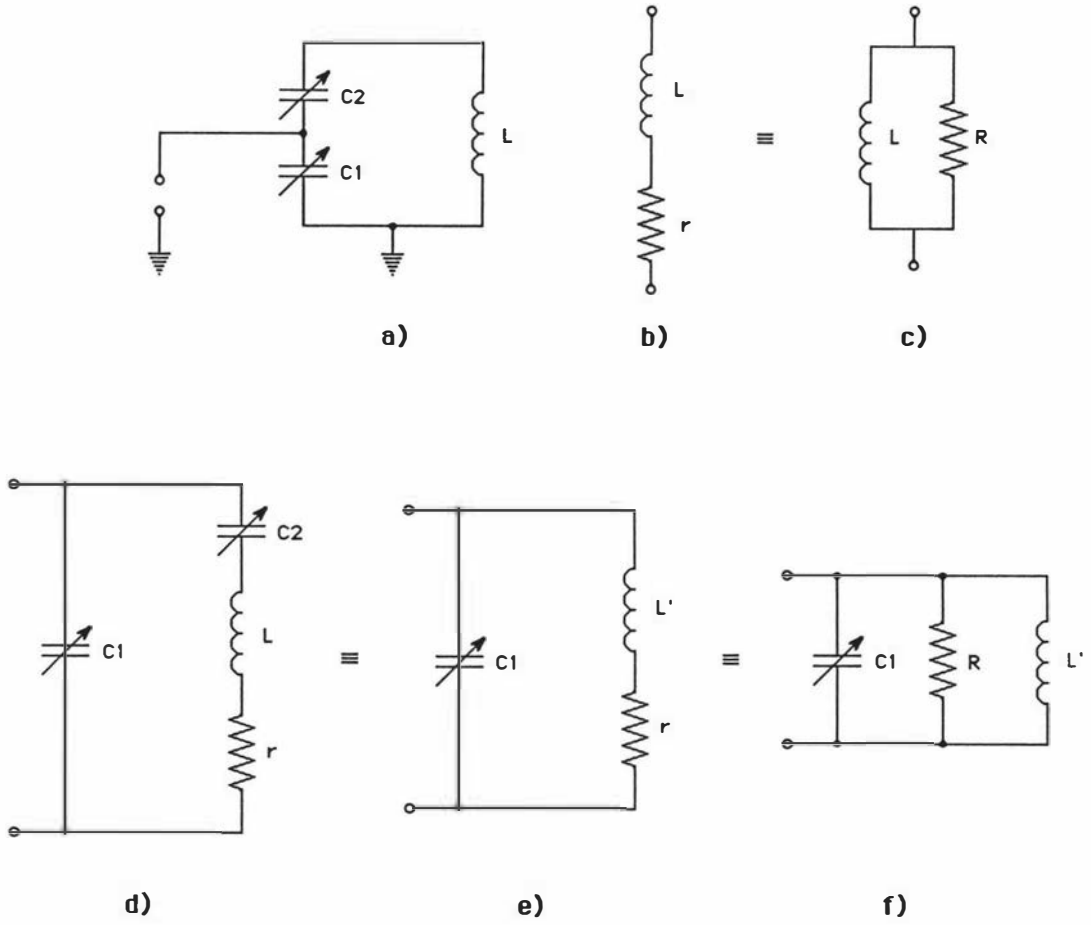

Figure E.1 Impedance matching equivalent circuits.

$$r = \frac{\omega^2 L^2 R}{R^2 + \omega^2 L^2} = \frac{R}{R^2/(\omega^2 L^2) + 1} \tag{E.3}$$

and

$$L = \frac{LR^2}{R^2 + \omega^2 L^2} = \frac{L}{(\omega^2 L^2/R^2) + 1}. \tag{E.4}$$

Equation E.4 can only be valid if $\omega^2 L^2 << R^2$. Substituting this result into equation E.3 gives

$$R = \omega^2 L^2/r = Q^2 r \tag{E.5}$$

where $Q^2 = \omega L/r$.

With this result we can now go on to analyse the tank circuit in figure E.1d. When tuned above their resonant frequency, C_2 and L will have an inductance L' (fig. E.1e). The equivalent parallel resistance R (fig. E.1f) will then be $\omega^2 L'^2/r$ from equation E.5. C_1 is selected so that

$$Z^{-1} = R^{-1} + (j\omega L')^{-1} + j\omega C_1 = R^{-1}$$

$$\Rightarrow (j\omega L')^{-1} = -j\omega C_1$$

$$\Rightarrow C_1 = (\omega^2 L')^{-1}. \tag{E.6}$$

Substituting for L' then gives

$$C_1 = (\omega^2 R r)^{-1/2} \tag{E.7}$$

but $r = \omega L/Q$ and so

$$C_1 = \left[\frac{Q}{\omega^3 R L}\right]^{1/2}. \tag{E.8}$$

Now if $C_1 >> C_2$ then $(\omega L)^{-1} \approx \omega C_2$ and so $L \approx (\omega^2 C_2)^{-1}$. Substituting this result into equation E.8 gives

$$C_1 = \left[\frac{Q\,C_2}{\omega\,R}\right]^{1/2}. \qquad (E.9)$$

Having measured L and Q it is therefore a straightforward procedure to calculate C_1 and C_2 for a desired value of R.

An alternative impedance matching circuit which works in much the same way is pictured in figure E.2a. This time C_2 and L are tuned slightly below resonance so as to look inductive. C_1 tunes out this inductance leaving the desired resistance R.

Circuit analysis is again fairly straightforward as can be seen from the equivalent circuits

In figure E.2c $\quad R = Q^2 r \qquad (E.10)$

In figure E.2d $\quad R = Q'^2 r' \qquad (E.11)$

$$\Rightarrow r' = Q^2 r / Q'^2$$

$$= [\omega^2 L^2 / r] / [\omega^2 L'^2 / r'^2]$$

$$\Rightarrow L' = ([r' L^2]/r)^{1/2} \qquad (E.12)$$

C_1 is adjusted to tune out L' so that

$$C_1 = (\omega^2 L')^{-1} = \left[\frac{r}{r' L^2 \omega^4}\right]^{1/2}. \qquad (E.13)$$

In this case $C_1 << C_2$ and so $\omega L \approx (\omega C_2)^{-1}$. Substituting for $Q = \omega L / r$ we find that

$$C_1 \approx \left[\frac{C_2}{r' Q \omega}\right]^{1/2}.$$

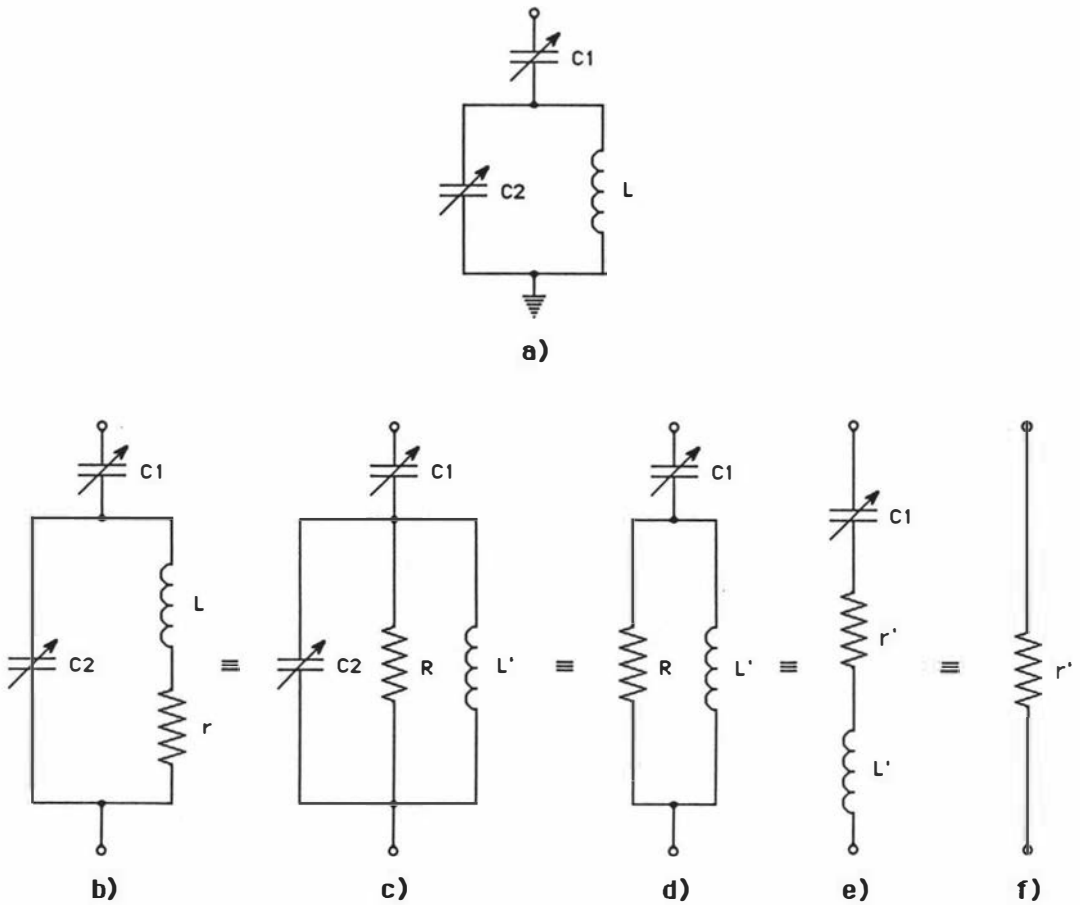

Figure E.2 Alternate impedance matching circuit.

APPENDIX F

A description of the interface and pulse sequencer hardware

F.1 TI-980A Interface

To communicate with the pulse sequencer it was necessary to design and build an interface circuit which could be plugged into the TI-980A computer. To simplify operations and ensure maximum data transmission rates, a parallel interface was chosen. A schematic for this board is given in figure F.1, while table F.1 lists the available outputs and the appropriate control codes required to activate them.

Table F.1 Pinouts for the TI-980A interface card

	P2 connections	P3 connections
Pin no.	Function	Function
1	gnd	sd 0D
2	sd E0[1]	sd 0E
3	sd 60	sd 0F
4	sd A0	sd 05
5	sd 20	sd 06
6	sd C0	gnd
7	sd 40	sd 04
8	sd 80	sd 0B
9	sd 00	sd 0A
10	D3	sd 09
11	D2	sd 08
12	D1	sd 03
13	D0	sd 02
14	sd 50	sd 07
15	sd 90	sd 0C
16	sd 10	n.c.
17	sd F0	n.c.
18	sd 70	n.c.
19	sd D0	n.c.
20	sd 30	n.c.
21	sd B0	n.c.

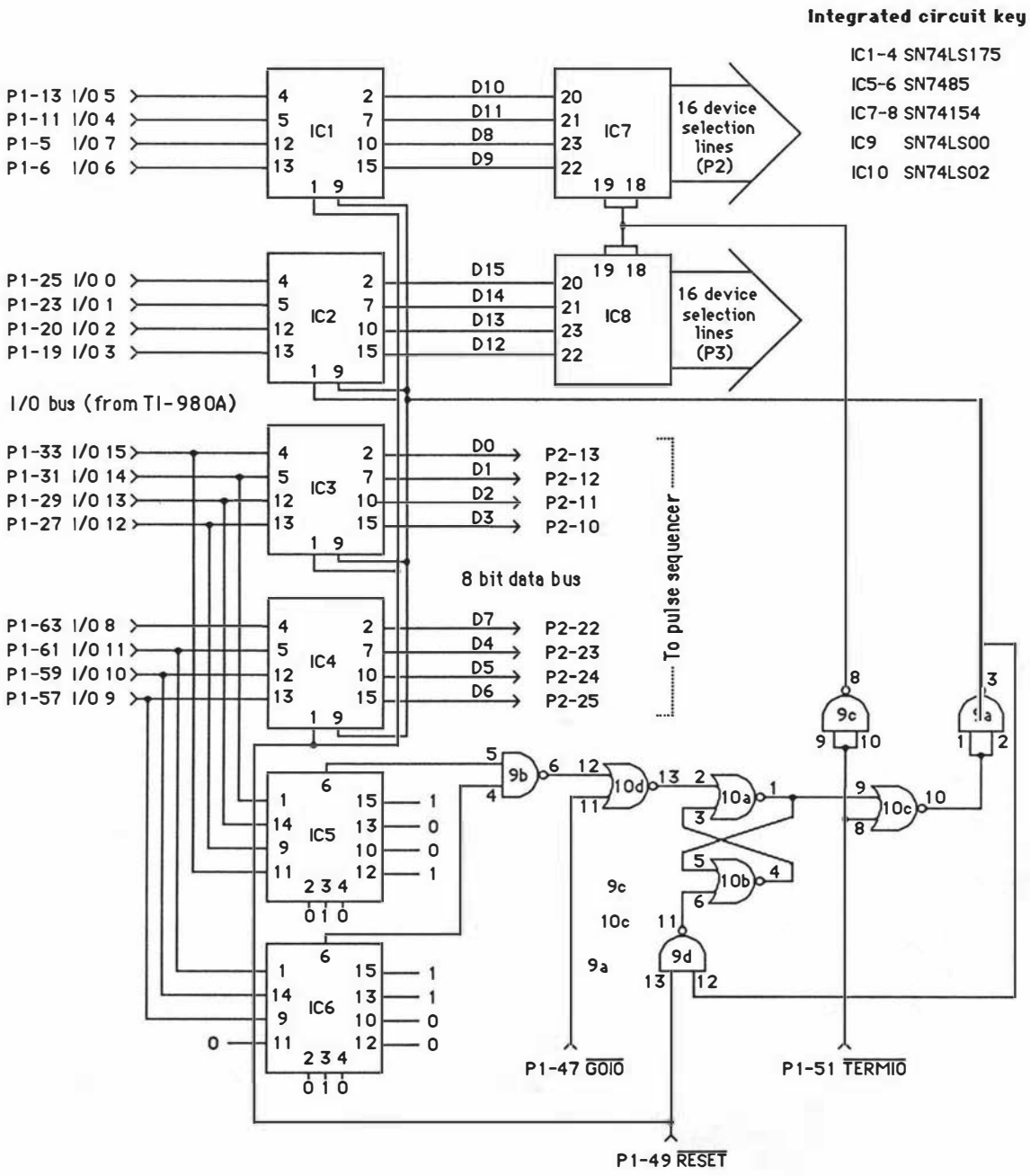

Figure F.1 TI-980A interface schematic.

22	D7	n.c.
23	D4	n.c.
24	D5	n.c.
25	D6	sd 00
26	reset	sd 01

Notes

1) The sd or select device codes correspond to the upper byte of the word being transferred to the interface. The lower byte contains the data (bits D0-D7).
2) Due to some T.I. idiosyncracy the most significant bit on the I/O bus is labelled I/O 0 rather than I/O 15. Hence the bit reversal in figure F.1 from input to output.
3) P1 refers to the 80 pin plug on the interface board which connects to the TI-980A computer. P2 and P3 are 26 pin plugs. P3 is presently unused while P2 is connected to the pulse sequencer via 3 metres of ribbon cable.

The 980A has a special output instruction (WDS - write direct single) which loads data onto a special 16 bit I/O bus. The particular unit to be accessed by this instruction is determined by 8 of the 16 bits in the WDS instruction. Only 6 of these bits are presently used in our system - allowing a total of 64 peripherals to be accesssed (these include the display, light pen, chart recorder, ADCs and other devices required to run the NMR experiment).

An understanding of the operation of the interface card can be gained by referring to the timing diagram in figure F.2 and the schematic in figure F.1. The computer's first step on issuing a WDS instruction is to place the 6 bit I/O address on the 16 bit data bus (lines I/O 9 to 15 in figure F.1). Line I/O10 determines when the computer has issued an input or output instruction; a WDS instruction sets this line high. This data is then compared with a reference address (33_{16}) by comparitors IC5 and IC6. When the address is stable (signified by a low level on the GOIO line) the result of this comparison is stored in an RS latch (IC 10a,b). A low pulse on the TERMIO line then indicates that stable data is present on lines I/O 0→15. This pulse transfers the data from the I/O bus to registers IC1→4 if the result of the comparison was true. The loop produced by IC10c and IC9a,d resets the latch in the event of a correct comparision so as to be ready for the next WDS instruction.

Initially it was planned to use the interface to drive a series of output registers which could directly control the imaging experiment. For this reason 8 bits of the data bus (D8-D15) have been decoded allowing 1 of 32 registers to be selected for output (see table F.1 for the control codes). The appropriate selection line goes low for the duration of the TERMIO pulse allowing data on the 8 bit bus to be transferred to the desired device. For the reasons mentioned in section 8.11 it was decided that this course of action would not be flexible enough for the range

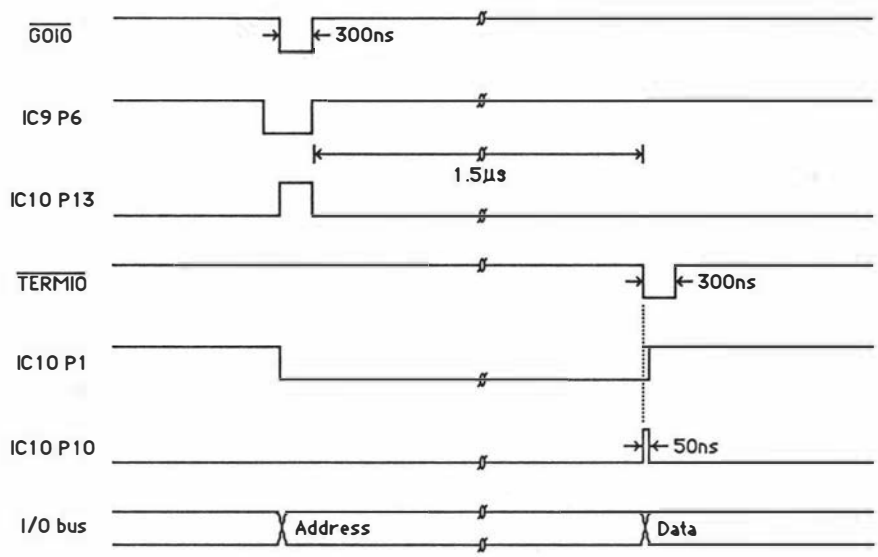

Figure F.2 TI-980A interface timing diagram.

of experiments envisaged, and so a separate pulse sequencer was designed. The number of selection outputs has therefore proved to be rather extravagant as only 3 are used at present (2 for the pulse sequencer and 1 for the graphics computer).

Initial testing of the interface showed that data transmission was unreliable because of the cross talk and interference present on the parallel output line. These problems were considerably reduced by rewiring the ribbon cable so that earth wires were interdigitated with the data lines (thereby reducing the characteristic impedance of the line). Further improvements in pulse shape were obtained by terminating the cable with a series of inverters (see figure F.3 for a schematic).

F.2 The pulse sequencer

The pulse sequencer is mounted on 3 double sided printed circuit cards (approximate dimensions 120 × 150mm) constructed using Bishop Graphics pcb artwork materials. The boards divide the sequencer into memory, timing and output units. Schematics for these boards may be found in figures F.4 to F.10.

The operation of the pulse sequencer may be divided into 2 parts; data loading and sequencing. The data loading operation is carried out by the following program (written in TI-980A assembly code, see mnemonic list on page 250).

Table F.2 Parallel data transfer routine

Address	Opcode	Mnemonic	Comment
1F38	0000	LDA (1F39)	
1F39	0100	DATA	
1F3A	C508	RMO A,ST	Enable external interrupts.
1F3B	1000	LDX (1F3C)	
1F3C	0000	DATA	Reset address counter.
1F3D	0000	LDA (1F3E)	
1F3E	3000	DATA	Initialise base register to point to
1F3F	C506	RMO A,B	the start of the pulse sequence.
1F40	0000	LDA (1F41)	
1F41	70DF	DATA	

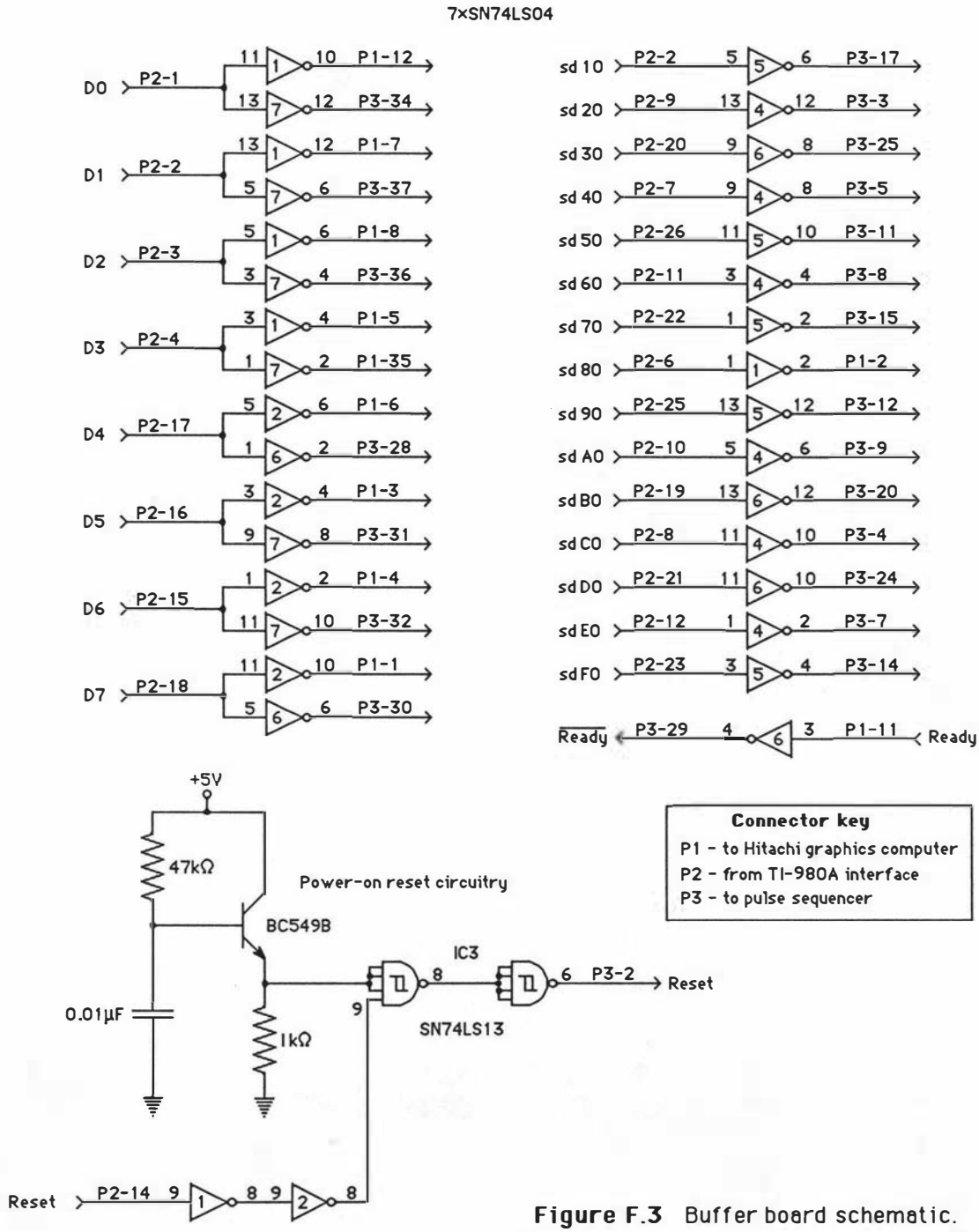

Figure F.3 Buffer board schematic.

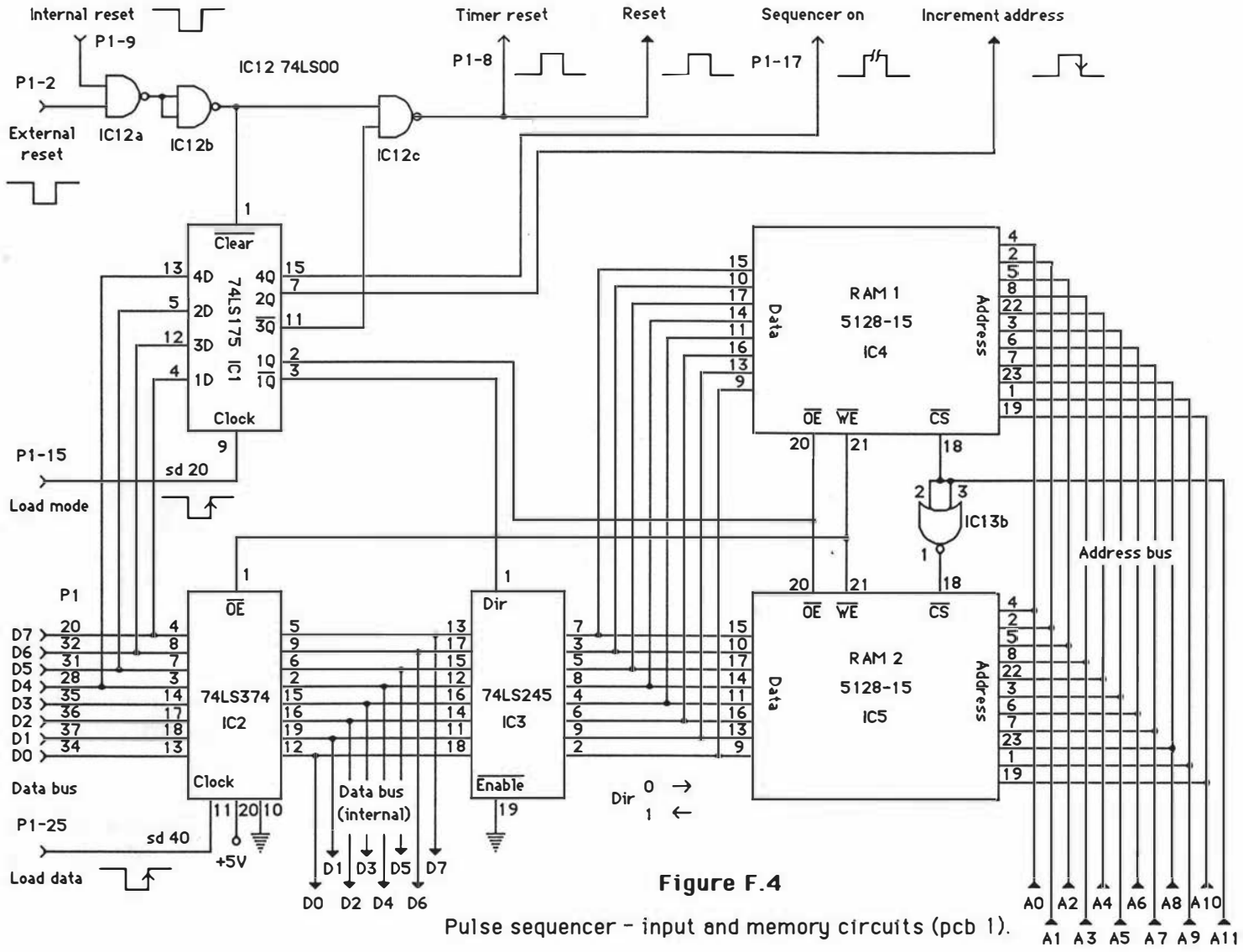

Figure F.4

Pulse sequencer - input and memory circuits (pcb 1).

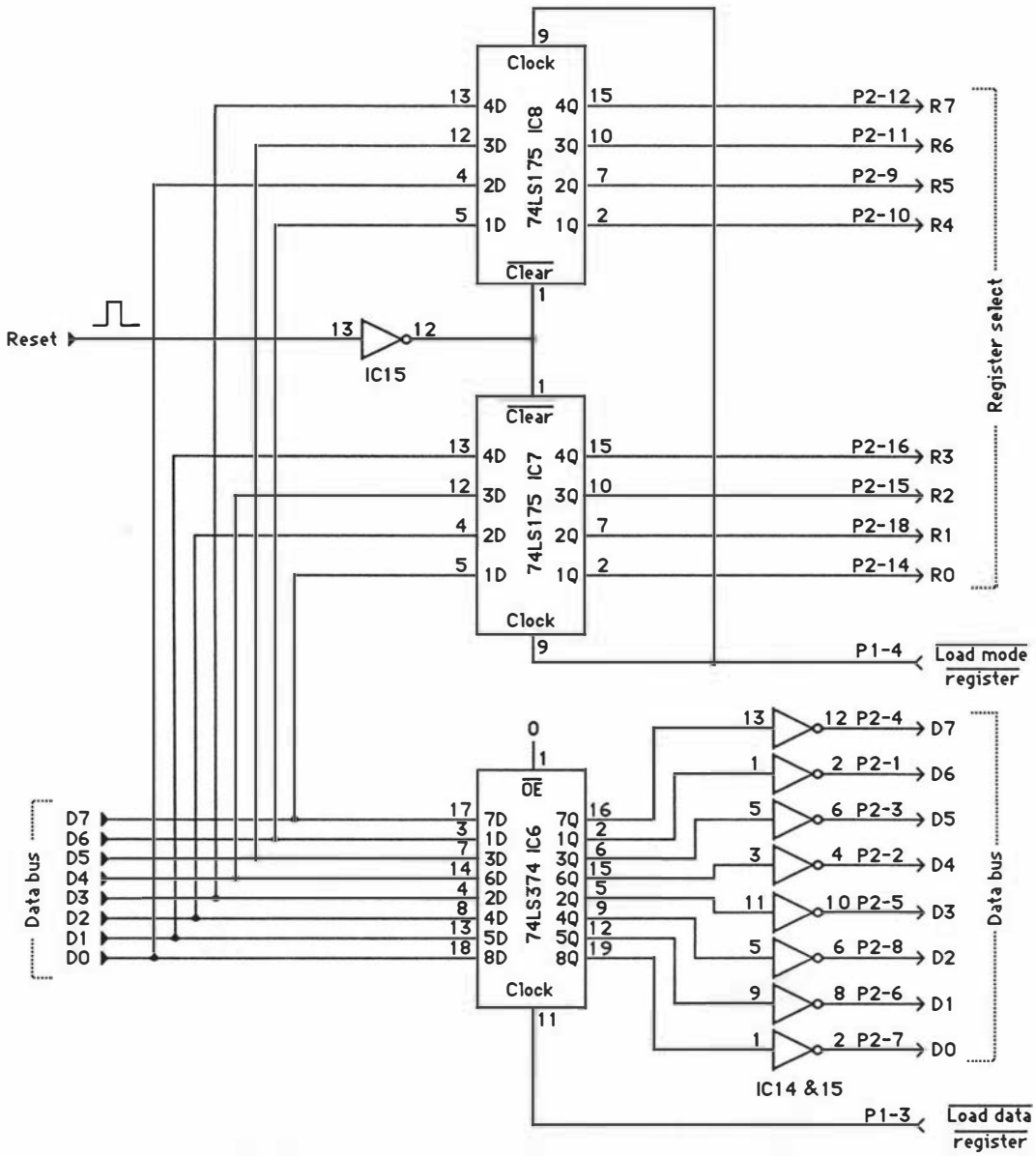

Figure F.5 Data output and control registers (pcb 1).

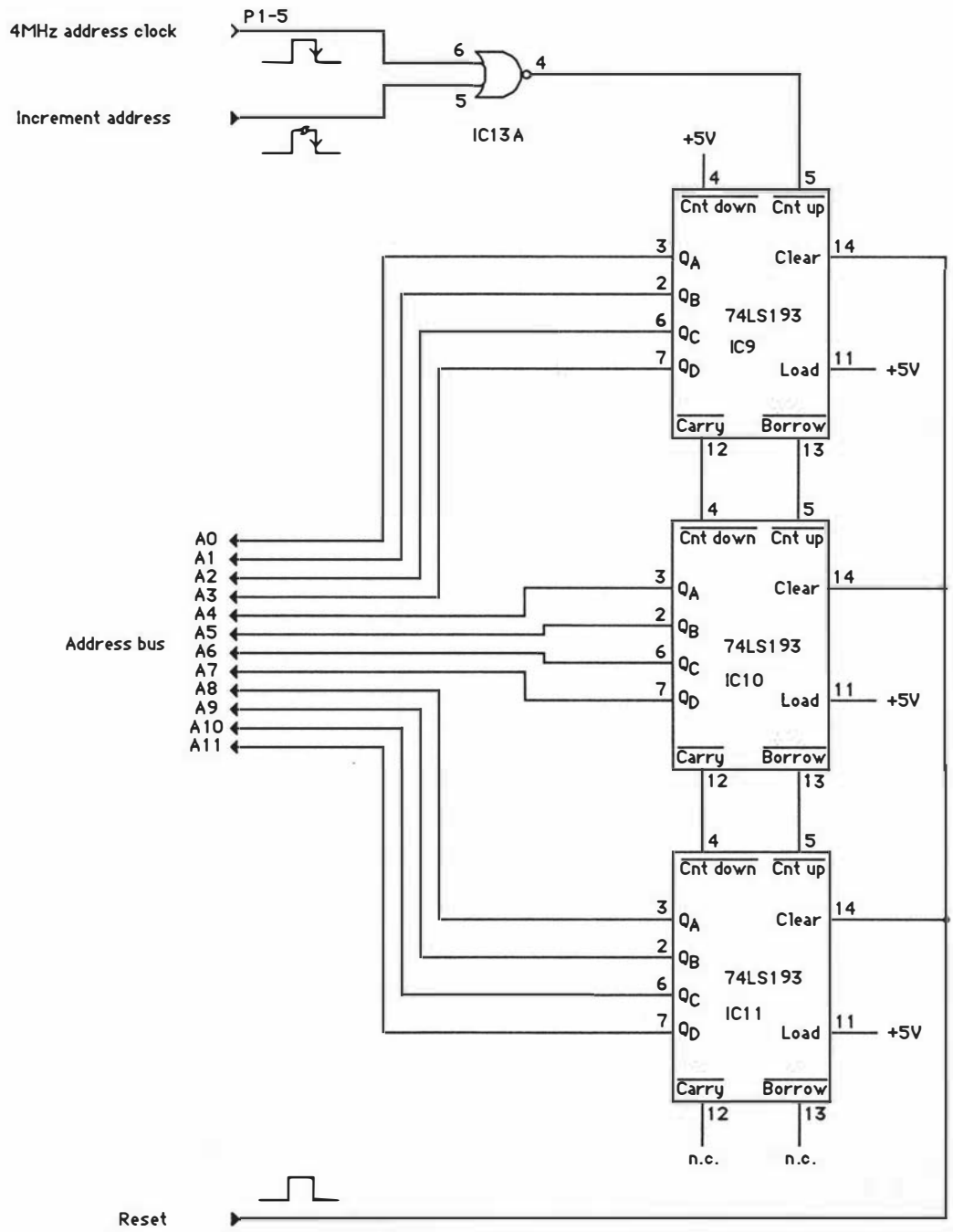

Figure F.6 Memory address counters (pcb 1).

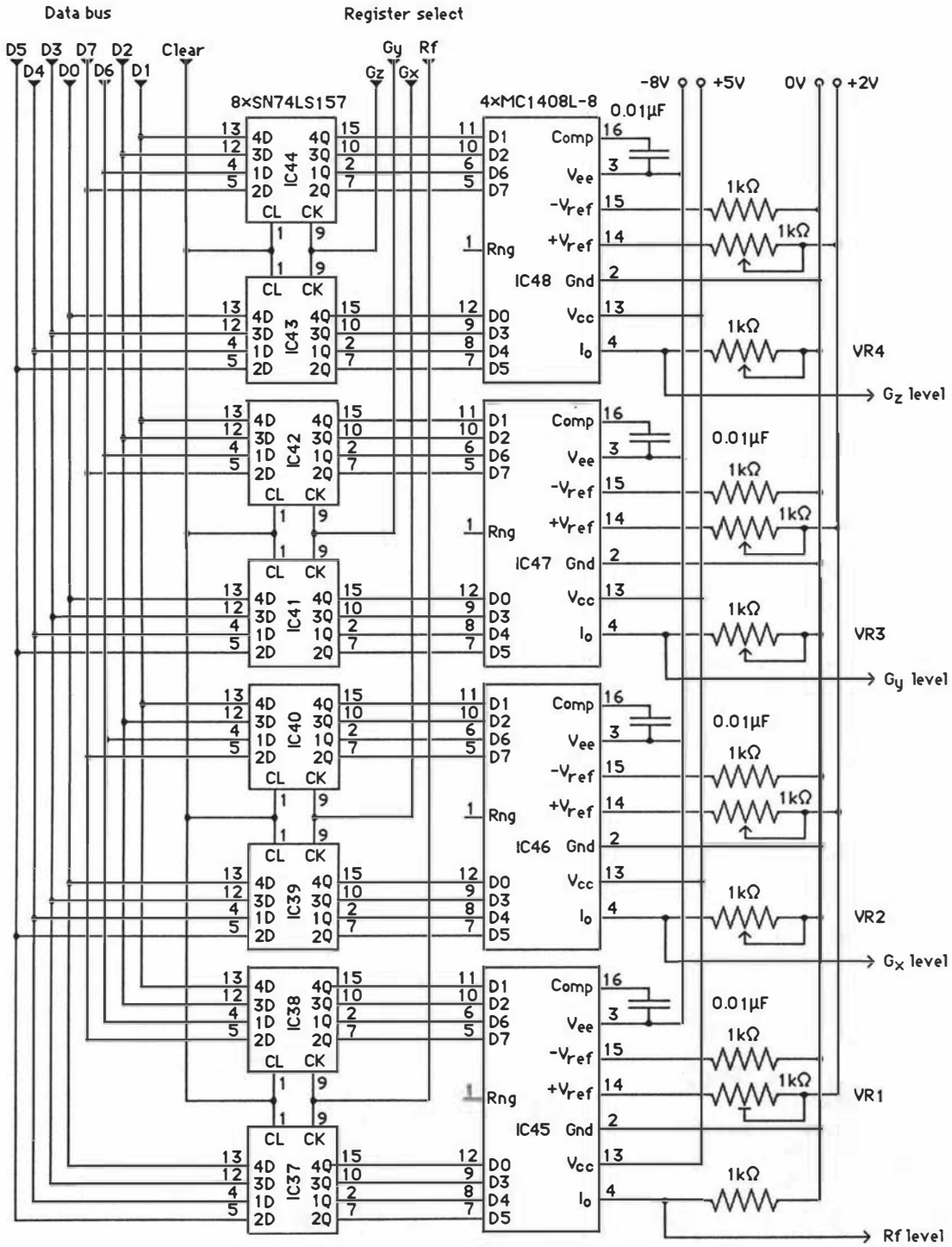
Data bus
Register select
D5 D3 D7 D2 Clear
D4 D0 D6 D1
Gy Rf
Gz Gx
8×SN74LS157
4×MC1408L-8
IC44
IC43
IC42
IC41
IC40
IC39
IC38
IC37
IC48
IC47
IC46
IC45
-8V +5V 0V +2V
0.01µF
1kΩ
VR4
VR3
VR2
VR1
Gz level
Gy level
Gx level
Rf level

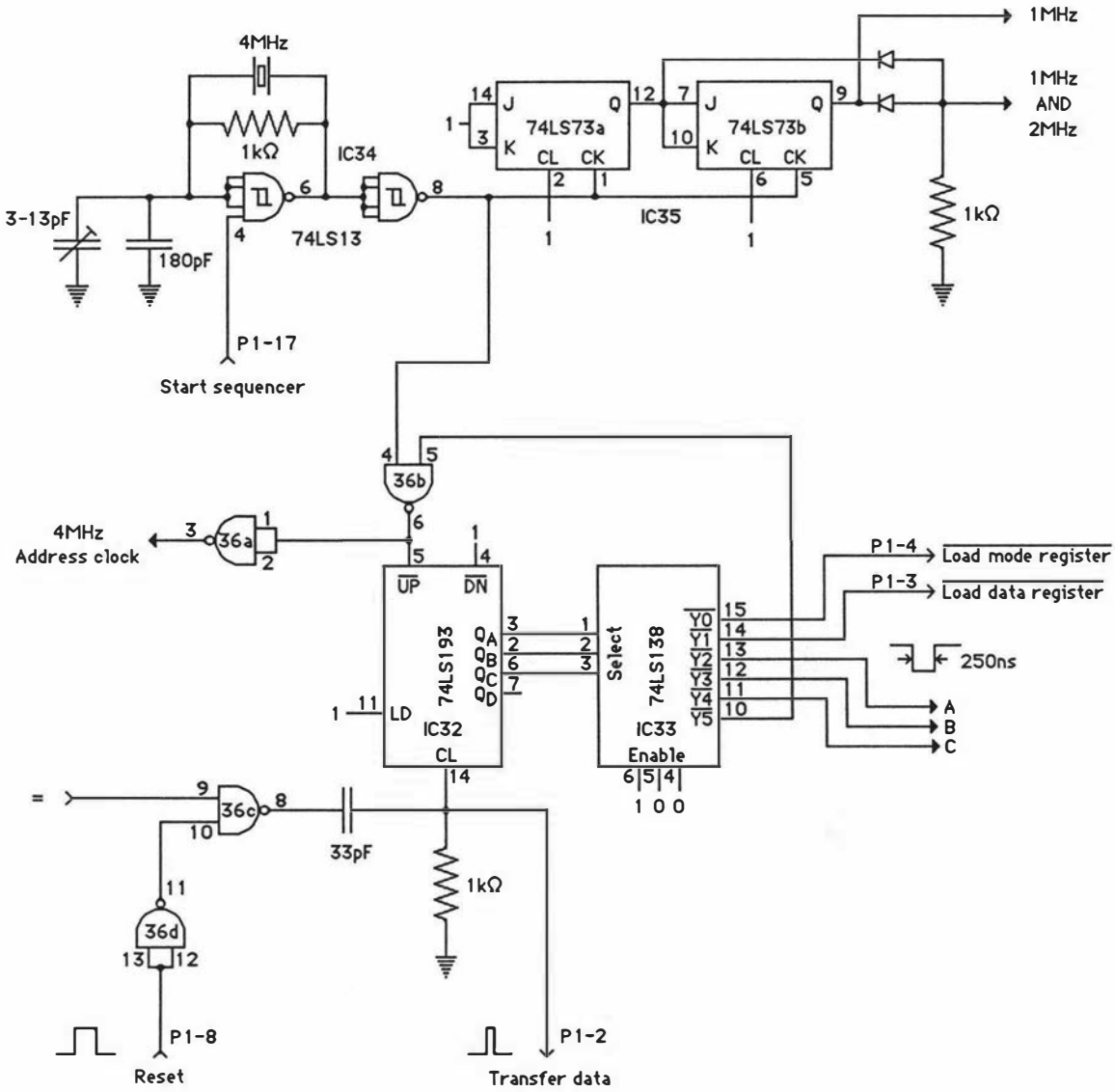

Figure F.8 Pulse sequencer and data distributor.

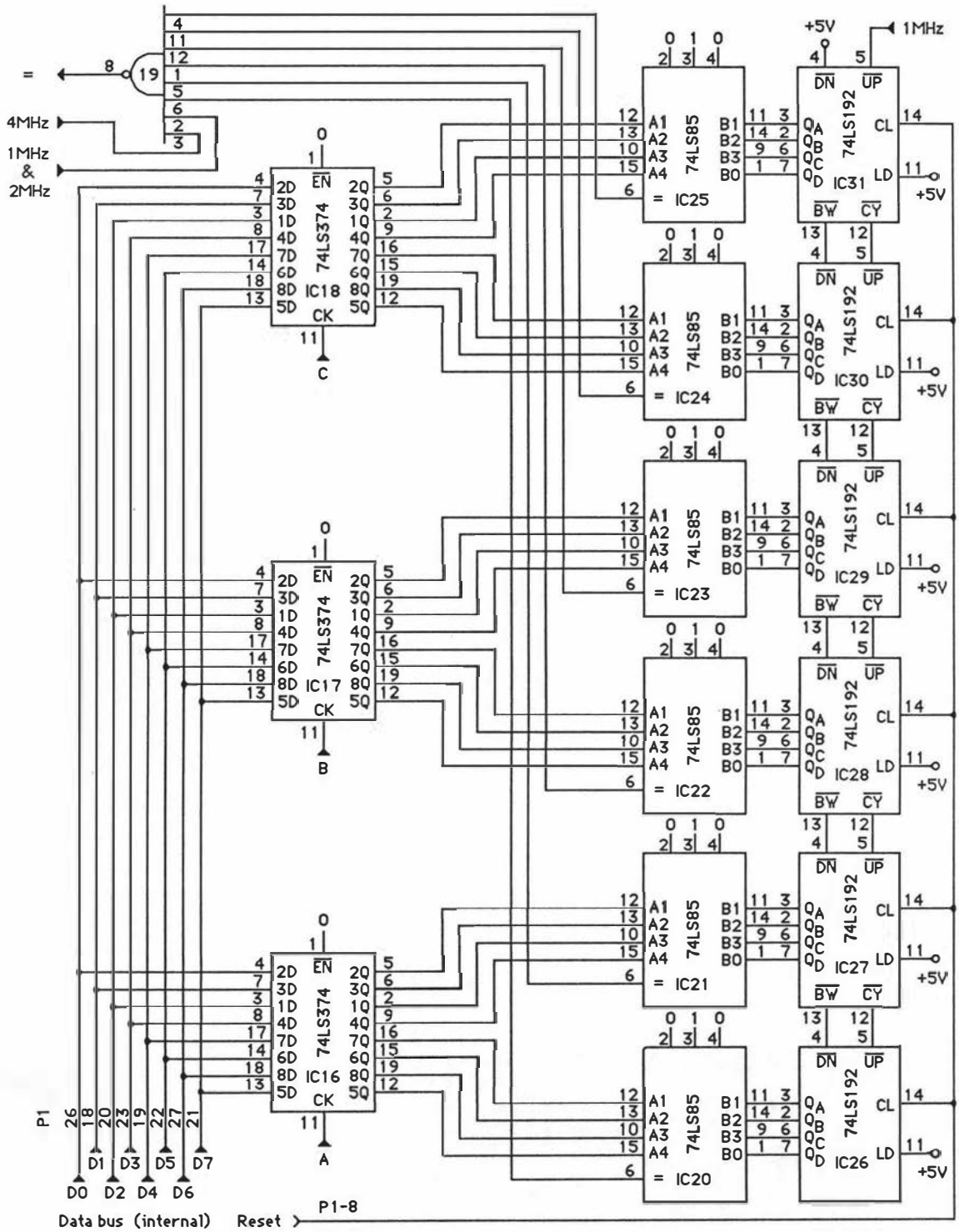
=
4MHz
1MHz & 2MHz
74LS374
IC18
IC17
IC16
74LS85
IC25
IC24
IC23
IC22
IC21
IC20
74LS192
IC31
IC30
IC29
IC28
IC27
IC26
+5V
1MHz
P1
D0 D1 D2 D3 D4 D5 D6 D7
Data bus (internal)
Reset
P1-8

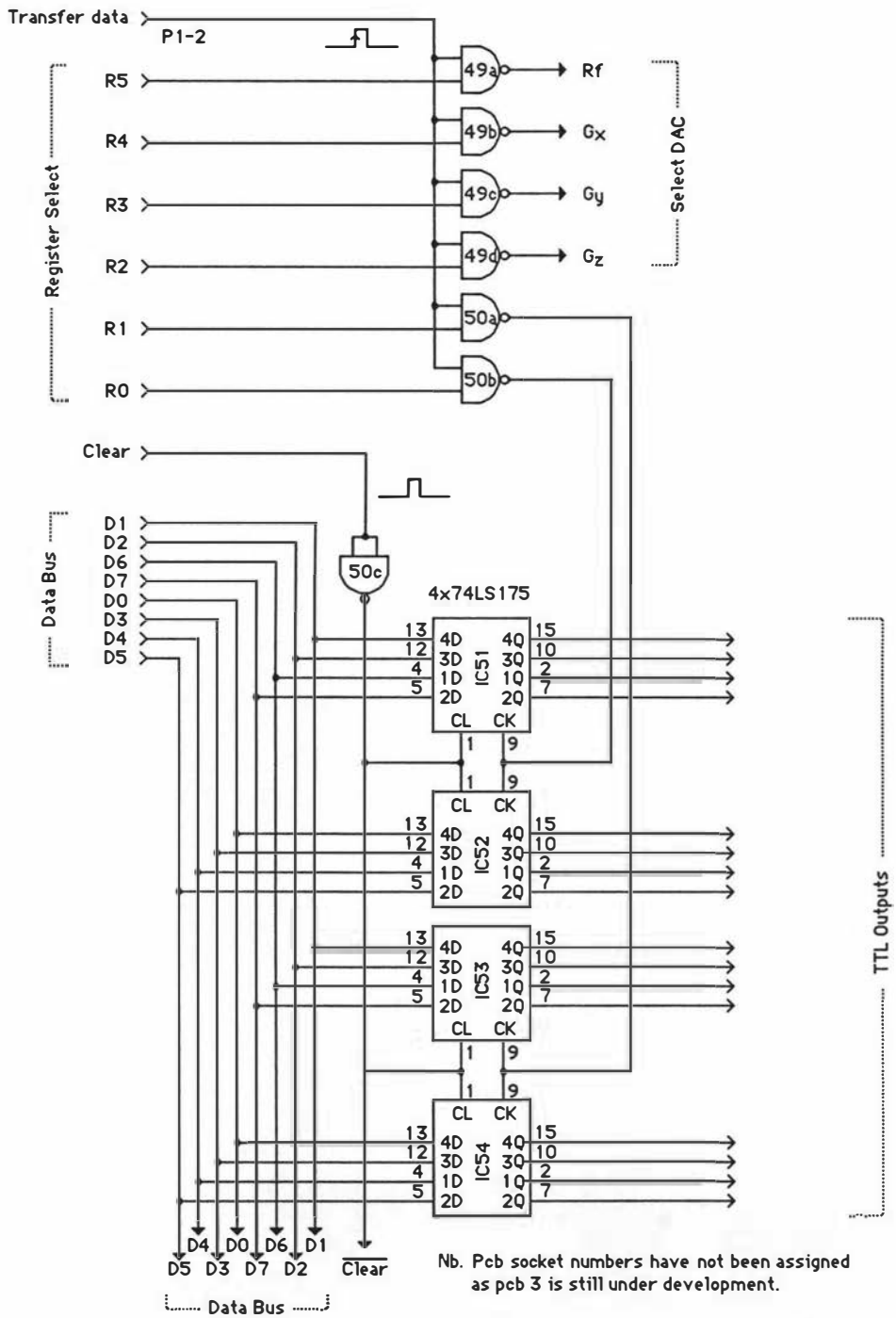

Figure F.10 TTL output registers and selection logic (pcb 3).

```
1F42    D833    WDS  13
1F43    0000    DATA A          Reset pulse sequencer.

1F44    0000    LDA  (1F45)
1F45    70EF    DATA
1F46    D833    WDS  13
1F47    0000    DATA A          Put pulse sequencer into its load mode.

1F48    0300    LDA  ((B) + (X))  Load data to be transferred
1F49    C200    RIV  A,A          Complement data (necessary due to inverters in buffer).
1F4A    3800    AND  (1F4B)       Remove upper byte.
1F4B    00FF    DATA
1F4C    3000    LOR  (1F4D)       Add command to transfer data to pulse
1F4D    3000    DATA              sequencer and not some other unit.

1F4E    D833    WDS  13
1F4F    0000    DATA A          Transfer data to pulse sequencer.

1F50    0000    LDA  (1F51)
1F51    70BF    DATA
1F52    D833    WDS  13
1F53    0000    DATA A          Increment pulse sequencer memory address.

1F54    C322    RIN  X,X        Increment memory pointer to look at next data value.

1F55    C520    RMO  X,A
1F56    6000    CPL  (1F57)
1F57    0200    DATA            Have all 256 data values been transferred?

1F58    CD20    SEQ
1F59    78EA    BRU  1F44       No, so transfer next data value.

1F5A    0000    LDA  (1F5B)
1F5B    70DF    DATA
1F5C    D833    WDS  13
1F5D    0000    DATA A          Reset pulse sequencer.

1F5E    0000    LDA  (1F5F)
1F5F    707F    DATA
```

```
1F60    D833    WDS  13
1F61    0000    DATA A          Start pulse sequencer.

1F62    0000    LDA  (1F63)
1F63    C000    DATA
1F64    D833    WDS  13
1F65    0000    DATA A
1F66    CE00    IDL             Wait for sampling interrupt.
```

The first step is to reset the pulse sequencer by loading 20_{16} into the input mode register IC1 (see lines 1F40→43 in the listing). Note that due to the inverters in the buffer all data must be sent to the pulse sequencer in an inverted form, hence 70DF not 7020 in line 1F41. (The 70 in this command is the selection code for the mode register). The reset pulse clears the address counters (IC9→11), decade counters (IC26→31), control registers (IC7→8) and output registers (IC37→44 and IC51→54).

The sequencer is placed in the 'load data mode' (lines 1F44→47) by loading 10_{16} into IC1. This sends pin 2 on IC1 high and pin 3 low. Pin 2 disables the output buffers on the RAM chips (IC4→5) while pin 3 configures IC2→5 so data will flow directly from IC2 to memory.

Lines 1F48→4F load data into IC2 from which it is transferred into the first location in memory. The memory address counter is then incremented (lines 1F50→53) by loading 40_{16} and then 10_{16} into IC1 (thereby toggling output 2Q). The next byte is then loaded and the process repeated until all pulse sequence data has been transferred.

With the data loaded (in the format described in section 8.11) the experiment can commence. The pulse sequencer is first reset (lines 1F5A→5D) to point the memory address counter to the first instruction, and is then placed in the run mode by loading 80_{16} in IC1 (lines 1F5E→61). This starts the clock (IC34) running and automatically puts IC3→5 into the read mode (i.e. data flow out of memory).

With reference to the timing diagram in figure F.11 we see that on the first 5 high to low transitions of the clock the control, data and timing bytes are transferred from memory to registers IC7 and 8, IC6, and IC16→18 respectively. Data distribution is handled by the ring counter (IC32→33). When the data on the output of the decade counters (IC26→31) matches that on the timing registers a low going 125ns pulse is produced by IC19 which resets the ring counter and transfers the data in the output register IC6 to one of 6 8-bit registers (IC37→44 and IC51→54) determined by the contents of IC7 and 8 (the control register). From here the data is

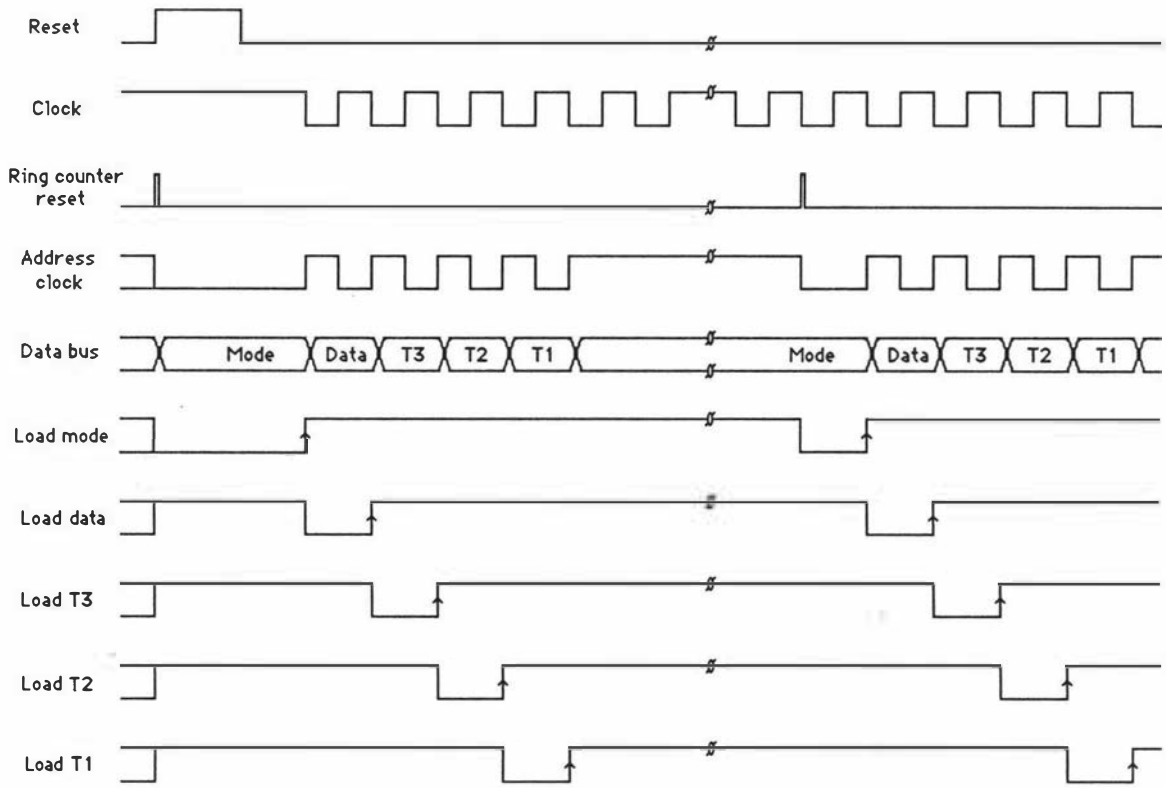

Figure F.11 Timing diagram for the pulse sequencer.

free to pass as either a 256 level analogue signal (IC45→48) or as a TTL level (IC51→54) to the outside world (e.g. the rf modulator and gradient controllers). The 8 bit digital to analogue converters produce a negative going signal which has a maximum magnitude of ~ 2V. This level may be adjusted with the preset pot VR1 or in the case of the gradients with the front panel controls VR2→4. Manual adjustment of the maximum gradient was found to be desirable as in many applications the range of gradient levels required is far below the maximum achievable (e.g. typical imaging gradients range from 0→10Gcm^{-1} while the maximum gradient is 100→200Gcm^{-1}).

When the ring counter is cleared the next 5 bytes are transferred from memory and the above process is repeated until an end of sequence flag is detected. This resets the pulse sequencer via IC12a and the system halts.

F.3 Graphics computer interface

Data transfer from the TI-980A to the Hitachi graphics computer is implemented with a very similar routine to the one just discussed except that the device selection code is now 80_{16}. The Hitachi is connected to the pulse sequencer buffer board via 6 metres of ribbon cable (see figure F.12 for a printed circuit board interconnection block diagram). A tristate buffer at the end of the cable (see figure F.13) plugs directly into the Hitachi Centronics port. This port is normally used to drive a printer and so to avoid conflicting logic levels when the computer is operating in a non-imaging mode the buffer board includes a transistor to switch the buffer outputs to a high impedance state when the voltage on pin 14 is high (the normal condition). When operating in the imaging mode the port is reconfigured to act as an input device and a zero logic level is sent to pin 14 to enable the buffer board).

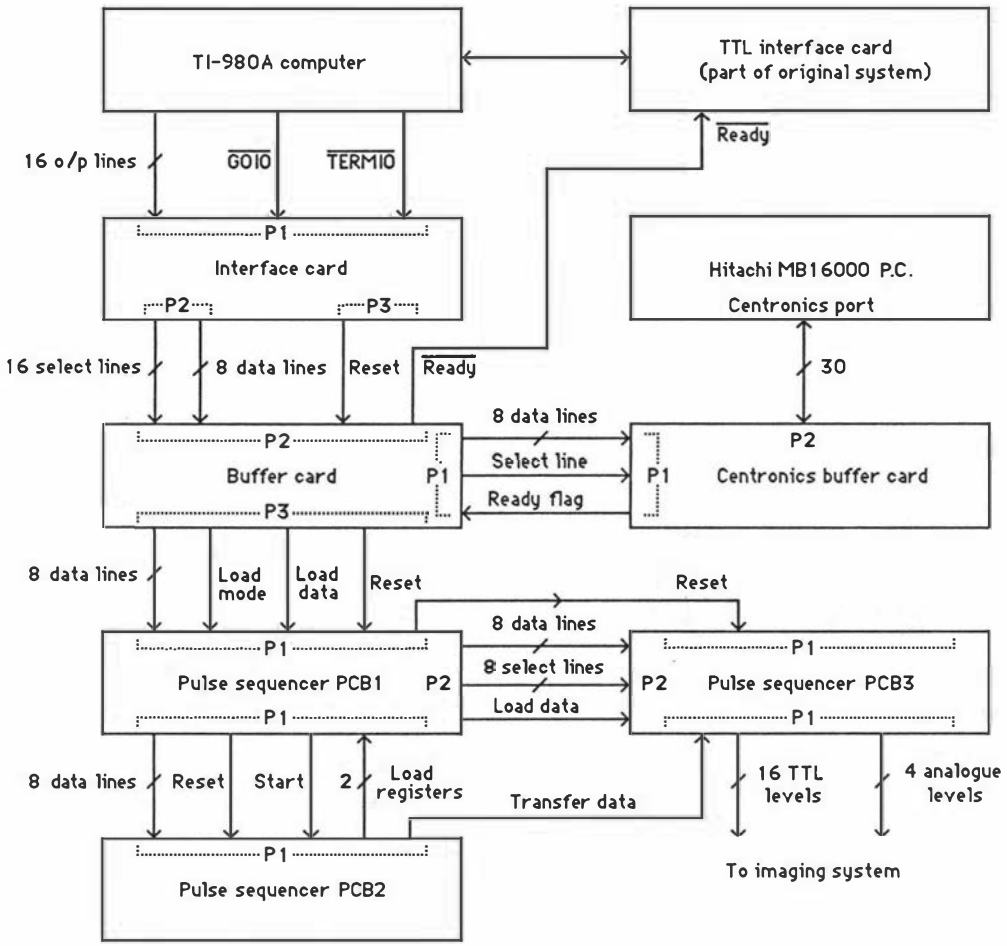

Figure F.12 PCB interconnections

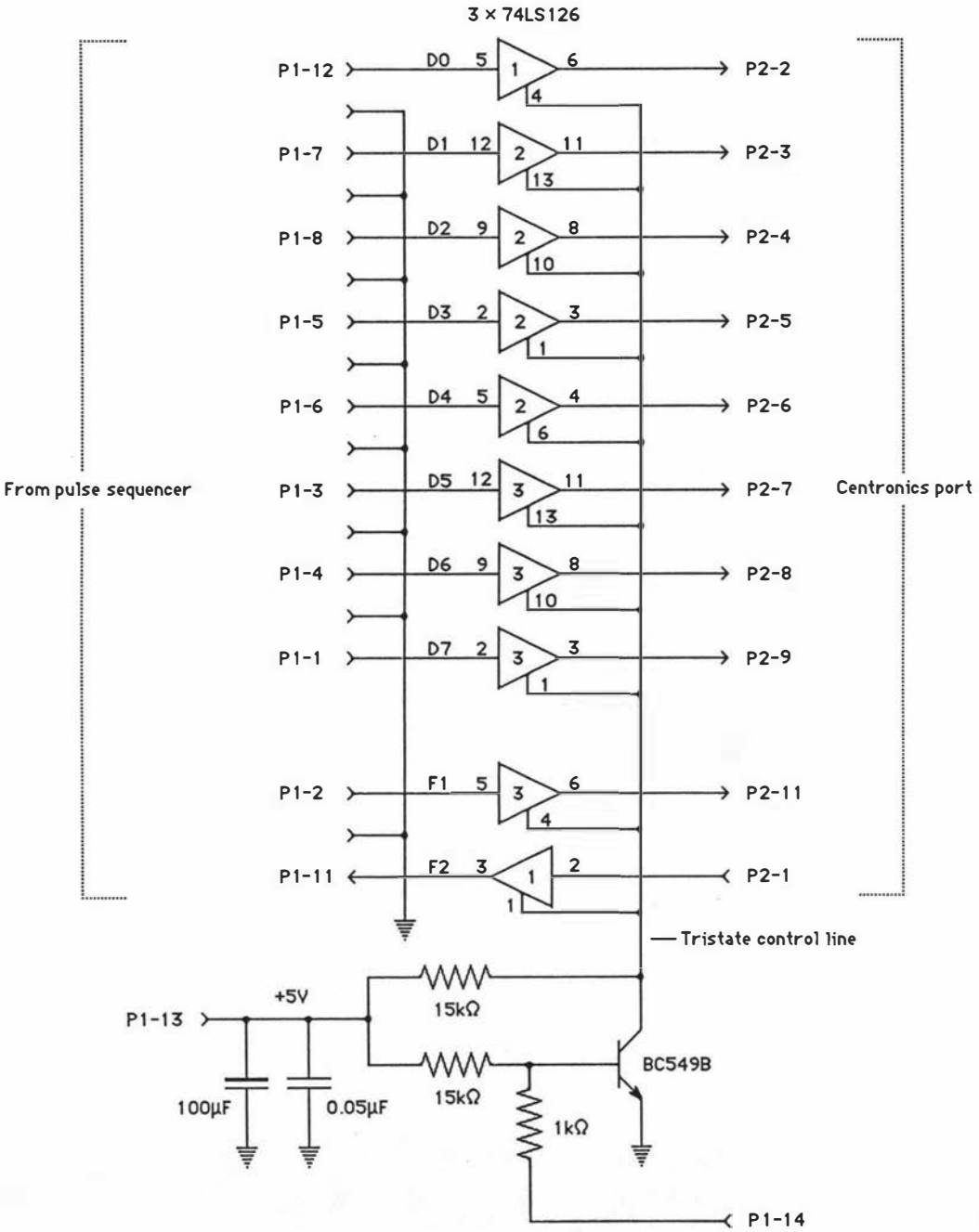

Figure F.13 Centronics buffer port.

APPENDIX G

G.1 Derivation of the attenuation coefficient R(G,δ,Δ)

To obtain an expression for the attenuation of the spin echo due to diffusion effects we must consider the motion of the nuclear spins during the pulse sequence outlined in section 9.2 and illustrated in figure 9.16.

Consider the motion of a group of magnetic moments which experience the same external fields. Following the application of the $90°|_x$ pulse (see figure G.1) the magnetization associated with this group will be directed along the y axis. At time τ, directly before the application of the 180° pulse the magnetization vector will be inclined at some angle φ to the y axis such that

$$\mathbf{M} = \mathbf{i}M_x \sin\varphi_0 + \mathbf{j}M_y \cos\varphi_0 \qquad (G.1)$$

and

$$\varphi_0 = \gamma \mathbf{G}.\mathbf{r_0} t \qquad (G.2)$$

where $\mathbf{r_0}$ is the position vector of the nucleus at the time the gradient pulse G is applied.

Following the application of the $180°|_y$ pulse the magnetization vector rotates about the y axis to give

$$\mathbf{M} = \mathbf{i}'M_x \sin\{-\varphi_0\} + \mathbf{j}'M_y \cos\{-\varphi_0\}. \qquad (G.3)$$

The application of the second gradient would, in the absence of any molecular motion, produce a clockwise precession about the z axis by an angle φ_0 thereby restoring the magnetization to its original position. However if we allow the nucleus to be displaced by $\mathbf{r}-\mathbf{r_0}$ during the time Δ we obtain the modified result

$$\mathbf{M} = \mathbf{i}'M_x \sin(\varphi_r-\varphi_0) + \mathbf{j}'M_y \cos(\varphi_r-\varphi_0) \qquad (G.4)$$

where the relative phase shift produced by this movement is

$$\varphi_r = \gamma \mathbf{G}.\mathbf{r}\ \delta. \qquad (G.5)$$

Equation G.4 can be handled more conveniently if we reexpress it in exponential form as

$$M(2\tau,\mathbf{G}) = M_0 \exp\{-j\gamma \mathbf{G}.(\mathbf{r}-\mathbf{r_0})\delta\}. \qquad (G.6)$$

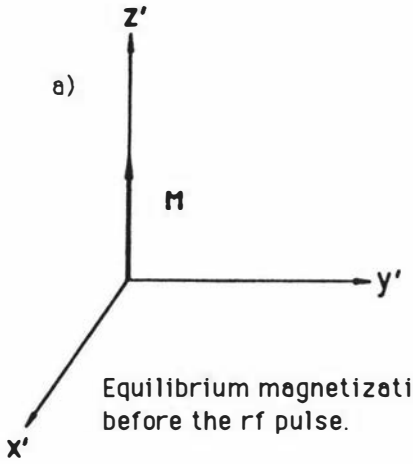

Equilibrium magnetization before the rf pulse.

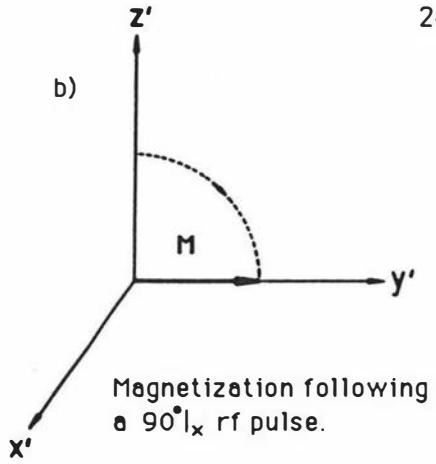

Magnetization following a $90^{\circ}|_x$ rf pulse.

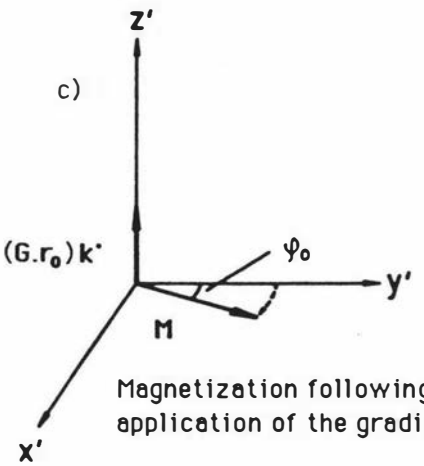

Magnetization following the application of the gradient pulse.

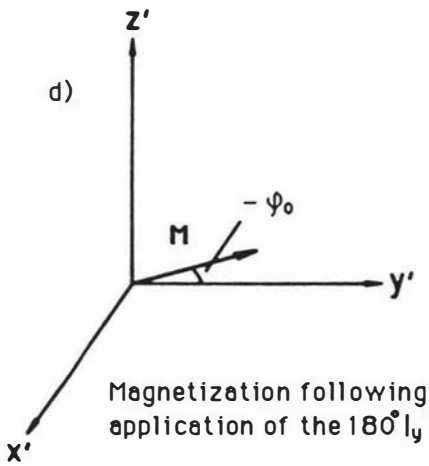

Magnetization following the application of the $180^{\circ}|_y$ pulse.

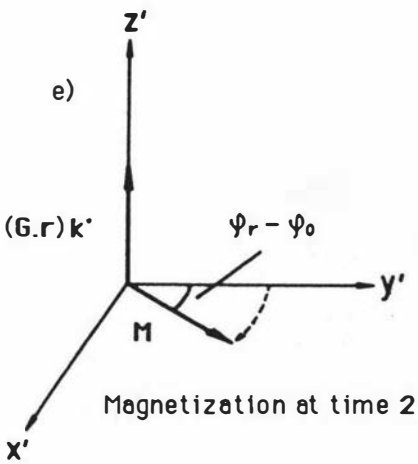

Magnetization at time 2τ.

Figure G.1 Motion of the magnetization vector due to a localized group of spins when the pulse sequence in figure 9.16 is applied.

The influence of relaxation may be incorporated by including a separate factor $\exp(-2\tau/T_2)$.

The net magnetization may be determined by summing the contribution from each group of spins. If we assume that our sample has uniform spin density the observed attenuation in the spin echo amplitude will be[39]

$$R(\mathbf{G},\delta,\Delta) = M(2\tau,G)/M(2\tau,0) = \int_V P_s(\mathbf{r_0}\,|\,\mathbf{r},\Delta)\ \exp\{-j\gamma\mathbf{G}.(\mathbf{r}-\mathbf{r_0})\delta\}\ dV. \qquad (G.7)$$

where $P_s(\mathbf{r_0}\,|\,\mathbf{r},\Delta)$ is a weighting function giving the probability that a spin will have moved from $\mathbf{r_0}$ to $\mathbf{r}$ in time Δ. We recall from section 3.1 that $(2\pi)^{-1}\gamma\mathbf{G}\delta$ may be identified as the reciprocal space coordinate $\mathbf{k}$, and so R may be viewed as the 3D Fourier transform of P_s.

For molecules undergoing free Brownian motion P_s is the solution to the isotropic diffusion equation

$$\partial P_s/\partial t = D\nabla^2 P_s \qquad (G.8)$$

which when evaluated gives

$$P_s = (2\pi\sigma^2)^{-3/2}\ \exp\{-(\mathbf{r}-\mathbf{r_0})^2/2\sigma^2\} \qquad (G.9)$$

where

$$\sigma^2 = 2Dt \qquad (G.10)$$

D being the molecular self diffusion coefficient. P_s corresponds to the product of the probabilities $P_s(x_0\,|\,x,\Delta)P_s(y_0\,|\,y,\Delta)P_s(z_0\,|\,z,\Delta)$ and so we identify σ^2 as the mean square displacement of molecules along one axis during time Δ. The mean square displacement in three dimensions is therefore given by the sum [47]

$$\sigma_r^2 = \sigma_x^2 + \sigma_y^2 + \sigma_z^2 = 6Dt. \qquad (G.11)$$

Having obtained an expression for P_s the attenuation factor is readily evaluated since

$$R(\mathbf{G},\delta,\Delta) = \int_V (2\pi\sigma^2)^{-3/2}\ \exp\{-(\mathbf{r}-\mathbf{r_0})^2/2\sigma^2\}\exp\{-j\ \mathbf{k}.\mathbf{r}\}\ dV \qquad (G.12)$$

This integral may be evaluated by separating the terms as follows

$$R(G,\delta,\Delta) = (2\pi\sigma^2)^{-3/2} \int_{-\infty}^{\infty} \exp\{-jk_x(x-x_0)-(x-x_0)^2/2\sigma^2\}dx$$
$$\times \int_{-\infty}^{\infty} \exp\{-jk_y(y-y_0)-(y-y_0)^2/2\sigma^2\}dy \int_{-\infty}^{\infty} \exp\{-jk_z(z-z_0)-(z-z_0)^2/2\sigma^2\}\}dz \quad (G.13)$$

Each integral may then be solved separately resulting in the following function

$$R(G,\delta,\Delta) = \exp\{-k_x^2\sigma^2/2\}\ \exp\{-k_y^2\sigma^2/2\}\ \exp\{-k_z^2\sigma^2/2\} = \exp\{-k_r^2\sigma^2/2\}$$
$$= \exp\{-\gamma^2G^2\delta^2D\delta\Delta\}. \quad (G.14)$$

Note that this result is an approximation which is only valid for times $\delta<<\Delta$. The exact expression for R has been derived by Stejskal and Tanner[34] who obtain

$$R(G,\delta,\Delta) = \exp\{-\gamma^2G^2\delta^2D(\Delta-\delta/3)\}. \quad (G.15)$$

Equation G.14 is therefore a good approximation in the domain $\delta<<\Delta$, but for those situations where this is not the case we can define an effective observation time which has the reduced value

$$\Delta_r = \Delta - \delta/3. \quad (G.16)$$

PUBLICATIONS

1. C.D. Eccles and P.T. Callaghan, "High-resolution imaging. The NMR microscope",Journal of Magnetic Resonance, **68**, p393, 1986.

2. P.T. Callaghan and C.D. Eccles, "Sensitivity and resolution in NMR imaging", Journal of Magnetic Resonance, **71**, p426, 1987.

3. C.D. Eccles and P.T. Callaghan, "NMR microscopy", Jeol News, **23A**, 10, 1987.

4. C.D Eccles, P.T. Callaghan, C.F. Jenner, "Combined pulsed gradient spin-echo/NMR imaging used to measure localised self-diffusion of water in wheat grain", Biophysical Journal, Submitted 1986.

BIBLIOGRAPHY

1. P.C. Lauterbur, Nature (London) **242**, p190, 1973.
2. P. Mansfield and P.K. Grannel, Journal of Physical Chemistry **6**, p422, 1973.
3. P.C. Lauterbur, Pure Applied Chemistry, **40**, p149, 1974.
4. W.S. Hinshaw, Journal of Applied Physics, **47**, p3709, 1976.
5. L.D. Hall, S. Luck and V. Rajanayagam, Journal of Magnetic Resonance, **66**, p349, 1986.
6. A. Abragam, **The Principles of Nuclear Magnetism**, Clarendon Press, Oxford, 1961.
7. D.C. Look and I.J. Lowe, Journal of Chemical Physics **44**, p2995, 1966.
8. P. Mansfield and P.G. Morris, Advances in Magnetic Resonance, Suppl. 2,1982.
9. P. Mansfield, A.A. Maudsley, P.K. Morris, and I.L. Pykett, Journal of Magnetic Resonance, **33**, p261, 1979.
10. D.R. Bailes and D.J. Bryant, Contemporary Physics, **25**, No. 5, 1984.
11. D.I. Hoult, Journal of Magnetic Resonance, **35**, p69, 1979.
12. A. Kumar, D.Welti and R.R. Ernst, Journal of Magnetic Resonance, **18** , p69, 1975.
13. W.A. Edelstein, J.M.S. Hutchinson and G. Johnson, Journal of Physics E, **13** , p947, 1980.
14. R.A. Brooks and G. DiChiro, Phys. Med. Bio. **21** , p689, 1976.
15. D.I. Hoult, Progress in NMR spectroscopy, **12** , p41, 1978.
16. D.I. Hoult and R.E. Richards, Journal of Magnetic Resonance, **24**, p71, 1976.
17. See for example J. Krauss and K. Carver, **Electromagnetics**, McGraw Hill, London,1981.
18. Ref. 6 page 83.
19. J.C. Lindon and A.G. Ferrige, Progress in NMR spectroscopy, **14** , p27, 1980.

20. R.R. Ernst, Advances in Magnetic Resonance, **2**, p1, 1966.

21. Ref. 8 page 36.

22. Ref. 6 page 93.

23. D.A. Ortendahl, L.E. Crooks and L. Kaufman, **30**, p692, 1983.

24. J.S. Waugh, Journal of Molecular Spectroscopy, **35**, p298, 1970.

25. A. Hasse, et al. , Journal of Magnetic Resonance, **67**, p258, 1986.

26. P.T. Callaghan and C.D. Eccles, Journal of Magnetic Resonance, **71**, p426, 1987.

27. N. Feng, J. Frahm, D.Matthaei, W Haniche and K.D. Merbolt, Journal of Magnetic Resonance, **66**, p385, 1986.

28. J.F. Martin, Journal of Magnetic Resonance, **65**, p291, 1985.

29. D. Roddy and J. Coolen, **Electronic communications**, Prentice-Hill, Reston Virginia, 1984.

30. W. Anderson, Review of Scientific Instruments, **32**, No. 3, 1961.

31. D.S. Webster and K.H. Marsden, Review of Scientific Instruments, **45**, No. 10,1974.

32. P.T. Callaghan, C.M. Trotter, and K.W. Jolley, Journal of Magnetic Resonance, **37**, p247, 1980.

33. G. Bergland, Communications of the ACM, **11** , No. 10, 1968.

34. E.O. Stejskal, Journal of Chemical Physics, **42**, p288, 1965.

35. R. Mills, The Journal of Physical Chemistry, **77**, No. 5, p685, 1973.

36. G.R. Donovan, C.F. Jenner, J.W. Lee and P. Martin, Australian Journal of Plant Physiology, **10**, p 31, 1983.

37. C.F. Jenner, private communication.

38. E.O. Stejskal, Journal of Chemical Physics, **43**, No. 10, p3597, 1965.

39. P.T. Callaghan, Australian Journal of Physics, **37**, p359, 1984.

40. P. Bendel, Ching-Ming Lai and P.C. Lauterbur, Journal of Magnetic Resonance, **38**, p343, 1980.

41. L.D. Hall, V Rajanayagam and S. Sukumar, Journal of Magnetic Resonance, **61**, p188, 1985.

42. A. Hasse and J. Frahm, Journal of Magnetic Resonance, **64**, p94, 1985.

43. L. Axel and L. Dougherty, Journal of Magnetic Resonance, **66**, p194, 1986.

44. C.D. Eccles and P.T. Callaghan, Journal of Magnetic Resonance, **68**, p393, 1986.

45. J.B. Aguayo, S.J. Blackband, J. Schoeniger, M.A. Mattingly and M. Hintermann, Nature, **322**, No.10, p190, 1986.

46. J.W. Cooley and J.W. Tukey, Mathematical Computing, **19**, p297, 1985.

47. P.T. Callaghan, private communication.